Hierarchical Metal Oxides for Photoelectrochemical Water Oxidation and Sensing Applications

A Dissertation Submitted to the

Indian Institute of Technology Guwahati

in Partial Fulfilment for the Degree of

DOCTOR of PHILOSOPHY

by

Suhaib Alam

DEPARTMENT OF CHEMISTRY

INDIAN INSTITUTE OF TECHNOLOGY GUWAHATI

GUWAHATI, ASSAM, INDIA

SEPTEMBER 2021

STATEMENT

I hereby declare that the scientific findings included in this thesis entitled, "**Hierarchical Metal Oxides for Photoelectrochemical Water Oxidation and Sensing Applications**" is the outcome of research work carried out by me under the supervision of Prof. Mohammad Qureshi, at Department of Chemistry, Indian Institute of Technology Guwahati, Guwahati, Assam, India, for the award of the degree of Doctor of Philosophy.

The work embodied in this thesis is the result of original research done by me except where otherwise stated in this thesis with proper citations. I confirm that the investigations were conducted in accord with the ethics policies and integrity standards of Indian Institute of Technology Guwahati and that the research data are presented honestly and without prejudice. The thesis work has not been submitted for a degree or professional qualification to any other university or institution.

IIT Guwahati **Suhaib Alam**

SEPTEMBER 2021 Candidate

Dr. Mohammad Qureshi
Professor
Department of Chemistry
Indian Institute of Technology Guwahati
Guwahati – 781039, India
Tel: +91 – 361 – 2582320;
Fax: +91 – 361 – 2582349
Email: mq@iitg.ac.in

Certificate

Certified that the work described in this thesis entitled "**Hierarchical Metal Oxides for Photoelectrochemical Water Oxidation and Sensing Applications**" by Mr. Suhaib Alam, Department of Chemistry, Indian Institute of Technology Guwahati has been carried out under my supervision and has not been submitted elsewhere for a degree.

Guwahati
SEPTEMBER 2021

Mohammad Qureshi
Thesis supervisor
Department of Chemistry
Indian Institute of Technology Guwahati
Guwahati – 781039, Assam, India

ACKNOWLEDGEMENT

First of all, I thank almighty Allah for giving me a gracious life, strength to chase my dreams, and being with me in all my failure and success

The successful outcome of my thesis work has many supporting hands without which it was not possible to make it a reality. Today, while bringing it to the end, I would like to thank everyone who supported me directly or indirectly throughout the years. Words are inadequate to express my gratitude to the people who have contributed to this thesis and supported me in one way or the other during this truly memorable and overwhelming journey.

It gives me immense pleasure to express my deepest gratitude to my thesis supervisor Prof. Mohammad Qureshi for providing me a precious opportunity to work in his group. His continuous support, scientific guidance, deep insights, patience and motivation encouraged me to take up the tasks that otherwise were hard and demanding. I sincerely thank him for having trust in me and giving me total freedom in choosing the direction of my research. I feel fortunate to having him as my mentor who always motivated me with his hard work, dedication and optimism. Thank you, sir, for continually being a path shower in my life.

I would also like to extend my heartiest thanks to my doctoral committee members, Dr. Kalyan Raidongia, Pro. Parameswar Krishnan Iyer, and Prof. Aditya Narayan Panda, for their valuable suggestions and periodic evaluation throughout my PhD work. I sincerely thanks to my collaborators, Dr. Nageswara Rao Peela and Devipriya Gogoi for their continuous helps and support. I also thank to Prof C. V. Sastri for providing CH instrument facility. I would like to thank all the faculty members and staff members of Chemistry department. My sincere thanks to the staffs of Central Instruments Facility, for their help and in hand guidance to several analytical instruments, required during my research work. Special thanks to Dr. Kula Kamal Senapati sir for giving me the opportunity to operate FESEM instrument. I wish to express my sincere gratitude to IIT Guwahati for fellowship and all other facilities that were made available to me and the Ministry of Science and Technology, India for the financial support.

Without a modicum of doubt MSL team deserve the best and utmost respect for their hard work, diligence, and indispensable input into the overall research work. I would like to thank all my senior group member Dr. Anindya Sundar Patra, Dr. Mohammad Shaad Ansari, Dr. Avishek Banik, Dr. Gaurangi Gogoi, Dr. Tushar Kanta Sahu

and present lab members Adit, Moite, Sourav, Manoj, Alpana and Nitul for their timely help, support and for creating a pleasant atmosphere in the lab. A special thanks to Dr. Shaad, and Dr. Avishek for teaching me basics, experiments and handling instruments in the initial periods of my research work.

A special thanks to all my seniors, juniors and friends from AMU; Afzal Bhai, Sameer Bhai, Akhtar Bhai, Sahnawaz Bhai, Wajid Bhai, Kripa Da, Zia bhai, Adil Afroz Bhai, Shaad Bhai, Kafeel Bhai, for giving me unforgettable moments and delightful experiences.

I am also thankful to my family members, Mr Ameen Ansari, Mr Zakir Hussian, Mr Mohd Zamin, Mr Ayyub Ansari, Mrs Husna Parveen, Mrs Nazma, Mr Shahbuddin, Mr Sulaiman, Firoz Ameen & Late Abdul Manan Ameen, Little stars my nephews, niece and nieces (Shifa, Falak, Hasnain, Zaidan, Tariq, Sariq)

Finally, my Ph. D. endeavor could not have been completed without the endless love, unending support, tolerance and blessings from my family. I would like to express my deepest gratitude to my parents (Mr Shakir Hussain & Mrs Shajahan Begum) for their prayers, unconditional love and sacrifices they have made to complete my dreams. I am also grateful to my sisters (Yasmin & Nasrin), brothers (Sajid) and cousins (Gulnaz, Sania, Mukarrama, Ikra, Ahmad, Rayyan and Unjila) for their eternal love, affection and emotional support which had immensely needed during Ph.D. tenure.

Still many more names are missing whose contribution and help is worth mentioning.

Suhaib

TABLE OF CONTENTS

TABLE OF CONTENTS

DEDICATED TO

MY PARENTS FOR THEIR

ENDLESS LOVE AND SUPPORT

Thesis Title:	**Hierarchical Metal Oxides for Photoelectrochemical Water Oxidation and Sensing Applications**
Name of the Candidate:	Mr. Suhaib Alam
Registration Number:	166122019
Thesis Supervisor:	Prof. Mohammad Qureshi
Department:	Chemistry
Institute:	Indian Institute of Technology Guwahati, Assam – 781039, India.

Thesis Overview

I: Recent advances in the design and development of semiconductor metal oxides, based on their morphologies and hetero-structures, enhances the charge transport as well as the light-harvesting ability are discussed. A brief discussion on the basic concepts, mechanism, and working principle of photoelectrochemical water splitting are also included. It also comprises a short description of the performance parameters associated with the photoanode. A summary of the literature survey and issues related to the design and development of semiconductors utilized for photoelectrochemical applications are included. Advantages and disadvantages associated with narrow and wide bandgap materials and strategies to improve the charge separation/injection and light-harvesting ability are discussed. Different surface modification strategies used for tuning the surface activity are of high cost, low abundance, and environmentally unfriendly. Therefore, low-cost and environmentally benign strategies have been applied to overcome the shortcomings encountered by these materials. A brief discussion related to the development of Chemiresistor device, basic architecture, and working principle for gas sensing is also included. Finally, the introduction part concludes with the motivation and objective behind the designing of different metal oxides-based photoanodes.

II: Interfacial Bridging Strategy for Charge Extraction/Injection in $BiVO_4$/CoSn-LDH p-n Heterojunction using GQDs for Enhanced Water Oxidation Kinetics

(Part of this chapter has been published in **J. Phys. Chem. Lett.,** 2021, 12, 8947-8955**)**

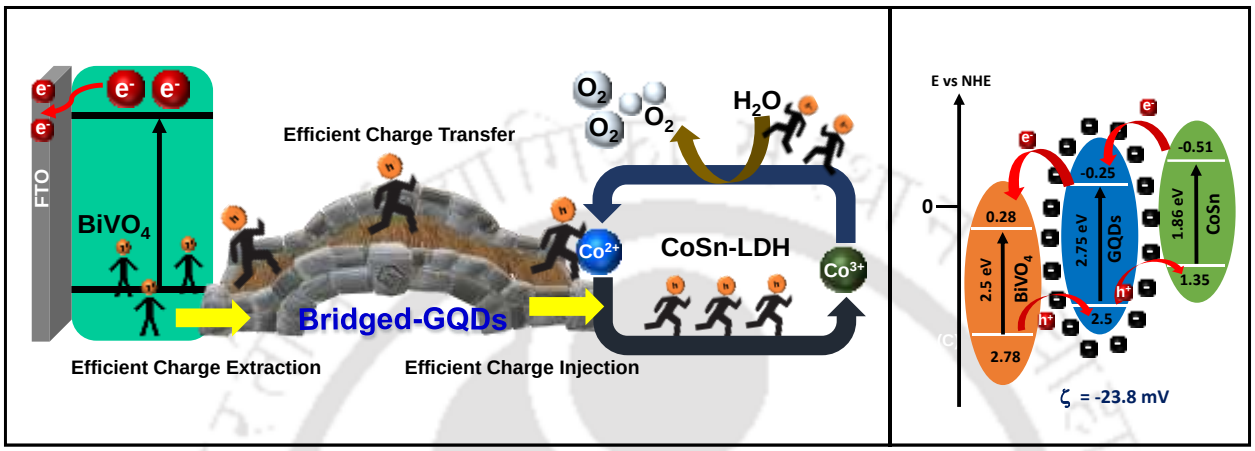

In this chapter, we have outlined the idea of a ternary photoanode $BiVO_4$/GQDs/CoSn-LDH, in which CoSn-LDH act as surface active sites and GQDs as a conductive linker to extract holes from the $BiVO_4$ surface. n-type $BiVO_4$ is an ideal candidate for photoanode material for solar driven photoelectrochemical water splitting, due to its proper band alignment, non-toxicity, and higher stability in alkaline and neutral pH. Cobalt based co-catalyst CoSn-LDH is prepared which shows the p-type conductivity to form a p-n heterojunction. But the difference in band positions of $BiVO_4$ and CoSn-LDH is a little bit high for efficient charge injection. Therefore, GQDs, a conductive linker is integrated between $BiVO_4$ and CoSn-LDH as a bridged. GQDs provides extra driving force to extract holes from $BiVO_4$ surface, due to the presence of negatively charged species and transfers to CoSn-LDH, which accelerate the transportation of holes to electrolyte for enhanced water oxidation reaction. Considering the possible built-in potential formed at the interface, the photo-excited holes in $BiVO_4$ are expected to be easily transferred to CoSn-LDH through bridged GQDs conductive linker.

III: Co(OH)F as a Noble Metal-Free Redox Mediator and Hole Extractor for Boosted Photoelectrochemical Water Oxidation in Worm-like Bismuth Vanadate

(Part of this chapter has been published in **ACS Sustainable Chem. Eng.** 2021, 9, 5155)

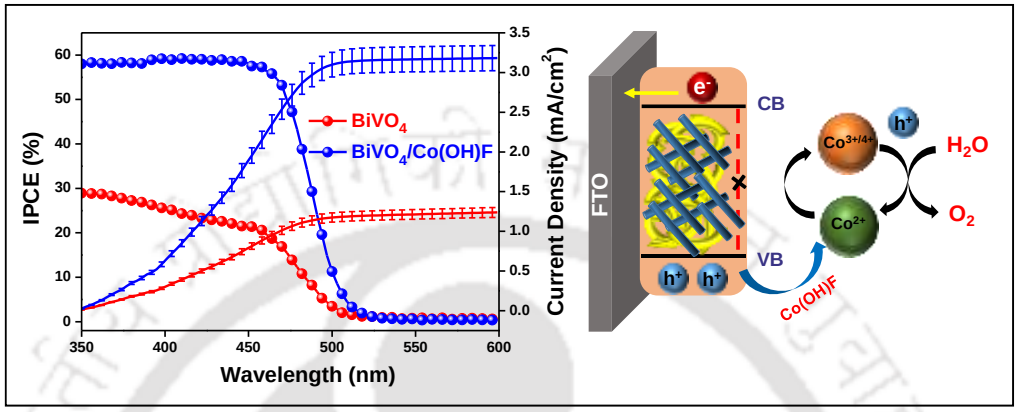

Cobalt based materials have long been recognized as promising co-catalysts for application in photoelectrochemical water splitting. Commonly used co-catalysts are Co-Pi, $Co(OH)_X$, Co_3O_4, and CoOOH. Compared to phosphorus and oxygen in Co─P and C─O systems, due to the higher electronegativity of fluorine, the Co─F bond provides more positive charges on the metal center for efficient shuttling of the redox couple, beneficial for enhanced OER. The catalytic activity of cobalt is enhanced after the incorporation of non-metal elements, as they tend to reduce the thermodynamic and kinetic barrier. The conductivity, as well as the charge mobility, is improved due to the presence of Fluoride in $Co(OH)_X$, thereby improving the electro-catalytic activity. Therefore, **Co(OH)F** nanorods have been designed as an efficient co-catalyst and coupled with $BiVO_4$ photoanode for efficient photoelectrochemical water oxidation. In comparison to their bulk counterparts, 1D nanostructures such as nanotubes, nanorods, and nanowires have advantages in many catalytic areas. These advantages were mainly due to facile charge separation and a shorter diffusion path for minority carriers to reach the photoanode/electrolyte interface.

IV: Bio-template Assisted Hierarchical ZnO Superstructures Coupled with Graphene Quantum Dots for Enhanced Water Oxidation Kinetics

(Part of this chapter has been published in **Sol. Energy**, 2020, 199, 39)

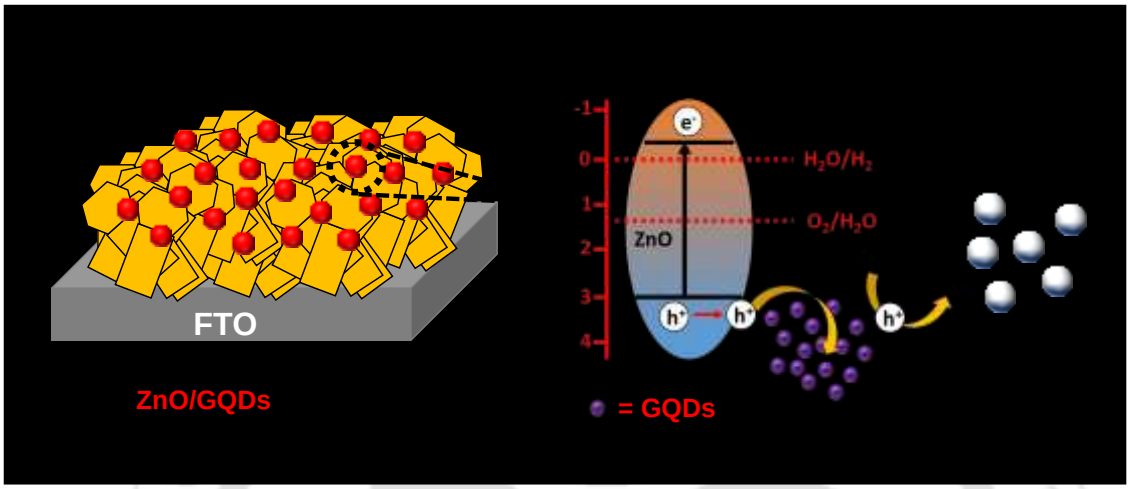

In this chapter, a rational approach is demonstrated to enrich the transport phenomenon with an improved collection of photo-excited holes, utilizing Graphene quantum dots as the hole extracting materials in achieving highly efficient photoelectrochemical water oxidation. Due to the anisotropic growth behavior and tunable electrical properties, ZnO nanostructures having dimensions such as 0-D, 1-D, 2-D, and 3-D are actively studied for their optoelectronic properties. Here, we have directly grown hierarchical ZnO superstructures over fluorine-doped tin oxide (FTO) under a controlled hydrothermal reaction. We have utilized an anionic polysaccharide “Polygalacturonic Acid” for monitoring the hetero-epitaxial aggregated growth of ZnO building blocks. The non-classical growth mechanism is accounted as the origin of these superstructures, through the interaction between the polysaccharide and ZnO nanocrystal growth units. It is evident from the growth mechanism; Polygalacturonic acid assisted as a self-assembling agent to fabricate the superstructures. Further, these hierarchical ZnO superstructures were decorated with Graphene Quantum Dots to get significant enrichment in photocurrent.

V: Ultrasensitive NO_X detection in Simulated Exhaled Air: Enhanced Sensing via Alumina Modification of *In-situ* Grown WO_3 Nano blocks

(Part of this chapter has been published in **Chem. – Asian J.**, 2019, 14, 4673)

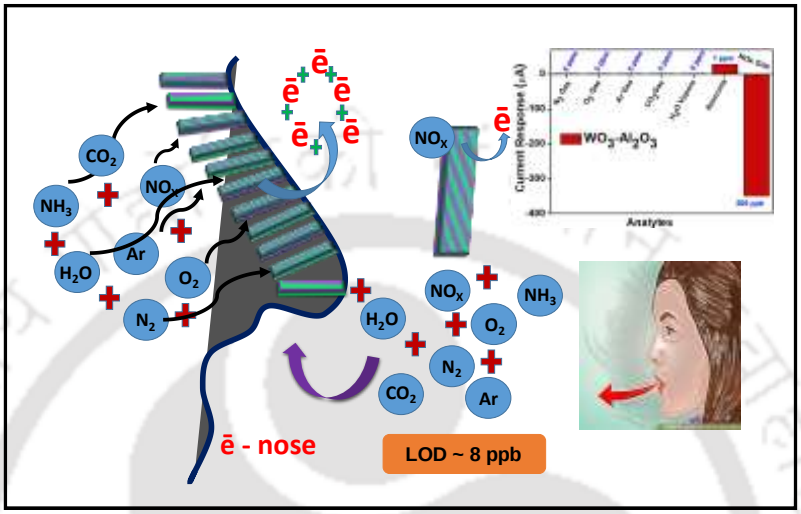

Vertically aligned Nano-structural features, which can minimize Ohmic contact between semiconductor and collecting electrode, will aid smoother transport of charge carriers, thereby enhancing the sensitivity of the devices. Such an approach is critical, wherein ultrasensitive detections are needed at very low concentrations of analytes, which results in smaller current values in terms of detection. Sensor, which can detect ultra-low concentrations of NO_X gas in the exhaled breath in presence of other interfering gases and volatile organic components, offers a simple, fast, and non-invasive diagnostics tool for pulmonary diseases like Asthma. In this chapter, we have fabricated a sensor device by directly growing a controlled phase of WO_3 in the form of Nano-blocks, over conductive glass substrate i.e., fluorine-doped tin oxide (FTO) under controlled hydrothermal conditions followed by the deposition of porous γ-Al_2O_3 for the selective detection of NO_X gas present in the human breath. Gas sensing is carried out by fabricating the two-terminal Chemiresistor devices based on bare and modified γ-Al_2O_3 - WO_3 structures.

CHAPTER 1

Introduction and literature survey

This chapter is a comprehensive overview of principles and literature on photoelectrochemical water oxidation and sensing. A brief survey of current state of art scenario and challenges associated with the design and development of photoanode materials utilized for photoelectrochemical water oxidation are discussed. Several strategies used to enhance the surface reaction kinetics of metal oxide-based photoanodes are discussed. In the later section, a brief discussion corresponds to the development of chemiresistor device, basic architecture, and working principle of sensor are also included.

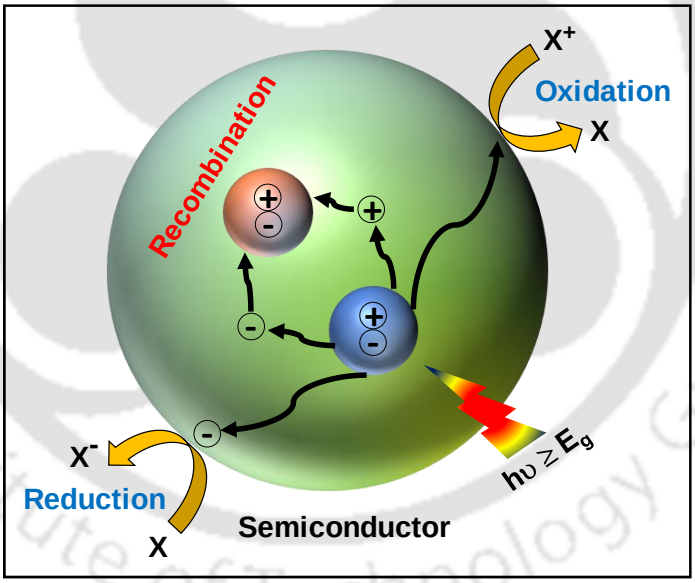

1.1 Global Energy Outlook

From the genesis of civilization to the commencement of industrial revolution, fossil fuels have been the primary resource of energy and human growth. Rapid advances in society with good living standards elevated the global energy consumption. In recent years, global energy consumption has increased substantially and is projected to increase continuously in the near future. It is estimated that in 2018, the world energy expenditure was around 575 exajoule (EJ) (EJ = 10^{18} Joules) whereas, in 2050, the speculated world energy expenditure will be around 725 EJ. The bar diagram presented in **Figure 1.1 (A)** shows the shift in global energy consumption as well as the estimated energy demand in future, while the pie chart in **Figure 1.1 (B)** shows the share of total energy supply from different sources in 2019[1-2].

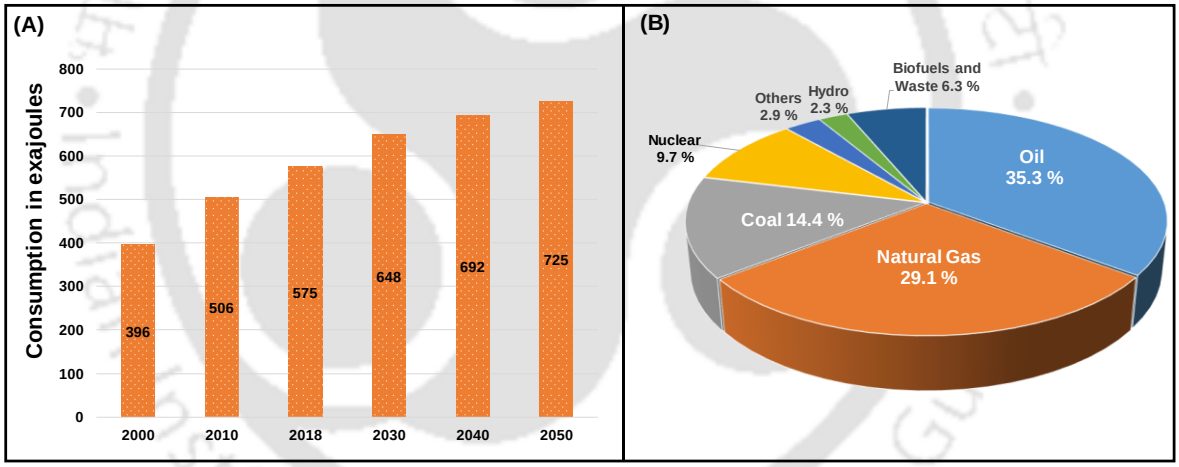

Figure 1.1 (A) Bar diagram showing worldwide energy consumption in past and estimated consumption in future in exajoules and (B) Pie chart showing the global energy supply from different resources in the year 2019

Here, it is noteworthy to mention that 80 % of the total energy consumption is predominantly contributed by the fossil fuels such as oil, natural gas, and coal. The burning of these fossil fuels releases several greenhouse gases particularly carbon dioxide (CO_2), triggering ecological imbalance, which has an adverse effect on the environment[3]. CO_2 emitted into the atmosphere absorbs infrared radiation and increases the average temperature of the earth. In addition, CO_2 emission has increased linearly throughout the decade with an average

growth rate of 2.3 ppm per year[3]. According to the report of the Intergovernmental Panel on Climate Change (IPCC), the temperature increase due to global warming should not exceed 2˚C and the carbon dioxide content in the atmosphere 450 ppm, to avoid the catastrophic consequences[3-4]. If fossil fuel emission rate continues this way, then the greenhouse gases accumulating in the atmosphere will pose a serious threat to the environment. Therefore, it is important to adopt alternative energy sources, to reduce greenhouse gas emissions and to meet current and future energy requirements. Simultaneously, it should also be ensure that the presented new energy sources must be free from the negative impact of carbonaceous fuels[5].

1.2 Renewable Energy Sources

Compared to the traditional geographically concentrated energy sources, renewable energy sources have the potential to be widely used on a large scale due to the globally dispersed resources. **Figure 1.2** offers a brief view of the energy reserves available on earth, which demonstrates the dominant position of solar energy among all the resources[6]. Of the available renewable energy sources, such as hydropower, geothermal energy, solar, wind, and biomass, solar energy is the only sustainable energy source that meets the energy need of a growing population. About 30 % of the incident solar radiation is reflected and plays no role in Earth's climate system. 70 % of solar energy absorbed by the earth per year is roughly equals to 3.85 million exajoules. In other words, the amount of solar energy hitting earth in one hour is more than enough to power the world for one year[6]. Undoubtedly, solar energy is the utmost abundant renewable energy source, which can be harvested and transformed into various forms of energy for practical applications to meet all energy requirements. Several technologies such as solar thermal, solar fuels, and photovoltaic are available for the utilization of solar energy[7]. Photovoltaic, as a model for solar energy utilization, is the fastest growing industry with the most disseminated technology and plays a vital role in capturing solar energy to convert into electrical energy. However, photovoltaic is limited to a great extent due to the difficulty in

storing the electricity produced by the technology. In this context, solar energy conversion into chemical energy/fuel supported by appropriate storage is considered a remarkable approach[8-9].

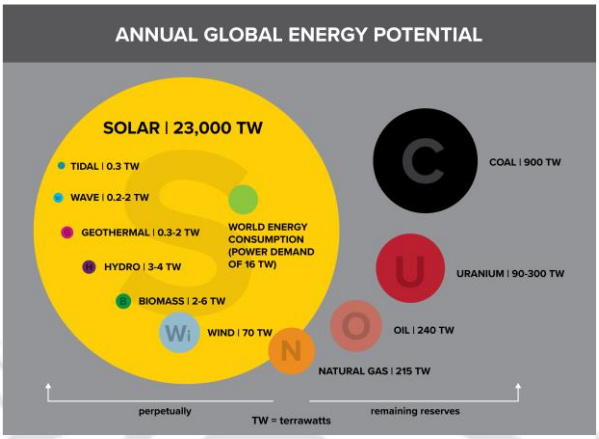

Figure 1.2 provides a brief view of the energy reserves available on the earth, which demonstrates the dominant position of solar energy among all renewable and non-renewable energy sources (Source: https://climatechange.ucdavis.edu/climate-change-definitions/how-is-solar-power-generated/)

Hydrogen (H_2) as a fuel is an elegant choice with a high gravimetric heating value (141.9 MJ/kg^{-1}), that does not emit any harmful substance. Combustion of hydrogen gives water as the only product, thus bringing forth a bright future for zero-emission processes[10]. Hydrogen can be produced by a wide variety of methods and depending on the raw material used; the process can be divided into two main categories, such as traditional and renewable energy sources. In the first category, i.e., from fossil fuels, H_2 can be generated by hydrocarbon reforming and pyrolysis processes through steam reforming and partial oxidation techniques. On the other hand, the second category, i.e., renewable energies include electrolysis, photo-electrolysis, and thermolysis or biological methods to produce H_2 from water and biomass respectively. Fossil fuels are accounted for 95 % of the global hydrogen production through the steam reforming technique, whereas 4 % hydrogen is produced from water using electricity and 1 % is produced from biomass[11-12]. Of the various techniques used to produce H_2 fuels, photoelectrochemical water splitting is fascinating and has the potential to become an extensive pathway for future energy production.

1.3 Photoelectrochemical (PEC) Water Splitting

An early breakthrough in solar energy conversion came when Fujishima and Honda reported the seminal work on photoelectrochemical water splitting using light energy to split water into hydrogen and oxygen. Since then, PEC water splitting has attracted growing interest and postulated as the most feasible approach to produce sustainable hydrogen fuel[13]. The working principle of PEC water splitting is the same as the conventional electrolysis where anode and cathode are immersed in an electrolyte solution to give oxygen and hydrogen at respective electrodes, when applied an electric current. The only difference is that, in PEC, the system-generated oxygen and hydrogen can be separated in a different compartment. In the PEC system, one of the photoelectrodes is a semiconductor, which has the ability to absorb light under illumination. Typically, when a photon having energy equal to or more than the semiconductor's bandgap energy strikes with the semiconductor surface, it generates an electron-hole pair, separated by the electric field between electrolyte and semiconductor. In an n-type photoanode, these holes (h^+) migrates to the semiconductor/electrolyte interface and oxidize water into O_2 whereas electron (e^-) moves to cathode through the external circuit to take part in the water reduction process to produce H_2[14-17]. A schematic representation of chemical reactions occurring at different electrodes is shown in **Figure 1.3.1** whereas the energetic view of H_2 production is summarized in equations:

$$\text{Cathode: } 2H^+ + 2e^- \rightarrow H_2\ ;\ E^0_{\text{reduction}} = 0V \qquad (1.1)$$

$$\text{Anode: } 2H_2O + 4h^+ \rightarrow O_2 + 4H^+\ ;\ E^0_{\text{oxidation}} = 1.23V \qquad (1.2)$$

$$\text{Overall water} - \text{splitting: } 2H_2O \rightarrow 2H_2(g) + O_2(g) \qquad (1.3)$$

Under standard conditions, + 237.2 KJ/mol of Gibbs free energy change (ΔG) is required to convert one molecule of H_2O into H_2 and ½ O_2, correspond to 1.23 eV. Therefore, a semiconductor material with a minimum bandgap of 1.23 eV is required to facilitate water splitting. Apart from the bandgap, another factor that dominates the water-splitting ability is

band positions. For a water-splitting reaction, the valence band of the semiconductor must be more positive than the oxidation potential of H_2O/O_2, whereas the conduction band of the semiconductor must be more negative than the reduction potential of H^+/H_2[18-20].

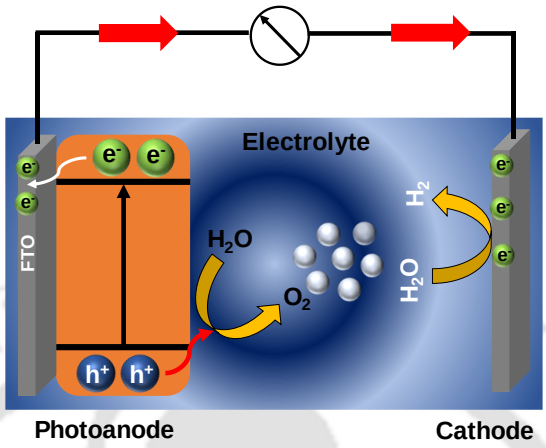

Figure 1.3.1 Schematic representation shows the basic diagram for photoelectrochemical water splitting to produce O_2 at photoanode and H_2 at the cathode

Since PEC is a complex process, therefore several phenomena need to be optimized for efficient PEC water splitting, such as (i) light-matter interaction or absorption, (ii) generation of electron-hole pair, (iii) charge separation and transfer, (iv) catalytic charge transfer to the electrolyte for water splitting[5]. Most of the solar radiation that strikes the Earth's surface is in the visible range, so it is important to choose a semiconductor material with an appropriate bandgap that can absorb the maximum amount of light. Recombination of photogenerated charge carriers is one of the major reasons that affect the performance of a PEC device. Therefore, a semiconductor must have a suitable bandgap as well as band positions for effective water splitting reactions. In addition, a semiconductor with high carrier mobility and long diffusion length is required to ensure reduced recombination. Due to the multi-electron transfer involved in the reaction mechanism of water oxidation, it generally requires high overpotential owing to the sluggish kinetics of the photoanode. To reduce the overpotential, photoelectrode must have high catalytic activity towards water oxidation and reduction[21-23]. Therefore, it is of paramount importance to develop a photoanode, which can oxidize water steadily and

effectively. An effective photoanode must meet the following important criteria for water oxidation such as; Visible light absorption, suitable band edge positions, efficient use of photogenerated carriers, efficient charge separation and injection to surface active sites, and high photoelectrochemical operational stability in a wide range of pH[24-27]. **Figure 1.3.2** represents the various processes involved in the PEC water splitting process.

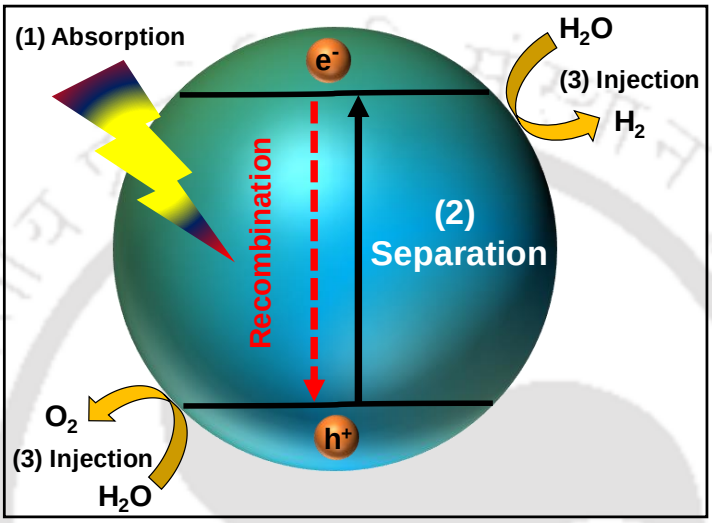

Figure 1.3.2 Schematic diagram for various processes involved in PEC water splitting

1.4 Design of Metal Oxide Photoelectrodes and Strategies to Enhance the Photoelectrochemical Activity

In order to enhance the photocatalytic activity, a wide range of semiconductor metal oxides have been investigated under UV or visible light irradiation. Designing the ideal photoactive material for efficient conversion of solar energy, improving light absorption**,** and enhancing the charge-carrier transport are two main approaches[16]. UV light contributes only ~4-6 % of the solar spectrum whereas; visible light contributes ~43 % of the solar spectrum. Therefore, research emphasis on the development of materials with absorption in the visible regions of the solar spectrum has received substantial attention. Several methods used to design and synthesis efficient visible light active photocatalysts include: (i) Electronic structure modification by foreign element doping, (ii) Synthesis of different morphological

nanostructures, (iii) Dye and quantum dot sensitization, (iv) Heterojunction formation, (v) Cocatalysts modification, and (vi) Hybridization with hole/electron extracting layers

1.4.1 Electronic Structure Modification by Foreign Element Doping

Modulating the bandgap of semiconductors to shift their absorption to the visible region by foreign element doping, is one of the most common strategies to enhance the optical and electrical properties of photoanodes. Band structural modification primarily involves cation or anion doping to change the electronic properties. Metal cation doping into the crystal lattice forms impurity energy levels within the forbidden band of a semiconductor, thus narrowing the bandgap[28] as shown in **Figure 1.4.1 (A & B)**. These impurity energy levels formed inside the bandgap of the semiconductor work as a donor or acceptor, depending upon the nature of the dopant. Though the impurity levels narrow the bandgap of the semiconductor, sometimes they act as recombination centers for the photogenerated charge carriers, resulting in the deterioration of PCE activity. Wang et al. investigated the effect of Co, Mn, and Fe doping on the performance of TiO_2 photoanode. Their observations reveal that only Fe doping has a positive effect on TiO_2 performance, whereas Co and Mn doping shows a negative effect on the charge carrier density of TiO_2. They demonstrated that Fe doping not only increases the absorption but also enhances the charge carrier density[29]. Therefore, optimization of the nature of dopants is of paramount importance for the development of efficient photoanodes. Introducing oxygen vacancies or doping with non-metal to create new energy levels inside the bandgap of semiconductor enables small energy transitions, therefore reduces the bandgap of the semiconductor. Sulfur doping creates unstable oxygen vacancies, Nitrogen, and Hydrogen doping enhances the visible light absorption and narrows the band gap[30-32]. Of the several-doped metal cations, Mo and W are considered as the most effective dopants as they create shallow donors for $BiVO_4$ to increase the carrier concentrations, resulted in enhanced

conductivity of $BiVO_4$[33-35]. Other dopants such as In and Gd have also been used as efficient dopant[36-37].

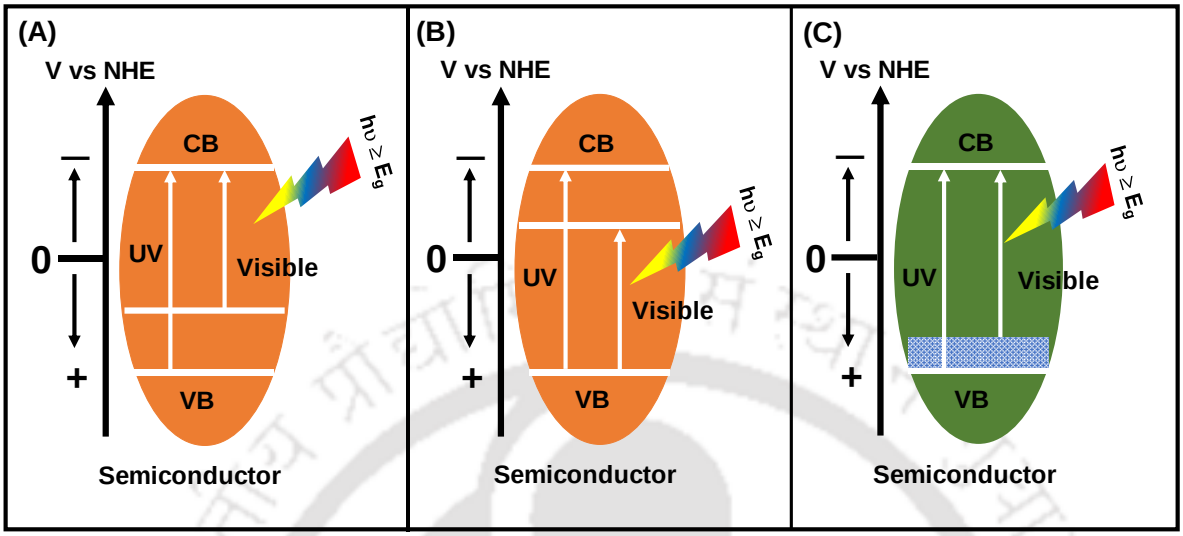

Figure 1.4.1 Narrowing the bandgap of a wide semiconductor by (A-B) metal doping and (C) nonmetal doping

In addition, doping of non-metals (**Figure 1.4.1 (C)**) such as Hydrogen and nitrogen also improves the charge carrier density as well as carrier lifetime[38-39]. Bismuth doped WO_3 shows enhanced photocurrent density due to the change in band positions[40]. Dopant concentration also plays a critical role in the separation of charge carriers as it is directly proportional to bend bending and inversely proportional to the width of the depletion layer. A higher concentration will lead to the formation of a thin depletion layer, difficult to separate the charge carriers[41]. Therefore, doping with a suitable concentration of dopant is required to enhance the PEC performance. Moreover, self-doping and co-doping are equally important strategies to enhance the PEC performance. Fe^{3+}/Fe^{2+} self-doped $FeVO_4$, Ti^{3+} self-doped TiO_2, and V^{4+} self-doped $BiVO_4$, shows the enhanced electrical conductivity, and thus improved the PEC activity[42-44]. Zr-W co-doped $BiVO_4$, N-Co co-doped ZnO, and Yb-W co-doped $BiVO_4$ show the extended light absorption to reduce the bandgap, hence improve the PEC performance[45-47].

1.4.2 Synthesis of Different Morphological Nanostructures

Optimizing the morphology of a semiconductor by controlling the growth process at the nanoscale level, is another feasible approach to enhance the PEC performance. With nanosize scale, the charge transport and light absorption increases due to the decoupled penetration depth and charge carrier diffusion length; assist the charges to transport to the electrolyte with improved active surface[5,48]. When the size of the materials reduces to the nanoscale, it reveals different properties such as; the number of ions or atoms that are exposed on the surface increases massively, resulting in an enhanced surface-to-volume ratio. It also increases the number of active sites for catalytic reactions to take place. Consequently, the nanosize morphologies show the high surface activity that does not exist in the bulk[49-50]. Semiconductors with different dimensions such as 0-D, 1-D, 2-D, and 3-D have been explored as suitable photoanode for PEC water splitting, shown in **Figure 1.4.2.**

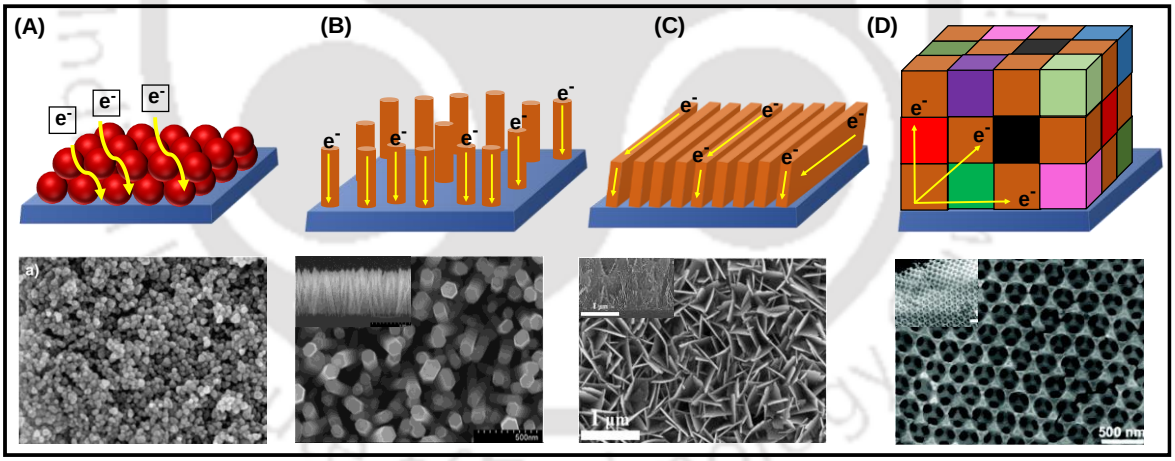

Figure 1.4.2 Synthesis of different nanostructure morphologies as photoanode in PEC water splitting and corresponding FESEM images taken from (Ref. 61-64)

In case of 0-D nanoparticles-based photoanode, the photogenerated electrons travel through the inter-particle or random pathways to reach the collecting electrode, as shown in **Figure 1.4.2 (A)**. The only drawback associated with 0-D nanostructures is that, the photogenerated electrons have more chances to recombine as electron tunneling occurs at the

inter-particle boundary with a high population of trap sites[50-51]. Unlike 0-D nanoparticles, 1-D nanomaterials possess one dimension from the nanoscale range to the micrometer scale and sometimes even longer. Nanowires, nanotubes, Nanobelts, nanofibers, and nanorods are the characteristic examples of this kind of structure. Increased optical path length provides a smooth pathway for the charge transport along the longitudinal direction in 1-D nanostructures, as shown in **Figure 1.4.2 (B)**. The charge separation in 1-D nanostructures is much more efficient as compared to 0-D, as the charge carriers are less localized in 1-D nanostructures[52-54]. For this reason, 1-D nanostructures have shown their significance as excellent charge transporter in solar energy conversion devices, but are restricted to some extent due to less exposed surface area. As can be seen from **Figure 1.4.2 (C)**, 2-D nanomaterials refer to materials with two dimensions out of the nanoscale range. 2-D nanostructures possess high surface area as compared to 1-D nanostructures, beneficial for the better contact between the photoanode and electrolyte. Nanosheets and nanoplates are the typical representatives of this kind of nanostructures. 2-D nanosheets with a high surface area act as physical support to form composites with other catalysts. For a 2-D thin film, the direction for charge carrier transport and light absorption is the same[55-56]. 3-D materials with the synergistic properties of 0-D, 1-D, or 2-D nanostructures can be assembled in a precise and orderly arrangement for enhanced PEC performance. A template or inherent force of nanoscale materials can guide these assemblies into 3-D ordered nanostructures. 3-D ordered structures with a high surface area have some desired properties such as light trapping and scattering, that cannot be attained with disordered or suspended building blocks. The photonic semiconductor crystal shown in **Figure 1.4.2 (D)**, is considered a typical example of a 3-D nanostructure that can form a photonic bandgap material. Light undergoes intense coherent multiple scattering as it enters the photonic crystals and propagates at very low group velocities near the edge of the photonic band. This phenomenon is known as the slow-light effect, which significantly increases the effective

optical path length[57-59]. It was noted that the absorption of light increased by several orders of magnitude[60]. Therefore, nanostructures with different dimensions are expected to be more efficient in the transportation and separation of charge carriers by reducing the diffusion length and increasing the photoanode/electrolyte interfacial area for water oxidation. **Figure 1.4.3** shows the several morphologies of metal oxide based photoanodes used for photoelectrochemical water splitting.

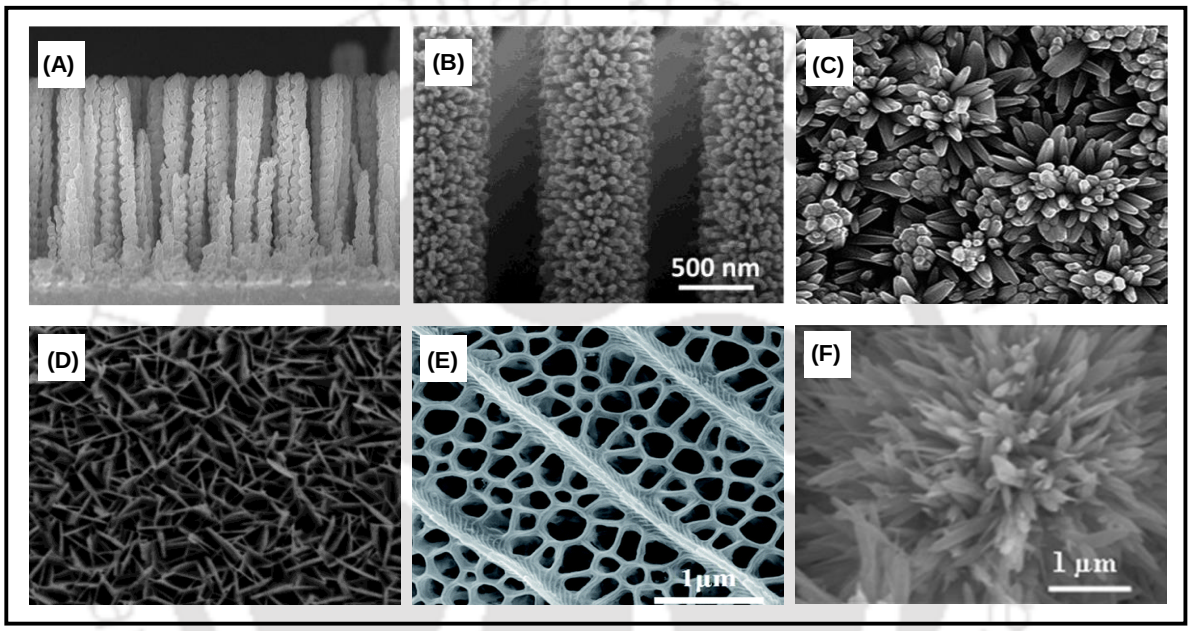

Figure 1.4.3 Some examples related to the utilization of different morphological structures of metal oxides, as a photoanode scaffold in PEC water oxidation (Ref 65-70)

1.4.3 Dye and Quantum Dot Sensitization

The pioneering work done by O'Regan and Gratzel in dye-sensitized solar cells paves a new pathway to design visible light active photoanodes from wide bandgap materials by decorating dye molecules[71]. Despite having several other advantages, the light absorption ability of wide bandgap semiconductors is limited, therefore sensitized with organic dyes to make them visible light active. Similar to the dye-sensitized solar cells, upon irradiation, the photogenerated electrons in dye molecules are injected into the conduction band of the semiconductor. After donating electrons, the oxidized dyes become unstable and regenerate

quickly with an electron donor. To make the charge transfer energetically compatible, LUMO (lowest unoccupied molecular orbital) of dye must be higher than the conduction band of the semiconductor, and HOMO (highest occupied molecular orbital) should lie between the valence band of the semiconductor and the oxidation reaction potential, shown in **Figure 1.4.4 (A)** [24,72]. A number of literatures are available where a wide bandgap semiconductor is sensitized with organic dye molecules to enhance the PEC performance[73-80].

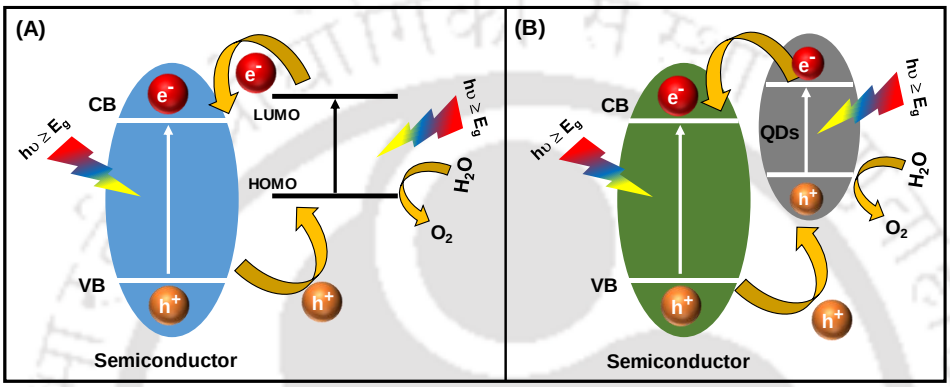

Figure 1.4.4 Schematic representation of sensitization of a wide bandgap semiconductor by (A) dye molecules and (B) quantum dots

Another perspective to stimulate the visible light absorption ability of semiconductor photoanode is the use of quantum dots, as shown in **Figure 1.4.4 (B)**. Their absorption can be tuned to the solar spectrum by changing the size of the particles. Quantum dots have various advantages over organic dyes as they can generate multiple electron-hole pairs per photon, resulting in improved performance of the device[81]. Some techniques including nitrogen-doped semiconductor sensitized with quantum dots and quantum dots sensitization with different sizes and types have been demonstrated to enhance the PEC performance[82-83]. In search of designing visible light active photocatalysts, semiconductors with different quantum dots have been used to improve the photocatalytic activity[84-86].

1.4.4 Construction of Different Heterojunctions

An alternate way to enhance the PEC performance is to improve the separation and transportation of photogenerated charge carriers by reducing their recombination. This

particular issue can be resolved by constructing the heterojunctions between semiconductors with proper band alignments. The advantage associated with heterojunctions formation is that they allow preferential band alignment in achieving visible light-responsive water splitting. Depending upon the band positions, three main types of heterojunctions such as type I, type II, and type III can be formed between two dissimilar semiconductors. The characteristic feature of type I heterojunction is that it consists of a smaller bandgap semiconductor (A) and a wide bandgap semiconductor (B). The valence band and conduction band of wide bandgap semiconductor are more positive and more negative respectively, compare to smaller bandgap semiconductor. These band positions facilitate the electrons and holes transfer in the same direction from wide bandgap semiconductor to smaller bandgap semiconductor. Fe_2O_3 (A)-TiO_2 (B) heterojunction is a prime example of this type of heterojunction, where electrons and holes transfer occur from TiO_2 to Fe_2O_3[87-89]. Unlike type I heterojunction, electrons and holes in type II heterojunctions travel in opposite directions, owing to the more negative conduction band of semiconductor (B) than semiconductor (A) and more positive valence band of semiconductor (A) than semiconductor (B). In this type of heterojunction structure, electron transfers from B to A, whereas holes transfer occurs from semiconductor A to B. WO_3 (A)-$BiVO_4$ (B) heterojunction is the best example of this type of system, where electron transfers from $BiVO_4$ to WO_3 and holes travels from WO_3 to $BiVO_4$, result in enhanced charge separation and thereby improves the PEC performance[90-92]. In type II heterojunction, the band positions of some semiconductor materials tend to construct Z-scheme, where electrons from the semiconductor (A) having lower conduction band combine with holes from higher valence band semiconductor (B). For example, ZnO/Au/SnO_2[93], g-C_3N_4/$BiVO_4$[94], and ZnO-WO_{3-x}[95] represent the Z-schemes for improved interfacial charge transfer. Similar to type II, type III heterojunctions have the same band structures. The only difference between type II and type III heterojunction is that, in type III heterojunctions the difference in the valence band and

conduction band of both semiconductors (A) and (B) is much higher. This higher difference in valence and conduction band provides a higher driving force to transfer the charge carriers. The electrons from semiconductor (A) combine with holes from semiconductor (B). On the other hand, holes from semiconductor (A) and electrons from semiconductor (B) take part in water oxidation and reduction reactions, respectively[96-97]. Moreover, the construction of a p-n heterojunction in which p-type photoanode is present on the electrolyte site is another feasible approach to enhance the PEC performance. Several photoanodes forming p-n heterojunctions such as $Cu_2O/BiVO_4$[98], $CuBi_2O_4/BiVO_4$[99], and Co_3O_4/Fe_2O_3[100] have been studied to improve the water oxidation performance. Besides the formation of heterojunctions, the construction of homo-junctions/phase-junctions between different crystal phases of a single semiconductor is another important strategy to improve the PEC performance[101-103].

1.4.5 Co-catalysts Modification

Due to multi-electron transfer in water oxidation, it requires high overpotential to split water. Therefore, it is of paramount importance to reduce this overpotential by modifying the photoanode surface with oxygen evolution catalysts: as they reduce the surface recombination and fasten the transport kinetics[104-105]. It is considered that, co-catalysts act as active sites for catalytic reactions to take place and improve the separation as well as injections of photogenerated charge carriers, driven by the interface between photoanode/co-catalyst[28]. Due to the strong activity and lower overpotential need for electrocatalytic water oxidation, noble metal-based co-catalysts such as RuO_2 and IrO_2 are among the best performing water oxidation evolution catalysts[50]. A cathodic shift of 200 mV in the onset potential was observed when IrO_2 was deposited over the hematite surface for efficient water oxidation[106]. Despite having strong activity, the high cost of Ru and Ir and their low abundance makes them difficult to use in water oxidation. Therefore, research emphasis on reducing the cost as well as improving the activity of co-catalyst has received a significant response. Of the available transition metal-based

catalysts, cobalt oxide has emerged as a robust and efficient co-catalyst for water oxidation, which operates under neutral/alkaline conditions. Fortunately, Nocera et al. reported cobalt-phosphate (Co-Pi) as an efficient oxygen evolution catalyst, deposited through electrodeposition over photoanode[107]. Co-Pi has received significant attention due to a negative shift in onset potential at neutral pH, comparable to IrO_2. The maximum shift of 440 mV in onset potential was observed, when Co-Pi was deposited over W-doped $BiVO_4$[108]. Since its inception, Co-Pi has been extensively associated with many photoanode materials such as Fe_2O_3, TiO_2, $BiVO_4$, ZnO, and WO_3, for water oxidation[109-113]. The mechanism for water oxidation using Co-Pi involves the formation of high-valent Co(IV)–O intermediates through Co^{II}/Co^{III} and Co^{III}/Co^{IV} redox couples, which can store up to four holes from the valence band of photoanode. After the injection of holes into the electrolyte for the water oxidation to generate O_2, it again regenerates Co^{II} centers[114-115]. Some electrocatalysts including, Mn-Bi[116], NiCo[117], CoAl[118], Ni-Bi[119], NiFe[120], CoFe-PB[121], Ni_4O_4[122], FeOOH[123], NiOOH[124], and CoOOH[125], have also been widely used to accelerate the oxygen evolution kinetics.

1.4.6 Hybridization with Hole/Electron Extracting Layer

Van de Krol et al. restated the role of oxygen evolution catalysts from the perspective of surface recombination and surface catalysis. They have used $BiVO_4$ as a model system and modified it with Co-Pi. Their observations suggest that the photocurrent of $BiVO_4$ is limited due to surface recombination, not due to surface reaction kinetics. Co-Pi reduces the surface recombination in $BiVO_4$ by a factor of 10-20, while the charge transfer rate constant is not affected. They concluded that the Co-Pi deposition onto the $BiVO_4$ surface does not enhance the water oxidation kinetics; it only reduces the surface recombination[126-127]. Therefore, the incorporation of electron/hole extracting materials to extract photogenerated electrons and holes is another feasible approach to enhance the PEC performance. Qin et al. demonstrated the role of graphene in $BiVO_4/TiO_2$/Graphene photoanode, where graphene is used as a hole

transport layer to improve hole tunneling efficacy[128]. Chen et al. inserted a $ZnFe_2O_4$ layer between Fe_2O_3 and ZnO to extract the stacked holes to the surface[129]. Zhang et al. demonstrate the use of black phosphorene as an efficient hole-extracting layer to enhance the ability of co-catalyst for water oxidation in $BiVO_4$ based photoanode[130]. A considerable amount of literature is available where different co-catalysts have been used in different manners to extract photogenerated holes, resulting in enhanced PEC performance[131-133]. Manipulating the hole accumulation behavior of catalyst during OER is another strategy to enhance the PEC performance[134]. Therefore, promoting hole extraction from photoanode surface to oxygen evolution co-catalysts by improving their interface resistance remains of widespread interest and importance for improving the PEC performance. Zero-dimensional (0-D) quantum dots and two-dimensional (2-D) materials with thin nanosheet structures can also be utilized as an efficient hole extraction layer. The schematic representation shown in **Figure 1.4.5** represents the various strategies such as (A) heterojunction formation, (B) surface modification with Co-catalysts, and (C) hybridization with electron/hole extracting materials, used for enhancing the PEC performance of metal-oxide based photoanodes.

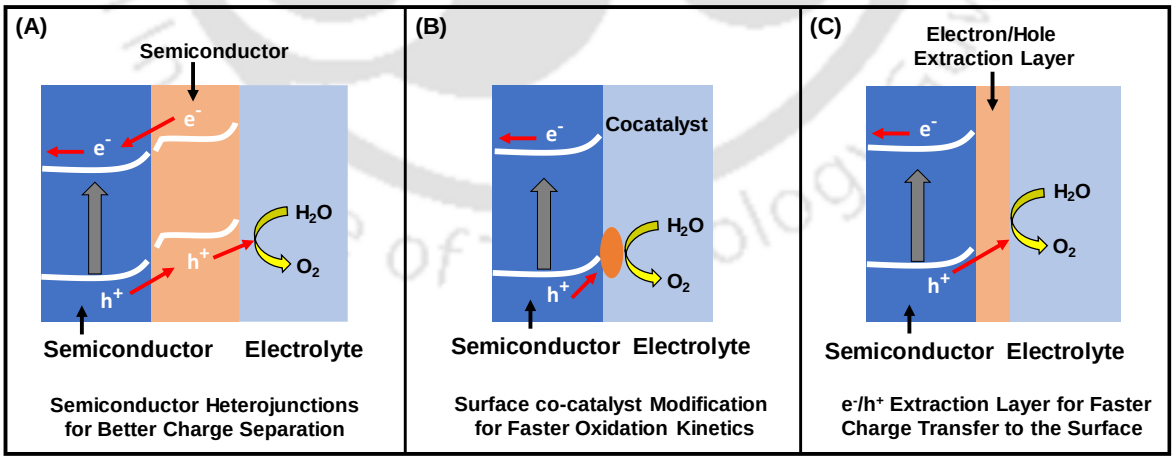

Figure 1.4.5 Schematics of different strategies (A) heterojunction formation, (B) Co-catalysts modification, and (C) Hybridization with electron/hole extracting layer, to improve the PEC performance of metal oxide-based photoanodes

1.5 Metal Oxide Based Chemiresistor Sensors

Due to rapid advances of several industrial technologies, environmental safety issues have become an alarming factor as they release several harmful gases. These toxic pollutants and gases coming out from industries need to be detected. Apart from this, the chemical signatures of volatile organic compounds (VOCs) in humans can be utilized for point-of-care (POC) diagnosis. VOCs generated in humans provide insights into one's healthy and diseased metabolic states, acting as a biomarker for identifying numerous diseases noninvasively[135]. Therefore, there is an impetus to develop a sensor that can easily detect these volatile organic compounds and toxic gases at ambient conditions. Chemical sensors are of vital importance for the detection and monitoring of these VOCs and gases in exhaled human breath[136].

Developing a non-invasive method that can diminish or eradicate the pain and discomfort associated with an invasive blood test, is a major driving force of diagnostic technology development. Several non-invasive methods have been utilized to monitor disease-related signals from humans such as breath, saliva, sweat, tears, and so on. Out of these, breath analysis is presumed to be the most promising method due to its potential associated with several human diseases[137]. The bulk of human breath contains Nitrogen, Oxygen, Carbon dioxide, water vapors, and inert gases while the remaining small fraction comprises more than 1000 volatile traces with concentrations ranging from parts per trillion (ppt) to parts per million (ppm). Endogenous molecules, products of metabolic processes have a strong correlation with a certain disease[138]. Non-invasive identification of Vapor Phase Components (VPCs)/Volatile Organic Components (VOCs) present in exhaled breath is of significant interest, because it is a simple and economical substitute to characterize irregularities related to medical conditions such as kidney disorder, asthma, diabetes, lung cancer, and halitosis[139]. It is well-known that the above-mentioned ailments are replicated by a biomarker of Ammonia[137], Nitric Oxide[140], Acetone[141], Toluene[142], and Hydrogen Sulfide[143] respectively.

1.5.1 Working Principle of Chemiresistor Sensor Device

Working principle of a Chemiresistor sensor device is the same as that of a gas sensor, schematic shown in **Figure 1.5.1** represents the same. As soon as the target analytes are exposed onto the sensor surface, it shows a change in resistance or conductance. Surface-induced adsorption, desorption, and oxidation reactions of the exposed analyte with the sensing material are primarily responsible for this change in resistance. Depending upon the nature of the analyte, it changes the charge carrier concentration, resulting in a change in electrical resistance. Generally, these devices notice changes in their electrical properties due to the gas-solid interaction[144-145]. In other words, when an analyte comes in contact with sensing materials or is chemically adsorbed onto the sensor surface, it alters the surface states resulting in a change in resistance of the device.

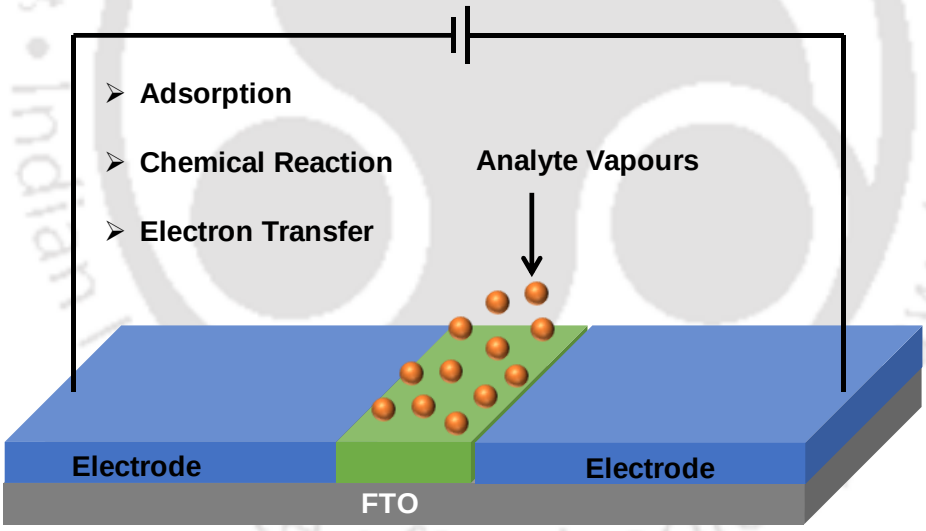

Figure 1.5.1 Schematic illustration of a Chemiresistor device, fabricated by sandwiching the sensing material between two electrodes act as source and drain respectively

Several parameters such as selectivity, response/recovery times, and limit of detection (LOD), are associated with the sensor device and their evaluation determines the performance of a Chemiresistor sensor device. Achieving high selectivity is probably one of the major challenges when designing a metal-oxide based sensor. Sensitivity of any sensor device is

mainly determined by the LOD value of that device, i.e., the lesser the LOD value, the better the sensitivity. The LOD can be calculated using the mathematical formula LOD = 3σ/S, where 'σ' represents the relative standard deviation in the current responses without the exposure of analyte and 'S' is the slope of the linearly fitted calibration curve.

Various techniques including mass chromatography, gas chromatography, and so on have been widely used to analyze different VOCs. The major drawback associated with this type of technique is its incorporation into real-time portable devices, because of the large size of equipment, operational difficulties, and high cost[146-147]. In contrast, metal oxide-based sensors offer usability for portable real-time sensors due to their small size, ease of fabrication, and low cost[148-149]. Morphology of sensing material can also affect the physicochemical properties by improving the sensing activity and thermochemical stability. Moreover, the synthesis of novel structures can also be used to fabricate high-sensitivity breath sensors. Morphology-dependent properties of micro, meso, and nanomaterials with controlled shape and size have been studied to enhance the sensing performance of metal oxide-based sensor[150-151]. Different morphologies such as nanoellipsoids[152], hexagonal microdiscs[153], nanoflowers[154], nanowires[155], nanorods[156], tetrapods[157], flower shaped[158], nanotubes[159], nanofibers[160], and walnut-like microstructures[161] have been utilized for gas sensing applications.

1.6 Motivation and Objectives of the Present Work

Several metal oxides such as ZnO, $BiVO_4$, WO_3, and Fe_2O_3 have been used as photoanodes for PEC water splitting, owing to their appropriate band positions, abundant resources, and stability in aqueous media under neutral and alkaline conditions. In the present work, we have used a wide bandgap semiconductor ZnO and a narrow bandgap semiconductor $BiVO_4$ for efficient PEC water splitting. Zinc oxide (ZnO), a wide bandgap (~3.2 eV) semiconductor photoanode has attracted much attention due to its high electron mobility, low toxicity, and more important its anisotropic growth behavior. Although ZnO has many advantages over

similar n-type materials, still the PEC activity is inferior to many photoanodes, due to the limited absorption profiles as well as limitation in charge carrier transport. Due to anisotropic growth behavior and tunable electrical properties, ZnO nanostructures having dimensions such as 0-D, 1-D, 2-D, and 3-D are actively studied for their optoelectronic properties. ZnO-based photoanodes suffer from unfavorable recombination of electron-hole pairs, which hinders its use in photoelectrochemical (PEC) water oxidation. $BiVO_4$ with a suitable bandgap of ~ 2.4 eV shows the best performance for PEC water oxidation among all the metal-oxide based photoanodes. Despite the knowledge that $BiVO_4$ is an ideal photoanode material, the reported photocurrent densities of pure $BiVO_4$ are still far less than its theoretical current value of 7.5 mA/cm^2. This is mainly due to poor charge separation and injection capabilities, short carrier diffusion length, and slow oxygen evolution kinetics at the interface. Although several strategies have been applied to enhance the surface properties of the photoanode, the bulk properties of the photoanodes are also the limiting factors for recombination losses of charge carriers before coming to the surface for chemical reactions. These key shortcomings of metal-oxide based photoanodes should be addressed to further improve their PEC performance. The objectives of the present thesis work are as follows:

(1) Design and development of different novel morphologies of existing metal oxides using biomass-derived templating agents to circumvent the shortcomings of charge carrier transport

(2) Sensitization of photoanode with novel morphology using narrow bandgap semiconductor quantum dots to enhance the optical properties

(3) Design and synthesis of new photoanode materials that possess unique combinations of properties suitable for PEC water splitting

(4) Surface modification of photoanodes with different co-catalysts and hole extracting materials to reduce the charge recombination and improve the surface kinetics

(5) Construction of a suitable p-n heterojunction for better charge transport through the interface

(6) Study the charge transfer and recombination kinetics at different interfaces for a better understanding

(7) Fabrication of Chemiresistor devices using WO_3 nanostructures and evaluate the sensing performance for NO_X gas sensing

1.7 References

(1) International Energy Agency (IEA), *Key World Energy Statistics*, 2020.

(2) https://www.statista.com/statistics/222066/projected-global-energy-consumption-by-source/

(3) J. Baxter, Z. Bian, G. Chen, D. Danielson, M. S. Dresselhaus, A. G. Fedorov, T. S. Fisher, C. W. Jones, E. Maginn, U. Kortshagen, A. Manthiram, A. Nozik, D. R. Rolison, T. Sands, L. Shi, D. Sholl and Y. Wu, *Energy Environ. Sci.*, 2009, **2**, 559.

(4) R. Lindsey, *Climate Change: Atmospheric Carbon Dioxide*, August 2020.

(5) C. Ros, T. Andreu and J. R. Morante, *J. Mater. Chem. A*, 2020, **8**, 10625.

(6) https://climatechange.ucdavis.edu/climate-change-definitions/how-is-solar-power-generated/

(7) S. Yun, Y. Qin, A. R. Uhl, N. Vlachopoulos, M. Yin, D. D. Li, X. Han and A. Hagfeldt, *Energy Environ. Sci.*, 2018, **11**, 476.

(8) M. O. Reese, S. Glynn, M. D. Kempe, D. L. McGott, M. S. Dabney, T. M. Barnes, S. Booth, D. Feldman and N. M. Haegel, *Nat. Energy*, 2018, **3**, 1002.

(9) J. H. Kim, D. Hansora, P. Sharma, J.-W. Jang and J. S. Lee, *Chem. Soc. Rev.*, 2019, **48**, 1908.

(10) S. S. Lam, V. H. Nguyen, M. T. N. Dinh, D. Q. Khieu, D. D. La, H. T. Nguyen, D. V. N. Vo, C. Xia, R. S. Varma, M. Shokouhimehr, C. C. Nguyen, Q. V. Le and W. Peng, *J. Mater. Chem. A*, 2020, **8**, 10571.

(11) S. E. Hosseini and M. A. Wahid, *Renew. Sustain. Energy Rev.*, 2016, **57**, 850.

(12) P. Nikolaidis and A. Poullikkas, *Renew. Sustain. Energy Rev.*, 2017, **67**, 597.

(13) A. Fujishima and K. Honda, *Nature*, 1972, **238**, 37.

(14) J. Joy, J. Mathew and S. C. George, *Int. J. Hydrogen Energy*, 2018, **43**, 4804.

(15) M. Bhatt and J. Lee, *J. Mater. Chem. A*, 2015, **3**, 10632.

(16) H. M. Chen, C. K. Chen, R.-S. Liu, L. Zhang, J. Zhang and D. P. Wilkinson, *Chem. Soc. Rev.*, 2012, **41**, 5654.

(17) V. M. Aroutiounian, V. M. Arakelyan and G. E. Shahnazaryan, *Sol. Energy*, 2005, **78**, 581.

(18) A. Wolcott, W. A. Smith, T. R. Kuykendall, Y. Zhao and J. Z. Zhang, *Small*, 2009, **5**, 104.

(19) M. G. Walter, E. L. Warren, J. R. McKone, S. W. Boettcher, Q. Mi, E. A. Santori and N. S. Lewis, *Chem. Rev.*, 2010, **110**, 6446.

(20) K. Sivula, F. Le Formal and M. Gr¨atzel, *ChemSusChem*, 2011, **4**, 432.

(21) J. Li and N. Wu, *Catal. Sci. Technol.*, 2015, **5**, 1360.

(22) A. Fujishima, X. T. Zhang and D. A. Tryk, *Surf. Sci. Rep.*, 2008, **63**, 515.

(23) R. Leary and A. Westwood, *Carbon*, 2011, **49**, 741.

(24) W. J. Youngblood, S. A. Lee, K. Maeda and T. E. Mallouk, *Acc. Chem. Res.*, 2009, **42**, 1966.

(25) J. R. Swierk and T. E. Mallouk, *Chem. Soc. Rev.*, 2013, **42**, 2357.

(26) Y. Xu and M. A. A. Schoonen, *Am. Mineral.*, 2000, **85**, 543.

(27) M. Kan, D. Xue, A. Jia, X. Qian, D. Yue, J. Jia and Y. Zhao, *Appl. Catal., B*, 2018, **225**, 504.

(28) S. Chen, D. Huang, P. Xu, W. Xue, L. Lei, M. Cheng, R. Wang, X. Liu and R. Deng, *J. Mater. Chem. A*, 2020, **8**, 2286.

(29) C. Wang, Z. Chen, H. Jin, C. Cao, J. Li and Z. Mi, *J. Mater. Chem. A*, 2014, **2**, 17820.

(30) C. Yang, Z. Wang, T. Lin, H. Yin, X. L¨u, D. Wan, T. Xu, C. Zheng, J. Lin, F. Huang, X. Xie and M. Jiang, *J. Am. Chem. Soc.*, 2013, **135**, 17831.

(31) G. Wang, X. Xiao, W. Li, Z. Lin, Z. Zhao, C. Chen, C. Wang, Y. Li, X. Huang, L. Miao, C. Jiang, Y. Huang and X. Duan, *Nano Lett.*, 2015, **15**, 4692.

(32) G. Wang, H. Wang, Y. Ling, Y. Tang, X. Yang, R. C. Fitzmorris, C. Wang, J. Z. Zhang and Y. Li, *Nano Lett.*, 2011, **11**, 3026.

(33) K. P. S. Parmar, H. J. Kang, A. Bist, P. Dua, J. S. Jang and J. S. Lee, *ChemSusChem*, 2012, **5**, 1926.

(34) A. J. Rettie, H. C. Lee, L. G. Marshall, J.-F. Lin, C. Capan, J. Lindemuth, J. S. McCloy, J. Zhou, A. J. Bard and C. B. Mullins, *J. Am. Chem. Soc.*, 2013, **135**, 11389.

(35) W.-J. Yin, S.-H. Wei, M. M. Al-Jassim, J. Turner and Y. Yan, *Phys. Rev. B: Condens. Matter Mater. Phys.*, 2011, **83**, 155102.

(36) X. Zhong, H. He, M. Yang, G. Ke, Z. Y. Zhao, F. Dong, B. Wang, Y. Chen, X. Shi and Y. Zhou, *J. Mater. Chem. A*, 2018, **6**, 10456.

(37) J. H. Baek, T. Gill, H. Abroshan, S. Park, X. Shi, J. K. Norskov, H. S. Jung, S. Siahrostami and X. Zheng, *ACS Energy Lett.*, 2019, **4**, 720.

(38) T.W. Kim, Y. Ping, G. A. Galli and K.-S. Choi, *Nat. Commun.*, 2015, **6**, 8769.

(39) J. H. Kim, Y. Jo, J. H. Kim, J. W. Jang, H. J. Kang, Y. H. Lee, D. S. Kim, Y. Jun and J. S. Lee, *ACS Nano*, 2015, **9**, 11820.

(40) S. S. Kalanur, I.-H. Yoo, K. Eom and H. Seo, *J. Catal.*, 2018, **357**, 127.

(41) G. Wang, Y. Ling, H. Wang, L. Xihong and Y. Li, *J. Photochem. Photobiol C Photochem. Rev.*, 2014, **19**, 35.

(42) J. Lee, Z. Li, L. Zhu, S. Xie and X. Cui, *Appl. Catal. B-Environ.*, 2018, **224**, 715.

(43) W. Wang, Y. Zhang, L. Wang and Y. Bi, *J. Mater. Chem. A*, 2017, **5**, 2478.

(44) G. Wang, Y. Ling, X. Lu, F. Qian, Y. Tong, J. Z. Zhang, V. Lordi, C. Rocha Leao and Y. Li, *J. Phys. Chem. C*, 2013, **117,** 10957.

(45) S. Saxena, A. Verma, N. K. Biswas, S. A. Khan, V. R. Satsangi, R. Srivastav and S. Dass, *Mater. Chem. Phys.*, 2021, **267**, 124675.

(46) P. P. Patel, P. J. Hanumantha, O. I. Velikokhatnyi, M. K. Datta, D. Hong, B. Gattu, J. A. Poston, A. Manivannan and P. N. Kumta, *J. Power Sources*, 2015, **299**, 11.

(47) U. Prasad, J. Prakash and A. M. Kannan, *Sustainable Energy Fuels*, 2020, **4**, 1496.

(48) A. U. Pawar, C. W. Kim, M. J. Kang and Y. S. Kang, *Nano Energy*, 2016, **20**, 156.

(49) X. Chen and S. S. Mao, *Chem. Rev.*, 2007, **107**, 2891.

(50) F. E. Osterloh, *Chem. Soc. Rev.*, 2013, **42**, 2294.

(51) Q. Zhang, C. S. Dandeneau, X. Zhou and G. Cao, *Adv. Mater.*, 2009, **21**, 4087.

(52) N. Wu, J. Wang, D. N. Tafen, H. Wang, J. Zheng, J. P. Lewis, X. Liu, S. S. Leonard and A. Manivannan, *J. Am. Chem. Soc.*, 2010, **132**, 6679.

(53) G. K. Mor, K. Shankar, M. Paulose and C. A. Grimes, *Nano Lett.*, 2005, **5**, 191.

(54) N. Murakami, Y. Kurihara, T. Tsubota and T. Ohno, *J. Phys. Chem. C*, 2009, **113**, 3062.

(55) J. Low, S. Cao, J. Yu and S. Wageh, *Chem. Commun.*, 2014, **50**, 10768.

(56) S. Ida and T. Ishihara, *J. Phys. Chem. Lett.*, 2014, **5**, 2533.

(57) X. Q. Chen, J. H. Ye, S. X. Ouyang, T. Kako, Z. S. Li and Z. G. Zou, *ACS Nano*, 2011, **5**, 4310.

(58) J. A. Garcia-Calzon and M. E. Diaz-Garci, *TrAC, Trends Anal. Chem.*, 2012, **35**, 27.

(59) T. Baba, *Nat. Photonics*, 2008, **2**, 465.

(60) A. Tao, P. Sinsermsuksakul and P. Yang, *Nat. Nanotechnol.*, 2007, **2**, 435.

(61) B. W. Chieng and Y. Y. Loo, *Mater. Lett.*, 2012, **73**, 78.

(62) Y. C. Liang, W. K. Liao and S. L. Liu, *RSC Adv.*, 2014, **4**, 50866.

(63) S. J. Young and L. T. Lai, *Microelectron. Eng.*, 2015, **148**, 40.

(64) X. Chen, J. Ye, S. Ouyang, T. Kako, Z. Li and Z. Zou, *ACS Nano*, 2011, **5**, 4310.

(65) X. Shi, I. Y. Choi, K. Zhang, J. Kwon, D. Y. Kim, J. K. Lee, S. H. Oh, J. K. Kim, and J. H. Park, *Nat Commun*, 2014, **5**, 4775.

(66) A. Kargar, K. Sun, Y. Jing, C. Choi, H. Jeong, G. Y. Jung, S. Jin and D. Wang, *ACS Nano*, 2013, **7**, 9407.

(67) X. Ren, A. Sangle, S. Zhang, S. Yuan, Y. Zhao, L. Shi, R.L.Z. Hoye, S. Cho, D. Li, and J. L. MacManus-Driscoll, *J. Mater. Chem. A*, 2016, **4**, 10203.

(68) H. He, S. P. Berglund, A. J. Rettie, W. D. Chemelewski, P. Xiao, Y. Zhang and C. B. Mullins, *J. Mater. Chem. A*, 2014, **2**, 9371.

(69) C. Yin, S. M. Zhu and D. Zhang, *RSC Adv.*, 2017, **7**, 27354.

(70) A. G. Tamirat, W.-N. Su, A. A. Dubale, C.-J. Pan, H.-M. Chen, D. W. Ayele, J.-F. Lee and B.-J. Hwang, *J. Power Sources*, 2015, **287**, 119.

(71) B. O'Regan and M. Gratzel, *Nature*, 1991, **353**, 737.

(72) J. R. Swierk and T. E. Mallouk, *Chem. Soc. Rev.*, 2013, **42**, 2357.

(73) W. J. Younpblood, S. H. A. Lee, Y. Kobayashi, E. A. Hernandez-Pagan, P. G. Hoertz, T. A. Moore, A. L. Moore, D. Gust and T. E. Mallouk, *J. Am. Chem. Soc.*, 2009, **131**, 926.

(74) L. Li, L. Duan, Y. Xu, M. Gorlov, A. Hagfeldt and L. Sun, *Chem. Commun.*, 2010, **46**, 7307.

(75) R. Brimblecombe, A. Koo, G. C. Dismukes, G. F. Swiegers and L. Spiccia, *J. Am. Chem. Soc.*, 2010, **132**, 2892.

(76) H. Lai, X. Liu, F. Zeng, G. Peng, J. Li and Z. Yi, *ACS Omega*, 2020, **5**, 2027.

(77) G. F. Moore, J. D. Blakemore, R. L. Milot, J. F. Hull, H.-e. Song, L. Cai, C. A. Schmuttenmaer, R. H. Crabtree and G. W. Brudvig, *Energy Environ. Sci.*, 2011, **4**, 2389.

(78) K.-R. Wee, B. D. Sherman, M. K. Brennaman, M. V. Sheridan, A. Nayak, L. Alibabaei and T. J. Meyer, *J. Mater. Chem. A*, 2016, **4**, 2969.

(79) Y. Gao, X. Ding, J. Liu, L. Wang, Z. Lu, L. Li and L. Sun, *J. Am. Chem. Soc.*, 2013, **135**, 4219.

(80) M. Yamamoto, L. Wang, F. Li, T. Fukushima, K. Tanaka, L. Sun and H. Imahori, *Chem. Sci.*, 2016, **7**, 1430.

(81) J. E. Murphy, M. C. Beard, A. G. Norman, S. P. Ahrenkiel, J. C. Johnson, P. Yu, O. I. Micic, R. J. Ellingson and A. J. Nozik, *J. Am. Chem. Soc.*, 2006, **128**, 3241.

(82) G. M. Wang, X. Y. Yang, F. Qian, J. Z. Zhang and Y. Li, *Nano Lett.*, 2010, **10**, 1088.

(83) H. M. Chen, C. K. Chen, C. C. Lin, R. S. Liu, H. Yang, W.-S. Chang, K.-H. Chen, T.-S. Chan, J.-F. Lee and D. P. Tsai, *J. Phys. Chem. C*, 2011, **115**, 21971.

(84) H. M. Chen, C. K. Chen, Y. C. Chang, C. W. Tsai, R. S. Liu, S. F. Hu, W. S. Chang and K. H. Chen, *Angew. Chem., Int. Ed.*, 2010, **49**, 5966.

(85) W. Sheng, B. Sun, T. Shi, X. Tan, Z. Peng and G. Liao, *ACS Nano*, 2014, **8**, 7163.

(86) J. Xiao, X. Hou, L. Zhao and Y. Li, *J. Catal.*, 2017, **346**, 70.

(87) S. J. Moniz, S. A. Shevlin, D. J. Martin, Z.-X. Guo and J. Tang, *Energy Environ. Sci.*, 2015, **8**, 731.

(88) K. Afroz, M. Moniruddin, N. Bakranov, S. Kudaibergenov and N. Nuraje, *J. Mater. Chem. A*, 2018, **6**, 21696.

(89) D. Barreca, G. Carraro, A. Gasparotto, C. Maccato, M. E. Warwick, K. Kaunisto, C. Sada, S. Turner, Y. Gonullu and T. P. Ruoko, *Adv. Mater. Interfaces*, 2015, **2**, 1500313.

(90) J. Su, L. Guo, N. Bao and C. A. Grimes, *Nano Lett.*, 2011, **11**, 1928.

(91) B. Jin, E. Jung, M. Ma, S. Kim, K. Zhang, J. I. Kim, Y. Son and J. H. Park, *J. Mater. Chem. A*, 2018, **6**, 2585.

(92) J. H. Seo, G. Park, K. H. Oh, S. H. Kang, H. C. Lee, S. K. Cho and K. M. Nam, *J. Electroanal. Chem.*, 2017, **789**, 17.

(93) J. M. Li, H. Y. Cheng, Y. H. Chiu and Y. J. Hsu, *Nanoscale*, 2016, **8**, 15720.

(94) J. Safaei, H. Ullah, N. A. Mohamed, M. F. M. Noh, M. F. Soh, A. A. Tahir, N. A. Ludin, M. A. Ibrahim, W. Isahak and M. A. M. Teridi, *Appl. Catal., B*, 2018, **234**, 296.

(95) Y. Chen, L. Wang, R. Gao, Y.-C. Zhang, L. Pan, C. Huang, K. Liu, X.-Y. Chang, X. Zhang and J.-J. Zou, *Appl. Catal., B*, 2019, **259**, 118079.

(96) S. N. F. M. Nasir, H. Ullah, M. Ebadi, A. A. Tahir, J. S. Sagu and M. A. Mat Teridi, *J. Phys. Chem. C*, 2017, **121**, 6218.

(97) Q. Li, X. Ma, H. Liu, Z. Chen, H. Chen and S. Chu, *ACS Appl. Mater. Interfaces*, 2017, **9**, 18836.

(98) S. Bai, J. Liu, M. Cui, R. Luo, J. He and A. Chen, *Dalton Trans.*, 2018, **47**, 6763.

(99) S. Liu, J. Zhou, Y. Lu and J. Su, *Sol. Energy Mater. Sol. Cells*, 2018, **180**, 123.

(100) S. S. Yi, B. R. Wulan, J. M. Yan and Q. Jiang, *Adv. Funct. Mater.*, 2019, **29**, 1801902.

(101) J. M. Lee, J. H. Baek, T. M. Gill, X. Shi, S. Lee, I. S. Cho, H. S. Jung and X. Zheng, *J. Mater. Chem. A*, 2019, **7**, 9019.

(102) J. Cen, Q. Wu, D. Yan, J. Tao, K. Kisslinger, M. Liu and A. Orlov, *Phys. Chem. Chem. Phys.*, 2017, **19**, 2760.

(103) F. Li, J. Li, F. Li, L. Gao, X. Long, Y. Hu and J. Ma, *J. Mater. Chem. A*, 2018, **6**, 13412.

(104) C. Jiang, S. J. Moniz, A. Wang, T. Zhang and J. Tang, *Chem. Soc. Rev.*, 2017, **46**, 4645.

(105) N. S. Lewis and D. G. Nocera, *Proc. Natl. Acad. Sci. U. S. A.*, 2006, **103**, 15729.

(106) S. D. Tilley, M. Cornuz, K. Sivula and M. Grätzel, *Angew. Chem., Int. Ed.*, 2010, **49**, 6405.

(107) M. W. Kanan and D. G. Nocera, *Science*, 2008, **321**, 1072.

(108) D. K. Zhong, S. Choi and D. R. Gamelin, *J. Am. Chem. Soc.*, 2011, **133**, 18370.

(109) B. Klahr, S. Gimenez, F. Fabregat-Santiago, J. Bisquert and T. W. Hamann, *J. Am. Chem. Soc.*, 2012, **134**, 16693.

(110) M. Bledowski, L. Wang, A. Ramakrishnan, A. Betard, O. Khavryuchenko and R. Beranek, *ChemPhysChem*, 2012, **13**, 3018.

(111) D. A. Reddy, Y. Kim, H. S. Shim, K. A. J. Reddy, M. Gopannagari, D. P. Kumar, J. K. Song and T. K. Kim, *ACS Appl. Energy Mater.*, 2020, **3**, 4474.

(112) E. M. P. Steinmiller and K. S. Choi, *Proc. Natl. Acad. Sci. U. S. A.*, 2009, **106**, 20633.

(113) Q. Liu, Q. Chen, J. Bai, J. Li, J. H. Li and B. Zhou, *J. Solid State Electrochem.*, 2014, **18**, 157.

(114) D. K. Zhong and D. R. Gamelin , *J. Am. Chem. Soc.*, 2010, **132**, 4202.

(115) D. K. Zhong, M. Cornuz, K. Sivula, M. Grätzel and D. R. Gamelin, *Energy Environ. Sci.*, 2011, **4**, 1759.

(116) H. Zhang, W. Tian, Y. Li, H. Sun, M. O. Tade and S. Wang, *J. Mater. Chem. A*, 2018, **6**, 24149.

(117) H. She, P. Yue, X. Ma, J. Huang, L. Wang and Q. Wang, *Appl. Catal., B*, 2020, **263**, 118280.

(118) R. Chong, B. Wang, C. Su, D. Li, L. Mao, Z. Chang and L. Zhang, *J. Mater. Chem. A*, 2017, **5**, 8583.

(119) J. Gan, X. Lu, B. B. Rajeeva, R. Menz, Y. Tong and Y. Zheng, *ChemElectroChem*, 2015, **2**, 1385.

(120) J. Guo, X. Yang, S. Bai, X. Xiang, R. Luo, J. He and A. Chen, *J. Colloid Interface Sci.*, 2019, **540**, 9.

(121) B. Moss, F. S. Hegner, S. Corby, S. Selim, L. Francas, N. Lopez, S. Gimenez, J. R. Galan-Mascaros and J. R. Durrant, *ACS Energy Lett.*, 2019, **4**, 337.

(122) B. Gao, T. Wang, X. Fan, H. Gong, P. Li, Y. Feng, X. Huang, J. He and J. Ye, *J. Mater. Chem. A*, 2019, **7**, 278.

(123) W. Zhang, J. Ma, L. Xiong, H.-Y. Jiang and J. Tang, *ACS Appl. Energy Mater.*, 2020, **3**, 5927.

(124) F. Malara, A. Minguzzi, M. Marelli, S. Morandi, R. Psaro, V. Dal Santo and A. Naldoni, *ACS Catal.*, 2015, **5**, 5292.

(125) C. H. Liu, Y. Xu, H. Luo, W. C. Wang, Q. Liang and Z. D. Chen, *Chem. Eng. J.*, 2019, **363**, 23.

(126) C. Zachaus, F. F. Abdi, L. M. Peter and R. van De Krol, *Chem. Sci.*, 2017, **8**, 3712.

(127) B. J. Trzesniewski, I. A. Digdaya, T. Nagaki, S. Ravishankar, I. Herraiz-Cardona, D. A. Vermaas, A. Longo, S. Gimenez and W. A. Smith, *Energy Environ. Sci.*, 2017, **10**, 1517.

(128) Q. Qin, Q. Cai, W. Hong, C. Jian and W. Liu, *Chem. Eng. J.*, 2020, **402**, 126227.

(129) S. Chen, J. H. Li, J. Bai, L. G. Xia, Y. Zhang, L. S. Li, Q. J. Xu and B. X. Zhou, *Appl. Catal., B*, 2018, **237**, 175.

(130) K. Zhang, B. Jin, C. Park, Y. Cho, X. Song, X. Shi, S. Zhang, W. Kim, H. Zeng and J. H. Park, *Nat. Commun.*, 2019, **10**, 2001.

(131) M. Zhong, T. Hisatomi, Y. Kuang, J. Zhao, M. Liu, A. Iwase, Q. Jia, H. Nishiyama, T. Minegishi, M. Nakabayashi, N. Shibata, R. Niishiro, C. Katayama, H. Shibano, M. Katayama, A. Kudo, T. Yamada and K. Domen, *J. Am. Chem. Soc.*, 2015, **137**, 5053.

(132) X. Chang, T. Wang, P. Zhang, J. Zhang, A. Li and J. Gong, *J. Am. Chem. Soc.*, 2015, **137**, 8356.

(133) X. Wang, K.-H. Ye, X. Yu, J. Zhu, Y. Zhu and Y. Zhang, *J. Power Sources*, 2018, **391**, 34.

(134) P. Zhang, W. Wang, H. Wang, Y. Li and C. Cui, *ACS Catal.*, 2020, **10**, 10427.

(135) A. Jalal, F. Alam, S. Roychoudhury, Y. Umasankar, N. Pala and S. Bhansali, *ACS Sens.*, 2018, **3**, 1246.

(136) R. Kumar, O. Al-Dossary, G. Kumar and A. Umar, *Nano-Micro Lett.*, 2015, **7**, 97.

(137) S.-Y. Yu, T.-W. Tung, H.-Y. Yang, G.-Y. Chen, C.-C. Shih, Y.-C. Lee, C.-C. Chen, H.-W. Zan, H.-F. Meng, C.-J. Lu, C.-L. Wang, W.-B. Jian and O. A. Soppera, *ACS Sens.*, 2019, **4**, 1023.

(138) H. G. Moon, Y. Jung, S. D. Han, Y.-S. Shim, W.-S. Jung, T. Lee, S. Lee, J. H. Park, S.-H. Baek, J.-S. Kim, H.-H. Park, C. Kim and C.-Y. Kang, *Sens. Actuators, B*, 2018, **257**, 295.

(139) H. G. Moon, Y. Jung, S. D. Han, Y. S. Shim, B. Shin, T. Lee, J. S. Kim, S. Lee, S. C. Jun, H. H. Park, C. Kim and C. Y. Kang, *ACS Appl. Mater. Interfaces*, 2016, **8**, 20969.

(140) P. I. Gouma and K. Kalyanasundaram, *Appl. Phys. Lett.*, 2008, **93**, 244102.

(141) J. Shin, S. J. Choi, I. Lee, D. Y. Youn, C. O. Park, J. H. Lee, H. L. Tuller and I. D. Kim, *Adv. Funct. Mater.*, 2013, **23**, 2357.

(142) G. Peng, U. Tisch, O. Adams, M. Hakim, N. Shehada, Y. Y. Broza, S. Billan, R. Abdah-Bortnyak, A. Kuten and H. Haick, *Nature Nanotech*, 2009, **4**, 669.

(143) J. H. Cha, D. H. Kim, S. J. Choi, W. T. Koo and I. D. Kim, *Anal. Chem.*, 2018, **90**, 8769.

(144) G. F. Fine, L. M. Cavanagh, A. Afonja and R. Binions, *Sensors*, 2010, **10**, 5469.

(145) Q. Meng, F. Zhang, Y. Zang, D. Huang, Y. Zou, J. Liu, G. Zhao, Z. Wang, D. Ji, C. Di, W. Hu and D. Zhu, *J. Mater. Chem. C*, 2014, **2**, 1264.

(146) K. Toda, J. Li and P. K. Dasgupta, *Anal. Chem.*, 2006, **78**, 7284.

(147) M. Hanada, H. Koda, K. Onaga, K. Tanaka, T. Okabayashi, T. Itoh and H. Miyazaki, *Anal. Chim. Acta*, 2003, **475**, 27.

(148) L. Wang, A. Teleki, S. E. Pratsinis and P. I. Gouma, *Chem. Mater.*, 2008, **20**, 4794.

(149) S. J. Choi, F. Fuchs, R. Demadrille, B. Greevin, B. H. Jang, S. J. Lee, J. H. Lee, H. L. Tuller and I. D. Kim, *ACS Appl. Mater. Interfaces*, 2014, **6**, 9061.

(150) B. Z. Jing and J. Zhan, *Adv. Mater.*, 2008, **20**, 4547.

(151) H. Nguyen and S. A. El-Safty, *J. Phys. Chem. C*, 2011, **115**, 8466.

(152) R. Sankar Ganesh, M. Navaneethan, V. L. Patil, S. Ponnusamy, C. Muthamizhchelvan, S. Kawasaki, P. S. Patil and Y. Hayakawa, *Sens. Actuators, B*, 2018, **255**, 672.

(153) R. S. Ganesh, E. Durgadevi, M. Navaneethan, V. L. Patil, S. Ponnusamy, C. Muthamizhchelvan, S. Kawasaki, P. S. Patil and Y. Hayakawa, *Chem. Phys. Lett.*, 2017, **689**, 92.

(154) R. S. Ganesh, E. Durgadevi, M. Navaneethan, V. L. Patil, S. Ponnusamy, C. Muthamizhchelvan, S. Kawasaki, P. S. Patil and Y. Hayakawa, *Sens. Actuators, B*, 2018, **269**, 331.

(155) T. Wang, Z. Sun, D. Huang, Z. Yang, Q. Jia, N. Hua, G. Yin, D. He, H. Wei and Y. Zhang, *Sens. Actuators, B*, 2017, **252**, 284.

(156) K. Shingange, Z. P. Tshabalala, O. Ntwaeaborwa, D. Motaung and G. Mhlongo, *J. Colloid Interface Sci.*, 2016, **479**, 127.

(157) F. Schutt, V. Postica, R. Adelung and O. Lupan, *ACS Appl. Mater. Interfaces*, 2017, **9**, 23107.

(158) W. Fang, Y. Yang, H. Yu, X. Dong, T. Wang, J. Wang, Z. Liu, B. Zhao and M. Yang, *RSC Adv.*, 2016, **6**, 106880.

(159) W.-T. Koo, S.-J. Choi, N.-H. Kim, J.-S. Jang and I.-D. Kim, *Sens. Actuators, B*, 2016, **223**, 301.

(160) D. H. Kim, J. S. Jang, W. T. Koo, S. J. Choi, S. J. Kim and I. D. Kim, *Sens. Actuators, B*, 2018, **259**, 616.

(161) J. Y. Shen, M. Di Wang, Y. F. Wang, J. Y. Hu, Y. Zhu, Y. X. Zhang, Z. J. Li and H. C. Yao, *Sens. Actuators, B*, 2018, **256**, 27.

CHAPTER 2

Experimental section

This chapter describes various instrumentation techniques used for the characterization of as-synthesized photoanode materials. A short discussion on the performance parameters of photoelectrochemical water splitting allied with the photoanodic materials is also included. At last, this chapter comprises the fabrication of a two-terminal Chemiresistor sensor device along with a short discussion on performance parameters.

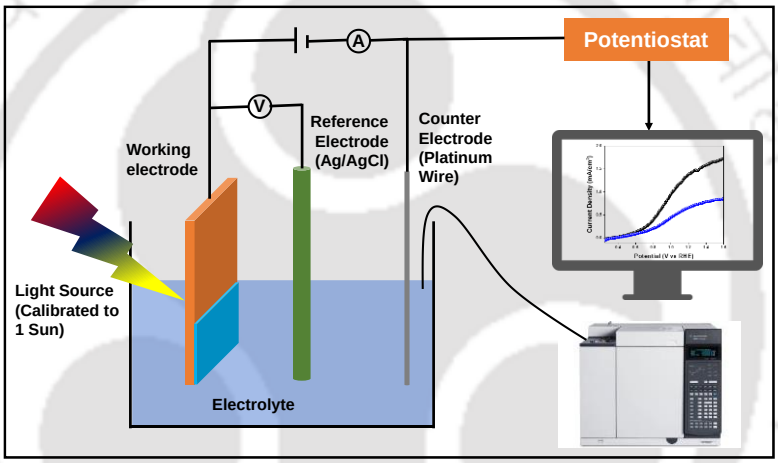

2.1 Introduction

This chapter describes the various steps involved in the synthetic and fabrication process of different metal oxide-based photoanodes, and their composites with superior charge transporting materials like graphene quantum dots (GQDs), Co(OH)F, and CoSn-LDH using electrodeposition and hydrothermal route. Several characterization techniques and performance parameters used to characterize the photoelectrochemical devices are discussed in detail. Chemicals and materials used in the synthesis process are listed. Moreover, we have also discussed the experimental setup used to characterize the photoelectrochemical devices. This chapter also comprises the fabrication process and performance parameters of a two-terminal Chemiresistor sensor device for vapor and gas/vapor-phase sensing.

2.2 Chemicals and Materials Used

Ammonium Metatungstate Hydrate (Sigma-Aldrich), Oxalic Acid (Merck), Zinc Nitrate Hexahydrate (Sigma-Aldrich), Polygalacturonic Acid (Sigma-Aldrich), Urea (Sigma-Aldrich), Hexamethylenetetramine (Merck), Citric acid (Merck), Bismuth Nitrate Pentahydrate (Sigma-Aldrich), Potassium Iodide (Merck), p-benzoquinone (Sigma-Aldrich), Vanadyl Acetylacetonate (Sigma-Aldrich), Cobalt Nitrate Hexahydrate (Sigma-Aldrich), Stannic Chloride Pentahydrate (Sigma-Aldrich), Aluminum Wire (Sigma-Aldrich), Hydrogen Peroxide (Merck), Zinc Dust (Sigma-Aldrich), Sodium Hydroxide (Merck), Ammonium Fluoride (Sigma-Aldrich), Boric Acid (Merck), Potassium Hydroxide (Merck), Sodium Sulfite (Sigma-Aldrich), Hydrazine Hydrate (Merck), Dimethyl Sulfoxide (Merck), Nitric Acid (Merck), Hydrochloric Acid (Merck), Fluorine doped tin oxide (FTO) (Sigma-Aldrich), PTFE Syringe Filter (Axiva Sichem Biotech Pvt. Ltd.) and Dialysis Bag (HIMEDIA) are purchased and used as it is, without any further purification. Milli-Q water (18.2 MΩ/cm^2) is used for all the synthesis protocols.

2.3 Characterizations of as-synthesized Materials, Photoelectrochemical and Chemiresistor Devices

All the synthesized materials as well as photoelectrochemical/Chemiresistor devices, were characterized using several analytical techniques. The instrumental techniques/tools used in the present studies comprise of:

(1) To confirm the formation and crystal phase purity of as-synthesized materials, X-ray diffraction analysis (XRD) was performed using Rigaku RINT 2500 TTRAX-III, with Cu–Kα (λ = 1.54 Å) X-ray source and Rigaku SmartLab9kW using Cu Kα (λ = 1.54 Å) as the source, operating at 40-45 kV voltage.

(2) UV-Vis spectra were recorded using JASCO Model V-650 and Perkin Elmer Lambda 750 UV/vis/NIR spectrophotometer.

(3) Steady-state Photoluminescence spectra were recorded using Horiba Scientific Fluoromax-4 spectrophotometer.

(4) To get an insight about the excited state charge transfer, Time-resolved photoluminescence (TRPL) measurements were carried out using LifeSpec II Edinburgh instrument, having a lamp with frequency 5MHz and Nd:YAG lasers of different excitation wavelengths.

(5) Fourier transformed infrared spectroscopic (FT-IR) studies were performed using Perkin Elmer (Spectrum-II) instrument with KBr pellet.

(6) Different modes of vibration present in the sample were characterized by micro-Raman spectroscopy using a laser micro-Raman system (Horiba Jobin Vyon, LabRam HR) with 488 nm laser excitation.

(7) Zeta potential (magnitude of the surface charge) of as-synthesized material was analyzed using ZETASIZER Nano series (Malvern), Model Nano-ZS90.

(8) SPIN-150 spin coater was used to deposit thin films over metal oxides.

(9) To investigate the morphology of as-synthesized materials field emission scanning electron microscopy (FESEM) analysis was carried out using Zeiss (Sigma-300) with an operating voltage of 3-5 kV.

(10) To evaluate the structural features of as-synthesized materials, transmission electron microscopy (TEM) analysis was carried out using JEOL (JEM-2100F) instrument operating at 200 kV voltage.

(11) To verify the elemental composition and their positioning in respective material, STEM-EDS mapping was carried out using INCA, Oxford instrument.

(12) Brunauer-Emmett-Teller (BET) Surface area analysis was done by nitrogen (N_2) adsorption at liquid N_2 temperature with a Beckman-Coulter SA 3100 N_2 adsorption apparatus.

(13) X-ray photoelectron spectroscopy (XPS) analysis were carried out using ESCALAB Xi+ (Made: Thermo Fisher Scientific Pvt. Ltd., UK) photoelectron spectrometer with a monochromatized Al-Kα ($h\nu$ = 1486.6 eV) source. C 1s spectrum (284.8 eV), as reference was used to compensate for surface charging effect. XPSPEAK 4.1 software was used to fit and deconvoluted the data.

(14) Cyclic voltammetry (CV) curves were recorded on a CHI1120B electrochemical workstation.

(15) The electrochemical impedance spectroscopy (EIS) measurements were performed using the CH Instruments model CHI680E, Inc., Austin, TX, in the frequency range of 0.1 Hz to 10^6 Hz under light illumination.

(16) Incident photon to current conversion efficiency for all devices was analyzed by using a Newport ORIEL IQE-200 instrument fitted with a 250 W quartz tungsten halogen lamp, calibrated with standard Si and Ge diodes.

(17) Anodization of the as-deposited Al layer was performed using Keithley source 2420 at room temperature.

(18) All the sensing measurements were conducted by using Keithley source meter 4200-SCS under ambient conditions.

2.4 Photoelectrochemical Measurements

Photoelectrochemical measurements of as-synthesized photoanodes were recorded using an electrochemical analyzer (model CH1120B) in a three-electrode configuration. For the measurements, 0.5 M potassium borate KBi (**Chapter 3 & 4**) and 1 M NaOH (**Chapter 3**) solutions were used as electrolytes. Before the measurements, these electrolytic solutions were purged with nitrogen gas for 30 min to eliminate the dissolved oxygen present in the electrolytic solutions. Linear sweep voltammetry analysis was performed between scan ranges of -0.6 to 1.0 V vs Ag/AgCl (**Chapter 3 & 4**) and -0.8 to 0.6 V vs Ag/AgCl (**Chapter 5**) with a scan rate of 10 mV/sec. As synthesized photoanodes, a Pt wire and Ag/AgCl were used as working electrodes, a counter electrode, and a reference electrode respectively. The applied potential was then converted into reversible hydrogen electrode (RHE) potential by using the following equation[1-2].

$$E_{RHE} = E_{Ag/AgCl} + (0.0591 * pH) + E^{\circ}_{Ag/AgCl} \quad (2.1)$$

Where E_{RHE} = RHE converted potential

$E_{Ag/AgCl}$ = Experimentally measured potential vs Ag/AgCl

$E^{\circ}_{Ag/AgCl}$ = Standard potential of Ag/AgCl reference electrode against RHE (0.1976)

pH = pH of electrolyte used

All the photoanodes were covered with Epoxy adhesive (Araldite®) leaving an exposed thin film area of 0.25 cm^2 for illumination. A tungsten halogen lamp of 300 W with light

intensity calibrated at 100 mW/cm^2 was used as a light source. Electrochemical impedance spectroscopy (EIS) measurements were performed using the CH Instruments model CHI680E, Inc., Austin, TX, in the frequency range of 0.1 Hz to 10^6 Hz under light illumination. Mott-Schottky plots for all the photoanodes were measured in a DC potential range of -1 to +1 V vs Ag/AgCl under dark conditions with an applied frequency of 1 kHz. The gas evolved during the PEC process was analyzed through online gas chromatography (7820A, Agilent Tech.) to calculate the Faradaic yield. **Figure 2.4.1** shows the schematic representation of the experimental setup for photoelectrochemical water splitting.

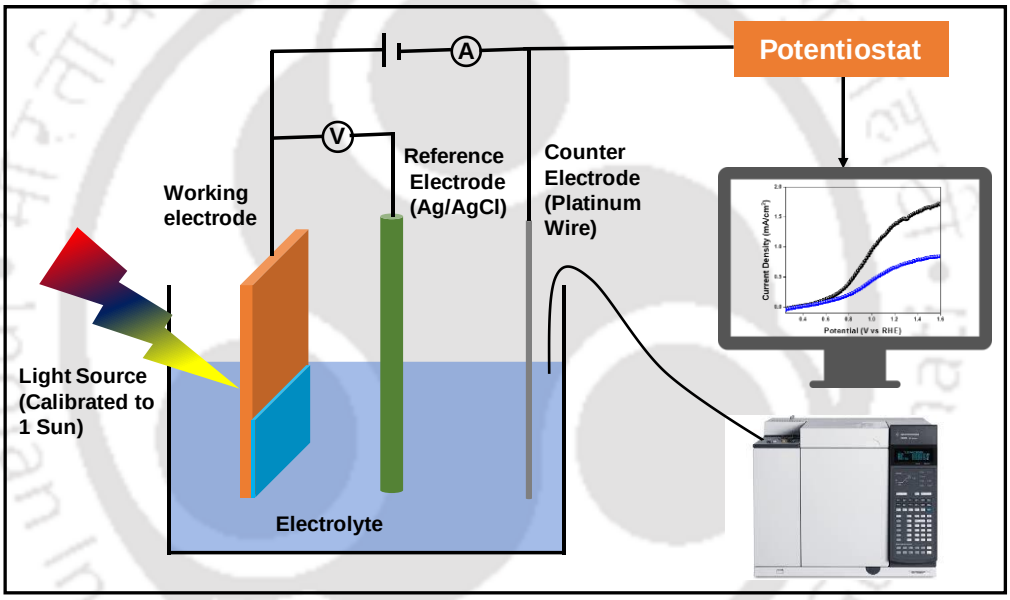

Figure 2.4.1 Schematic representation of the experimental setup for photoelectrochemical water splitting

2.5 Photoelectrochemical Performance Parameters

Performance parameters of a photoelectrochemical device capable of splitting water need to be assessed to get the optimal result. Several parameters, which shows the competitiveness of any photoanode, are as follows:

2.5.1 Quantum Efficiency Measurement of a Photoelectrochemical Device

Incident photon-to-current conversion efficiency (IPCE) or external quantum efficiency (EQE) is considered a crucial parameter to estimate the performance of a photoelectrochemical

device. In general, the IPCE of a device is indicative of its light-harvesting efficiency, photo-excited electrons injection efficiency, and charge collection efficiency. Moreover, EQE is the measure of how efficiently the device converts incident light into electrical energy at a given wavelength. It can be expressed using equation (2.2):

$$\mathrm{IPCE} = 1240 \times \frac{J_{sc}}{\lambda \times P_{in}(\lambda)} \qquad (2.2)$$

Along with EQE, the internal quantum efficiency (IQE) of a device should also be evaluated. IQE is responsible for the losses allied with the incident photons, reflected from the surface of a photoelectrochemical cell. IPCE is measured as a function of the wavelength of incident photons in a confined range. A monochromator equipped with gratings allows the light to pass through to create the scanning monochromatic light. The light is then passed through the optical chopper, falls onto the photoelectrochemical device, and a signal is amplified by a Merlin lock-in amplifier unit, before getting detected by the detector.

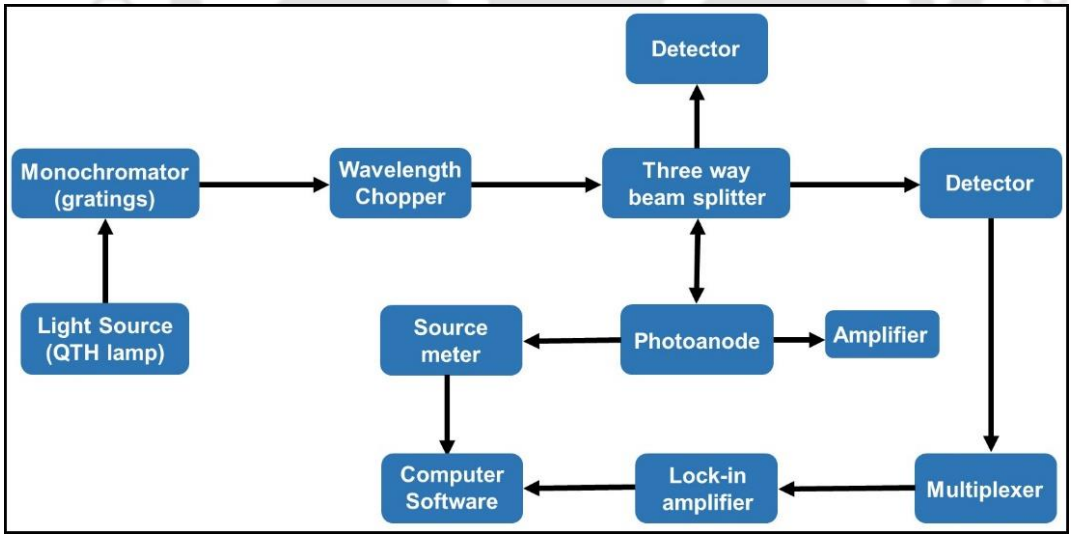

Scheme 2.5.1 Block diagram of incident photon-to-current conversion efficiency analyzer, Oriel IQE 200

2.5.2 Charge Separation and Charge Injection Efficiencies

Charge separation and injection efficiencies play a vital role in defining the performance of a particular photoelectrochemical device. Performance of a particular metal

oxide is limited due to the recombination of electron-hole pairs at the surface caused by sluggish water oxidation kinetics. Charge separation and injection efficiencies are calculated by the addition of hole scavengers in electrolyte solutions, owing to their faster oxidation kinetics in comparison to water oxidation. It is considered that these hole scavengers solve the interfacial barrier problem by scavenging the photogenerated holes and further transport these holes to the outer surface, resulting in enhanced water oxidation kinetics. Equation 2.3 represents the photocurrent density for water splitting[3].

$$J_{H_2O} = J_{abs} * \eta_{sep} * \eta_{inj} \quad (2.3)$$

Where J_{abs} is the photocurrent density after the complete conversion of absorbed photons to current, η_{inj} represent the hole injection efficiency and η_{sep} represent is the charge separation efficiency respectively, can be expressed by equation 2.4 and 2.5.

$$\eta_{sep} = \frac{J_{hole\ scavenger}}{J_{abs}} \quad (2.4)$$

$$\eta_{inj} = \frac{J_{H_2O}}{J_{hole\ scavenger}} \quad (2.5)$$

2.5.3 Faradaic Yield

Faradaic yield calculation is the most useful technique to understand that the obtained photocurrent is solely due to water oxidation and not due to the photocorrosion of photoanode or other side reactions. It can be estimated by dividing the actual gas (H_2 or O_2) evolved by the theoretically evolved gas (H_2 or O_2) based on the measured photocurrent using the following equations[4]:

$$Faradaic\ Yield = \frac{Experimental\ gas\ evolution}{Theoretical\ gas\ evolution} \quad (2.6)$$

$$= \frac{Oxygen\ evolution\ measured}{Gas\ evolution\ based\ on\ the\ photocurrent} \quad (2.7)$$

$$= \frac{Oxygen\ evolution\ measured}{\left(\frac{J_{photo}\ XA\ X\ T}{e}/4\right)/N_A} \quad (2.8)$$

The unit of gas produced is in moles; J_{photo} is the photocurrent density (A/cm^2) produced during the measurement time T (s); A is the light-exposed photoelectrode area (cm^2); e is the electron charge (1.602 x 10^{-19} C) and N_A is the Avogadro constant (6.02 x 10^{23} mol^{-1}). Apart from the sacrificial reagents, dissolved O_2 present in the cathodic site of the cell is also responsible for the loss in Faradaic yield. This O_2 reduces to $O_2^{-\bullet}$ competes with H_2 evolution and further reacts with water to form H_2O_2, a typical by-product detected in the cathodic compartment when the electrolyte is not purged with an inert gas before the PEC experiment, or if the anode material/electrolyte combination favors H_2O_2 production over O_2 production[5].

2.5.4 Applied Bias Photon-to-Current Efficiency (ABPE)

Among all the efficiency metrics, Solar-to-hydrogen (STH) conversion efficiency is one of the most valuable efficiency parameters as it furnishes the overall efficiency of a PEC system under zero bias conditions. Zero bias means, no potential is applied between working and counter electrodes and STH is of no use if there is a need for applying bias for overall water splitting. Under applied bias conditions between working and counter electrodes, current extracted from the system is higher than the bias-free condition, therefore it requires a new efficiency value called applied bias photon-to-current efficiency[6-7]. ABPE is analog to STH and it serves as a diagnostic measurement in materials development according to equation 2.9.

$$\text{ABPE}\ (\%) = \left[\frac{J_{sc}(\text{mA cm}^{-2})\times(1.23-V_b)(V)\times\eta_F}{P_{Total}(\text{mW cm}^{-2})}\right] \quad (2.9)$$

Where J_{SC} is the photocurrent under the applied bias of V_b.

2.6 Electrochemical Impedance Spectroscopy (EIS) Analysis

Electrochemical impedance spectroscopy is a crucial technique, where a small potential sinusoidal perturbation is applied to the system and the amplitude and phase shift of the resulting current response are measured[8]. As an alternating current (AC) technique, EIS is capable of differentiating between resistive and capacitive responses of metal-oxide interfaces based on the frequency dependence of the observed current. The effectiveness of EIS stems from its ability to differentiate multiple interfaces within devices[9]. **Figure 2.6.1 (A)** represents the Nyquist plot, carried out under illumination at potential correspond to 1.23 V_{RHE} between the frequency ranges of 0.1-10^6 Hz. Theoretically, the Nyquist plot shows two semicircles at high, and mid-frequency regions respectively. The semicircle at the high-frequency region is due to charge transfer occurring at the counter electrode/electrolyte interface. The semicircle at the mid-frequency region is due to charge transfer at the working electrode/electrolyte interface, is of paramount importance in determining the interfacial properties. A lower charge transfer resistance (R_k) value specifies a better charge-transport ability at the photoanode/electrolyte interface. From the inset of figure 2.6.1 (A), the Nyquist plot can also give information about the impedance of the Nernst diffusion of redox species (R_D) in the electrolyte. However, the semicircle associated with the Nernst diffusion process appears at low-frequency (10^{-1} to 10^{-2} Hz) which needs a longer time for complete analysis. All the parameters such as R_s, $R_{ct/k}$, R_{trap}, $C_{trap,}$ and C_{bulk} can be determined by fitting the Nyquist plots using the equivalent circuit diagram shown in **Figure 2.6.1 (B)**. R_{trap} acting as a recombination center is responsible for surface-state trapping electrons from the conduction band and holes from the valence band. $C_{trap,}$ $C_{bulk,}$ and R_S represent the trap-state capacitance, the space-charge depletion region capacitance, and series resistance of the cell respectively.

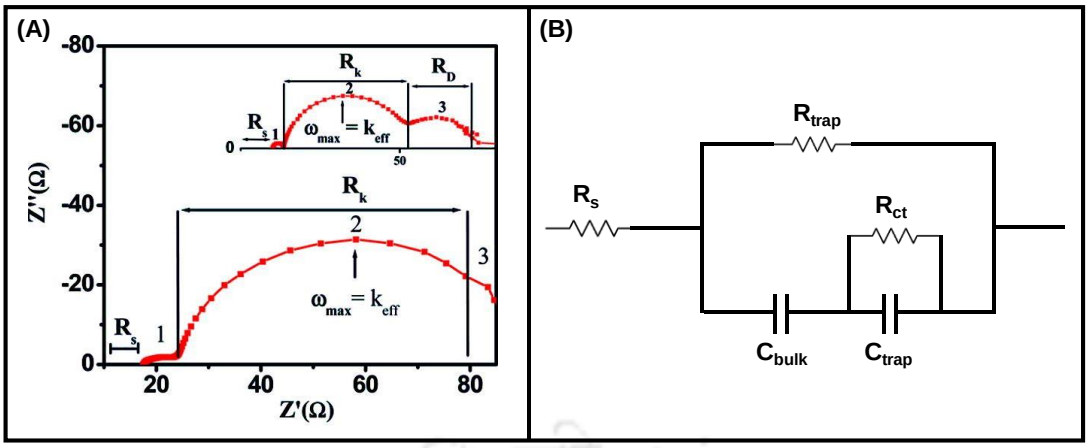

Figure 2.6.1 (A) Depicts the Nyquist plot for a semiconductor photoanode, inset of the same plot shows the Nyquist plot having all three semicircles, observed at different interfaces and (B) Equivalent circuit diagram

Another important parameter, which affects the performance of a photoelectrode is the charge carrier density, determined by the Mott-Schottky (M-S) analysis. Defining the flat band potential E_{fb}, (helpful in estimating the band edge positions in new materials) is also based on the Mott-Schottky relationship[10]. M-S analysis measures the capacitance of the space charge layer of the photoelectrode as a function of applied potential, according to the equation:

$$\frac{1}{C^2} = \frac{1}{A^2 N_D e \varepsilon \varepsilon_0} \left[E - E_{FB} - \frac{kT}{e}\right] \qquad (2.10)$$

Where C is the capacitance of semiconductor, e is the charge of an electron, E is the applied potential, A is the surface area of the photoelectrode, ε is the dielectric constant of the semiconductor, ε_0 is the permittivity of free space, N_D is the charge carrier density of semiconductor, k is the Boltzmann constant, and T is the temperature.

M-S is a type of technique, which is difficult to perform and interpret if the system is not ideal. N_D plays a vital role in determining the bulk and surface semiconductor properties such as the width of the depletion layer and rate of recombination. Based on the type of slope (Figure 2.6.2) i.e. negative or positive, the conductivity type can also be revealed by M–S analysis. The M–S plot possesses a negative slope for p-type materials and a positive slope for n-type materials[7].

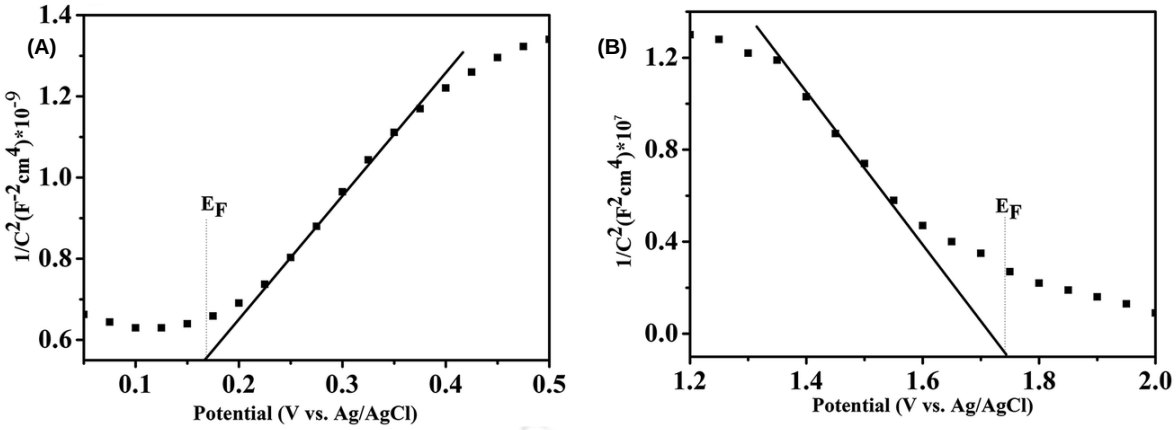

Figure 2.6.2 A typical Mott-Schottky plot for semiconductor photoanode, showing the nature of conductivity, taken from (Ref. 11)

2.7 Fabrication of a Two-Terminal Chemiresistor Sensor Device

To make the active sensing area (channel) for a two-terminal Chemiresistive device, first, fluorine-doped tin oxide substrates were etched with Zinc dust and concentrated HCl. **Scheme 2.7.1** represents the step-by-step fabrication process of a two-terminal sensing device. In the next step, sensing materials are deposited on the active sensing area and create a Schottky barrier with conductive FTO. Chemiresistor device having FTO on both sides, act as source and drain. Now, the sensing device is ready for all kinds of electrical measurements related to vapor phase sensing.

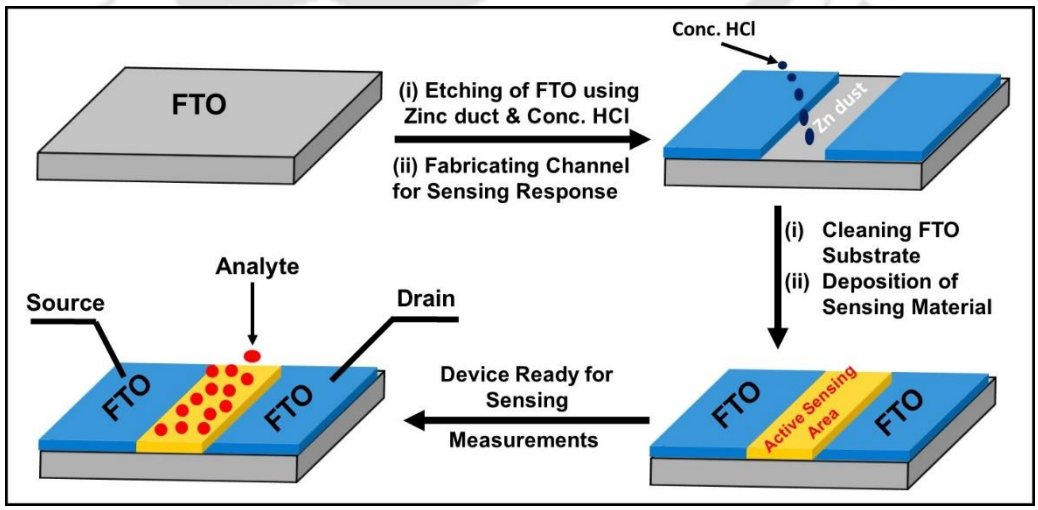

Scheme 2.7.1 Schematic representation of step-by-step fabrication of two-terminal Chemiresistor device for gas sensing

2.8 Gas Sensing Assembly

After the fabrication of the Chemiresistor device, all sensing experiments are performed at room temperature with a specific relative humidity level. Schematic illustration of the whole gas sensing assembly is presented in **Scheme 2.8.1**.

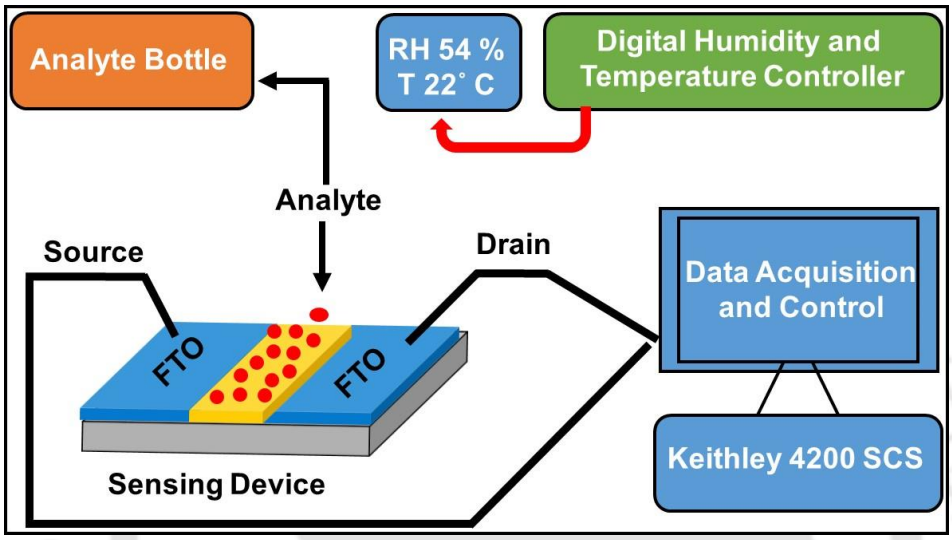

Scheme 2.8.1 Schematic drawing related to experimental set-up for NO_x gas sensing assembly

2.9 Gas Sensing Performance Parameters

Limit of detection (LOD) is a crucial parameter to evaluate the performance of a Chemiresistor device. LOD, which reflects the sensitivity of the device is defined as the minimum amount of analyte concentration detected by a sensing device. Therefore, in order to calculate LOD, the calibration curve of change in current response as a function of different concentrations of analyte is plotted, shown in **Figure 2.9.1 (A)**. Afterward, this calibration curve is fitted linearly to get the values of slope and correlation coefficient (R^2). The LOD is calculated using the mathematical formula LOD = 3σ/S, where 'σ' represents the relative standard deviation in the current responses without the exposure of analyte vapors and 'S' is the slope of the linearly fitted calibration curve[12]. The sensitivity of any sensor device is mainly determined by the limit of detection (LOD) of that device i.e. lesser the limit of detection better the sensitivity.

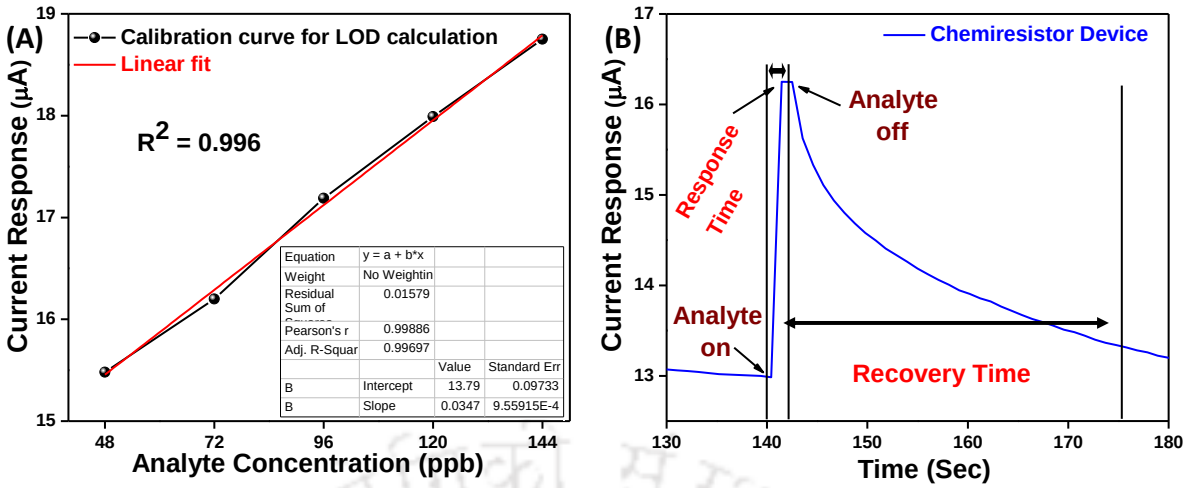

Figure 2.9.1 (A) Calibration curves of sensing device for LOD calculation and (B) Exhibits the response and recovery time of sensing device

Another essential parameter that determines the efficient usability of the gas-phase sensor is response and recovery time, represented in **Figure 2.9.1 (B)**. Response time of a sensing device is the time required to change the 90 % of the current response after exposing the analyte on the device while recovery time is the time elapsed in changing the 90 % of the current response to reach the original position after turning off the analyte vapor. A sensing device with a slower response/recovery time is considered to be highly sensitive, suitable for the rapid detection of analyte vapors.

2.10 References

(1) H. Chen, S. Wang, J. Wu, X. Zhang, J. Zhang, M. Lyu, B. Luo, G. Qian and L. Wang, *J. Mater. Chem. A*, 2020, **8**, 13231.

(2) M. Kato, J. Z. Zhang, N. Paul and E. Reisner, *Chem. Soc. Rev.*, 2014, **43**, 6485.

(3) D. K. Lee, D. Lee, M. A. Lumley and K.-S. Choi, *Chem. Soc. Rev.*, 2019, **48**, 2126.

(4) S. Chandrasekaran, L. Yao, L. B. Deng, C. Bowen, Y. Zhang, S. Chen, Z. Q. Lin, F. Peng and P. X. Zhang, *Chem. Soc. Rev.*, 2019, **48**, 4178.

(5) S. Kment, F. Riboni, S. Pausova, L. Wang, L. Wang, H. Han, Z. Hubicka, J. Krysa, P. Schmuki and R. Zboril, *Chem. Soc. Rev.*, 2017, **46**, 3716.

(6) X. Shi, L. Cai, M. Ma, X. Zheng and J. H. Park, *ChemSusChem*, 2015, **8**, 3192.

(7) Z. Chen, H. Dinh and E. Miller, *Photoelectrochemical Water Splitting*, *Springer*, 2013.

(8) T. Lopes, L. Andrade, H. A. Ribeiro and A. Mendes, *Int. J. Hydrogen Energy*, 2010, **5**, 11601.

(9) A. R. C. Bredar, A. L. Chown, A. R. Burton and B. H. Farnum, *ACS Appl. Energy Mater.*, 2020, **3**, 66.

(10) A. Hankin, F. Bedoya-Lora, J. Alexander, A. Regoutz and G. Kelsall, *J. Mater. Chem. A*, 2019, **7**, 26162.

(11) Y. Feng, C. Liu, J. Chen, H. Che, L. Xiao, W. Gu and W. Shi, *RSC Adv.*, 2016, **6**, 38290.

(12) M. S. Ansari, A. Banik, A. Kalita, P. K. Iyer and M. Qureshi, *J. Mater. Chem. A*, 2018, **6**, 15868.

CHAPTER 3

Interfacial bridging strategy for charge extraction/injection in $BiVO_4$/CoSn-LDH p-n heterojunction using GQDs for enhanced water oxidation kinetics

In this chapter, we have deposited a p-type mixed metal hydroxide CoSn-LDH directly over $BiVO_4$ surface to form a p-n heterojunction. This p-n heterojunction generates an internal build-in electric field to accelerate the charge transfer. In addition, this p-n junction was bridged with a conductive linker (graphene quantum dots) to extract holes from $BiVO_4$ surface and injected to surface active sites in CoSn-LDH. Incorporation of GQDs and CoSn-LDH not only increases the oxidation kinetics but also improves the stability of $BiVO_4$/GQDs/CoSn-LDH photoanode in alkaline conditions.

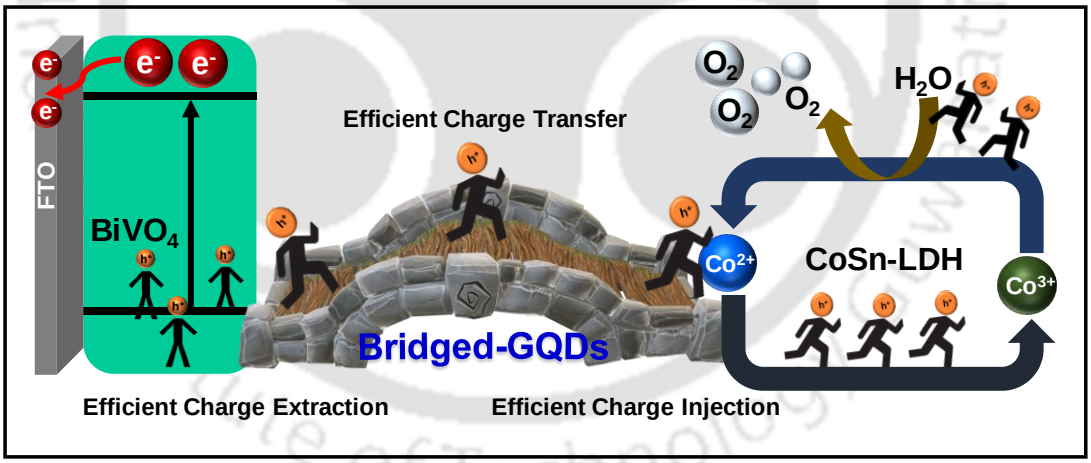

S. Alam et al., **J. Phys. Chem. Lett.,** 2021, 12, 8947-8955

3.1 Introduction

Efficient charge separation, transfer of charge carriers and reduced charge recombination are critical parameters in achieving efficient photoelectrochemical water splitting. Design of a suitable heterojunction with a built-in-potential at interface facilitates an efficient charge carrier separation and transportation. $BiVO_4$ is an ideal candidate for photoanode material for solar driven photoelectrochemical water splitting, due to its non-toxicity, abundant resources and higher stability in alkaline and neutral pH[1]. However, the reported current density of $BiVO_4$ based photoanode is far less than its theoretical possible value (7.5 mA/cm^2) [2]. This photoelectrochemical activity of $BiVO_4$ photoanode is severely limited to a great extent by some inherent disadvantages such as bulk phase recombination due to lower charge mobility, shorter hole diffusion length, and the surface recombination caused by sluggish surface oxygen kinetics[3-4]. To circumvent these shortcomings and to understand the potential of $BiVO_4$ based photoanode, enormous efforts including foreign element doping[5], morphological tuning[6], and construction of different heterojunction[7], facet engineering[8] and plasmonic enhancement[9], have been made to improve the surface kinetics as well as the charge separation. In contrast to these, expensive but effective catalysts such as RuO_2 and IrO_2[10] have been used as effective oxygen evolution reaction (OER) catalysts. Due to their high cost, a large-scale demonstration of OER is limited. Therefore, there is a need to develop a low cost OER catalyst. Within a wide range of OER catalysts, transition metals such as Fe, Co, Ni, based OER catalysts have been considered as one of the best choices due to their low cost as well as abundance in nature. Among the non-noble metal co-catalysts reported, Co based co-catalysts are utilized as an effective alternatives to that of the conventional OER catalysts. Cobalt, which is easily accessible non-noble metal is known to have variable oxidation states, a basic requirement for obtaining multi-electron transfer, which is one of the critical steps for water oxidation. Highly reactive CoO_x is known to be formed during the decomposition and loss of

Part of this chapter has been published in **J. Phys. Chem. Lett., 2021, 12, 8947-8955**

coordinated ligands because of the harsh experimental conditions for water splitting[11]. Even a small amount of CoO_x formed from cobalt complexes can effectively oxidize water, therefore it become mechanistically hard to assess whether Cobalt based complexes retain their identity or act as pre-catalysts to generate CoO_x[12]. Typically, surface reactions on the nano-sized semiconductor surfaces are hindered due to strong recombination kinetics of as-generated charge carriers caused by various factors. Effective transfer of charges (holes to drive OER) in the cocatalysts allow efficient redox reactions by lowering the over-potential of electron transfer reactions, similar to that of the electrocatalysis[13-15]. Introducing the mixed metal hydroxides as a co-catalyst is believed to be an effective way to influence the electrocatalytic activity. Moreover, Tin (Sn) inclusion into the cobalt hydroxide-based catalyst has positive effect on catalysis in terms of improving the catalytic activity of cobalt hydroxide, thereby improving the conductivity, which will expand the application field of cobalt hydroxide. Therefore, we have synthesized CoSn mixed metal LDH and incorporated with $BiVO_4$ to enhance the water oxidation kinetics. CoSn-LDH proves to form a p-n heterojunction with $BiVO_4$ for efficient separation of charge carriers at the interface. Despite the extensive use of LDH for water splitting, reports of LDH forming p-n heterojunction with semiconductor are less known[16-18].

Another perspective to stimulate the water oxidation kinetics of $BiVO_4$ based photoanode is to integrate an interlayer between metal oxide and oxygen evolution catalyst. Several materials such as rGO[19], Al_2O_3[20], and Nb_2O_5[21] have been used as an interlayer to enhance the water oxidation performance. Recently n-type graphene quantum dots (GQDs) have attracted considerable attention due to their size-dependent optical and electronic properties. Addition of graphene quantum dots onto semiconductor surface helps in suppressed recombination of photogenerated charge carriers. GQDs provides extra driving force to extract holes from $BiVO_4$ surface due to the presence of negatively charged species and transfers to

Part of this chapter has been published in **J. Phys. Chem. Lett., 2021, 12, 8947-8955**

oxygen evolution catalyst (OEC), which accelerate the transportation of holes to electrolyte for enhanced water oxidation reaction. Apart from charge extraction and injections, higher surface area of quantum dots provides a number of active sites for efficient PEC water splitting[22-23]. Although, limited literatures are reported where p-n heterojunction strategy have been studied; p-n heterojunction bridged with conductive linker to extract hole from photoanode surface are less reported.

Herein, we have examined the function of CoSn-LDH over $BiVO_4$ surface and then integrated GQDs as an interlayer (bridged) between $BiVO_4$ and CoSn-LDH for efficient extraction of holes from $BiVO_4$ surface. $BiVO_4$/GQDs/CoSn-LDH photoanode exhibits a significant improvement in photocurrent density when compared with pristine $BiVO_4$. The current density value of the composite photoanode reached up to 4.15 mA/cm^2 at 1.23 V vs. RHE with a cathodic shift of ~250 mV in onset potential, accounted for suppressed recombination of photogenerated carriers, improved charge injection, and hole injection efficiency.

3.2 Experimental Section

3.2.1 Fabrication of $BiVO_4$ Photoanode (Scheme 3.2.1, Step 1-2)

$BiVO_4$ photoanodes were electro-deposited over fluorine-doped tin oxide (FTO) using a three-electrode system. Prior to electrodeposition, FTO substrates were cleaned using soap solution, distilled water, acetone, and isopropanol. A calculated amount of KI (3.32 gm) was added into 50 mL of distilled water and the pH of this solution was adjusted to ~1.5 through dropwise addition of HNO_3 under stirring. To the above solution, 0.97 gm of $Bi(NO_3)_3.5H_2O$ was added as a Bi precursor and stirred for another 15 min. On the other hand, another solution was prepared by adding 0.49 gm of p-benzoquinone to 20 mL of ethanol. Before the electrodeposition, both solutions were mixed and stirred for 30 min. Electrodeposition of BiOI was performed at -0.1 V vs Ag/AgCl for 200 sec using chronoamperometric technique. As

Part of this chapter has been published in **J. Phys. Chem. Lett., 2021, 12, 8947-8955**

deposited BiOI films were cleaned properly with plenty of water and kept to dry at 100˚C for 60 min. A chemical-thermal treatment route was applied to convert these BiOI electrodes into $BiVO_4$ photoanodes. For the same, a calculated amount of $VO(acac)_2$ (0.183 gm) was added to 3 mL of DMSO solvent under constant stirring. A 60 μL of this Vanadyl solution was drop-casted over as-deposited BiOI surface and kept for drying at 100˚C for 60 min. Finally, these films were annealed at 450˚C in a furnace for 120 min at a heating ramp of 2˚C/min. Once this annealing and cooling process was completed, obtained films were soaked into NaOH solution to remove the impurities from the surface, and obtained films were cleaned with distilled water to get pure $BiVO_4$.

3.2.2 Hydrothermal Synthesis of Graphene Quantum Dots (GQDs)

For the synthesis of GQDs, the precursor solution comprises a calculated amount of citric acid (2.1 gm) and urea (1.8 gm) in 20 mL of distilled water under vigorous stirring for 30 min. Then, the above solution was transferred into an autoclave and maintained at 200˚C for 5 hr. The obtained solution was filtered using a 0.22 μm syringe filter and dialyzed for 24 hr before drying at 100˚C to get GQDs.

3.2.3 Fabrication of $BiVO_4$/GQDs Photoanode (Scheme 3.2.1, Step 3)

To fabricate $BiVO_4$/GQDs photoanode, GQDs solution was spin-coated over $BiVO_4$ surface at 4000 rpm for 45 sec and dried at 150˚C for 15 min, and named as $BiVO_4$/GQDs-1. This spin coating procedure was repeated several times to get an optimized loading of GQDs over $BiVO_4$ and named hereafter $BiVO_4$/GQDs-2, and $BiVO_4$/GQDs-3 respectively.

3.2.4 Fabrication of $BiVO_4$/CoSn-LDH and $BiVO_4$/GQDs/CoSn-LDH Photoanode (Scheme 3.2.1, Step 4)

In order to fabricate the $BiVO_4$/GQDs/CoSn-LDH photoanode, the precursor solution was prepared by dissolving a calculated amount of $Co(NO_3)_2.6H_2O$ (220 mg) and $SnCl_4.5H_2O$

Part of this chapter has been published in **J. Phys. Chem. Lett., 2021, 12, 8947-8955**

(87 mg) in 30 mL of distilled water. Then 150 mg of urea was added to the above solution before transferring it to the autoclave. $BiVO_4$/GQDs films were placed at the bottom of the autoclave and maintained the reaction temperature to 120˚C for 4 hr. As obtained $BiVO_4$/GQDs/CoSn-LDH photoanodes were rinsed with distilled water and dried at 60˚C. To get an optimized loading of CoSn-LDH different reactions were carried out by changing the Co to Sn ratio in the precursor solution. Under the same experimental conditions, CoSn-LDH was deposited over the $BiVO_4$ electrode to get $BiVO_4$/CoSn-LDH photoanodes. The systematic fabrication procedure of $BiVO_4$/GQDs/CoSn-LDH is depicted in **Scheme 3.2.1**.

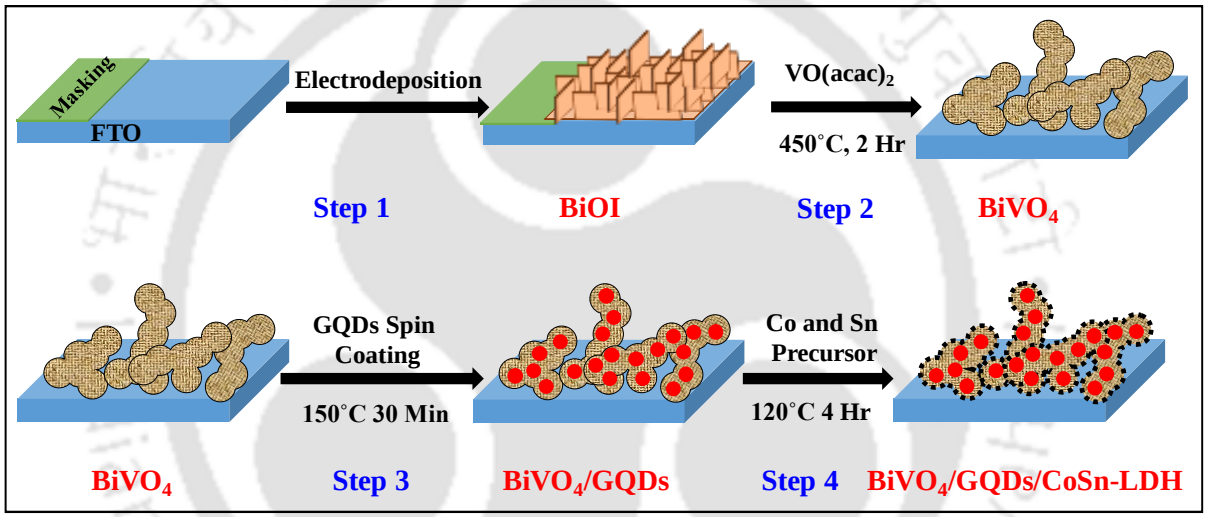

Scheme 3.2.1 Step by step fabrication procedure for $BiVO_4$/GQDs/CoSn-LDH photoanode, (Step 1) electrodeposition of BiOI over FTO, (Step 2) drop-casting of vanadyl solution and thermal annealing, (Step 3) spin coating of GQDs over as-synthesized $BiVO_4$, and (Step 4) hydrothermal deposition of CoSn-LDH over $BiVO_4$/GQDs photoanode

3.3 Results and Discussions

3.3.1 Powder X-ray Diffraction (XRD) Analysis

Powder X-ray diffraction analysis technique was employed to investigate the formation and crystal phase purities of as-synthesized $BiVO_4$, GQDs, CoSn-LDH, and different composites, as depicted in **Figure 3.3.1**. Figure 3.3.1 trace (a) shows the XRD pattern for bare $BiVO_4$ and all diffraction peaks at 2θ values of 18.88˚, 28.86˚, 30.57˚, 34.77˚, 35.17˚, 40.03˚,

Part of this chapter has been published in **J. Phys. Chem. Lett., 2021, 12, 8947-8955**

42.52˚, 45.93˚, 47.25˚, 50.27˚, and 53.42˚ matches to their crystal planes (110), (121), (040), (200), (002), (211), (051), (132), (042), (202), and (161) respectively, are in good agreement with the monoclinic phase (JCPDS number 14-0688). Sharp and intense peaks specifies the crystalline nature of as-deposited $BiVO_4$. Trace (b) represents the XRD spectra of as-synthesized GQDs, exhibits a broad peak at 25.06˚ correspond to (002) crystal plane of graphitic carbon. Trace (c) represents the XRD spectra of CoSn-LDH. Diffraction peaks indexed in red and black color matches to the hydroxides of Tin (JCPDS 01-084-5001) and Cobalt (JCPDS 00-048-0083) respectively, ratify the mixed phase of as-synthesized CoSn-LDH. Trace (d) represents the XRD pattern for $BiVO_4$/GQDs/CoSn-LDH photoanode, showing the retention of the crystal structure of $BiVO_4$ after the immobilization of GQDs and CoSn-LDH. In this spectrum, the absence of characteristic diffraction peaks for GQDs or CoSn-LDH, attributed to the fact that the lower loading of GQDs or CoSn-LDH and higher crystallinity of $BiVO_4$ makes it difficult to detect in composite structures.

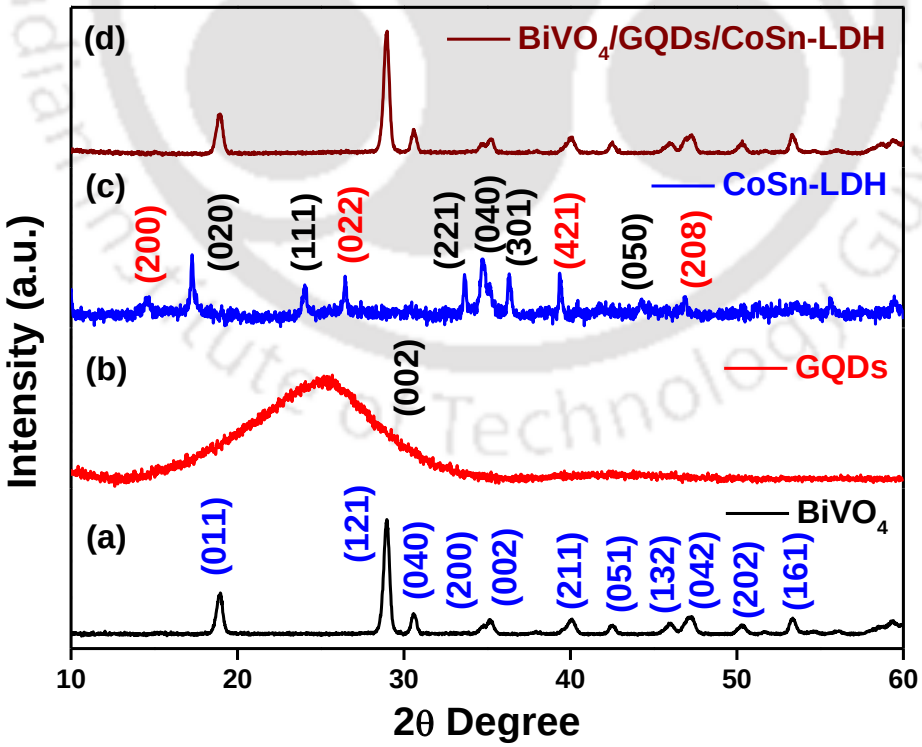

Figure 3.3.1 X-ray diffraction spectra of (a) Pristine $BiVO_4$, (b) GQDs only, (C) Bare CoSn-LDH, and (d) $BiVO_4$/GQDs/CoSn LDH photoanode, perfectly indexed to their crystal plane

3.3.2 Fourier Transform Infrared Spectroscopy (FT-IR) Analysis

To identify the attached functional groups onto GQDs, FT-IR analysis was carried out, and **Figure 3.3.2** represents the same. The peak at 3423 cm^{-1} belongs to the stretching vibrations of –O-H and –N-H, while the peak at 2918 cm^{-1} is attributed to sp^2 –C-H stretching frequency. Two peaks at 1650 cm^{-1} and 1380 cm^{-1} belong to the asymmetric and symmetric vibrations of –COOH group respectively. The peak at 1230 cm^{-1} corresponds to the –C-O-C group. Due to the presence of these functional groups, GQDs are highly soluble in water[24-25].

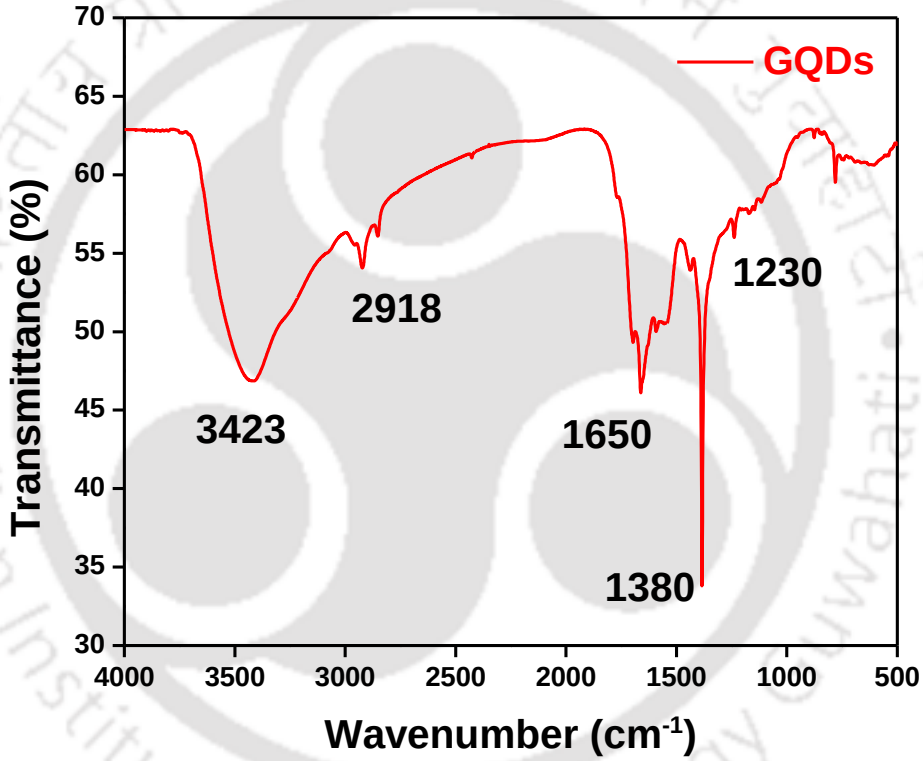

Figure 3.3.2 FT-IR spectra of as-synthesized Graphene Quantum Dots

3.3.3 Raman Spectroscopy Analysis

Raman spectra of as-synthesized GQDs presented in **Figure 3.3.3** shows two different peaks at 1377 cm^{-1} and 1547 cm^{-1}, corresponding to D and G band respectively. D band is due to the defects induced bonding and antibonding orbitals of sp^3 carbon atoms with breathing mode of A_{1g} phonon while G band is due to the in-plane stretching vibrations of ordered sp^2 carbon atoms with optical E_{2g} phonons. Therefore, D band is due to disordered or defects states

while G band is due to the ordered state, and the intensity ratio of these two bands (I_D/I_G) gives an idea about the extent of structural defects or degree of disorder. Here, the observed I_D/I_G ratio is greater than 1, revealing the significant number of defects at GQDs surface[26-27].

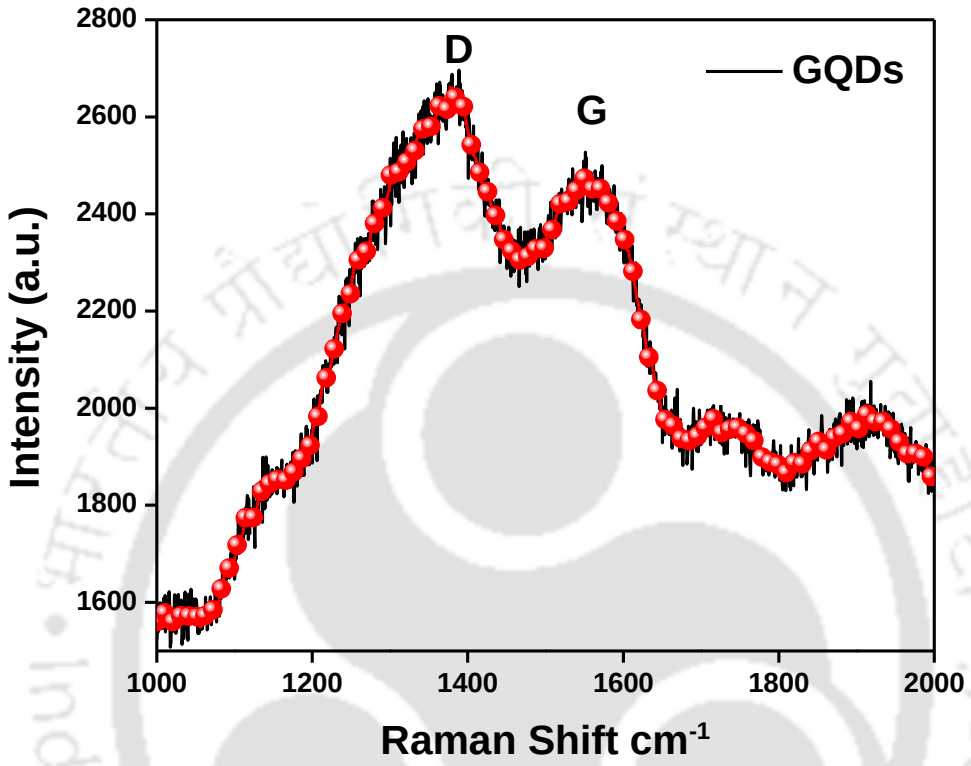

Figure 3.3.3 Raman spectra of as-synthesized Graphene Quantum Dots showing the presence of D and G bands and their ratio, indicative of defects at the surface

3.3.4 UV-Visible and Photoluminescence Spectra Analysis

In order to investigate the optical properties of as-synthesized GQDs, UV-visible and Photoluminescence spectra were recorded, and **Figure 3.3.4** represents the same. UV-Vis spectra of GQDs comprises two different peaks at 250 nm and 340 nm correspond to π–π* transition of sp^2 carbon and n-π* transition of carbon lattice respectively[28-29]. A strong and sharp emission peak at 430 nm was observed upon excitation at 340 nm indicative of the fluorescent nature of GQDs. Inset to figure 3.3.4; images of GQDs are shown under UV and Visible light.

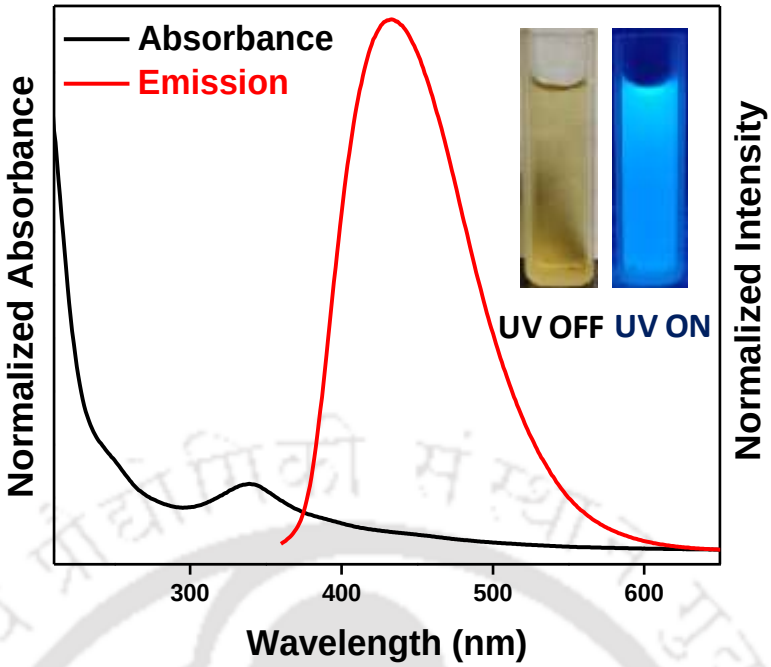

Figure 3.3.4 Absorbance (black) and Emission (red) spectra of as-synthesized GQDs, inset of the figure shows images of GQDs under UV and visible light

3.3.5 Morphological and Structural Analysis

Detailed observations for the morphological evolution of as-synthesized $BiVO_4$, $BiVO_4$/GQDs, $BiVO_4$/CoSn-LDH, and $BiVO_4$/GQDs/CoSn-LDH were characterized using FESEM analysis, as depicted in **Figure 3.3.5**. Figure 3.3.5 (A) represents the FESEM image of evenly deposited BiOI nano-flakes. These orderly arranged nano-flakes act as a template and Bi source in order to fabricate $BiVO_4$. Moreover, these 2D nano-flakes are positioned loosely to provide sufficient area for volume diffusion/expansion after the injection of vanadium ions. During the annealing process, these BiOI nano-flakes are transformed into a worm-like $BiVO_4$ structure with a smoother surface, illustrated in figure 3.3.5 (B). Here, it is important to mention that these morphological structures display robust adhesion and good ohmic contact for efficient charge transfer, as they are deposited directly over FTO without any seed layer. Further, a thin layer of graphene quantum dots is spin-coated over the $BiVO_4$ surface without disturbing the morphology, illustrated in figure 3.3.5 (C). Figure 3.3.5 (D) represents the FESEM image of $BiVO_4$ loaded with CoSn-LDH.

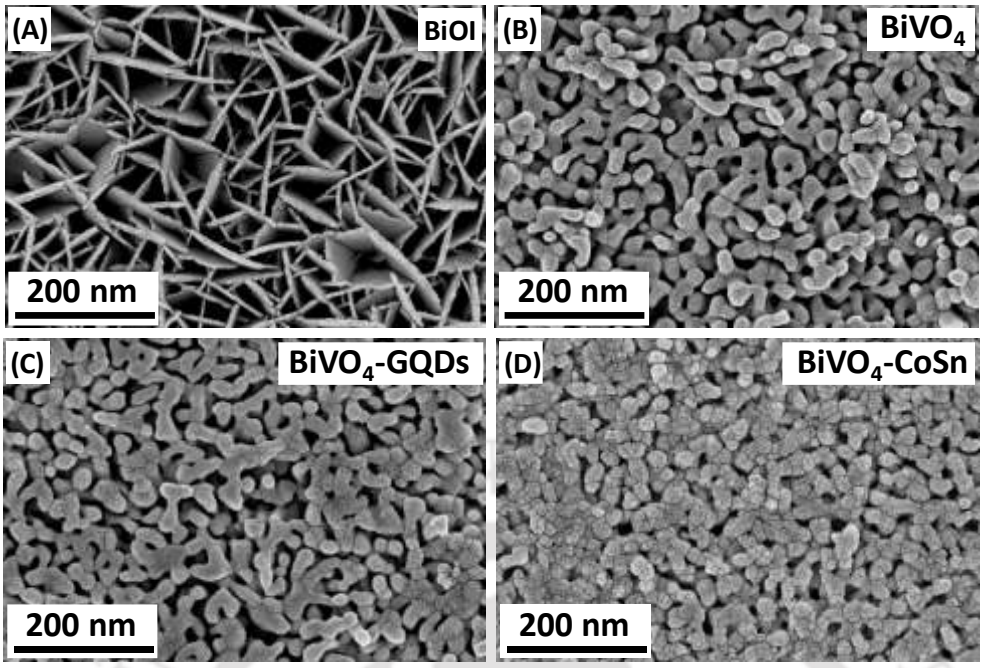

Figure 3.3.5 FESEM images of (A) as-deposited BiOI nanoflakes, (B) worm-like $BiVO_4$ structures derived from BiOI nanoflakes, (C) GQDs coated over $BiVO_4$, and, (D) as-deposited CoSn-LDH over $BiVO_4$

Further validation for successful deposition of GQDs and CoSn-LDH over $BiVO_4$ surface was ascertained by TEM analysis, illustrated in **Figure 3.3.6**. Figure 3.3.6 (traces A and B) represent the TEM and HRTEM images of pristine $BiVO_4$ respectively, showing the fringes with an interplanar distance of 0.30 nm correspond to (121) crystal plane of $BiVO_4$. Figure 3.3.6 (traces C and D) represent the TEM and HRTEM images of GQDs respectively, with an interplanar distance of 0.22 nm, correspond to the (110) plane of graphite. In addition, the typical size of as-synthesized GQDs is turn out to be 4.7 nm. Figure 3.3.6 (traces E and F) represent the TEM and HRTEM images of GQDs coated $BiVO_4$ photoanode. From the micrograph, it is evident that GQDs are attached to the $BiVO_4$ surface. HRTEM image of $BiVO_4$ coated with GQDs, reveals the well-defined lattice fringes with an interplanar distance of 0.30 nm, correspond to (121) plane of $BiVO_4$ while a d-spacing of 0.35 nm corresponds to (002) plane of graphite. Traces (G and H) represent the TEM and HRTEM images of $BiVO_4$/CoSn-LDH respectively. From trace (G), it is apparent that a thin layer of CoSn-LDH is wrapped over the $BiVO_4$ surface. HRTEM micrograph of CoSn-LDH modified $BiVO_4$ shows

the lattice fringes with an inter-planar spacing of 0.29 and 0.36 nm well matches with the (040) and (111) plane of pristine $BiVO_4$ and CoSn-LDH, respectively.

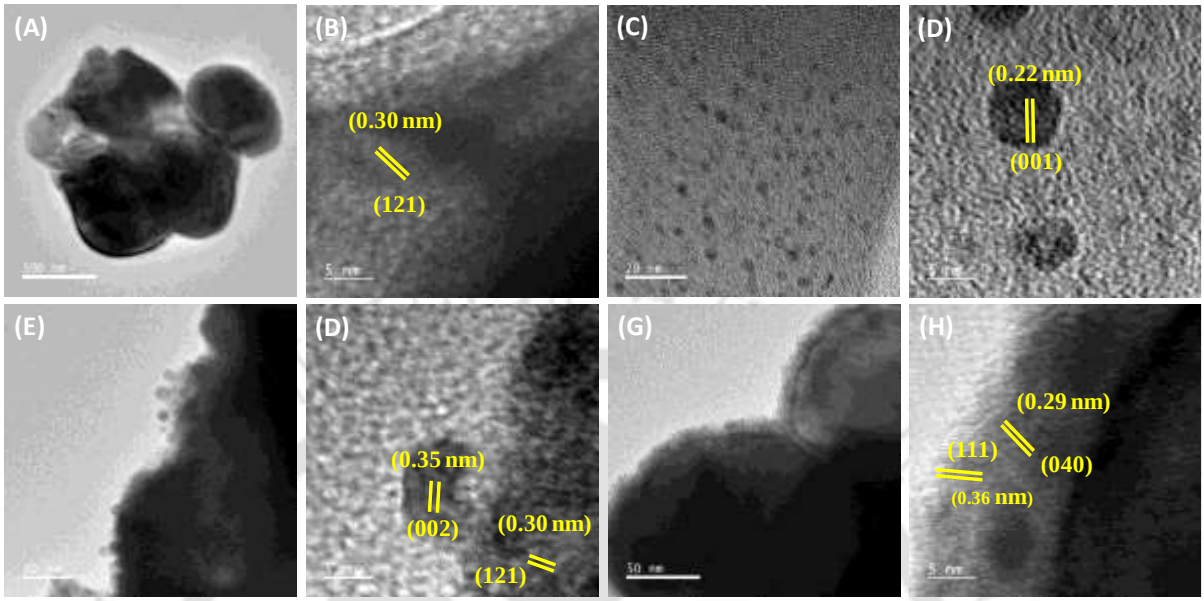

Figure 3.3.6 (A-B) TEM and HRTEM images of as-synthesized $BiVO_4$, (C-D) TEM and HRTEM images of as-synthesized GQDs only, (E-F) TEM and HRTEM images of GQDs coated $BiVO_4$, and (G-H) TEM and HRTEM images of as-synthesized $BiVO_4$/CoSn-LDH photoanode, respectively

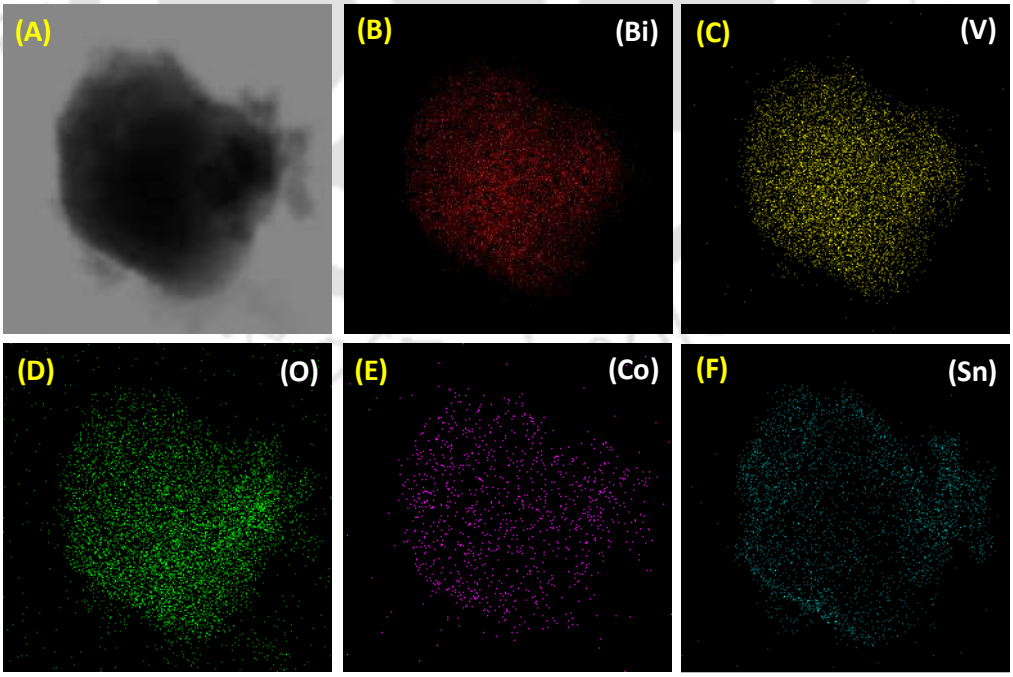

Figure 3.3.7 Elemental mapping of $BiVO_4$/CoSn-LDH composite showing the presence of the elements i.e. Bi (Red), V (Yellow), O (Green), Co (Purple), and Sn (Cyan)

To verify the elemental composition and their positioning in $BiVO_4$/CoSn-LDH photoanode, STEM-EDS mapping was carried out, as demonstrated in **Figure 3.3.7**. From corresponding images, it is evident that all the elements such as Bi, V, O, Co and Sn are evenly dispersed throughout the sample in the scan area.

3.3.6 X-ray Photoelectron Spectroscopy (XPS) Analysis

To substantiate the chemical states of the elements in as-synthesized photoanodes, XPS analysis was carried out, and resulted spectra are summarized in **Figure 3.3.8**. From the survey spectra (figure 3.3.8 (A)), the respective peak for each element is observed, which verifies the chemical composition of individual photoanode. Figure 3.3.8 (B) represents the core level spectra for Bi (4f), shows two different peaks at binding energies of 159.11eV and 164.43 eV, correspond to $4f_{7/2}$ and $4f_{5/2}$ respectively. Separation of binding energies between the two states confirms the existence of Bi^{3+} in $BiVO_4$[30]. Similarly, the high-resolution spectra of V (2p) (figure 3.3.8 (C)) shows two peaks at binding energies of 516.65 eV and 524.10 eV, assigned to $2p_{3/2}$ and $2p_{1/2}$ respectively, indicates the existence of Vanadium in +5 (V^{5+}) state for both photoanodes[31]. After the decoration of $BiVO_4$ with GQDs and CoSn-LDH, the $BiVO_4$/GQDs/CoSn-LDH photoanode shows two peaks for Bi (4f) i.e. $4f_{7/2}$ and $4f_{5/2}$ at binding energies of around 158.83 eV and 164.13 eV respectively. Wherein, the composite photoanode shows the peaks for V (2p) i.e $2p_{3/2}$ and $2p_{1/2}$ at binding energies of around 516.37 eV and 523.77 eV respectively. This shift in Bi (4f) and V (2p) peaks towards the lower binding energy is the indication of strong electronic interaction among GQDs, CoSn-LDH and $BiVO_4$[32-33]. Figure 3.3.8 (D) represents the high-resolution spectra of O 1s for both bare and modified $BiVO_4$. O 1s spectra of both bare and modified $BiVO_4$ are further deconvoluted into three different peaks. Peaks at lower binding energies i.e. at 529.78 eV for bare $BiVO_4$ and 529.43 eV for modified $BiVO_4$ are designated to lattice oxygen. Peaks at 530.31 and 530.68 eV are allocated to hydroxyl groups combined with a metal cation, while peaks at higher binding

energies are specified to surface adsorbed water[18, 34]. This shift in binding energies for Bi, V, and O are due to the binding interactions among $BiVO_4$, GQDs, and CoSn-LDH, which resulted in change in local electron density distributions among the individual components in the composite[19, 35].

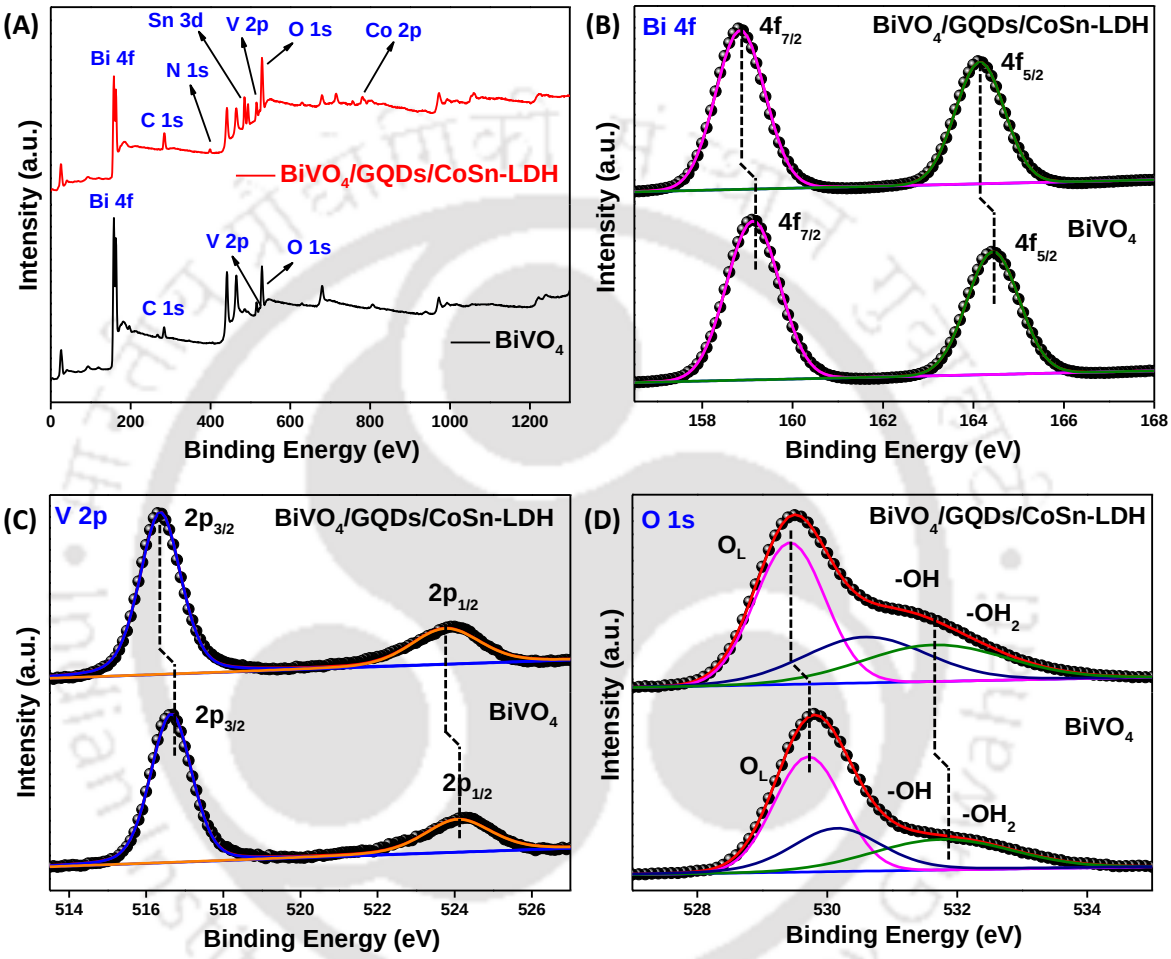

Figure 3.3.8 (A) Survey spectra for $BiVO_4$ and $BiVO_4$/GQDs/CoSn-LDH photoanodes, showing the presence of all elements, (B) Core level XPS spectra of Bi 4f, (C) V 2p, and (D) O 1s depicting the chemical state of Bismuth and Vanadium and their subsequent interactions for improved PEC water oxidation

Figure 3.3.9 (A) represents the core level spectra for Co 2p, further deconvoluted to confirm the different oxidation states of Co present in the composite photoanode. It is evident from figure 3.3.9 (A) that two peaks present at binding energies 780.82 eV and 796.78 eV, correspond to $2p_{3/2}$ and $2p_{1/2}$ respectively, confirm the presence of Co^{2+}. Moreover, these peaks

Part of this chapter has been published in **J. Phys. Chem. Lett., 2021, 12, 8947-8955**

ally with two satellite peaks at binding energies around 785.91 eV and 803.83 eV respectively. Peak present at binding energy 780.82 eV is further fitted with two different peaks at 780.49 eV and 782.01 eV; indexed to Co^{3+} and Co^{2+} species respectively. Similarly, in $2p_{1/2}$, the peaks fitted to 796.24 eV and 797.271 eV belong to Co^{3+} and Co^{2+} configurations, respectively[36]. Figure 3.3.9 (B) represents the core level spectra of Sn 3d, showing two peaks at binding energies of 486.62 and 495.04 eV correspond to $3d_{5/2}$ and $3d_{3/2}$ respectively. Figure 3.3.9 (C) represent the core level spectra of C 1s. After deconvolution this peak is further fitted into three distinct peaks at binding energies of 284.72 eV, 286.1 eV, and 288.04 eV, correspond to aliphatic or graphitic (C─C/C=C), oxygenated (C─O/C=O) and C─N carbon atoms respectively. Figure 3.3.9 (D) represents the XPS core-level spectra of N 1s. Upon deconvolution, N 1s peak further fitted into two peaks at binding energies of 399.66 eV and 400.3 eV, correspond to pyrrolic, and graphitic nitrogen groups, respectively.

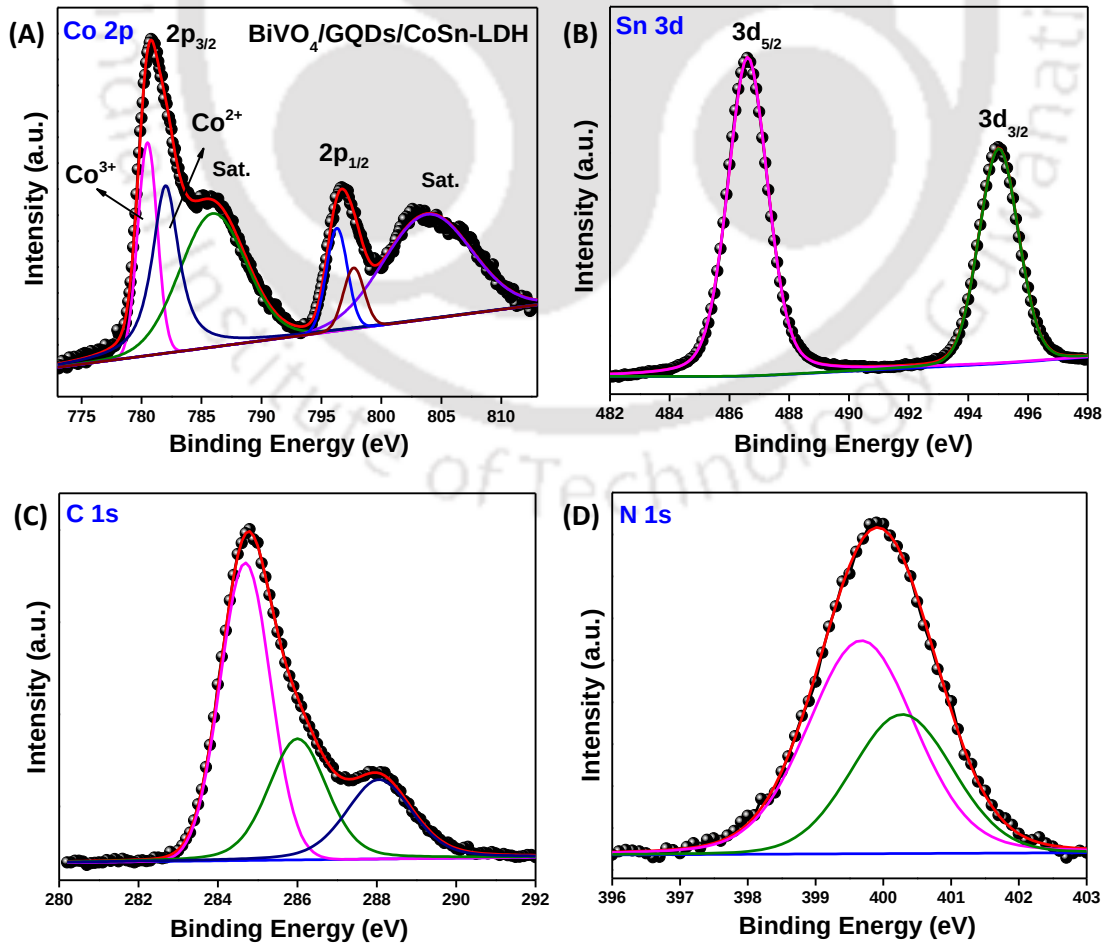

Part of this chapter has been published in **J. Phys. Chem. Lett., 2021, 12, 8947-8955**

Figure 3.3.9 Core level XPS spectra of (A) Co 2p, (B) Sn 3d, (C) C 1s, and (D) N 1s, in $BiVO_4$/GQDs/CoSn-LDH photoanode

3.3.7 Time-resolved Photoluminescence (TRPL) Analysis

To confirm the charge transfer phenomenon, time resolved photoluminescence (TRPL) analysis was carried out and **Figure 3.3.10** represent the same. The corresponding decay patterns are fitted using tri-exponential function and average lifetime is calculated using equation 3.1. Fitted parameters such as (α_1, α_2, α_3), (τ_1, τ_2, τ_3) and $< \tau >$ are summarized in Table 3.3.1.

$$< \tau > = \frac{a_1\tau_1^2 + a_2\tau_2^2 + a_3\tau_3^2}{a_1\tau_1 + a_2\tau_2 + a_3\tau_3} \qquad (3.1)$$

The observed average lifetime values for GQDs and $BiVO_4$/GQDs/CoSn-LDH are found to be 9.90 ns and 1.55 ns respectively. This improved average lifetime value for $BiVO_4$/GQDs/CoSn-LDH indicates charge transfers among the components present.

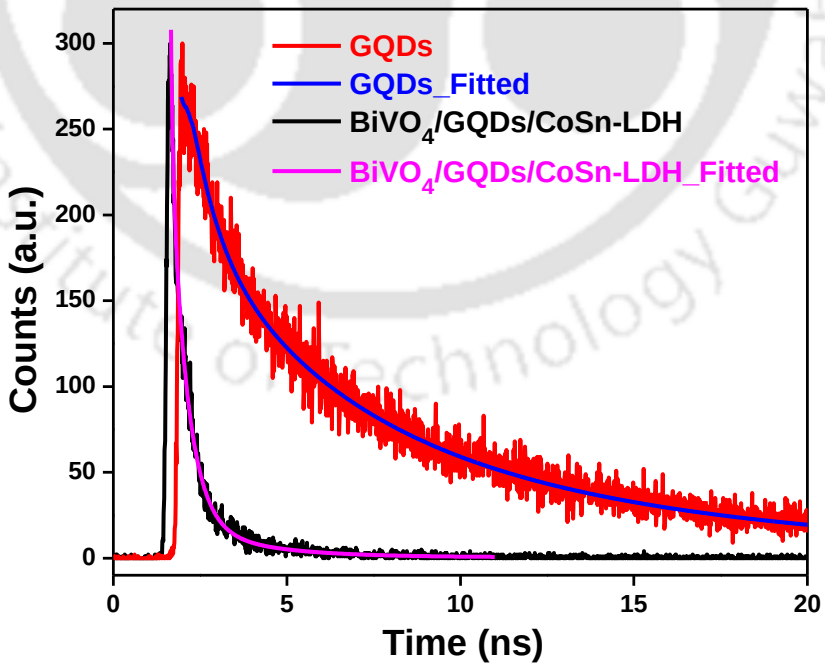

Figure 3.3.10 Time resolved photoluminescence (TRPL) decay curves for GQDs and $BiVO_4$/GQDs/CoSn-LDH for charge transfer among the components present in composite

Table 3.3.1.

Sample	χ^2	τ_1	τ_2	τ_3	α_1	α_2	α_3	$< \tau >$ ns
GQDs	1.120	0.695	3.385	10.868	5.939	27.972	66.089	9.90
$BiVO_4$/GQDs/CoSn-LDH	1.033	0.051	0.454	2.089	2.758	66.767	30.475	1.55

3.3.8 Photoelectrochemical Measurements

To evaluate the synergistic effect of GQDs interlayer and CoSn-LDH as co-catalyst on water oxidation performance, current density-voltage responses were assessed in a 0.5 M potassium borate (pH~11) solution under simulated 1 Sun irradiation, illustrated in **Figure 3.3.11**. Photoelectrochemical activities of $BiVO_4$ photoanodes, loaded with different amounts of GQDs as well as CoSn-LDH are analyzed to get the optimized condition for improved water oxidation, and figure 3.3.11 (B & C) represent the same. Figure 3.3.11 (A) exhibits the LSV curve for bare and modified $BiVO_4$ as a function of applied bias under optimized conditions. Photocurrent densities of all the photoanodes increases linearly with applied voltage, indicative of an n-type diode behavior of a semiconductor[37]. From figure 3.3.11 (A), it is evident that $BiVO_4$ shows a comparatively low photocurrent density of 1.33 mA/cm^2 at 1.23 V vs RHE with an onset potential of 0.60 V_{RHE}. When this $BiVO_4$ photoanode is loaded with an optimized amount of GQDs, the photocurrent density increases to 2.83 mA/cm^2. In another case, when $BiVO_4$ is modified with only CoSn-LDH, the photocurrent density reaches up to 3.35 mA/cm^2 at 1.23 V vs RHE with an onset potential of 0.42 V_{RHE}. This shift in the onset potential is an indication of a lower over-potential needed to boost water oxidation, originated from the loading of CoSn-LDH. $BiVO_4$ photoanode is modified with GQDs and CoSn-LDH compounds synergistically, the photocurrent density increases drastically and reaches a maximum of 4.15 mA/cm^2 at 1.23 V vs RHE, which is ~3 times higher than pristine $BiVO_4$, and reaching more than 50 % of the theoretical current density achievable (7.5 mA/cm^2) for $BiVO_4$[2]. This drastic

improvement in photocurrent density value is mainly associated with the reduced recombination of charge carriers, faster transfers followed by efficient injections of carries into the CoSn-LDH from $BiVO_4$ surface through GQDs bridging. Incorporation of GQDs and CoSn-LDH may lead to the formation of a favorable junction, facilitating the interfacial charge transfer and charge injections for improved PEC water oxidation.

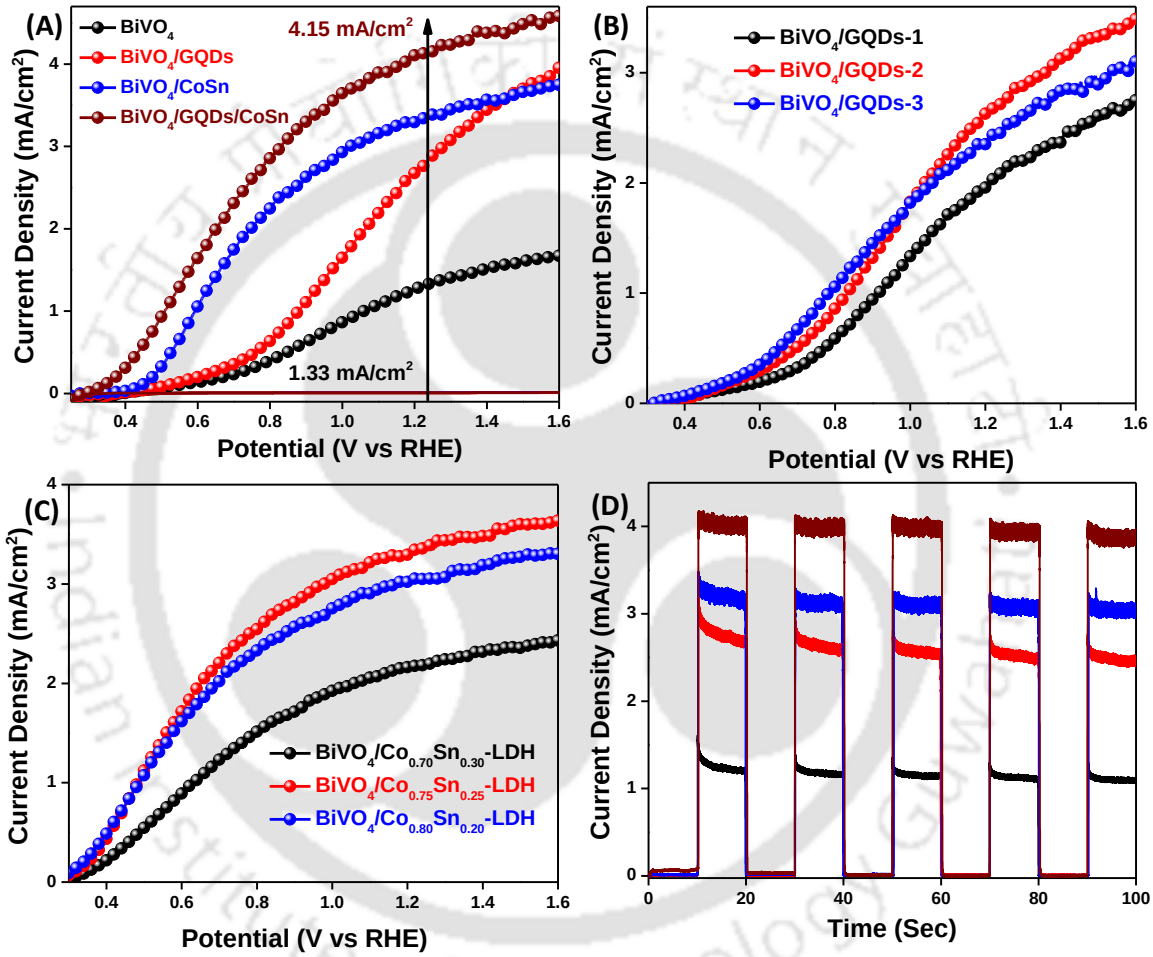

Figure 3.3.11 Current density-Voltage curves for $BiVO_4$, $BiVO_4$/GQDs, $BiVO_4$/CoSn-LDH, and $BiVO_4$/GQDs/CoSn-LDH, recorded under illumination, (B) Current density-Voltage curves for $BiVO_4$ coated with different layers of GQDs, (C) Current density-Voltage curves for $BiVO_4$ modified with different ratio of CoSn-LDH, and (D) Chronoamperomettry curves for $BiVO_4$, $BiVO_4$/GQDs, $BiVO_4$/CoSn-LDH and $BiVO_4$/GQDs/CoSn-LDH photoanodes recorded at 1.23 V vs RHE

To further validate the reduced recombination of photogenerated charge carriers, chrono-amperometric analysis of all photoanodes were carried out, and **Figure 3.3.11 (D)**

Part of this chapter has been published in **J. Phys. Chem. Lett., 2021, 12, 8947-8955**

represents the same. These photo responses are recorded under chopped illumination at a fixed potential, correspond to 1.23 V vs RHE. From figure 3.3.11 (D), it is clear that the photocurrent densities of these photoanodes under illumination follow the order **$BiVO_4$/GQDs/CoSn-LDH > $BiVO_4$/CoSn-LDH > $BiVO_4$/GQDs > $BiVO_4$**, which is in close agreement with the results obtained from LSV analysis. When the light is subjected to ON and OFF through chopping, all the photoanodes show a drastic change in photocurrent density values and more importantly, with reduced anodic spikes compared to the pristine $BiVO_4$. These anodic spikes are known to arise because of the accumulation of holes at the $BiVO_4$ surface followed by the recombination with the photogenerated electrons. Loading of GQDs and CoSn-LDH could synergistically decrease the number of aggregated holes at $BiVO_4$ surface and restrict the further charge recombination, indicating the faster kinetics for efficient water oxidation reaction.

To give an explication to the aforementioned phenomenon, the electrocatalytic activity of synthesized CoSn-LDH was also measured, and **Figure 3.3.12 (A)** represents the same. The over-potential at 10 mA/cm^2 for CoSn-LDH is found to be 300 mV. Further, the Tafel slope is evaluated using the LSV curve to study the kinetics of CoSn-LDH and found to be 89 mV/dec., according to **Figure 3.3.12 (B)**.

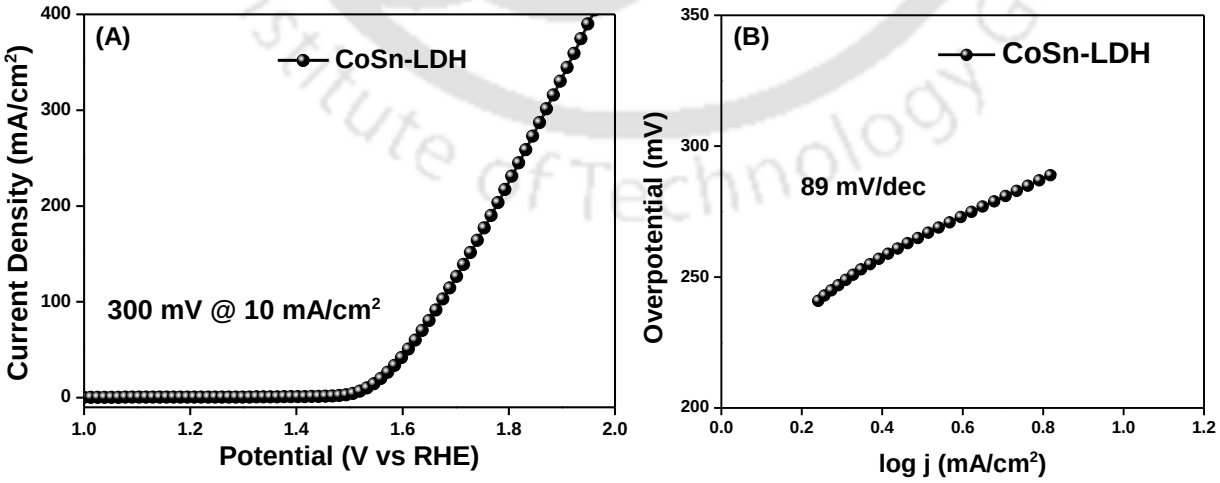

Figure 3.3.12 (A) Linear sweep voltammetry curve for bare CoSn-LDH under dark condition, and (B) corresponding Tafel plot

Further quantitative analysis of water oxidation efficacy was done by evaluating applied bias photon-to-current efficiency (ABPE) values, derived from corresponding I-V curves and **Figure 3.3.13 (A)** represent the same. It is evident that $BiVO_4$/GQDs/CoSn-LDH photoanode achieves an impressive ABPE of ~1.26 % at a low potential of 0.74 V_{RHE}. In contrast to this ABPE values of 0.22 % at 0.95 V_{RHE}, 0.47 % at 0.92 V_{RHE}, and 0.98 % at 0.76 V_{RHE} belongs to $BiVO_4$, $BiVO_4$/GQDs, and $BiVO_4$/CoSn-LDH photoanodes respectively. It is worth mentioning that the negative shift in the peak position of $BiVO_4$/GQDs/CoSn-LDH photoanode is associated to enhance current density value at a lower applied potential. Therefore, incorporation of GQDs and CoSn-LDH effectively stimulates the PEC performance.

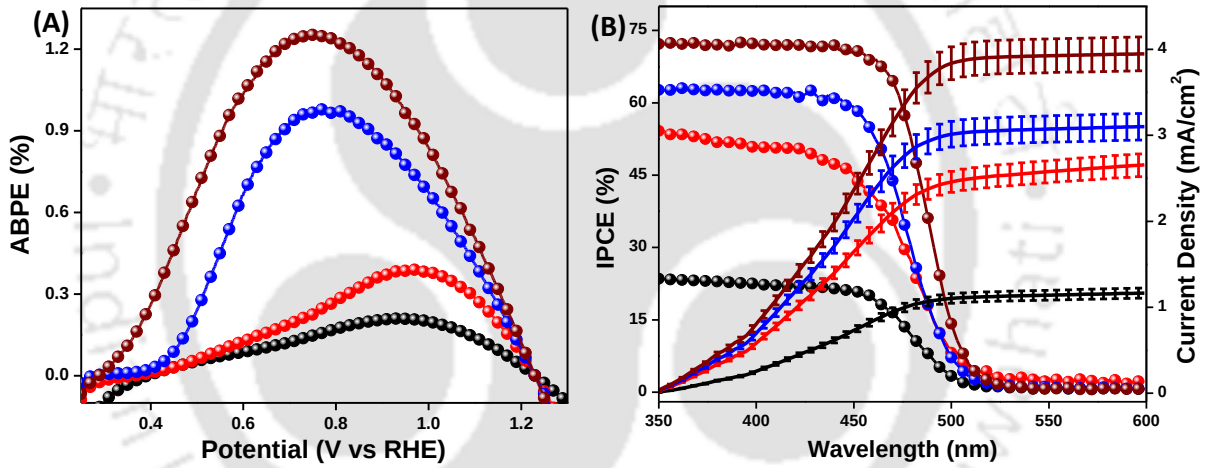

Figure 3.3.13 (A) ABPE curves for $BiVO_4$ (black), $BiVO_4$/GQDs (red), $BiVO_4$/CoSn-LDH (blue) and $BiVO_4$/GQDs/CoSn-LDH (wine) photoanodes, derived from current density-voltage curves, and (B) IPCE spectra for $BiVO_4$ (black), $BiVO_4$/GQDs (red), $BiVO_4$/CoSn-LDH (blue) and $BiVO_4$/GQDs/CoSn-LDH (wine) photoanodes, and corresponding integrated current values

Additionally, this enhanced photocurrent density was further confirmed by evaluating IPCE values as a function of the wavelength of incident light in a confined range of 300-600 nm, displayed in **Figure 3.3.13 (B)**. Moreover, these IPCE curves are integrated throughout the whole range in order to calculate the corresponding photocurrent value. From figure 3.3.13 (B), it is clear that $BiVO_4$/GQDs/CoSn-LDH photoanode exhibits an impressive IPCE value of

Part of this chapter has been published in **J. Phys. Chem. Lett., 2021, 12, 8947-8955**

~72 % as compared to IPCE value of ~23 % for bare $BiVO_4$ photoanode. On the other hand, the IPCE value of 53 % and 63 % belongs to $BiVO_4$/GQDs and $BiVO_4$/CoSn-LDH photoanodes respectively. Therefore, obtained higher IPCE for $BiVO_4$/GQDs/CoSn-LDH photoanode confirms the higher photocurrent density value achieved from LSV curve, also matches well with the integrated current density values. This enhanced IPCE value may be due to the fact that the loading of GQDs and CoSn-LDH can form a suitable junction onto $BiVO_4$, which dramatically improves the charge injection and reduces the charge recombination, thereby facilitating PEC water oxidation performance.

3.3.9 Electrochemical Impedance Spectroscopy (EIS) Analysis

To get an idea about the charge transfer and recombination kinetics that occurred at different interfaces of as-fabricated photoanodes, EIS analysis was carried out under illumination at potential correspond to 1.23 V_{RHE} between the frequency range of 0.1-10^6 Hz. **Figure 3.3.14** represents the Nyquist plot plotted from EIS measurements. The inset to figure 3.3.14 comprises the equivalent circuit diagram used to fit the Nyquist plots and fitted parameters such as series resistance (R_s), charge transfer resistance (R_{CT}), and constant phase element (CPE) are summarized in **Table 3.3.2**. From figure 3.3.14, it is evident that all the photoanodes show a single semicircle in the mid-frequency region, indicative of charge transfer resistance R_{CT} at semiconductor/electrolyte interface, which is of vital importance in enlightening the interfacial properties. As the arc of the semicircle is the indication of charge transfer, therefore the smallest radius of $BiVO_4$/GQDs/CoSn-LDH photoanode with the R_{CT} value of 771 Ω specifying the dramatically accelerated charge transfer kinetics at the interface. In contrast to this, pristine $BiVO_4$ photoanode shows the highest R_{CT} value of 3353 Ω, indicative of poor charge transfer ability of the photoanode observed in the form of lower current density value from the LSV curve. On the other hand, the R_{CT} values of 1650 Ω and 1253 Ω belong to $BiVO_4$/GQDs and $BiVO_4$/CoSn- LDH photoanodes respectively. From the

observations, it is apparent that the loading of GQDs alone onto the $BiVO_4$ surface reduces the resistance, however, the surface trap states still exist in the GQDs interlayer, observed from hole scavenger and transient photocurrent measurements. This type of surface trap state in the GQDs layer can be recognized as a form of hole-storage behavior. Although this GQDS interlayer can extract holes from $BiVO_4$ surface for catalytic reaction, still the surface kinetics of the GQDs layer is not yet so fast because of these traps. After the incorporation of CoSn-LDH to GQDs interlayer, $BiVO_4$/GQDs/CoSn-LDH photoanode shows drastically reduced transfer resistance, indicative of better charge transfer ability at the interface.

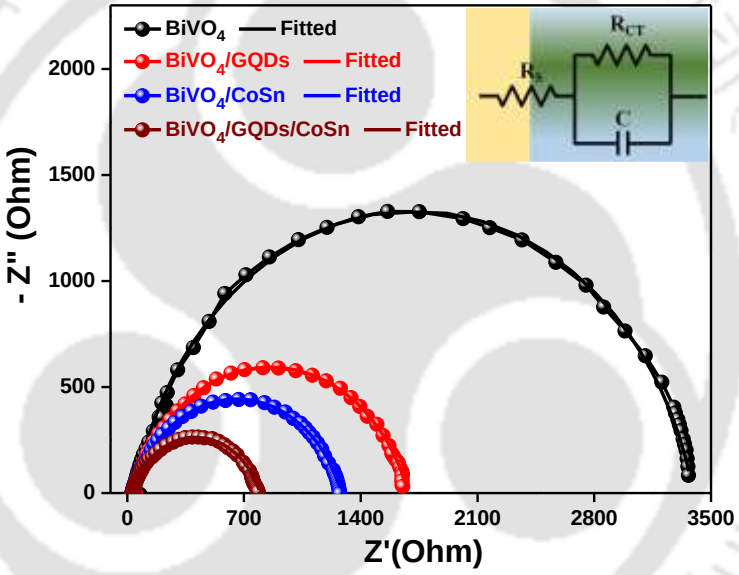

Figure 3.3.14 Nyquist plots for all the photoanodes at 1.23 V_{RHE} under illumination, and inset of the figure shows the circuit diagram used to fit the obtained data

Rate constant for charge transfer is calculated using the formula $R_{CT} \times C = 1/k_{tr}$, where R_{CT} is the charge transfer resistance and C is the capacitance obtained from EIS measurements and k_{tr} is the rate constant for charge transfer. As calculated values for rate constant are found to be 2.485×10^{-5} S^{-1}, 2.528×10^{-5} S^{-1}, 2.955×10^{-5} S^{-1}, and 4.053×10^{-5} S^{-1} for $BiVO_4$, $BiVO_4$/GQDs, $BiVO_4$/CoSn-LDH, and $BiVO_4$/GQDs/CoSn-LDH respectively. Rate constant for charge transfer is increasing continuously from bare $BiVO_4$ to $BiVO_4$/GQDs/CoSn-LDH, representing the improved charge transfer at the interfaces. Therefore, this improved water

oxidation kinetics suggest that the loading of GQDs and CoSn-LDH can significantly stimulate the charge transport kinetics and accelerates the separation of charge carriers at the photoanode/electrolyte interface.

Table 3.3.2 Fitted results of Nyquist plot from the equivalent circuit

Photoanode	R_S (Ohm)	R_{CT} (Ohm)	CPE (μF)
$BiVO_4$	41	3353	12
$BiVO_4$/GQDs	35	1650	24
$BiVO_4$/CoSn-LDH	31	1253	27
$BiVO_4$/GQDs/CoSn-LDH	**25**	**771**	**32**

3.3.10 Charge Injection and Separation Efficiency (Hole Scavenger)

In order to quantify the charge separation and charge injection efficiencies, LSV curves for the combination of photoanodes were recorded by adding 0.5 M Na_2SO_3 as a hole scavenger in 0.5 M KBi electrolyte solution, and obtained results are depicted in **Figure 3.3.15**. It is considered that the hole transfer resistance at the interface is almost negligible, because the Na_2SO_3 oxidation is kinetically as well as thermodynamically faster than the water oxidation, resulted in a higher photocurrent value for all the photoanodes. From **Figure 3.3.15 (A)**, it is evident that the photocurrent density value of bare $BiVO_4$ in presence of Na_2SO_3 is much higher as compared to photocurrent density in absence of Na_2SO_3, demonstrate that the majority of the photogenerated holes recombine at $BiVO_4$ surface, rather than participating in the water oxidation process. Moreover, for $BiVO_4$/GQDs/CoSn-LDH photoanode, the gap between the photocurrent density value with and without Na_2SO_3 is reduced (from bar diagram 3.3.15 (B)), signifying that the restrictions caused by surface recombination and sluggish kinetics of $BiVO_4$ can be addressed by incorporating GQDs and CoSn-LDH.

Part of this chapter has been published in **J. Phys. Chem. Lett., 2021, 12, 8947-8955**

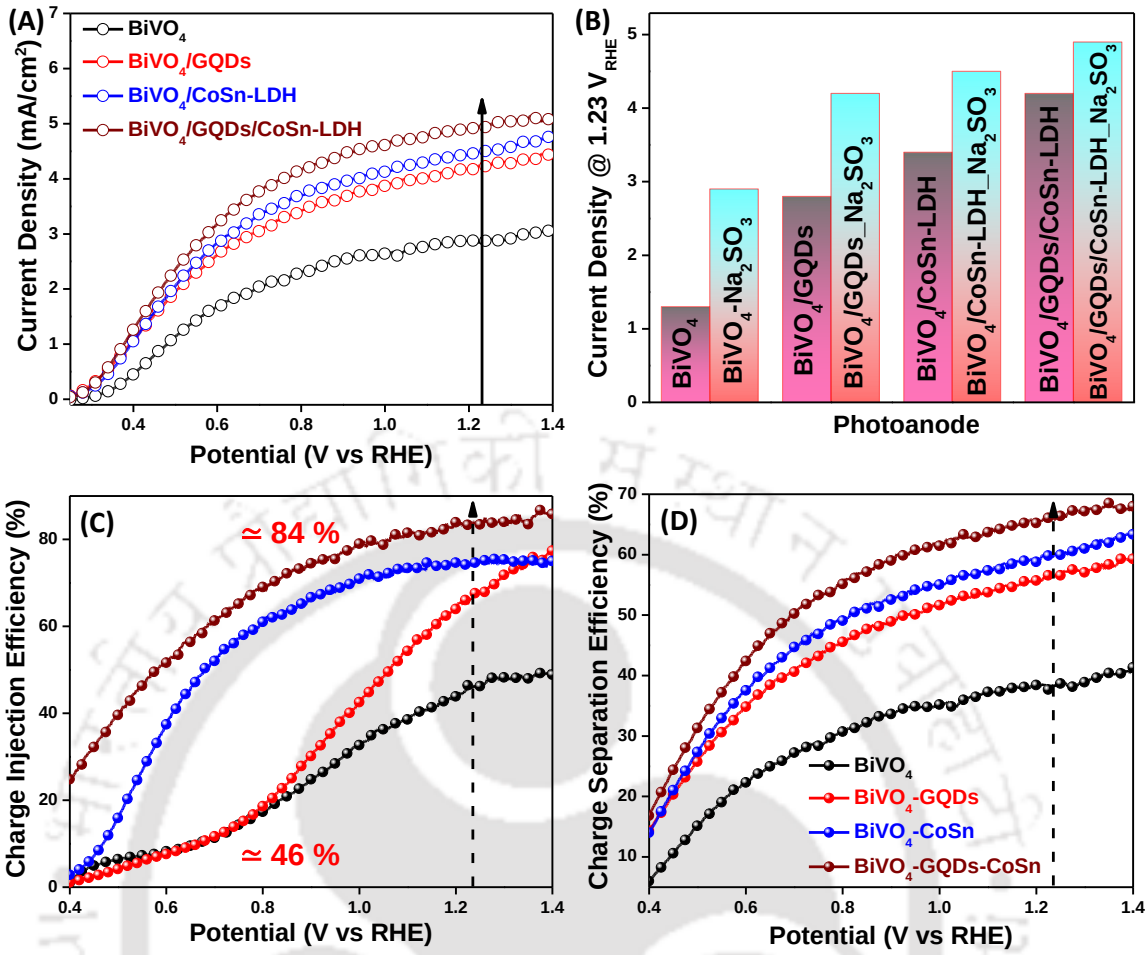

Figure 3.3.15 (A) Current density-voltage curves for $BiVO_4$, $BiVO_4$/GQDs, $BiVO_4$/CoSn-LDH, and $BiVO_4$/GQDs/CoSn-LDH photoanodes measured in the presence of Na_2SO_3 as hole scavenger, (B) corresponding bar diagram for all the photoanodes in presence and absence of hole scavenger, (C) charge separation and (D) charge injection efficiencies of $BiVO_4$ (black), $BiVO_4$/GQDs (red), $BiVO_4$/CoSn-LDH (blue), and $BiVO_4$/GQDs/CoSn-LDH (wine) photoanodes respectively

Charge injection efficiency is another vital component, which determines the proportion of holes that are participating in water oxidation. From **Figure 3.3.15 (C)**, it is observed that the hole injection efficiency for pristine $BiVO_4$ photoanode is found to be 46 %. On the other hand, the hole injection efficiency for $BiVO_4$/GQDs/CoSn-LDH photoanode increases dramatically and is found to be 84 %, indicative of reduced recombination of photogenerated electron-hole pairs at the interface, owing to the formation of a junction between $BiVO_4$ and CoSn-LDH. In contrast to this, the hole injection efficiencies of 67 % and

75 % belong to $BiVO_4$/GQDs and $BiVO_4$/CoSn-LDH photoanodes respectively. Apart from injection efficiency, separation efficiency also plays an important role in enhancing the water oxidation process, and **Figure 3.3.15 (D)** represents the same. From figure 3.3.15 (D), the charge separation efficiencies of 38 %, 57 %, 60 %, and 66 % at 1.23 V_{RHE} belong to $BiVO_4$, $BiVO_4$/GQDs, $BiVO_4$/CoSn-LDH, and $BiVO_4$/GQDs/CoSn-LDH photoanodes respectively. These results further confirm that the loading of GQDs and CoSn-LDH is of significant importance as they play a crucial role in promoting the surface reaction by efficient and rapid consumption of photogenerated holes.

3.3.11 Electrochemical Surface Area (ECSA) Analysis

To calculate the number of active sites, electrochemical active surface area analysis (ECSA) was performed. The adsorption/desorption ability of an electro-catalyst is reflected by ECSA, also the number of active sites is directly proportional to this ECSA. ECSA of any catalyst can be obtained by measuring the double-layer capacitance (C_{dl}). The difference of current densities ($J_{anodic} - J_{cathodic}$) at a particular potential is plotted against the scan rate, further fitted linearly to get the slope value, which is twice the C_{dl} value. **Figure 3.3.16 (A-D**) represents the cyclic voltammetry curves for $BiVO_4$, $BiVO_4$/GQDs, $BiVO_4$/CoSn-LDH, and $BiVO_4$/GQDs/CoSn-LDH photoanodes respectively, measured at different scan rates. Then the difference in current at 0.85 V_{RHE} is plotted against scan rate and **Figure 3.3.16 (E-H)** represents the same. Therefore, based on these curves the C_{dl} value of 50 $\mu F/cm^2$, 159 $\mu F/cm^2$, 187 $\mu F/cm^2$, and 212 $\mu F/cm^2$ belongs to $BiVO_4$, $BiVO_4$/GQDs, $BiVO_4$/CoSn-LDH, and $BiVO_4$/GQDs/CoSn-LDH photoanodes respectively. This result further confirms that the loading of GQDs and CoSn-LDH over $BiVO_4$ surface increases the active sites, which take part in the oxidation process. This enhancement in the ECSA value is useful for the improved adsorption of the water molecules onto the surface and facilitates the charge transfer, resulting in an enhanced oxidation reaction.

Part of this chapter has been published in **J. Phys. Chem. Lett., 2021, 12, 8947-8955**

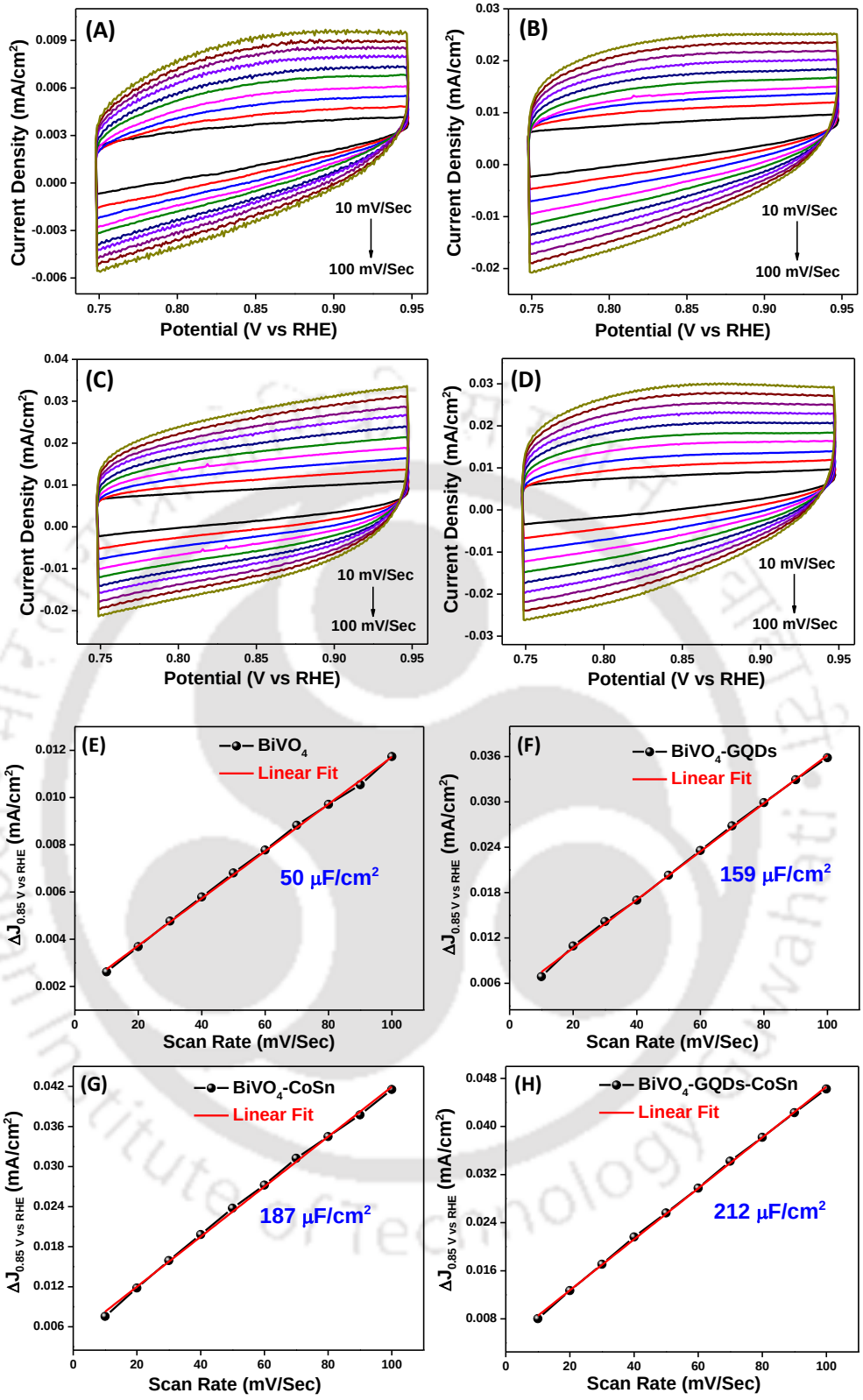

Figure 3.3.16 (A-D) Cyclic voltammetry curves for $BiVO_4$, $BiVO_4$/GQDs, $BiVO_4$/CoSn-LDH, and $BiVO_4$/GQDs/CoSn-LDH photoanodes respectively, measured at different scan rates, and (E-H) Current at 0.85 V_{RHE} vs scan rate curves for $BiVO_4$, $BiVO_4$/GQDs, $BiVO_4$/CoSn-LDH, and $BiVO_4$/GQDs/CoSn-LDH photoanodes respectively, linear fitted to get C_{dl} value

Part of this chapter has been published in **J. Phys. Chem. Lett., 2021, 12, 8947-8955**

3.3.12 Stability and Faradaic Yield Measurements

Apart from the catalytic activity, operational stability is equally important parameter for practical applications. Therefore, a long-term stability test of each photoanode was carried out under continuous illuminations at 1.23 V_{RHE}, represented in **Figure 3.3.17 (A)**. From figure 3.3.17 (A), it is apparent that the photocurrent density of bare $BiVO_4$ shows a considerable downward trend and attenuated by 35 % after 4 hr. In contrast to this, $BiVO_4$/GQDs/CoSn-LDH photoanode retained its ~90 % current density under the same conditions. Therefore, these observations specify that the loading of GQDs and CoSn-LDH improve the stability of photoanode for water oxidation kinetics.

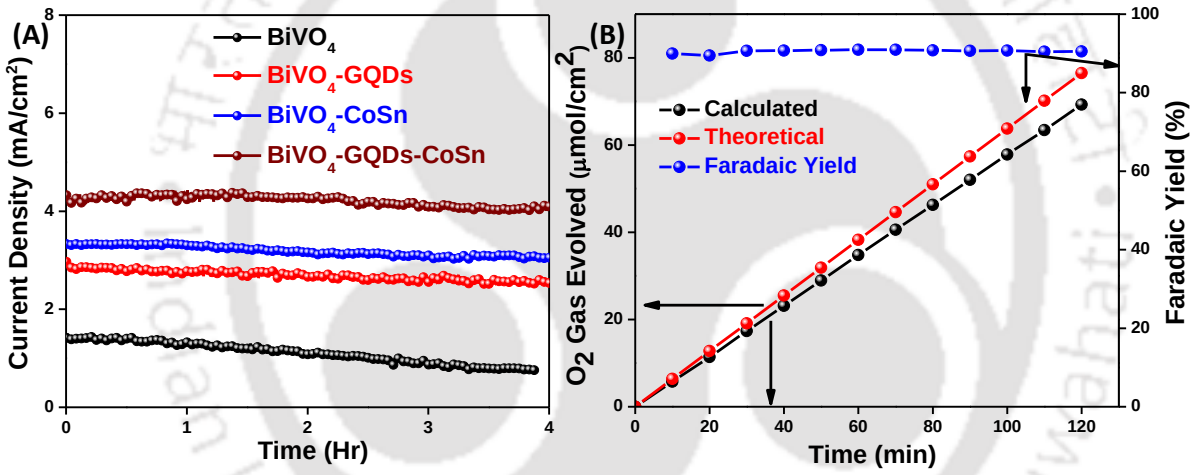

Figure 3.3.17 (A) Operational stability of $BiVO_4$, $BiVO_4$/GQDs, $BiVO_4$/CoSn-LDH, and $BiVO_4$/GQDs/CoSn-LDH photoanodes recorded at 1.23 V_{RHE} under continuous illumination and (B) Faradaic yield of $BiVO_4$, $BiVO_4$/GQDs, $BiVO_4$/CoSn-LDH, and $BiVO_4$/GQDs/CoSn-LDH photoanodes in µmol/cm^2

To confirm that the obtained photocurrent density is mainly due to O_2 evolution rather than the side reactions or self-oxidation, O_2 evolution of $BiVO_4$/GQDs/CoSn-LDH photoanode as a function of time was measured in the headspace of an air-tight cell by online GC at 10 min interval for 120 min. at a constant applied potential of 1.23 V_{RHE}. From **Figure 3.3.17 (B)**, the actual amount of O_2 produced for $BiVO_4$/GQDs/CoSn-LDH photoanode is 38 µmol/cm^2 after 60 min. The actual amount of O_2 produced is then divided by the theoretically achievable O_2

Part of this chapter has been published in **J. Phys. Chem. Lett., 2021, 12, 8947-8955**

to get the Faradaic yield. An impressive Faradaic yield of ~91 % is obtained, revealing that the resulted photocurrent density is only due to water oxidation.

3.3.13 Mott-Schottky Analysis

Depending upon the majority charge carrier, the transport nature of a semiconductor (n-type or p-type conductivity) can be revealed by Mott-Schottky analysis, represented in **Figure 3.3.18**. It is considered that the negative slope of the Mott-Schottky plot is due to p-type conductivity whereas a positive slope is due to n-type conductance. From the figure 3.3.18 (A), $BiVO_4$ shows a positive slope, indicates the n-type behavior of $BiVO_4$ photoanode with electrons as majority charge carriers. On the other hand, CoSn-LDH shows a negative slope, revealing the p-type nature with holes as majority charge carriers.

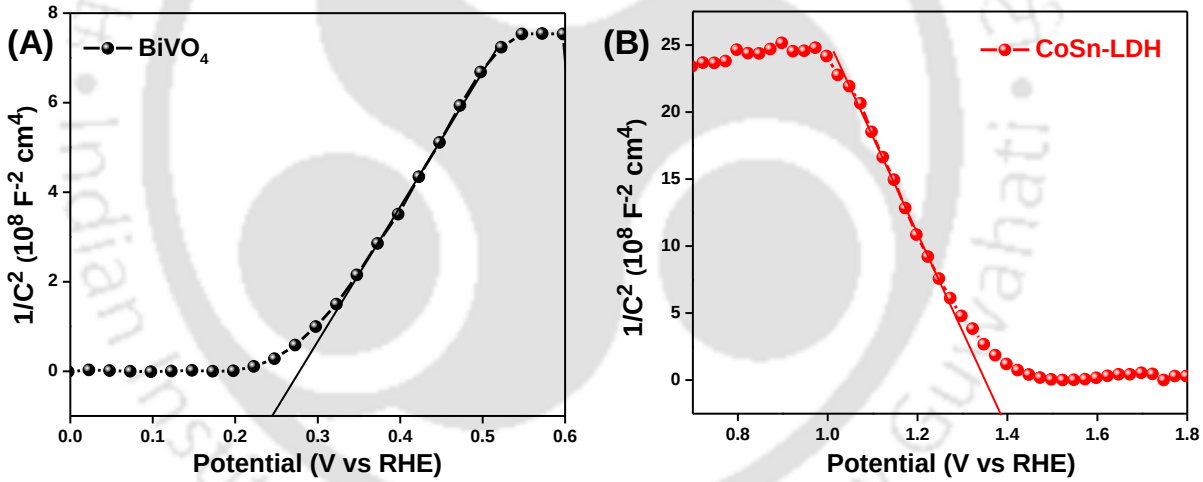

Figure 3.3.18 Mott-Schottky analysis for (A) $BiVO_4$ and (B) CoSn-LDH, showing the nature of conductivity

3.3.14 Cyclic Voltammetry Analysis

Cyclic voltammetry curves were recorded to confirm the active redox species involved in CoSn-LDH for water oxidation, as shown in **Figure 3.3.19**. Figure 3.3.19 shows the oxidation-reduction peaks correspond to Co (II)/Co (III), confirms that only cobalt is the active site in CoSn mixed metal LDH.

Part of this chapter has been published in **J. Phys. Chem. Lett., 2021, 12, 8947-8955**

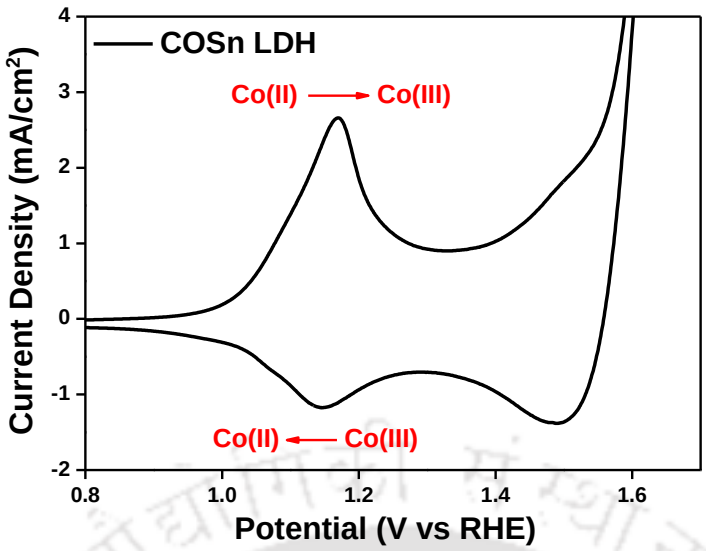

Figure 3.3.19 Cyclic Voltammetry curve for CoSn-LDH, depicting the presence of different oxidation states of Cobalt

3.3.15 Zeta Potential Analysis

To confirm the hole extracting ability of GQDs, zeta potential analysis was carried out, and **Figure 3.3.20** represent the same. Negative potential of - 23.8 mV with 6.62 mV deviation is observed for GQDs. Negatively charged GQDs have the tendency to extract the positively charged ions. Therefore, GQDs promote the hole extraction from $BiVO_4$ surface.

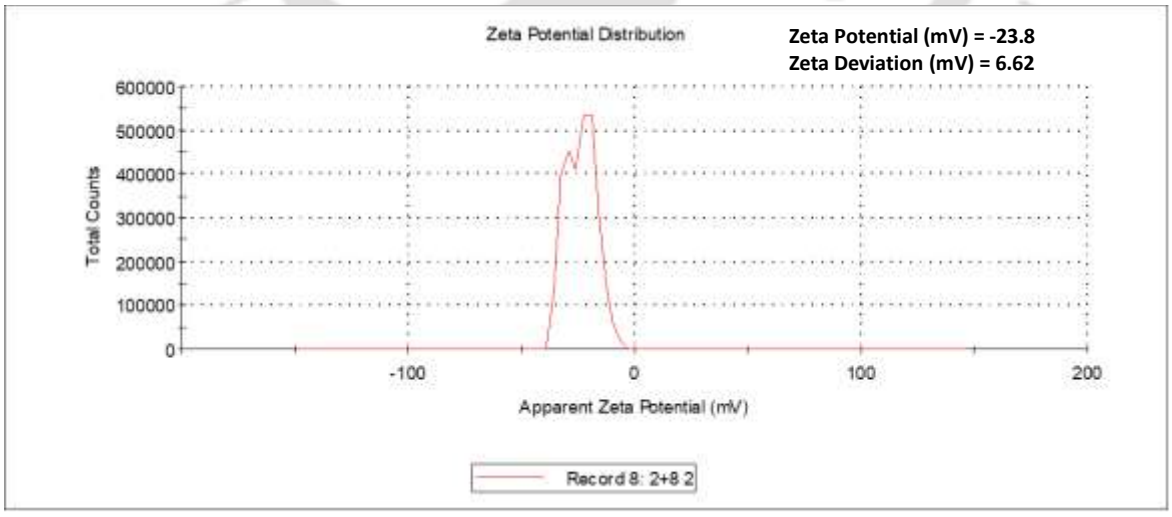

Figure 3.3.20 Zeta potential analysis of GQDs

3.3.16 Mechanism for Enhanced Water Oxidation Kinetics

Based on the above discussions, a schematic representation of the mechanism contributing to enhanced water oxidation in ternary photoanode $BiVO_4$/GQDs/CoSn-LDH is shown in **Figure 3.3.21**. Under illumination, the photogenerated electrons jumped into the conduction band of $BiVO_4$ leaving holes behind in the valence band as shown in figure 3.3.21 (A). Due to the sluggish oxidation kinetics, this electron-hole separation in pristine $BiVO_4$ suffers from the recombination on its surface. Decoration of GQDs onto the $BiVO_4$ surface leads to the formation of a heterojunction at the interface, beneficial for reduced recombination of photogenerated charge carriers as shown in figure 3.3.21 (B). Due to the presence of negative surface charges, GQDS extracts holes from the $BiVO_4$ surface.

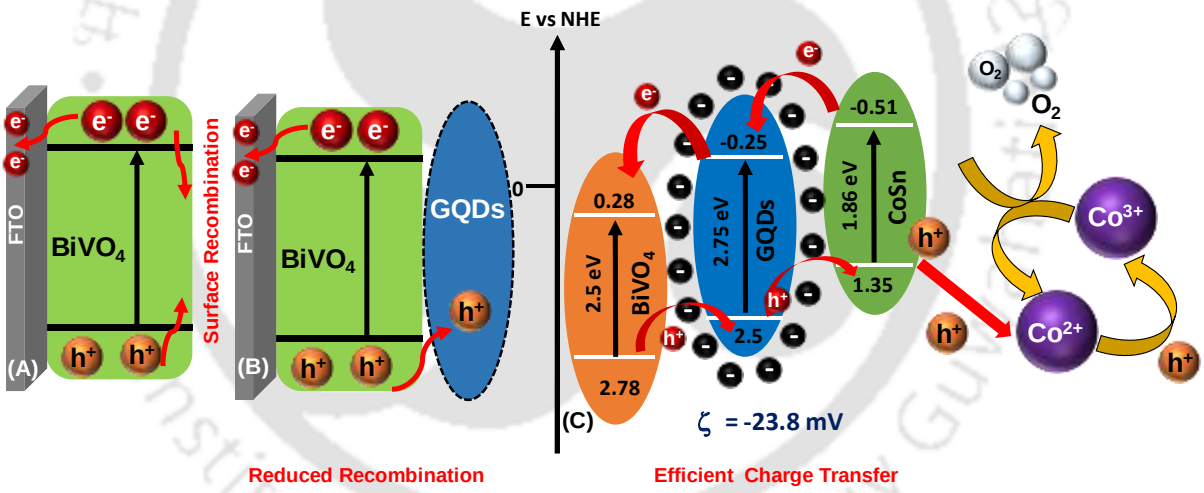

Figure 3.3.21 Schematic representation of mechanism for enhanced water oxidation kinetics showing (A) recombination of photogenerated charge carriers, (B) efficient extraction of holes from $BiVO_4$ surface and injection to CoSn-LDH, and (C) efficient transportation of holes to active species for the water oxidation reaction

Additionally, incorporation of a p-type CoSn-LDH onto $BiVO_4$/GQDs surface forms a p-n heterojunction with GQDs bridging, wherein CoSn-LDH transports holes to the surface due to its redox activity coupled with the conductivity as shown in figure 3.3.21 (C). This p-n heterojunction generates an internal build-in electric field to accelerate the charge transfer.

Apart from this, these holes are preferentially used to oxidize the low valence Co^{2+} in CoSn-LDH to high valence Co^{3+}. These high valence species then oxidize water and release oxygen and reduces to low valence species Co^{2+} again to complete a catalytic cycle. The cyclic process continues to promote charge separation and enhances hole transfer, resulting in the acceleration of OER kinetics and the improvement of the PEC properties. Cyclic voltammetry analysis reveals that only cobalt is the electro-active species in CoSn-LDH for the water oxidation process, keeping the Sn^{2+} as a spectator ion, which largely contributes to the overall conductivity of the LDH helping in the transfer of holes to active surface sites for water oxidation to happen.

3.4 Conclusions

In summary, we have outlined the idea of a ternary $BiVO_4$/GQDs/CoSn-LDH photoanode in which CoSn-LDH surface active sites and GQDs acts as a conductive linker to extract holes from the $BiVO_4$ surface. The photocurrent density of $BiVO_4$/GQDs/CoSn-LDH photoanode increases up to 4.15 mA/cm^2, which is 3-fold higher than pristine $BiVO_4$, owing to the synergistic effect of GQDs and CoSn-LDH in extracting and transporting the holes to the surface reaction site. Moreover, a negative shift of ~250 mV in onset potential after the introduction of GQDs and CoSn-LDH is accounted for the inhibition of photogenerated electron-hole pair recombination resulted in reduced overpotential as well as the efficacy of the water oxidation. Operational stability of $BiVO_4$/GQDs/CoSn-LDH photoanode is improved, as it preserved ~90 % of the initial value after 4 hr of continuous illumination. Presented new findings paves the path to understand the mechanism of hetero-structured photoanodes with intermittent bridge compounds and would inspire to design newer photo-electrode systems for improved water oxidation.

Part of this chapter has been published in **J. Phys. Chem. Lett., 2021, 12, 8947-8955**

3.5 References

(1) H. L. Tong, Y. Jiang, Q. Zhang, W. C. Jiang, K. L. Wang, X. X. Luo, Z. Lin and L. X. Xia, *ACS Sustainable Chem. Eng.*, 2019, **7**, 769.

(2) T. Tran-Phu, Z. Fusco, I. Di Bernardo, J. Lipton-Duffin, C. Y. Toe, R. Daiyan, T. Gengenbach, C. H. Lin, R. Bo, H. T. Nguyen, G. M. J. Barca, T. Wu, H. Chen, R. Amal, and A. Tricoli, *Chem. Mater.*, 2021, **33**, 3553.

(3) U. Prasad, J. Prakash and A. M. Kannan, *Sustainable Energy Fuels*, 2020, **4**, 1496.

(4) G. J. Liu, J. Eichhorn, C. M. Jiang, M. C. Scott, L. H. Hess, J. M. Gregoire, J. A. Haber, I. D. Sharp and F. M. Toma, *Sustainable Energy Fuels*, 2019, **3**, 127.

(5) X. Zhong, H. He, M. Yang, G. Ke, Z. Y. Zhao, F. Dong, B. Wang, Y. Chen, X. Shi and Y. Zhou, *J. Mater. Chem. A*, 2018, **6**, 10456.

(6) Y.-S. Chen and L.-Y. Lin, *J. Power Sources*, 2019, **436**, 226842.

(7) Y. Liu, B. R. Wygant, K. Kawashima, O. Mabayoje, T. E. Hong, S.-G. Lee, J. Lin, J.-H. Kim, K. Yubuta, W. Li, J. Li and C. B. Mullins, *Appl. Catal., B*, 2019, **245**, 227.

(8) D. Li, R. Chen, P. Wang, Z. Li, J. Zhu, F. Fan, J. Shi and C. Li, *ChemCatChem*, 2019, **11**, 3763.

(9) L. Zhang, C. Y. Lin, V. K. Valev, E. Reisner, U. Steiner and J. J. Baumberg, *Small*, 2014, **10**, 3970.

(10) K. A. Stoerzinger, L. Qiao, M. D. Biegalski and Y. Shao-Horn, *J. Phys. Chem. Lett.*, 2014, **5**, 1636.

(11) S. Biswas, S. Bose, J. Debgupta, P. Das and A. N. Biswas, *Dalton Trans.*, 2020, **49**, 7155.

(12) J. W. Wang, P. Sahoo and T. B. Lu, *ACS Catal.*, 2016, **6**, 5062.

(13) X. Lu, A. Bandara, M. Katayama, A. Yamakata, J. Kubota, and K. Domen, *J. Phys. Chem. C*, 2011, **115**, 23902.

(14) A. T. Garcia-Esparza and K. Takanabe, *J. Mater. Chem. A*, 2016, **4**, 2894.

(15) B. Mei, K. Han, and G. Mul, *ACS Catal.*, 2018, **8**, 9154.

(16) P. Yue, H. She, L. Zhang, B. Niu, R, Lian, J. Huang, L. Wang and Q. Wang, *Appl. Catal. B*, 2021, **286**, 119875.

(17) X. Zhang, X. Bian, H. Xu, and W. Wu, *Appl. Surf. Sci.*, 2021, **542**, 148579.

(18) S. Bai, Q. Li, J. Han, X. Yang, X. Shu, J. Sun, L. Sun, R. Luo, D. Li and A. Chen, *Int. J. Hydrogen Energy*, 2019, **44**, 24642.

Part of this chapter has been published in **J. Phys. Chem. Lett., 2021, 12, 8947-8955**

(19) H. Chen, S. Wang, J. Wu, X. Zhang, J. Zhang, M. Lyu, B. Luo, G. Qian and L. Wang, *J. Mater. Chem. A*, 2020, **8**, 13231.

(20) S. Zhang, Z. Liu, D. Chen and W. Yan, *Appl. Catal., B*, 2020, **277**, 119197.

(21) S. H. Kang, S. Y. Lee, M. G. Gangc, K. S. Ahnb and J. H. Kim, *Electrochim. Acta*, 2014, **133**, 262.

(22) X. Q. Wu, J. Zhao, S. J. Guo, L. P. Wang, W. L. Shi, H. Huang, Y. Liu and Z. H. Kang, *Nanoscale*, 2016, **8**, 17314.

(23) X. H. Xia, L. Liu, X. H. Li, S. S. Gao, and T. G. Yang, *J. Catal.*, 2019, **374**, 401.

(24) H. B. Yang, Y. Q. Dong, X. Wang, S. Y. Khoo and B. Liu, *ACS Appl. Mater. Interfaces*, 2014, **6**, 1092.

(25) J. Peng, W. Gao, B. K. Gupta, Z. Liu, R. Romero-Aburto, L. Ge, L. Song, L. B. Alemany, X. Zhan and G. Gao, *Nano Lett.*, 2012, **12**, 844.

(26) J. Ryu, E. Lee, S. Lee and J. Jang, *Chem. Commun.*, 2014, **50**, 15616.

(27) S. Ahirwar, S. Mallick and D. Bahadur, *ACS Omega*, 2017, **2**, 8343.

(28) C. Zhu, S. W. Yang, G. Wang, R. W. Mo, P. He, J. Sun, Z. F. Di, Z. H. Kang, N. Y. Yuan, J. N. Ding, G. Q. Ding and X. M. Xie, *J. Mater. Chem. B*, 2015, **3**, 6871.

(29) S.-H. Lee, D.-Y. Kim, J.-M. Lee, S.-B. Lee, H. Ham, Y.-Y. Kim, S.-C. Mum, S.-H. In, T.-H. Kim and O.-O. Park, *Nano Lett.*, 2019, **19**, 5437.

(30) S. Bai, J. Liu, M. Cui, R. Luo, J. He, A. Chen and K. Domen, *Dalton Trans.*, 2018, **47**, 6763.

(31) T. Palaniselvam, L. Shi, G. Mettela, D. H. Anjum, R. Y. Li, K. P. Katuri, P. E. Saikaly and P. Wang, *Adv. Mater. Interfaces*, 2017, **4**, 1700540.

(32) T. W. Kim, Y. Ping, G. A. Galli, and K. S. Choi, *Nat Commun*, 2015, **6**, 8769.

(33) D. A. Reddy, Y. Kim, H. S. Shim, K. A. J. Reddy, M. Gopannagari, D. P. Kumar, J. K. Song and T. K. Kim, *ACS Appl. Energy Mater.*, 2020, **3**, 4474.

(34) W. He, R. Wang, L. Zhang, J. Zhu, X. Xiang and F. Li, *J. Mater. Chem. A*, 2015, **3**, 17977.

(35) X. Han, Y. Wei, J. Su and Y. Zhao, *ACS Sustainable Chem. Eng.*, 2018, **6**, 14695.

(36) H. Bai, X. Li, Y. Zhao, W. Fan, Y. Liu, Y. Gao, D. Xu, J. Ding, and W. Shi, *Appl. Surf. Sci.*, 2021, **538**, 148150.

(37) Z. Zeng, F.-X. Xiao, X. Gui, R. Wang, B. Liu and T. Y. T. Tan, *J. Mater. Chem. A*, 2016, **4**, 16383.

CHAPTER 4

Co(OH)F as a noble metal-free redox mediator and hole extractor for boosted photoelectrochemical water oxidation in worm-like bismuth vanadate

This chapter deals with the low-temperature hydrothermal synthesis of 1-D Co(OH)F nanorods as a noble metal-free redox mediator and coupled with $BiVO_4$ photoanode for efficient photoelectrochemical water oxidation. 1-D nanostructures have several advantages in catalytic reaction compared to their bulk counterparts due to facile charge separation and shorter diffusion path for minority charge carriers to reach the photoanode/electrolyte interface. Modification of Co(OH)F led to a considerable improvement in PEC performance due to suppressed surface charge recombination as well as enhancement in the hole extraction ability by virtue of the redox mediator.

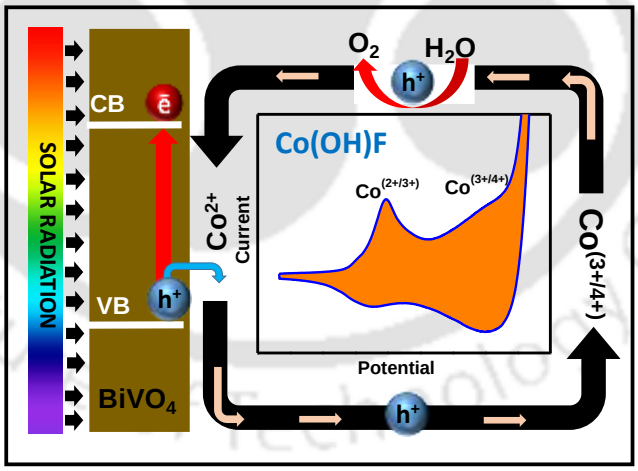

S. Alam *et al.*, **ACS Sustainable Chem. Eng.** 2021, 9, 5155−5165

4.1 Introduction

Splitting of water into H_2 and O_2 by means of artificial photosynthesis provides a desirable approach to solve the energy crisis. Research emphasis on the implementation of solar energy to drive thermodynamically upward reactions to produce fuels has received considerable attention[1-2]. A feasible alternative is, to develop the photo-anodic material which can accelerate the kinetics to oxidize water into O_2[3]. Due to the multi-electron transfer involved in the reaction mechanism of water oxidation, it generally requires high over-potential owing to the sluggish kinetics of the photoanode. Therefore, more research-focused to develop an efficient photoanodic system, which can oxidize water into O_2 in a stable and efficient manner[4]. The main challenge is to explore an appropriate photoanode material that fulfills the criteria of visible light absorption, suitable band edge positions, efficient use of photogenerated carriers, and high photoelectrochemical operational stability[5]. Based on the above requirements, several photoanodic materials such as ZnO[6], TiO_2[7], WO_3[8], Fe_2O_3[9] and, $BiVO_4$[10] have been studied extensively. Among these materials, $BiVO_4$ has significant potential due to its non-toxicity, appropriate positions of band edges, abundant resources, and high stability in aqueous media at neutral and alkaline pH[11]. Despite the knowledge that $BiVO_4$ is an ideal photoanode material, the reported photocurrent densities of pure $BiVO_4$ are still far less than its theoretical current value of 7.5 mA/cm^2 [12]. This is mainly due to poor charge separation and injection capabilities, short carrier diffusion length, and slow oxygen evolution kinetics[13]. To realize the potential of $BiVO_4$ photoanode, various strategies such as controlled synthesis of different morphologies[14], metal and non-metallic doping[15-16], heterojunction formation[17], plasmonic enhancement[18], crystal facet engineering[19,] and similar approaches have also been utilized to enhance the surface kinetics and charge separation as well as injection efficiencies. Apart from these strategies, the use of expensive but very effective catalysts like IrO_2 and RuO_2[20-21] have also been used to improve the kinetics of $BiVO_4$ based photoanodes. Guided by the incentives to

Part of this chapter has been published in **ACS Sustainable Chem. Eng. 2021, 9, 5155−5165**

reduce cost, researchers began to pay attention to the development of non-noble-metal OER co-catalysts. Among the earth-abundant transition metal-based catalysts, Cobalt-based materials such as mixed metal oxides[22], perovskites oxide[23], nitrides[24], phosphates[25], porphyrin[26], metal-organic coordination complex[27], molecular OEC[28,] and chalcogenides[29], have emerged as potential candidates due to their low cost, natural abundance, stability in neutral and alkaline pH and environmental benign characteristics for electrochemical water splitting. Compared to phosphorus and oxygen in Co─P and C─O systems, due to the higher electronegativity of fluorine, the Co─F bond provides more positive charges on the metal center for efficient shuttling of the redox couple, beneficial for enhanced OER. The catalytic activity of cobalt is enhanced after the incorporation of non-metal elements, as they tend to reduce the thermodynamic and kinetic barrier. The conductivity, as well as the charge mobility, is improved due to the presence of Fluoride in Co(OH)F, thereby improving the electro-catalytic activity[30-31].

Motivated by the aforementioned merits, herein we report $BiVO_4$/Co(OH)F composite, wherein Co(OH)F acts as an efficient hole extractor by virtue of its redox ability and assists the carrier transportation due to its one dimensional features[32]. Therefore Co-based electro-catalyst Co(OH)F has been incorporated as a co-catalysts to improve the charge injection as well as to reduce the recombination of photogenerated charge carriers by virtue of its hole extraction ability. It is noteworthy to mention here that, $BiVO_4$ is the main photo-electro-catalyst and Co(OH)F has been used to improve the surface kinetics. This combination of $BiVO_4$/Co(OH)F is improving the overall efficiency. The Co(OH)F/$BiVO_4$ photoanode displayed a considerable improvement in the photocurrent value as compared to pure $BiVO_4$. The photocurrent density of the composite electrode reached 3.4 mA/cm^2 at 1.23 V vs RHE with onset potential shifted 160 mV in the negative direction, which can be accounted for the enhanced charge separation as well as hole injection efficiency.

Part of this chapter has been published in **ACS Sustainable Chem. Eng. 2021, 9, 5155−5165**

4.2 Experimental Section

4.2.1 Synthesis of $BiVO_4$ over FTO

Fluorine-doped Tin Oxide (FTO) was used as a conductive substrate to deposit $BiVO_4$ by electrodeposition method. In a typical synthetic process, solution (A) was prepared by dissolving a calculated amount of potassium iodide (3.32 gm, 0.04 M) into 50 mL of distilled water and allowed to stir at room temperature for 15 min. Then HNO_3 was added dropwise to the above solution to maintain the pH to 1.4. After this $Bi(NO_3)_3.5H_2O$ (0.97 gm, 0.04 M) was added to solution A and kept stirring for 15 min. On the other hand, solution (B) was prepared by dissolving (0.497 gm, 0.23 M) of p-Benzoquinone into 20 mL of ethanol. In the last step, solution (A) and solution (B) were mixed and left for stirring for another 30 min. A three-electrode system was used to carry out the electrodeposition of BiOI over FTO substrate. In a beaker filled with as prepared precursor solution, FTO, Ag/AgCl, and Pt wire were used as working, reference, and counter electrodes respectively. Before the electrodeposition, FTOs were cleaned sequentially in a soap solution, distilled water, acetone, and 2-propanol. Electrodeposition was carried out using the Chronoamperometry technique, by passing a voltage of -0.1 V for 200 sec on bare FTO. After electrodeposition, BiOI films were rinsed with plenty of DI water and subjected dry in an electric oven for 12 hr at 60˚C. After this, a chemical-thermal process was used to convert as-deposited BiOI films into $BiVO_4$. For this, a solution of $VO(acac)_2$ (0.23 M) in DMSO was prepared. Then 50 µL of the as-prepared solution was drop-casted over the surface of BiOI films. At last, these films were heated in a muffle furnace for 2 hr at 450˚C at a heating rate of 2˚C/min. After the completion of this calcination process, these films were allowed to cool down at room temperature and placed in 1 M NaOH solution for 30 min for the complete removal of the residual V_2O_5. Finally, the resulting $BiVO_4$ photoanodes were rinsed with plenty of water and subjected to dry for 1 hr at 60 °C in the oven.

Part of this chapter has been published in **ACS Sustainable Chem. Eng. 2021, 9, 5155−5165**

4.2.2 Hydrothermal Synthesis of Co(OH)F

For the synthesis of the Co(OH)F, 1 mmol (0.291 gm) of $Co(NO_3)_2.6H_2O$, was dissolved in 30 mL of distilled water with continuous stirring. Then 2 mmol (100 μL) of hydrazine hydrate was added dropwise to the above solution. The color of the solution changes from transparent to dark blue. After this 5 mmol (0.186 gm) of NH_4F was added to this solution and continued to stir for 30 min. Finally, this solution was poured into a 50 mL autoclave and hydrothermal treatment was carried out in an electric oven for 6 hr at 120°C. After the hydrothermal treatment, as obtained precipitate was centrifuged several times with distilled water and ethanol before drying in an oven at 60˚C for 12 hr. During the course of the reaction, hydrazine hydrate provides a basic environment for the precipitation of Co^{II} and prevents the oxidation of Co^{II} due to its reductive nature. On the other hand, fluoride anions have been used as a templating agent in several nanostructures' syntheses. To avoid the poor conductivity of organic surfactants, as a limitation in electro-catalysis, Fluorine-directed surfactant-free synthesis has been used. Here used fluorine anion also exists in the product as a composition element.

4.2.3 Fabrication of $BiVO_4$/Co(OH)F Photoanode

$BiVO_4$/Co(OH)F composite was prepared by the drop-casting method. Briefly, for the preparation of $BiVO_4$/Co(OH)F composite, a calculated amount of Co(OH)F (5 mg/mL) was dissolved in ethanol via sonication for 30 min. Then 100 μL of this solution was drop-casted over as prepared $BiVO_4$ films. These drop-casted films were subjected to dry in an electric oven for 12 hr at 60˚C. **Scheme 4.2.1** represents the detailed synthetic procedure of $BiVO_4$/Co(OH)F photoanode. Based on the ICP-MS (Inductively Coupled Plasma Mass Spectroscopy) analysis, the actual amount of Co(OH)F loading was found to be ~0.54 mg/cm^2, ~0.65 mg/cm^2, ~0.86 mg/cm^2, and ~0.94 mg/cm^2 respectively.

Part of this chapter has been published in **ACS Sustainable Chem. Eng. 2021, 9, 5155−5165**

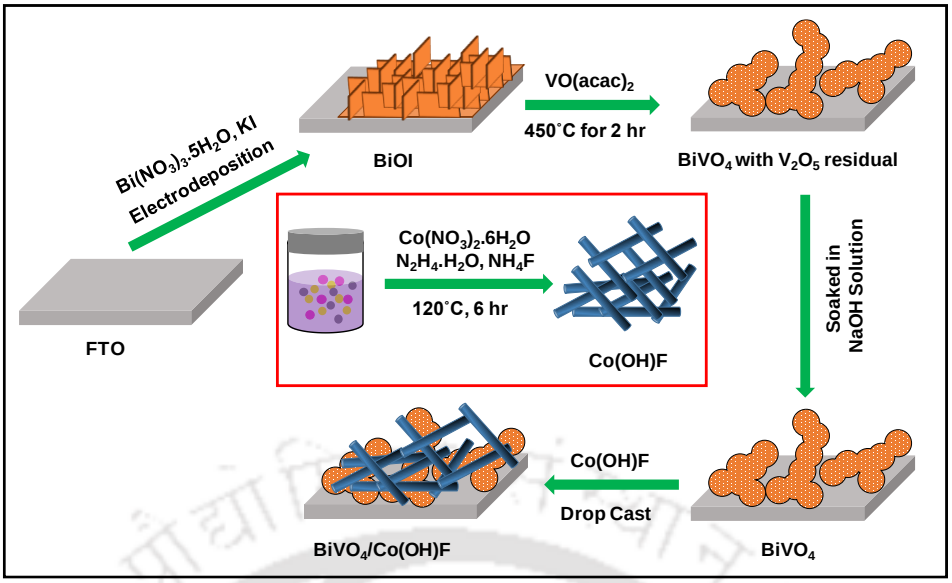

Scheme 4.2.1 Schematic representation for step-by-step fabrication of $BiVO_4$/Co(OH)F photoanode, inset of the scheme shows the hydrothermal synthesis of Co(OH)F

4.3 Results and Discussions

4.3.1 Powder X-ray Diffraction (XRD) Analysis

To confirm the formation and the crystal phase purity of as-synthesized bare $BiVO_4$, Co(OH)F, and $BiVO_4$/Co(OH)F composites, X-ray diffraction analysis was performed and shown in **Figure 4.3.1**. From trace (A), the diffraction peaks at 2θ values of 18.87˚, 28.98˚, 30.56˚, 34.63˚, 37.78˚, 40.02˚, 42.51˚, 45.92˚, 46.84˚, 47.11˚, 50.29˚, and 53.37˚ correspond to their crystal plane (110), (121), (040), (200), (220), (112), (051), (132), (240), (042), (202), and (161) respectively, indexed to the monoclinic phase of $BiVO_4$ (JCPDS number 14-0688). From trace (B), the diffraction peaks at 2θ values of 20.80˚, 32.21˚, 33.44˚, 34.87˚, 35.56˚, 38.71˚, 39.89˚, 43.63˚, 51.80˚, 52.69˚, 56.95˚, 58.99˚, and 61.55˚ correspond to their crystal plane (110), (311), (201), (400), (111), (211), (410), (311), (221), (420), (511), (002) and (601) were indexed to the orthorhombic phase of Co(OH)F (JCPDS number 50-0827). As for the XRD pattern of $BiVO_4$/Co(OH)F photoanode (trace C), the dominant diffraction peaks for both i.e. monoclinic $BiVO_4$ and orthorhombic Co(OH)F could be indexed, indicated that $BiVO_4$ and Co(OH)F exists with separate phases in the system.

Part of this chapter has been published in **ACS Sustainable Chem. Eng. 2021, 9, 5155−5165**

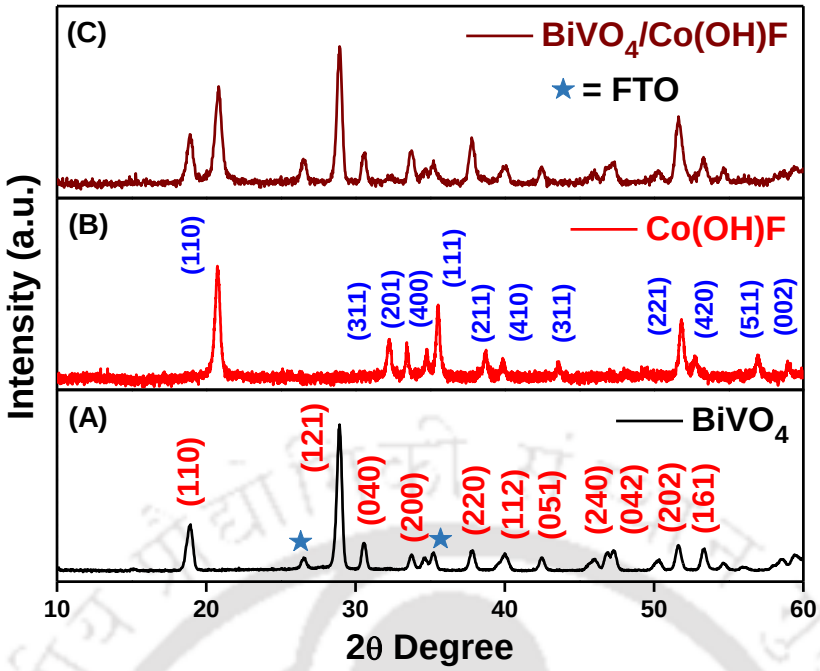

Figure 4.3.1 X-ray diffraction pattern of (A) electrodeposited $BiVO_4$, indexed to monoclinic phase (black line), (B) as-synthesized Co(OH)F nanorods, indexed to orthorhombic phase (red line), and (C) $BiVO_4$/Co(OH)F composite (wine-red line) shows signature peaks for both the compounds (★ Indicates FTO)

4.3.2 UV−Visible Absorption Spectra Analysis

The optical behavior of as-synthesized $BiVO_4$, Co(OH)F, and $BiVO_4$/Co(OH)F composite was studied by analyzing UV-Vis absorption spectra in the wavelength range of 350-750 nm, as depicted in **Figure 4.3.2 (A)**. From the figure, the absorption edges of $BiVO_4$, Co(OH)F, and $BiVO_4$/Co(OH)F were observed at ~510 nm, ~645 nm, and ~509 nm respectively, corresponding to a bandgap of ~2.43 eV, ~1.92 eV, and ~2.43 eV. These band gaps were in close agreement with the approximate values obtained from Tauc plots, as displayed in **Figure 4.3.2 (B)**.

Part of this chapter has been published in **ACS Sustainable Chem. Eng. 2021, 9, 5155−5165**

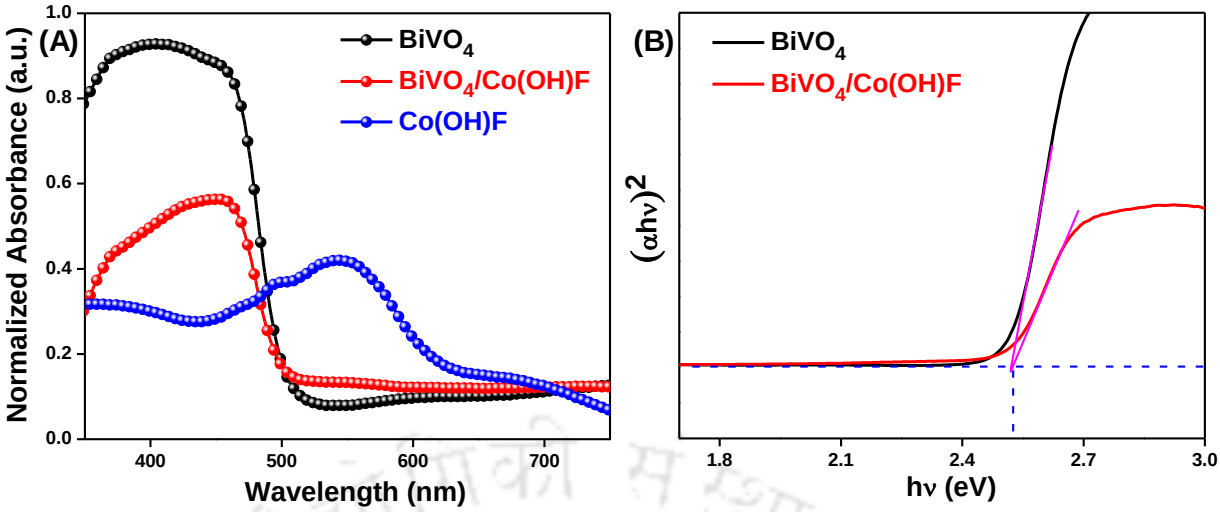

Figure 4.3.2 (A) UV-Vis absorption spectra of as-deposited $BiVO_4$ (black line), Co(OH)F (blue line), and $BiVO_4$/Co(OH)F (red line) and (B) represents corresponding Tauc plots for bandgap calculation

4.3.3 Morphological and Structural Analysis

To investigate the morphology of as-synthesized $BiVO_4$, Co(OH)F, and $BiVO_4$/Co(OH)F, FESEM was carried out, represented in **Figure 4.3.3**. Figure 4.3.3 (A) showed that as-deposited BiOI composed of uniformly deposited nano-flakes. These nano-flakes were placed loosely to find ample space for volume expansion after the implantation of vanadium ions. After the phase transformation of BiOI to $BiVO_4$, a thin film of a wormlike structure having a smoother surface was derived from original nano-flakes structures, as shown in figure 4.3.3 (B). An important point of these hierarchical structures was that they were deposited directly over FTO, without using a seed layer to reduce the Ohmic resistance for smooth charge injections. Figure 4.3.3 (C) showed the FESEM image of as-synthesized Co(OH)F nanorods structure. In comparison to their bulk counterparts, 1D nanostructures such as nanotubes, nanorods, and nanowires have advantages in many catalytic areas. These advantages were mainly due to the facile charge separation and a shorter diffusion path for minority carriers to reach the photoanode/electrolyte interface. The presence of Fluoride in Co(OH)F is expected to improve the conductivity, charge mobility, and stability. Figure 4.3.3 (D) showed the FESEM image for $BiVO_4$/Co(OH)F composite. From the figure, it was clear that nanorods covered the entire surface of $BiVO_4$.

Part of this chapter has been published in **ACS Sustainable Chem. Eng. 2021, 9, 5155−5165**

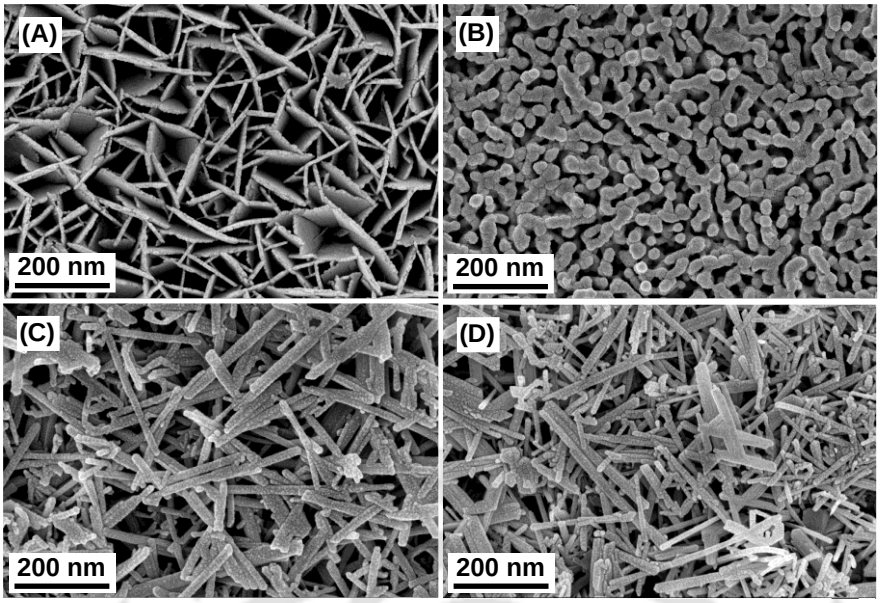

Figure 4.3.3 Typical FESEM images (top view) of (A) as-deposited BiOI film shows nano-flake structures (B) represent FESEM images of $BiVO_4$ shows worm-like structures (C) as-synthesized Co(OH)F shows nanorods and (D) FESEM image of $BiVO_4$/Co(OH)F composite

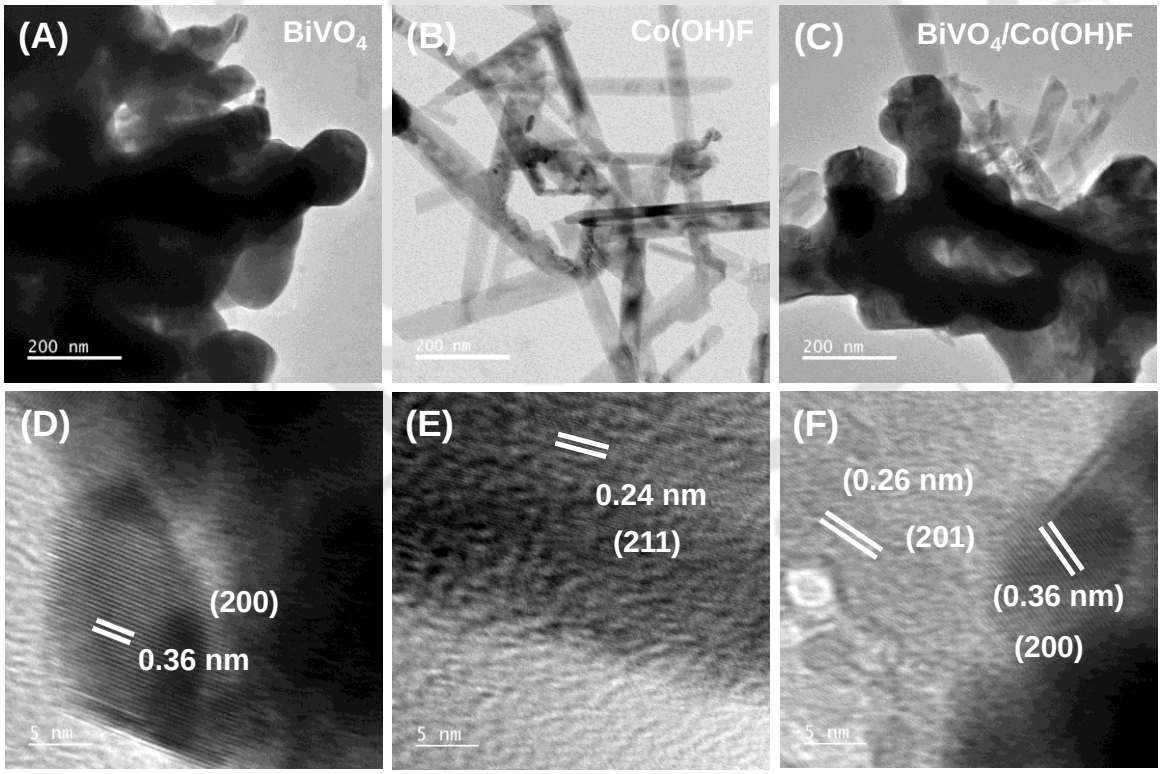

Figure 4.3.4 (A&D) TEM and HRTEM images show the structural features of as-deposited $BiVO_4$, (B&E) (A&D) TEM and HRTEM images of Co(OH)F nanorods and (C&F) TEM and HRTEM images of BiVO4/Co(OH)F composite shows the presence of both $BiVO_4$ and Co(OH)F

Part of this chapter has been published in **ACS Sustainable Chem. Eng. 2021, 9, 5155−5165**

Structural features of as-synthesized $BiVO_4$, Co(OH)F, and $BiVO_4$/Co(OH)F, were confirmed using TEM analysis. **Figure 4.3.4** (A&D) showed the TEM and HRTEM images of bare $BiVO_4$ respectively. Figure 4.3.4 (D), lattice fringes having a d-spacing of 0.36 nm, correspond to (200) crystal plane of $BiVO_4$. Figure 4.3.4 (B&E) represented the TEM and HRTEM images of Co(OH)F nanorods respectively. From the HRTEM image, lattice fringes having an interplanar distance of 0.24 nm correspond to the (211) plane of Co(OH)F. Figure 4.3.4 (C&F) exhibited the TEM and HRTEM images of $BiVO_4$/Co(OH)F respectively. From the figure, wormlike structures for $BiVO_4$ as well as nanorods for Co(OH)F were observed. Also, from HRTEM images lattice fringes with an interplanar distance of 0.26 nm and 0.36 nm attributed to the (201) crystal plane for Co(OH)F and (200) crystal plane for $BiVO_4$ respectively.

Scanning transmission electron microscopy (STEM) was performed to confirm the elemental composition of $BiVO_4$/Co(OH)F composite as depicted in **Figure 4.3.5**. From corresponding figures, all the constituent elements viz. Bi, V, O, Co and F were homogeneously distributed throughout the sample.

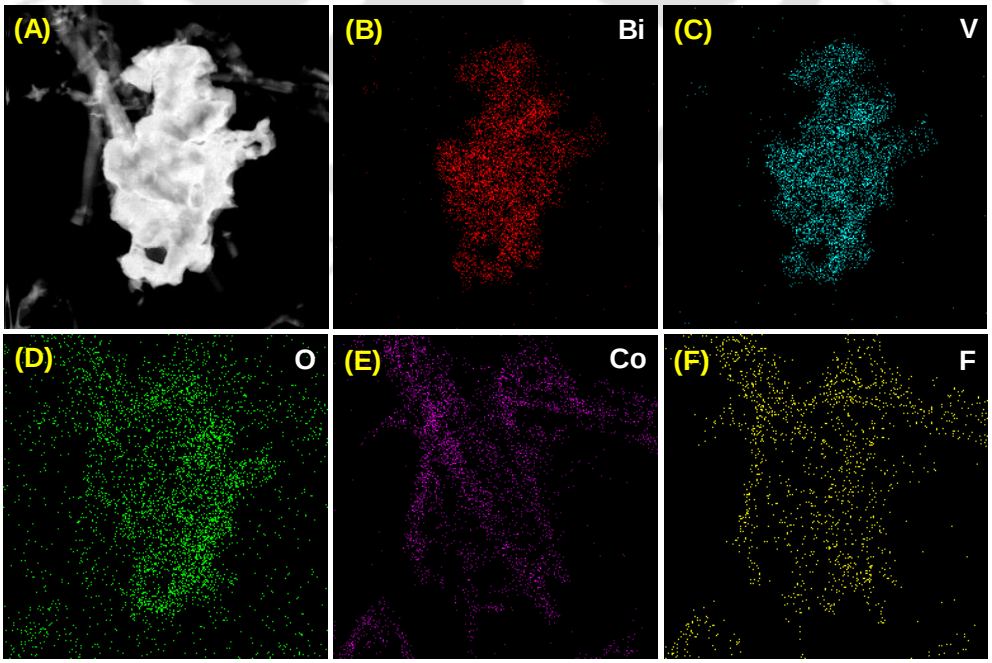

Figure 4.3.5 Elemental mapping of $BiVO_4$/Co(OH)F composite showing the presence of the elements

Part of this chapter has been published in **ACS Sustainable Chem. Eng. 2021, 9, 5155−5165**

4.3.4 X-ray Photoelectron Spectroscopy (XPS) Analysis

To know the chemical states as well as the interaction between Co(OH)F and $BiVO_4$, XPS analysis was performed, presented in **Figure 4.3.6**. Trace (A) showed the survey spectra, wherein characteristic peaks for Bi, V, and O were present in bare $BiVO_4$, while $BiVO_4$/Co(OH) showed the characteristic peaks for Bi, V, O, Co and F. Trace (B) represent the high-resolution XPS spectra for Bi, showed two peaks at binding energies 158.8 eV and 164.04 eV can be ascribed to $4f_{7/2}$ and $4f_{5/2}$ respectively, confirm the presence of Bi^{3+} in $BiVO_4$[33]. On the other hand, the peaks for $4f_{7/2}$ and $4f_{5/2}$ for $BiVO_4$/Co(OH)F were found to be at binding energies 159.10 eV and 164.38 eV respectively.

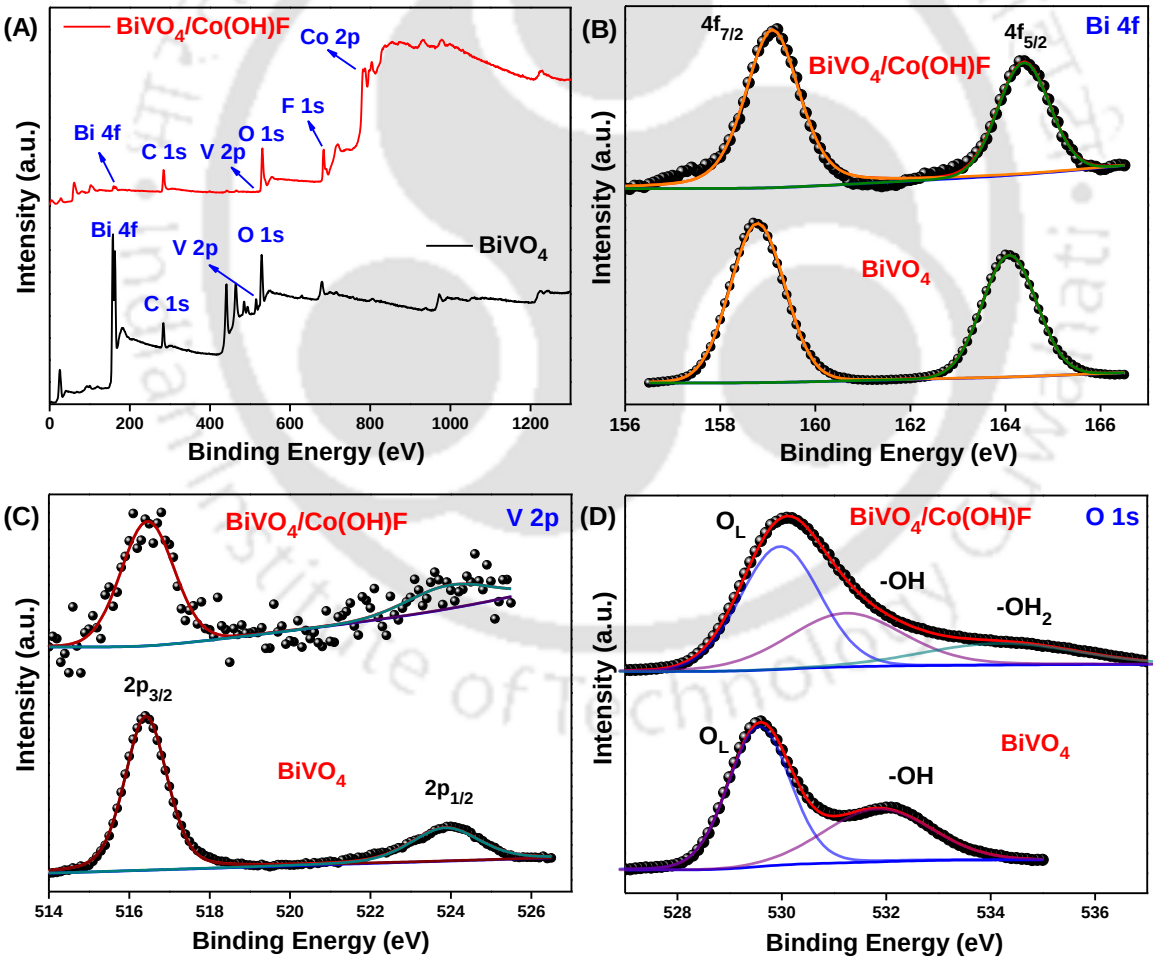

Figure 4.3.6 Core level XPS spectra of $BiVO_4$ and $BiVO_4$/Co(OH)F, (A) survey spectra, (B) Bi 4f, (C) V 2p, and (D) O 1s, depicting the chemical state of Bismuth and Vanadium and their subsequent interactions with Co(OH)F for improved PEC water oxidation

Part of this chapter has been published in **ACS Sustainable Chem. Eng. 2021, 9, 5155−5165**

Trace (C) represented the high-resolution XPS spectra for vanadium, showing two peaks at binding energies 516.36 eV and 523.86 eV for V $2p_{3/2}$ and V $2p_{1/2}$ in $BiVO_4$, while peaks at 516.45 eV and 523.96 eV for V $2p_{3/2}$ and V $2p_{1/2}$ in $BiVO_4$/Co(OH)F respectively. These splitting signals for vanadium 2p in both were indicative of the presence of vanadium in +5 (V^{5+}) oxidation state. Also, a shift in the peak positions towards higher binding energies was indicative of a change in the electronic environment after the modification due to the interaction of $BiVO_4$ with Co(OH)F[34-35]. Trace (D) represented the core level spectra for O 1s. Upon deconvolution, this O 1s spectra for bare $BiVO_4$ and $BiVO_4$/Co(OH)F were fitted into two and three peaks, respectively. In both cases, the peak at 529.60 eV and 530.10 eV were assigned to lattice oxygen[34]. Peak at 531.84 eV for $BiVO_4$ was assigned to surface hydroxyl ions[34], while in case of $BiVO_4$/Co(OH)F peak at 531.30 eV was assigned to that from metal hydroxide[36-37]. In case of $BiVO_4$/Co(OH)F, an additional peak at 534.12 eV can be attributed due to the water molecule[36, 38] .

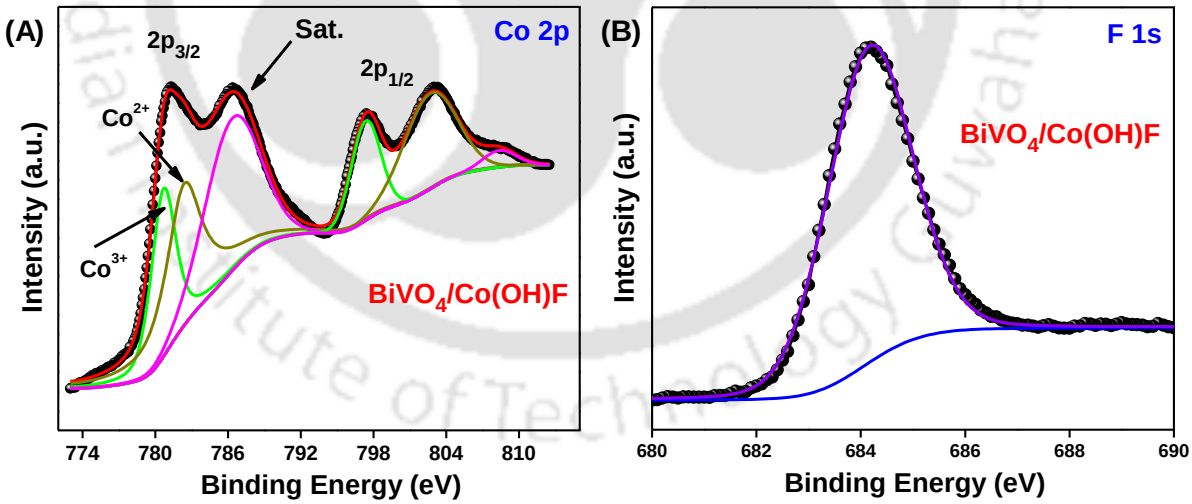

Figure 4.3.7 Core level XPS spectra of (A) Co 2p and (B) F 1s, depicting the different oxidation states of cobalt in $BiVO_4$/Co(OH)F composite

Figure 4.3.7 (A) showed the high-resolution XPS spectra for Co 2p. The valence state of Co species was confirmed by deconvoluting the Co 2p spectra. Two peaks present at binding

Part of this chapter has been published in **ACS Sustainable Chem. Eng. 2021, 9, 5155−5165**

energies 781.27 eV and 797.41 eV confirmed the existence of Co^{2+} species in the composite material. Co $2p_{3/2}$ spectra was fitted into two Gaussian peaks at 780.70 eV and 782.50 eV. Broad nature and positions of satellite peaks agreed with Co $2p_{3/2}$ signals from Co^{2+} species having 3d unpaired electrons as reported in the literature. However, as Co(OH)F was washed and subjected to 80˚C, because of the defects of Co(OH)F, some of the Co^{2+} on the surface oxidized to Co^{3+} [39-40]. **Figure 4.3.7 (B)** showed the XPS core-level spectra for F 1s. The peak at 684.20 eV was in close agreement with the peak of F ion in metal hydroxyl fluoride[41].

4.3.5 Time-resolved Photoluminescence (TRPL) Analysis

To gain insight into the charge transfer between Co(oH)F and $BiVO_4$, we have resorted to dynamic photo luminescent measurement. Time-resolved photoluminescence (TRPL) measurement was carried out for both Co(OH)F and $BiVO_4$/Co(OH)F and the corresponding decay pattern is shown in **Figure 4.3.8**. The decay patterns were fitted using the tri-exponential function and the average lifetime was calculated using equation 4.1.

$$< \tau > = \frac{a_1\tau_1^2 + a_2\tau_2^2 + a_3\tau_3^2}{a_1\tau_1 + a_2\tau_2 + a_3\tau_3} \qquad (4.1)$$

Calculated average lifetime values for Co(OH)F and $BiVO_4$/Co(OH)F were found to be 9.063 ns and 2.866 ns respectively. This faster average lifetime value for $BiVO_4$/Co(OH)F suggesting a better charge transfer between Co(OH)F and $BiVO_4$. The values of fitted parameters were summarized in **Table 4.3.1**.

Table 4.3.1 Estimated fitting parameters such as χ^2, exciton lifetimes (τ_1, τ_2, τ_3) (ns) pre-exponential factors (α_1, α_2, α_3) and average exciton lifetimes ($<\tau>$) (ns) for Co(OH)F and $BiVO_4$/Co(OH)F

Sample	χ^2	τ_1	τ_2	τ_3	α_1	α_2	α_3	$< \tau >$ **ns**
Co(OH)F	1.021	0.557	2.347	12.265	40.390	39.055	20.555	9.063
$BiVO_4$/Co(OH)F	1.019	0.064	0.532	3.485	13.845	53.938	32.216	2.866

Part of this chapter has been published in **ACS Sustainable Chem. Eng. 2021, 9, 5155−5165**

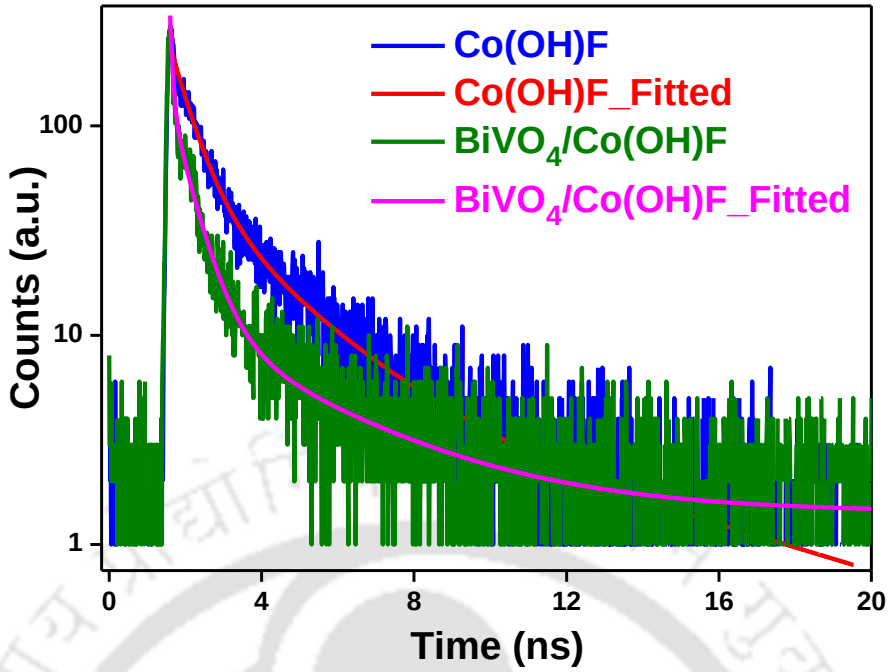

Figure 4.3.8 Time-resolved photoluminescence (TRPL) spectra for Co(OH)F and BiVO4/Co(OH)F shows the effective charge transfers among the components present

4.3.6 Photoelectrochemical Measurements

In order to compare the water oxidation kinetics as a function of the redox couple, a systematic investigation of water oxidation involving Co(OH)F and $BiVO_4$ has been carried out. PEC performance was analyzed using Linear Sweep Voltammetry (LSV) as a function of applied bias, depicted in **Figure 4.3.9**. Photoelectrochemical measurements were performed in a conventional three-electrode system in N_2 purged 0.5 M potassium borate solution as electrolyte under 1 Sun illumination. As shown in figure 4.3.9 (B), PEC performance of $BiVO_4$/Co(OH)F at different concentrations of Co(OH)F i.e. 1 mg/mL, 3 mg/mL, 5 mg/ml, and 7 mg/mL were systematically optimized in order to obtain the best suitable condition for preparing $BiVO_4$/Co(OH)F photoanodes. From figure 4.3.9 (A), the photocurrent density of bare $BiVO_4$ was found to be 1.45 mA/cm^2 at 1.23 V with an onset potential of 0.52 V vs RHE. In contrast, when $BiVO_4$ was modified with Co(OH)F, the photocurrent density was increased to 3.4 mA/cm^2 at 1.23 V with an onset potential of 0.36 V vs RHE, which is 2.4 times higher than the bare $BiVO_4$. Suppressed recombination of the photogenerated carriers, improved

Part of this chapter has been published in **ACS Sustainable Chem. Eng. 2021, 9, 5155−5165**

charge extraction, and faster surface kinetics are primarily responsible for the enhanced photocurrent value. Also, cathodic shift in the onset potential specified that a lower over-potential is required for water oxidation when coupled with Co(OH)F. Co(OH)F modification could efficiently stimulate the water oxidation performance of photoanode. The compact contact between $BiVO_4$ and Co(OH)F facilitates the charge separation at electrolyte/electrode surface feasible, results in enhanced oxygen evolution kinetics at the photoanode.

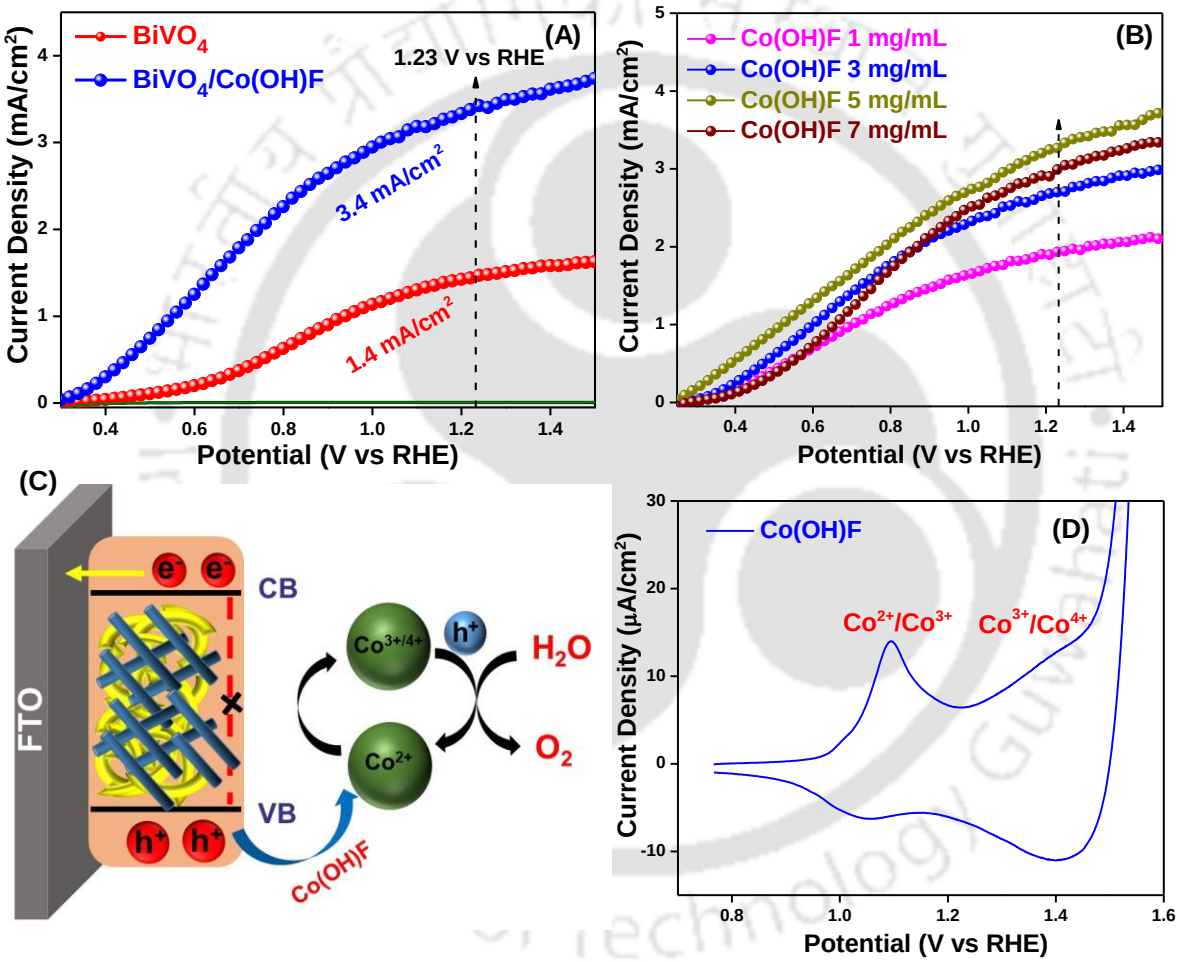

Figure 4.3.9 Current density-voltage curves for (A) $BiVO_4$ and $BiVO_4$/Co(OH)F, (B) Optimization curve for $BiVO_4$ modified with different amounts of Co(OH)F, (C) Schematic representation of possible mechanism involving different species for efficient oxygen reaction, and (D) Cyclic voltammetry curve for Co(OH)F depicting the presence of different oxidation states of cobalt

In $BiVO_4$/Co(OH)F system, $BiVO_4$ acts as an absorber layer for solar light, where electrons in the valence band were excited to the conduction band to generate carriers.

Part of this chapter has been published in **ACS Sustainable Chem. Eng. 2021, 9, 5155−5165**

Photogenerated electrons transferred to the FTO, while these photogenerated holes transferred to the surface, driven by the applied potential. Due to the sluggish water oxidation kinetics of $BiVO_4$, these surface-reaching holes were inclined to accumulate and recombine with the electrons. On the other hand, upon modification with Co(OH)F nanorods, these holes migrated to the oxygen evolution catalyst surface, restricted the charge recombination. Mechanistically, Co^{2+} ions are known to act as active sites to receive holes from semiconductors and oxidized to Co^{3+} or/and Co^{4+} [42]. Subsequently these active species, Co^{3+} or/and Co^{4+} release the positive charge to produce O_2 and recover to the initial state, as represented in **Figure 4.3.9 (C)**[43-44]. To further confirm the active redox species involved in Co(OH)F for water oxidation, cyclic voltammetry (CV) measurement was carried out as shown in **Figure 4.3.9 (D)**, which shows two distinguishable redox peaks for $Co^{2+/3+}$ and $Co^{3+/4+}$ respectively.

Further, the superiority and the uniqueness of as-synthesized Co(OH)F cocatalyst was compared with benchmark Co-based cocatalysts reported in the literature such as Co_3O_4[45] and $Co(OH)_X$[46] and presented in **Figure 4.3.10** under similar experimental conditions. Figure 4.3.10 (A) represents the linear sweep voltammetry curve for bare and Co_3O_4 modified $BiVO_4$. After the modification of $BiVO_4$ with Co_3O_4, the current density value was found to be 2.75 mA/cm^2. Apart from this figure 4.3.10 (B) represents the current-voltage curve for bare and $Co(OH)_X$ modified $BiVO_4$. In case of $Co(OH)_X$ modified $BiVO_4$ the current density was found to be 2.4 mA/cm^2. Therefore, the incorporation of F not only enhances the conductivity but also results in enhanced charge mobility. This enhanced OER activity of Co(OH)F was mainly because of its 1D structures. Apart from this Co(OH)F also has intrinsic better OER performance than $Co(OH)_2$, due to its, inter alia, superior bulk conductivity[32]. Therefore, incorporation of fluoride ions into cobalt-based catalyst not only increases the conductivity but also helps in enhancing the overall stability. Figure 4.3.10 (C) represents the bar diagram for bare $BiVO_4$ and modified with different catalysts.

Part of this chapter has been published in **ACS Sustainable Chem. Eng. 2021, 9, 5155−5165**

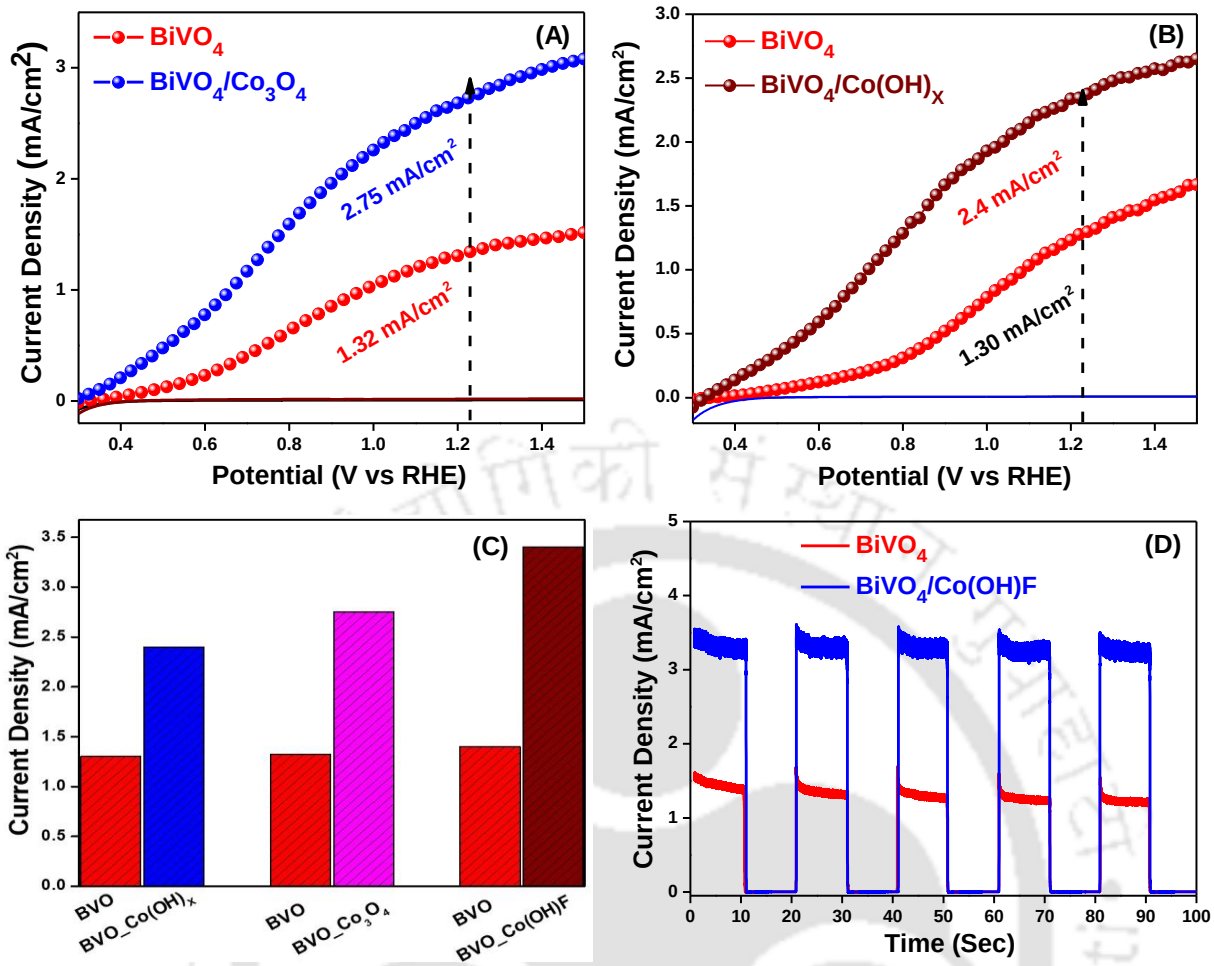

Figure 4.3.10 Linear sweep voltammetry curves for (A) Bare $BiVO_4$ and Co_3O_4 modified $BiVO_4$, (B) Bare $BiVO_4$ and $Co(OH)_X$ modified $BiVO_4$, recorded under similar experimental conditions (C) Bar diagram for different compositions and (D) Transient photocurrent plots for pristine and Co(OH)F modified $BiVO_4$ recorded at 1.23 V vs RHE using Chronoamperometry

In addition, transient photocurrent measurements were performed to investigate the electron-hole pair recombination at the photoanode surface. From **Figure 4.3.10 (D)**, it was confirmed that the photocurrent density of $BiVO_4$/Co(OH)F was 2.4 fold higher than that of pristine $BiVO_4$. Moreover, with illumination, sharp anodic spikes were observed in case of pristine $BiVO_4$. This was ascribed to the fact that photogenerated holes accumulated at the photoanode/electrolyte interface and were subsequently used in the recombination process. However, transient anodic spikes were reduced in the presence of the Co(OH)F redox couple, indicative of a reduced electron-hole pair recombination processes at the photoanode surface.

Part of this chapter has been published in **ACS Sustainable Chem. Eng. 2021, 9, 5155−5165**

To study the electrochemical behavior (OER property) of Co(OH)F as an electro-catalyst in order to characterize parameters such as Tafel plot and turn over frequency (TOF), LSV analysis was conducted under dark conditions, as represented in **Figure 4.3.11**. From trace (A) the overpotential at 10 mA/cm^2 for Co(OH)F was found to be 440 mV. Further, Tafel slop has been evaluated using LSV curve to study the kinetics of Co(OH)F as an electrocatalyst. From figure 4.3.11 (B) Tafel slop value for Co(OH)F was found to be 71 mV/dec. To further comment on the efficacy of the electro-catalyst, turnover frequency (TOF) was calculated at 1.6 V potential vs RHE and found to be 0.408/Sec.

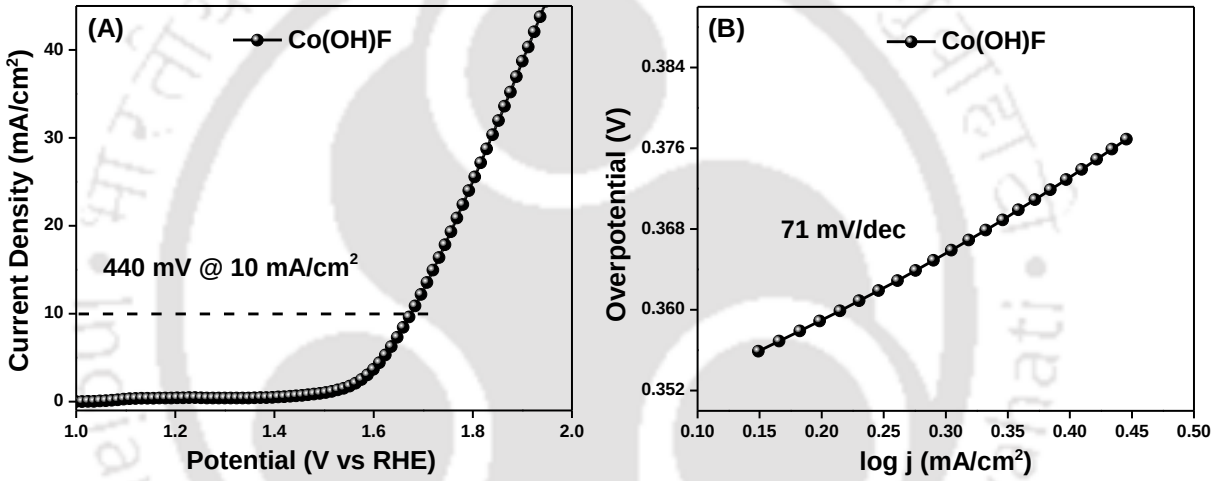

Figure 4.3.11 (A) Linear Sweep Voltammetry curve for Co(OH)F drop casted over FTO, under dark conditions and (B) Corresponding Tafel plot

To estimate the efficacy of pristine and Co(OH)F modified $BiVO_4$ photoanode, applied bias photon-to-current efficiencies (ABPE), were determined, as showed in **Figure 4.3.12 (A)**. The curves were plotted based on current-voltage plots, recorded in backlight illumination mode, in a three-electrode system. As obtained from the figure, Co(OH)F modification had a positive effect on the ABPE of the $BiVO_4$ derived electrodes. For the $BiVO_4$ and $BiVO_4$/Co(OH)F, modification, ABPE maxima of 0.30 % and 0.98 % were obtained, respectively, correspond to an increased APBE by a factor of 3.3.

Part of this chapter has been published in **ACS Sustainable Chem. Eng. 2021, 9, 5155−5165**

To further validate photon conversion of as-synthesized pristine and Co(OH)F modified photoanode, IPCE measurement was carried out in the wavelength range of 350-600 nm and integrated the same to get the corresponding current density values, as illustrated in **Figure 4.3.12 (B)**. In the figure, $BiVO_4$/Co(OH)F displayed a much better EQE value viz. ~ 60 % in comparison with pristine $BiVO_4$ based photoanode i.e., ~ 30 %. As obtained higher EQE value of $BiVO_4$/Co(OH)F photoanode was the confirmation of the higher current value attained from the LSV curve. Enhancement in IPCE was related to the reduced recombination of photogenerated charge carriers and improved charge injection, by virtue of the formation of an interface between Co(OH)F nanorods and $BiVO_4$.

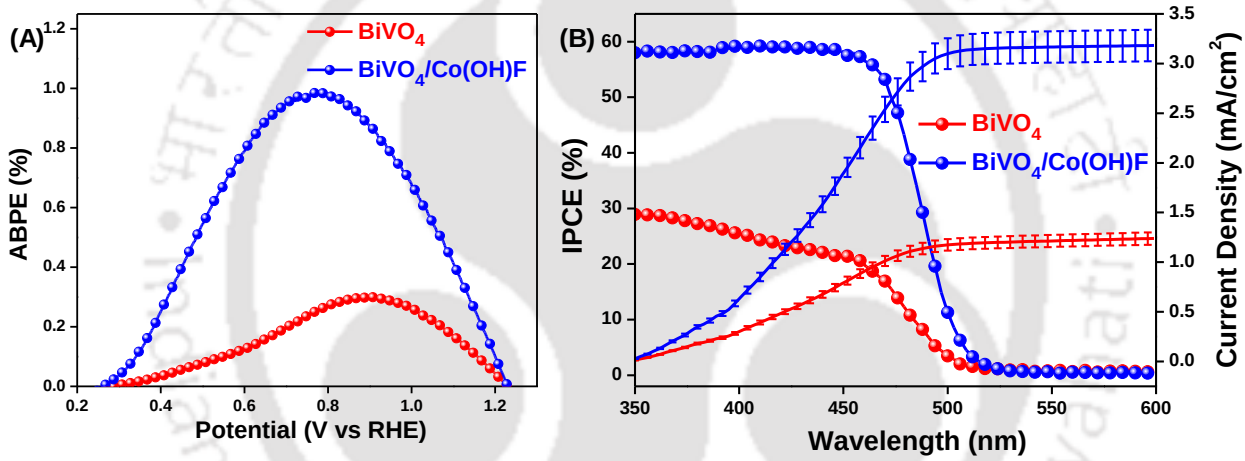

Figure 4.3.12 (A) Applied bias photon-to-current efficiency (ABPE) curves for bare $BiVO_4$, and Co(OH)F modified $BiVO_4$, (B) Displays corresponding integrated incident photon to current conversion (IPCE) curves with reference to the obtained current densities.

4.3.7 Electrochemical Impedance Spectroscopy (EIS) Analysis

To investigate the interfacial charge separation and transport kinetics as a function of the redox mediator, of fabricated photoanodes, EIS analysis was carried out at 1.23 V vs RHE under illumination. **Figure 4.3.13** represented the EIS spectra as Nyquist plot. This Nyquist spectrum was interpreted using an equivalent circuit diagram as shown in the inset of the figure and corresponding fitted parameters such as R_S, and R_{CT} were obtained. The radius of the arc in the Nyquist curve was due to charge transfer at the electrolyte/electrode interface. **Figure**

Part of this chapter has been published in **ACS Sustainable Chem. Eng. 2021, 9, 5155−5165**

4.3.13 included a semicircle for both the photoanodes at the mid-frequency region, due to the charge transfer resistance (R_{CT}) at the electrolyte/electrode interface, which is important for characterizing the interfacial activity. R_S represented the ohmic resistance between FTO and photoanode. Since a smaller semicircle or smaller R_{CT} value indicated the better charge transport ability, therefore lesser R_{CT} value for $BiVO_4$/Co(OH)F photoanode confirmed that the transport was improved significantly as compared to pristine $BiVO_4$. It was clear that pristine $BiVO_4$ showed a higher R_{CT} of 4.60 KΩ, specified the poor charge transport, observed in low photocurrent value (LSV curve). After the incorporation of Co(OH)F with $BiVO_4$, charge transfer resistance decreases significantly. In case of $BiVO_4$/Co(OH)F, the charge transfer resistance was 2.36 KΩ, suggested the improved interfacial transport of charges with minimum contact resistance. Incorporation of Co(OH)F changed the electrode/electrolyte interface properties. This improved charge transport behavior could be ascribed to the better hole extraction efficiency or lesser recombination of charge carriers at the photoanode/electrolyte interface.

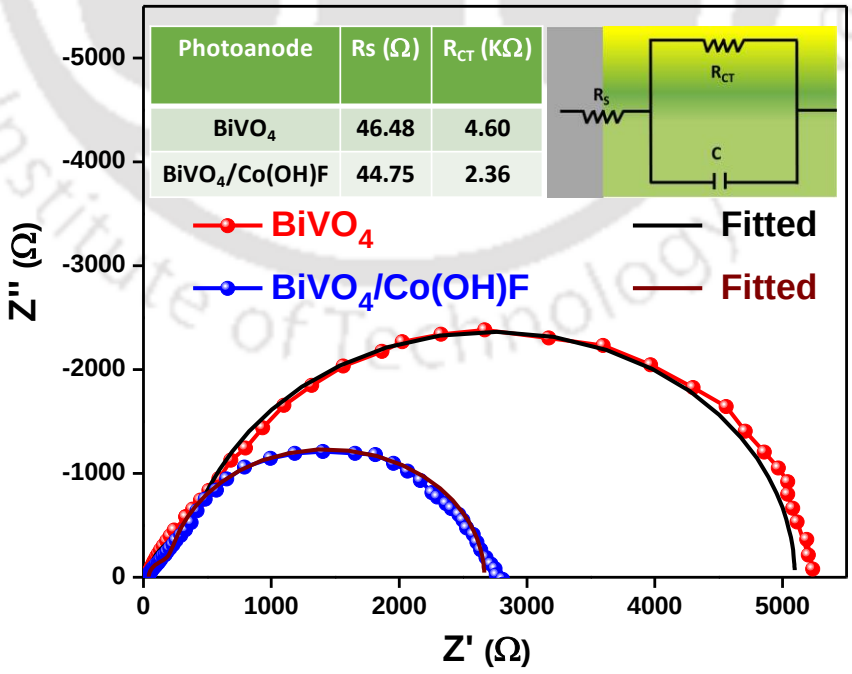

Figure 4.3.13 Represents Nyquist plots of as-synthesized pristine and Co(OH)F modified $BiVO_4$ under light illumination at 1.23 V vs RHE

Part of this chapter has been published in **ACS Sustainable Chem. Eng. 2021, 9, 5155−5165**

4.3.8 Charge Injection and Separation Efficiency (Hole Scavenger Test)

To investigate the hole transfer efficiency of pristine and Co(OH)F modified $BiVO_4$ photoanode, 0.5 M Na_2SO_3 was used as hole scavenger, and results were illustrated in **Figure 4.3.14**. As observed from figure 4.3.14 (A) and (B), after the addition of Na_2SO_3, the anodic current value was improved several times. This increment in the photocurrent density is primarily because of sulfite oxidation, which is kinetically faster in comparison to the oxidation of water. Thus, a significant increment in the current value after the addition of sulfite indicated that the current of $BiVO_4$ photoanode was mainly limited due to poor water oxidation kinetics on its surface. This result suggested that Co(OH)F could effectively reduce the recombination of photogenerated electron-hole pairs on the photoanode surface to promote the water oxidation kinetics[47-48].

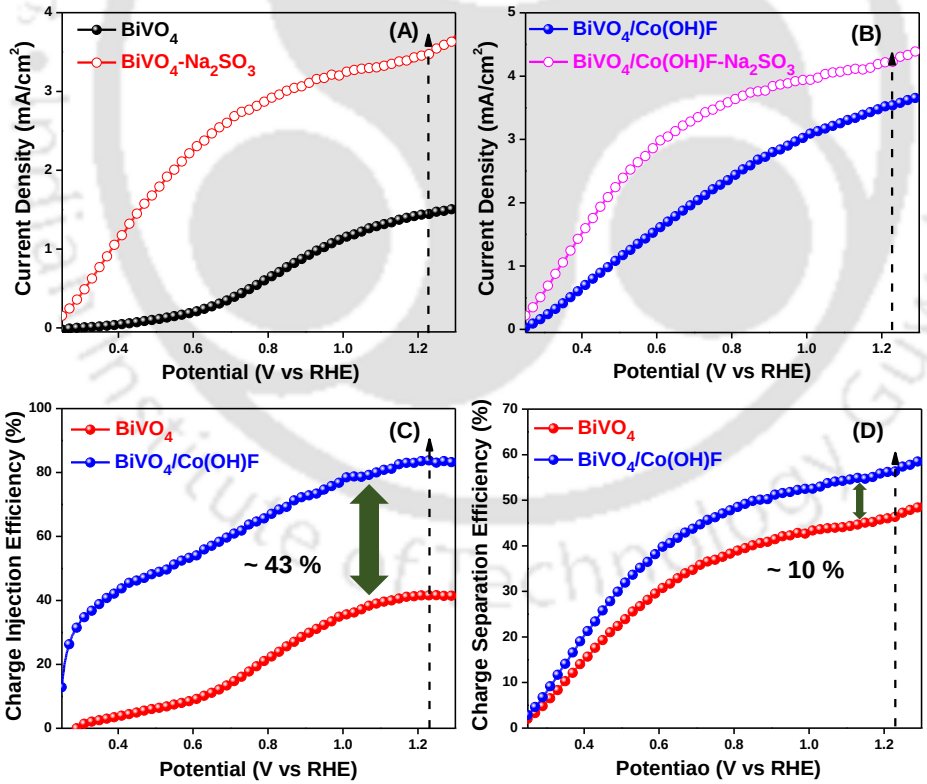

Figure 4.3.14 (A-B) Photocurrent density vs potential curves for bare and Co(OH)F modified $BiVO_4$, with and without Na_2SO_3 hole scavenger, (C-D) Represents Charge injection and Charge separation efficiencies for pristine $BiVO_4$ and Co(OH)F modified $BiVO_4$ respectively, calculated from current density-voltage curves with and without Na_2SO_3 as hole scavenger

Part of this chapter has been published in **ACS Sustainable Chem. Eng. 2021, 9, 5155−5165**

The hole injection efficiency of pristine $BiVO_4$ was 41 % which indicated that more than half of the photogenerated holes were wasted because of the bulk recombination. Due to the high oxidation rate of sulfite, $J_{water}/J_{surface}$ ratio was considered as the yield of holes that contribute to the water oxidation reaction that occurred at the semiconductor/electrolyte interface. As observed from figure 4.3.14 (C) that the hole injection efficiency of $BiVO_4$/Co(OH)F photoanode increased dramatically as compared to pristine $BiVO_4$. The hole injection efficiency reached up to ~84 % at 1.23 V vs RHE, indicated that the surface recombination were greatly reduced after Co(OH)F modification. It is clear that modification of $BiVO_4$ with Co(OH)F could form an interface between $BiVO_4$ and Co(OH)F which was favorable for the water oxidation reaction between semiconductor and electrolyte. As shown in Figure 4.3.14 (D), the charge separation efficiency of the $BiVO_4$/Co(OH)F electrode at 1.23 V vs. RHE is 56 %, which is higher than that of the $BiVO_4$ electrode. This result further reconfirmed the enhanced separation of electrons and holes after loading the redox mediator.

4.3.9 Electrochemical Surface Area (ECSA) Analysis

To calculate electrochemical active surface area, which is directly proportional to the number of active sites, cyclic voltammetry analysis was performed. These number of active sites can be estimated using the electrochemical bilayer capacitance (C_{dl}) model. ECSA of $BiVO_4$ and $BiVO_4$/Co(OH)F photoanodes were estimated by the capacitive current of the cyclic voltammogram in the non-faradaic region, depicted in **Figure 4.3.15**. Cyclic voltammograms were carried out at different scan rates ranging from (10-100 mV/Sec) in 0.5 M potassium borate solution. Then the electrochemically active surface area was estimated by determining the capacitive current related to double layer charging, from the scan rate dependence of the CV. The double-layer capacitance (C_{dl}) was determined from the relationship between $\Delta J = (J_a - J_c)$ of Ag/AgCl at 0.90 V and the scan rate. From **Figure 4.3.15 (C-D)**, the linear slope is equivalent to that twice the C_{dl} value can be used to symbolize an

Part of this chapter has been published in **ACS Sustainable Chem. Eng. 2021, 9, 5155−5165**

electrically active surface area. Based on these curves C_{dl} values for $BiVO_4$ and $BiVO_4$/Co(OH)F were found to be 57 μF/cm^2 and 95 μF/cm^2 respectively, which further confirmed that the Co(OH)F loading enhanced the active surface area and enriched the active sites.

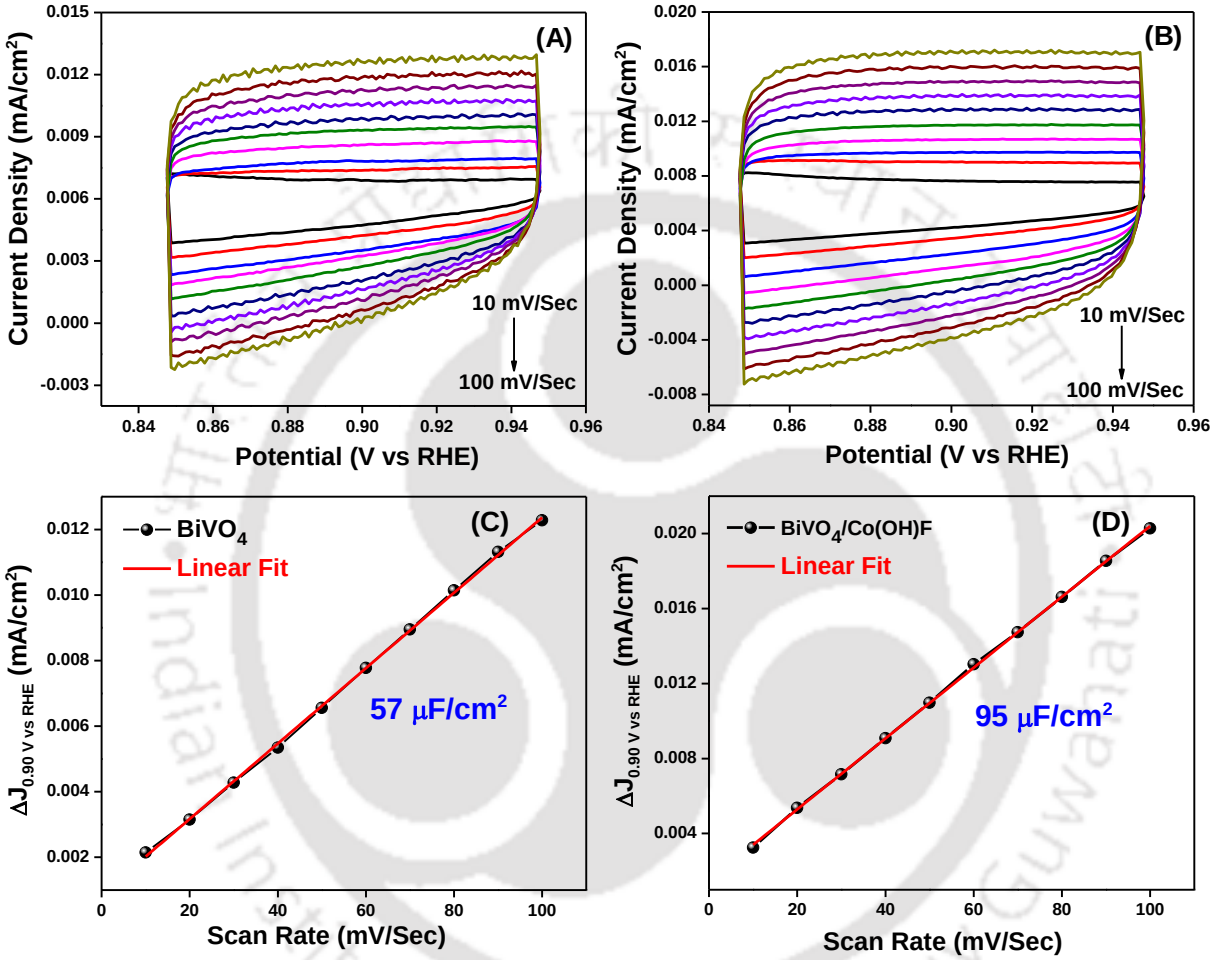

Figure 4.3.15 (A-B) Cyclic voltammetry curves for $BiVO_4$ and $BiVO_4$/Co(OH)F at different scan rates in the non-faradaic region respectively and (C-D) Plot of current density (at 0.90 V vs RHE) vs the scan rate of $BiVO_4$, and $BiVO_4$/Co(OH)F for the determination of C_{dl} values

4.3.10 Faradaic Yield and Stability Measurements

To determine the Faradaic yield on the photoanode, the amount of oxygen evolved was measured to confirm that the generated photocurrent was solely due to the water oxidation as presented in **Figure 4.3.16 (A)**. Faradaic yield is the ratio of gas evolved experimentally to that

Part of this chapter has been published in **ACS Sustainable Chem. Eng. 2021, 9, 5155−5165**

of the theoretically calculated oxygen production rate. The amount of oxygen obtained experimentally and oxygen generated theoretically were almost similar, and after 100 minutes a remarkable average Faradaic yield of ~ 95% was detected, which implies that the obtained photocurrent was only due to water oxidation.

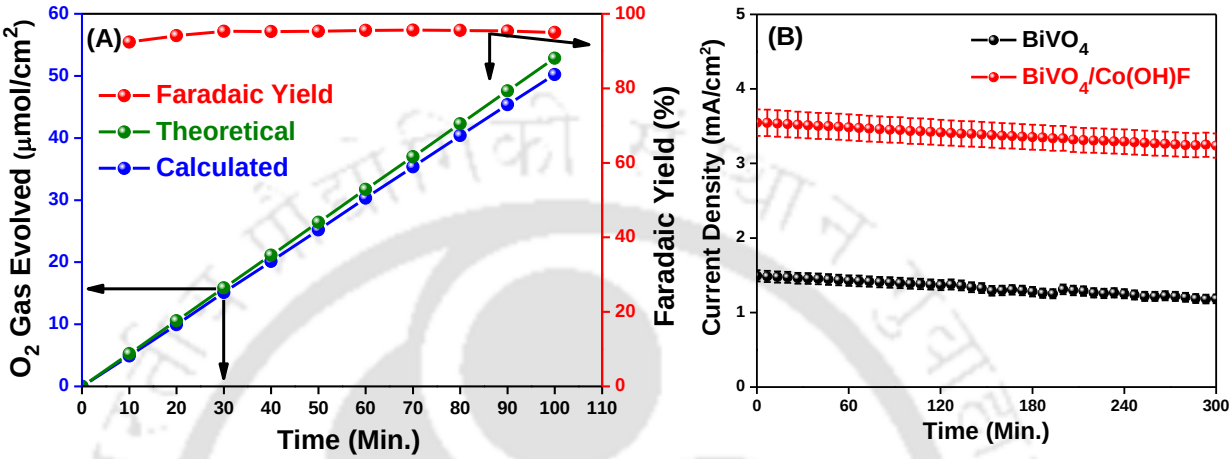

Figure 4.3.16 (A) Represents the Faradaic yield of $BiVO_4$/Co(OH)F (red line), the theoretical value of O_2 evolved (green line) in μmol/cm^2, the calculated value of O_2 (blue line) in μmol/cm^2 and (B) Demonstrate photoelectrochemical operational stability of $BiVO_4$ and $BiVO_4$/Co(OH)F, recorded at 1.23 V vs RHE in KBi electrolyte under continuous illumination with an error bar of 5 %

Photoelectrochemical operational stability was performed at 1.23 V vs RHE under continuous illumination for 5 hr depicted in **Figure 4.3.16 (B)**. From the figure, it was clear that even after the continuous illumination for 5 hr, there is no substantial change in the photocurrent value, suggesting the stability of the proposed system under harsh alkaline conditions.

4.4 Conclusions

Loading of Co(OH)F onto $BiVO_4$ resulted in enhanced photocurrent density up to 3.4 mA/cm^2 which was 2.4 times higher than the photocurrent obtained for pristine $BiVO_4$ (1.45 mA/cm^2). Modification of Co(OH)F led to a considerable improvement in PEC performance due to suppressed surface charge recombination as well as enhancement in the hole extraction

Part of this chapter has been published in **ACS Sustainable Chem. Eng. 2021, 9, 5155−5165**

ability by virtue of the redox mediator. Also, modification of Co(OH)F lowers the onset potential to 160 mV, indication of an efficient co-catalyst. This result provides a promising way to achieve highly efficient water oxidation kinetics using a noble metal-free redox couple with a semiconductor. Also, this modification suggested that the incorporation of several nanostructures, as well as the composition tuning on the $BiVO_4$/Co(OH)F photoanode, can be a potential path in order to fabricate an effective water-splitting photoanode.

4.5 References

(1) L. Wu, M. Eberhart, A. Nayak, M. K. Brennaman, B. Shan and T. J. Meyer, *J. Am. Chem. Soc.*, 2018, **140**, 15062.

(2) R. Liu, Z. Zheng, J. Spurgeon and X. Yang, *Energy Environ. Sci.*, 2014, **7**, 2504.

(3) I. Concina, Z. H. Ibupoto and A. Vomiero, *Adv. Energy Mater.*, 2017, **7**, 1700706.

(4) K. K. Dey, S. Gahlawat and P. P. Ingole, *J. Mater. Chem. A*, 2019, **7**, 21207.

(5) M. Kan, D. Xue, A. Jia, X. Qian, D. Yue, J. Jia and Y. Zhao, *Appl. Catal., B*, 2018, **225**, 504.

(6) B. Wang, R. Li, Z. Zhang, X. Wu, G. Cheng and R. Zheng, *Catal. Today*, 2019, **321**, 100.

(7) T. Butburee, Y. Bai, H. Wang, H. Chen, Z. Wang, G. Liu, J. Zou, P. Khemthong, G. Q. M. Lu and L. Wang, *Adv. Mater.*, 2018, **30**, 1705666.

(8) J. Huang, Y. Zhang and Y. Ding, *ACS Catal.*, 2017, **7**, 1841.

(9) R. Chong, B. Wang, C. Su, D. Li, L. Mao, Z. Chang and L. Zhang, *J. Mater. Chem. A*, 2017, **5**, 8583.

(10) Y. Q. Gao, Y. D. Li, G. Q. Yang, S. S. Li, N. Xiao, B. R. Xu, S. Liu, P. Qiu, S. J. Hao and L. Ge, *ACS Appl. Mater. Interfaces*, 2018, **10**, 39713.

(11) M. de Respinis, K. S. Joya, H. J. M. De Greet, F. D'Souza, W. A. Smith, R. van de Krol and B. Dam, *J. Phys. Chem. C*, 2015, **119**, 7275.

(12) J. M. Lee, J. H. Baek, T. M. Gill, X. Shi, S. Lee, I. S. Cho, H. S. Jung and X. Zheng, *J. Mater. Chem. A*, 2019, **7**, 9019.

(13) Q. Wang, T. Niu, L. Wang, C. Yan, J. Huang, J. He, H. She, B. Su and Y. Bi, *Chem. Eng. J.*, 2018, **337**, 506.

Part of this chapter has been published in **ACS Sustainable Chem. Eng. 2021, 9, 5155−5165**

(14) H. He, S. P. Berglund, A. J. Rettie, W. D. Chemelewski, P. Xiao, Y. Zhang and C. B Mullins, *J. Mater. Chem. A*, 2014, **2**, 9371.

(15) S. K. Cho, H. S. Park, H. C. Lee, K. M. Nam and A. J. Bard, *J. Phys. Chem. C*, 2013, **117**, 23048.

(16) X. Zhong, H. He, M. Yang, G. Ke, Z. Y. Zhao, F. Dong, B. Wang, Y. Chen, X. Shi and Y. Zhou, *J. Mater. Chem. A*, 2018, **6**, 10456.

(17) C. Liu, J. Zhou, J. Su and L. Guo, *Appl. Catal., B*, 2019, **241**, 506.

(18) R. R. Wang, L. Luo, X. L. Zhu, Y. Yan, B. Zhang, X. Xiang and J. He, *ACS Appl. Energy Mater.*, 2018, **1**, 3577.

(19) S. Wang, P. Chen, J. H. Yun, Y. Hu and L. Wang, *Angew. Chem., Int. Ed.*, 2017, **56**, 8500.

(20) Y. Lee, J. Suntivich, K. J. May, E. E. Perry and Y. Shao-Horn, *J. Phys. Chem. Lett.*, 2012, **3**, 399.

(21) K. A. Stoerzinger, L. Qiao, M. D. Biegalski and Y. Shao-Horn, *J. Phys. Chem. Lett.*, 2014, **5**, 1636.

(22) Y. Hermans, S. Murcia-L´opez, A. Klein, R. van de Krol, T. Andreu, J. R. Morante, T. Toupance and W. Jaegermann, *Phys. Chem. Chem. Phys.*, 2019, **21**, 5086.

(23) X. Long, C. Wang, S. Wei, T. Wang, J. Jin and J. Ma, *ACS Appl. Mater. Interfaces*, 2019, **12**, 2452.

(24) X. Wan, J. Su, and L. Guo, *Eur. J. Inorg. Chem.*, 2018, **22**, 2557.

(25) H. L. Tong, Y. Jiang, Q. Zhang, W. C. Jiang, K. L. Wang, X. X. Luo, Z. Lin and L. X. Xia, *ACS Sustainable Chem. Eng.*, 2019, **7**, 769.

(26) C. Xu, W. Sun, Y. Dong, C. Dong, Q. Hu, B. Ma and Y. Ding, *J. Mater. Chem. A*, 2020, **8**, 4062.

(27) T. Tian, C. Dong, X. Liang, M. Yue and Y. Ding, *J. Catal.*, 2019, **377**, 684.

(28) X. Cao, C. Xu, X. Liang, J. Ma, M. Yue and Y. Ding, *Appl. Catal., B*, 2020, **260**, 118136.

(29) A. Sivanantham, S. Hyun, M. Son and S. Shanmugam, *Electrochim. Acta*, 2019, **312**, 234.

(30) P. Chen, T. Zhou, S. Wang, N. Zhang, Y. Tong, H. Ju, W. Chu, C. Wu and Y. Xie, *Angew. Chem., Int. Ed.*, 2018, **57**, 15471.

(31) Z. Liu, H. Liu, X. Gu and L. Feng, *Chem. Eng. J.*, 2020, **397**, 125500.

(32) M. Song, Z. Zhang, Q. Li, W. Jin, Z. Wu, G. Fu and X. Liu, *J. Mater. Chem. A*, 2019, **7**, 3697.

(33) S. Bai, J. Liu, M. Cui, R. Luo, J. He and A. Chen, *Dalton Trans.*, 2018, **47**, 6763.

(34) T. Palaniselvam, L. Shi, G. Mettela, D. H. Anjum, R. Y. Li, K. P. Katuri, P. E. Saikaly and P. Wang, *Adv. Mater. Interfaces*, 2017, **4**, 1700540.

(35) Z. Sun, Z. Yu, Y. Liu, C. Shi, M. Zhu and A. Wang, *J. Colloid Interface Sci.*, 2019, **533**, 251.

(36) M. Chen, Y. Wu, Y. Han, X. Lin, J. Sun, W. Zhang and R. Cao, *ACS Appl. Mater. Interfaces*, 2015, **7**, 21852.

(37) S. Wan, J. Qi, W. Zhang, W. Wang, S. Zhang, K. Liu, H. Zheng, J. Sun, S. Wang and R. Cao, *Adv. Mater.*, 2017, **29**, 1700286.

(38) J. C. Wang, J. Ren, H. C. Yao, L. Zhang, J. S. Wang, S. Q. Zang, L. F. Han and Z. J. Li, *J. Hazard. Mater.*, 2016, **311**, 11.

(39) J. Lv, X. Yang, H.-Y. Zang, Y.-H. Wang and Y.-G. Li, *Mater. Chem. Front.*, 2018, **2**, 2045.

(40) T. Y. Ma, S. Dai, M. Jaroniec and S. Z. Qiao, *J. Am. Chem. Soc.*, 2014, **136**, 13925.

(41) Y. Peng, H.-Y. Zhou and Z.-H. Wang, *CrystEngComm*, 2012, **14**, 2812.

(42) S. Bai, H. Chu, X. Xiang, R. Luo, J. He and A. Chen, *Chem. Eng. J.*, 2018, **350**, 148.

(43) D. K. Zhong and D. R. Gamelin, *J. Am. Chem. Soc.*, 2010, **132**, 4202.

(44) A. Indra, P. W. Menezes, N. R. Sahraie, A. Bergmann, C. Das, M. Tallarida, D. Schmeisser, P. Strasser and M. Driess, *J. Am. Chem. Soc.*, 2014, **136**, 17530.

(45) X. Chang, T. Wang, P. Zhang, J. Zhang, A. Li and J. Gong, *J. Am. Chem. Soc.*, 2015, **137**, 8356.

(46) W. He, R. Wang, L. Zhang, J. Zhu, X. Xiang and F. Li, *J. Mater. Chem. A*, 2015, **3**, 17977.

(47) D. K. Zhong, S. Choi and D. R. Gamelin, *J. Am. Chem. Soc.*, 2011, **133**, 18370.

(48) F. F. Abdi, N. Firet and R. van de Krol, *ChemCatChem*, 2013, **5**, 490.

Part of this chapter has been published in **ACS Sustainable Chem. Eng. 2021, 9, 5155−5165**

CHAPTER 5

Bio-template assisted hierarchical ZnO superstructures coupled with graphene quantum dots for water oxidation kinetics

This chapter explains the synthesis of hierarchical ZnO superstructures, assembled from the ZnO nanocones using Polygalacturonic acid. Effect of different reaction conditions such as temperature, reaction time, and concentrations have been examined to understand the growth mechanism. As fabricated photoanodes with hierarchical ZnO superstructures were further modified with Graphene Quantum Dots to improve the photoelectrochemical activity. The surface functionalities of Polygalacturonic acid such as hydroxyl and carboxylic groups were accountable for the oriented assembly of the ZnO nanocones to form hierarchical ZnO superstructures due to the interaction of the ZnO polar surfaces. Also, the lower intensity ratio of (100) to (002) crystal planes suggested anisotropic growth along c-axis.

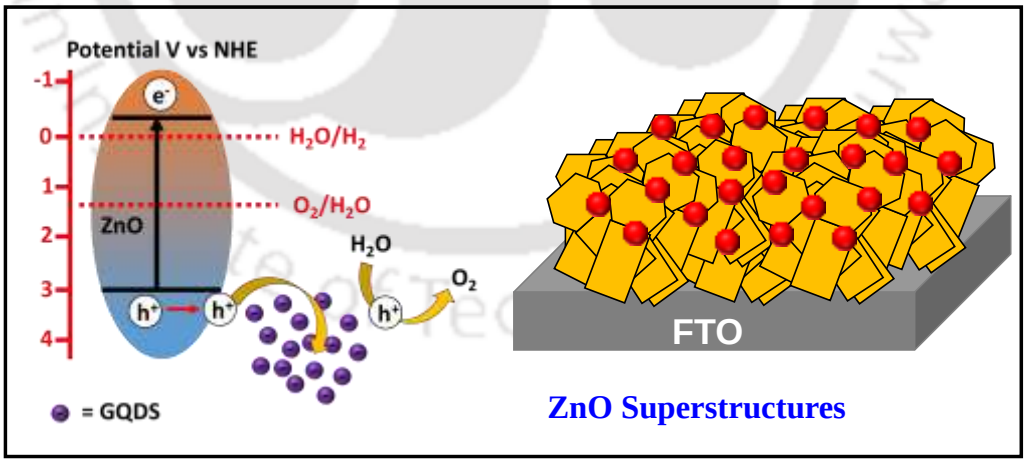

S. Alam *et al.*, **Sol. Energy**, 2020, 199, 39-46

5.1 Introduction

Splitting of water into hydrogen and oxygen is an attractive alternate to harvest solar energy for the future energy crisis. In this regard, photoelectrochemical (PEC) water splitting has received much attention to effectively couple solar irradiation with the electrochemical processes[1-2]. During the past few decades, several metal oxides such TiO_2[3], ZnO[4], WO_3[5], Fe_2O_3[6], $BiVO_4$[7], have been used as photo-electrodes for PEC water splitting. Among these n-type metal oxides, Zinc oxide (ZnO), a wide bandgap (~3.2 eV) semiconductor photoanode has attracted much attention due to its attractive optical properties, high electron mobility, low toxicity, and its anisotropic growth behavior[8]. Although ZnO has many advantages over similar n-type materials, still the PEC activity is inferior to many photoanodes due to its sluggish water oxidation kinetics. Recently, ZnO has been modified with different strategies to overcome the aforementioned drawbacks[9]. Recent developments in the synthetic strategies of inorganic semiconductors having different morphologies with controlled shape and size have gained significant interest due to their catalytic and charge transport properties[10]. The significant scientific and technological importance of nanomaterials and their synthetic procedures are still challenging, and require additional efforts for the complete utilization of their potential for application[11-12]. Different structures of ZnO such as 3D branched nanowires[13], star-like structures[14], Nano tree, and nanocluster structures[15], nanowires[16], nanorods[17], nanoplates assemble sphere like structures[18], have been utilized for PEC water oxidation. Semiconductors having hierarchical morphologies can be an effective way to enhance the PEC performance because of their improved charge transfer, surface area, and sensitizer loading capabilities apart from their strong light scattering effects and efficient electron transport[19]. Compared to the 1D nanostructure, hierarchical superstructures are more advantageous as they provide long optical pathways for efficient light absorption and multiple reflections, short channels for faster charge transport, and a large interfacial area for water redox reactions[20]. Several growth patterns based

Part of this chapter has been published in **Sol. Energy, 2020, 199, 39-46**

on their crystal growth behavior have been used to synthesize a regularly ordered structure such as template-derived homo or heteroepitaxial growth behavior[21]. Here, we have utilized a naturally occurring biomass-derived templating agent as an alternative to conventional templating agents. The use of such templating agent is not only economical but also environmentally benign under moderate conditions. Templating agent with several functionalities is accountable for the alteration of nanostructure morphologies by adsorbing at the surface of the crystal and confine the crystal growth in a specific crystal plane[22].

An essential requirement to enhance the PEC water oxidation performance is the efficient separation of photogenerated electron-hole pairs. For this, 2D materials such as reduced graphene oxide (RGO) have been widely used to assist the photogenerated electron-hole separation[23]. Notably, quantum dots due to their size-dependent electronic and optical properties have been attracting substantial attention. The recombination of photogenerated electron-hole pairs can be greatly reduced with quantum dots sensitization. Moreover, due to the large specific surface area provided by quantum dots, a number of surface-active sites will be available for efficient PEC water splitting. Quantum dots are also known to be passivating surface states by mass-assembly over the photoanode surface[24]. Despite having several physical-co-chemical properties of GQDs, reports on the rational design of semiconductor/GQDs nanocomposites are still rare[25].

5.2 Experimental Section

5.2.1 *In-situ* Growth of Hierarchical ZnO Superstructures onto Fluorine Doped Tin Oxide Substrate

Bio-template (Polygalacturonic Acid) assisted *in-situ* growth of hierarchical ZnO superstructures, directly over the FTO was carried out by the hydrothermal method. In a typical synthetic procedure, a calculated amount of Zinc Nitrate Hexahydrate (1 mmol, 297 mg) was dissolved into 25 mL of deionized water with continuous stirring for 10 min. After this 0.1 wt%

Part of this chapter has been published in **Sol. Energy, 2020, 199, 39-46**

of Polygalacturonic acid (1 mg/ml) was added to the above solution and stirred for another 15 min. This solution became more viscous after the addition of Polygalacturonic acid, due to the interaction of inorganic salt and bio template. After this 0.25 M of Hexamethylenetetramine was added to the above solution and leave the solution for 30 min. After continuous stirring, this solution became light yellow. This yellow-colored solution was then transferred into a 50 mL Teflon lined stainless steel autoclave and precleaned FTO substrates were immersed into the solution by facing down the conductive side. After this, the autoclave was sealed tightly and maintain the temperature at 140˚C for 4 hr for the growth of hierarchical ZnO superstructures. After the completion of the reaction, the autoclave was allowed to cool down at room temperature and the substrates were cleaned with plenty of water and ethanol for the complete removal of residual from the surface, and then these substrates were dried at 100˚C for 12 hr. In the last step, these substrates were annealed at 500˚C for 1 hr in an electric furnace with a heating rate of 10˚/min. In order to understand the effect of Hexamethylenetetramine additive, we have also studied the reaction in detail by varying the amount of Hexamethylenetetramine keeping the other reaction conditions same. In addition, we also studied the reaction by changing the reaction temperature as well as the reaction time to understand the growth process of hierarchical ZnO superstructures.

5.2.2 Synthesis of Graphene Quantum Dots (GQDs)

Water-soluble graphene quantum dots were synthesized by a facile hydrothermal route. A calculated amount of Citric acid (2.1 gm) dissolved in 20 mL of deionized water with continuous stirring. After the complete suspension of Citric acid, 1.8 gm of Urea was added to the above solution. This solution was then transferred into a 50 mL Teflon-lined stainless-steel autoclave and heated at 200˚C for 5 hr. After the completion of the hydrothermal reaction, this autoclave was allowed to cool down at room temperature and the obtained solution was filtered through a 0.22 μm syringe filter, to separate the larger particles. This filtered solution was then

Part of this chapter has been published in **Sol. Energy, 2020, 199, 39-46**

dialyzed through a dialysis bag (Da = 1000) and water for 24 hr. The water used in this process was changed after every 6 hr. This dialyzed solution was dried at 100˚C for 48 hr to obtain the desired graphene quantum dots.

5.2.3 Fabrication of Hierarchical ZnO Superstructures/Graphene Quantum Dots Composite Photoanodes

For the fabrication of hierarchical ZnO superstructures and Graphene Quantum Dots hybrid device, a measured amount of GQDs (1.5 mg/mL) was dissolved in deionized water under stirring overnight. This GQDs solution was then spin-coated over as-synthesized hierarchical ZnO superstructures at 3000 rpm for 30 sec, and heated at 120˚C for 10 min to complete one cycle and named as ZnO/GQDs-1. This process of GQDs spin coating was repeated and named hereafter ZnO/GQDs-2, and ZnO/GQDs-3 respectively. Finally, all the samples were heated at 150˚C for 60 min.

5.3 Results and Discussions

5.3.1 X-ray Diffraction (XRD) Analysis

To elucidate the formation and crystal phase purity of as-synthesized hierarchical ZnO superstructures, X-ray diffraction (XRD) analysis was performed. **Figure 5.3.1** represents the X-ray diffraction pattern of as-synthesized pristine and graphene quantum dots coated ZnO thin films, recorded for 2θ values of 20˚-80˚ with a scan speed of 3˚/min. From figure 5.3.1, the diffraction peaks for all samples at 2θ values of 31.82˚, 34.39˚, 36.23˚, 47.63˚, 56.63˚, 62.88˚, 66.38˚, 68.03˚, and 69.13˚ with their respective crystal planes (100), (002), (101), (102), (110), (103), (200), (112), and (201) were indexed to the hexagonal wurtzite phase with $P6_3mc$ space group symmetry according to JCPDS card no. 36-1451. Based on this observation, it was clear that all films were polycrystalline. From figure 5.3.1, it is also evident that there was no diffraction peak-related impurity has been observed. From figure 5.3.1 trace C, there was no peak of graphene quantum dots, which is due to the low content and scattering cross-section of

Part of this chapter has been published in **Sol. Energy, 2020, 199, 39-46**

graphene quantum dots as well as the high crystallinity of ZnO as compared to graphene quantum dots.

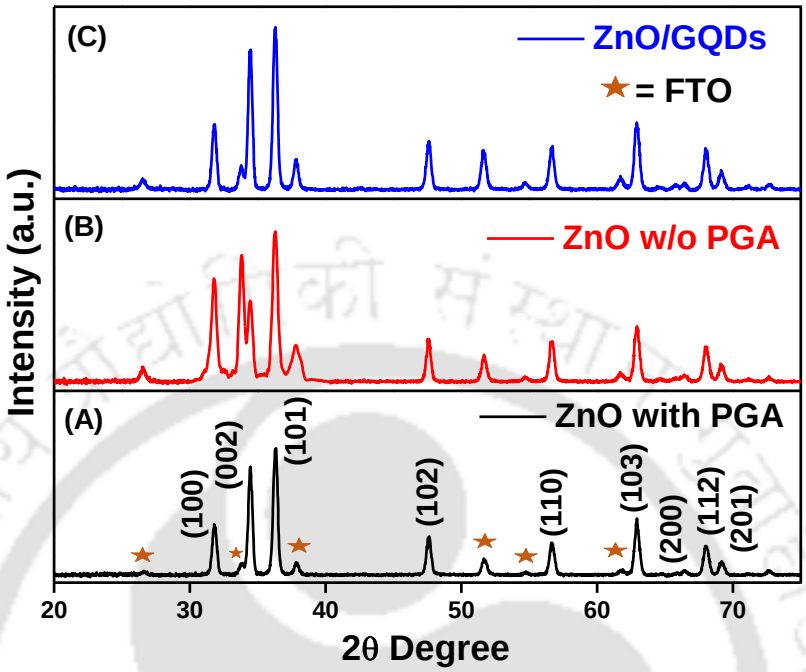

Figure 5.3.1 X-ray diffraction pattern of as-synthesized (A) Hierarchical ZnO superstructures with Polygalacturonic acid, (b) ZnO without Polygalacturonic acid, and (c) Hierarchical ZnO superstructures coated with Graphene Quantum Dots (GQDs)

It is important to mention that the intensity ratio of (100) to (002) crystal planes changed significantly, indicative of different tropism of products under different reaction conditions. Because of the anisotropic property of ZnO, nano-cones systematized themselves and attached to each other along the c-axis to minimize the surface energy. Therefore, varying the surface energy of crystal planes could be an effective way to modulate the crystal growth behavior to acquire different morphologies in ZnO. Polygalacturonic acid was used to reduce the surface energy of the crystal planes because of the electrostatic interaction between the polar surface of ZnO and the ions of Polygalacturonic acid[26]. A smaller value of intensity ratio suggested the crystal growth along the c-axis while a higher value specified the retarded growth along the c-axis[27]. From the diffraction pattern, the intensity ratios of (100) to (002) crystal planes were

Part of this chapter has been published in **Sol. Energy, 2020, 199, 39-46**

found to be 0.48 and 0.84 for ZnO superstructures (with PGA) and ZnO nano-cones (w/o PGA, only Hexamine) respectively. A smaller value of intensity ratio was achieved when hierarchical ZnO superstructures were synthesized in presence of PGA and hexamine, specified anisotropic growth along the c-axis. In contrast to this, a higher value of intensity ratio was obtained when ZnO (nano-cones) were synthesized with only hexamine, suggested retarded growth along the c-axis.

5.3.2 Fourier Transform Infrared Spectroscopy (FTIR) Analysis

The formation and presence of the different functional groups in as-synthesized graphene quantum dots were confirmed by FT-IR analysis, presented in **Figure 5.3.2**. The broad peak present at 3230-3600 cm^{-1} could be attributed to the stretching vibration of ─O─H. The peaks at 1660 cm^{-1} and 1558 cm^{-1} exhibited the vibrational stretching of ─C=O and ─N─H bending. Peaks appeared at 1390 cm^{-1} was due to the symmetric stretching of the ─COOH group while the peak at 1175 cm^{-1} was due to the ─C─O─C group. It is noteworthy to mention that the presence of hydroxyl and carboxyl groups, ensured high dispersion of GQDs in an aqueous medium[28].

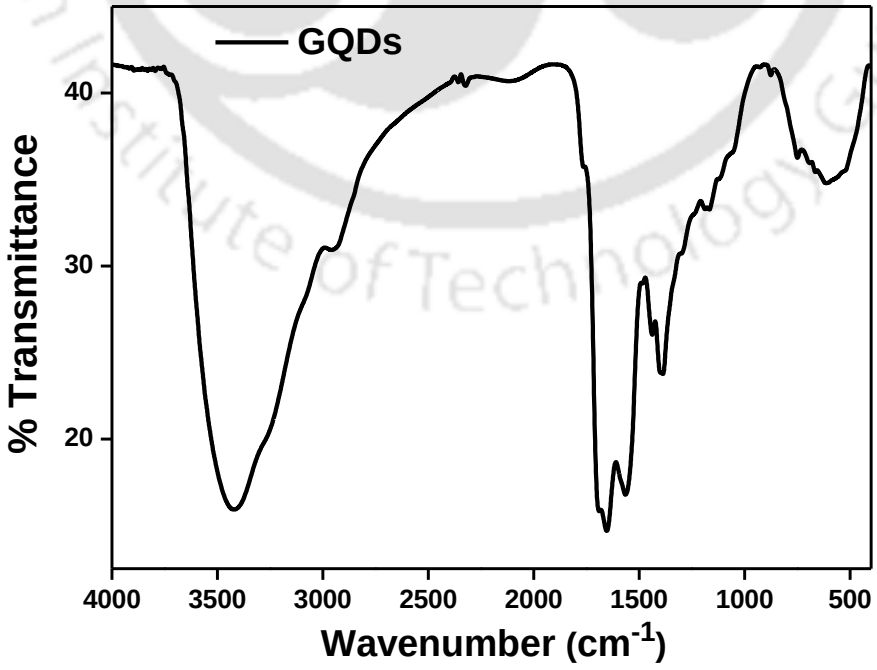

Figure 5.3.2 FT-IR spectra of as-synthesized Graphene Quantum Dots

Part of this chapter has been published in **Sol. Energy, 2020, 199, 39-46**

5.3.3 Raman Spectroscopy Analysis

Graphene quantum dots were further characterized by Raman analysis, depicted in **Figure 5.3.3.** Raman spectra of as-synthesized GQDs showed two bands: D band at 1356 cm^{-1} and G band at 1548 cm^{-1}. D band can be attributed to the bonding and anti-bonding orbitals i.e. defect-induced breathing mode of A_{1g} phonons while G band arises due to optical E_{2g} phonons at Brillouin zone center. The degree of disorder can be determined by the intensity ratio of I_D to I_G (I_D/I_G ratio), which is inversely proportional to the average size of the crystallite size domain. Average crystallite size can be determined using the following equation[29].

$$I_D/I_G = C(\lambda)/L_a \qquad (5.1)$$

Where I_D is the intensity of D band, I_G is the intensity of G band, $C(\lambda)$ is the empirical constant depends on the wavelength of the excitation laser and L_a is the crystallite size. Using above equation 5.1, the calculated average crystallite size was found to be ~4.1 nm, which is in close agreement with the size of GQDs determined by TEM analysis. Observed I_D/I_G value was greater than 1, indicative of several defects present at GQDs surface[30].

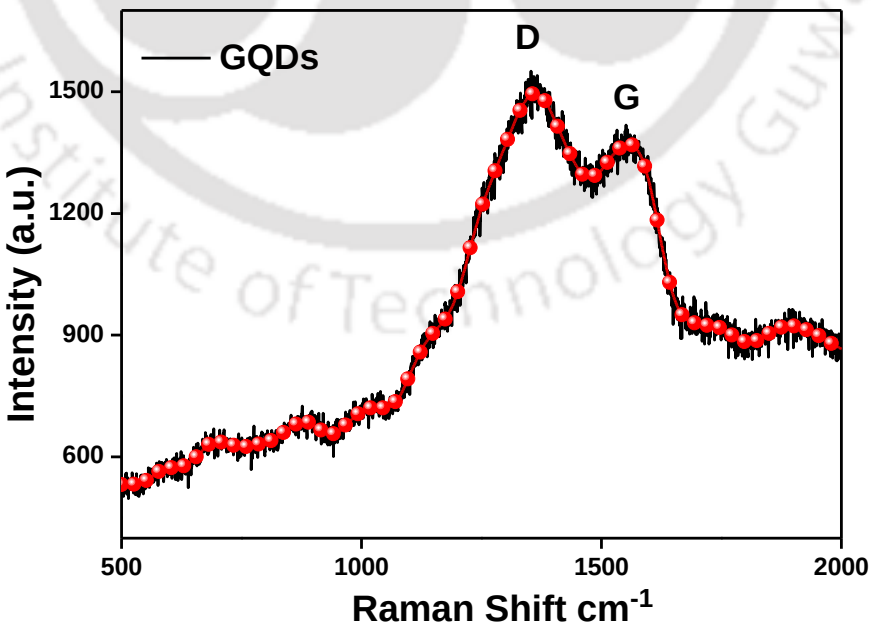

Figure 5.3.3 Raman spectra of as-synthesized Graphene Quantum Dots showing the presence of D and G bands and their ratio, indicative of defects at the surface

Part of this chapter has been published in **Sol. Energy, 2020, 199, 39-46**

5.3.4 Morphological and Structural Analysis

Morphological features of *in-situ* grown hierarchical ZnO superstructures were evaluated using field emission scanning electron microscope (FESEM) analysis as depicted in **Figure 5.3.4**. From the figure, it is clear that as grown hierarchical ZnO superstructures were uniformly distributed throughout the FTO substrate. The superiority of these structures is that they were grown directly over FTO without any seed layer and displayed robust adhesion and good Ohmic contact to the FTO substrates. The average dimension of as-grown ZnO superstructures was observed in the micron range. From figure 5.3.4 (A), it is clear that these structures were formed by connecting different nano-cones. The surface functionalities of Polygalacturonic acid such as hydroxyl and carboxylic groups were accountable for the oriented assembly of the ZnO nano-cones to form hierarchical ZnO superstructures, due to the interaction of ZnO polar surfaces. Polygalacturonic acid was used as a bio-template to govern the growth as well as an accumulating agent to construct the hierarchical ZnO superstructures. It is evident from figure 5.3.4 (A) that, these hierarchical ZnO superstructures were closely connected due to which the inter-particle connectivity was increased which helps in effective charge transfer by minimizing the surface traps for electron-hole recombination. Figure 5.3.4 (B) depicted the FESEM image of hierarchical ZnO superstructures coated with GQDs. The surface morphology of as-synthesized ZnO in the absence of Polygalacturonic acid was also analyzed, presented in figure 5.3.4 (C). In addition to the top view, cross-sectional analysis was also carried out for better understanding, depicted in figure 5.3.4 (D). A systematic approach has been used to understand the growth mechanism and evolution of hierarchical ZnO superstructures under controlled experimental conditions by changing the concentration of hexamine as well as by varying the reaction time and temperature. Morphological changes under different reaction conditions were characterized by performing FESEM analysis.

Part of this chapter has been published in **Sol. Energy, 2020, 199, 39-46**

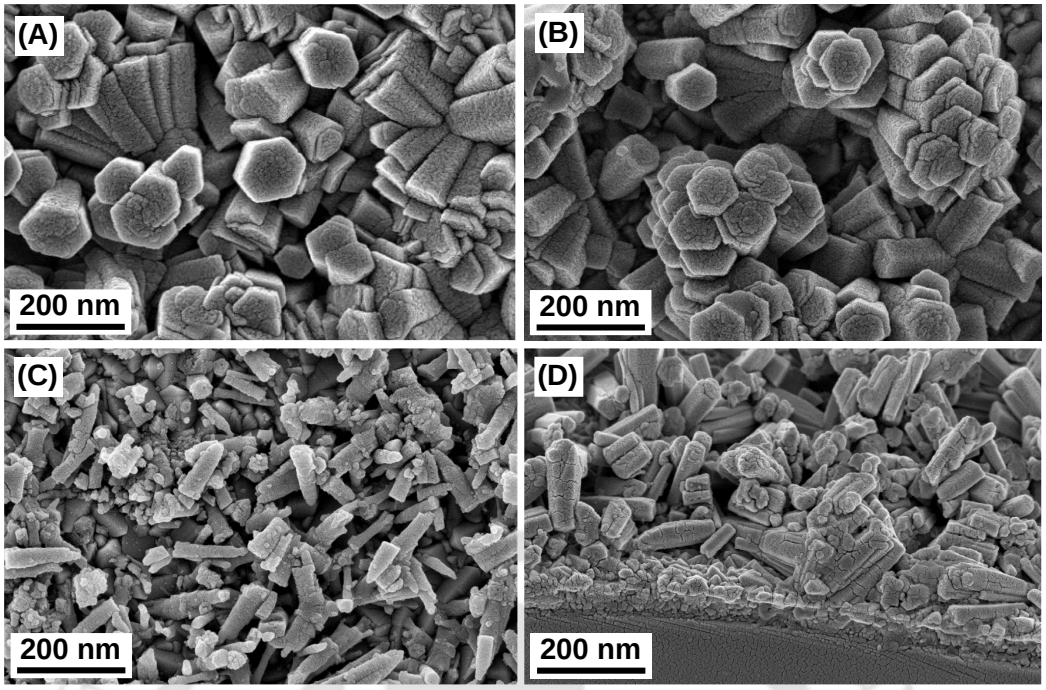

Figure 5.3.4 (A) Depicts FESEM images of as-synthesized hierarchical ZnO superstructures at 140˚C for 4 hr in the presence of Polygalacturonic acid, (B) Hierarchical ZnO superstructures coated with GQDs, (C) FESEM image of ZnO nano-cones without using Polygalacturonic acid, and (D) Cross-section images of as-synthesized hierarchical ZnO superstructures

Figure 5.3.5 (A-D) represented the FESEM images of ZnO structures grown at different concentrations of Hexamethylenetetramine i.e. 0.10 M, 0.20 M, 0.25 M, and 0.35 M. Hexamethylenetetramine concentration maintained the pH of the solution. When the concentration of Hexamethylenetetramine was fixed at 0.10 M at 140˚C for 4 hr, nucleation of the ZnO growth unit started. As we further increase the concentration of Hexamethylenetetramine from 0.10 M to 0.20 M, these growth units became larger and started taking the shape of nanocones. In addition, these growth units were distributed throughout the surface uniformly. As the concentration of Hexamethylenetetramine reached 0.25 M, ZnO structures were formed nicely by connecting these nanocones. As we further increase the Hexamethylenetetramine concentration to 0.35 M, although we get the joined nanocones but they were not aggregated to form superstructures. These nanocones were spread over the entire surface in different directions.

Part of this chapter has been published in **Sol. Energy, 2020, 199, 39-46**

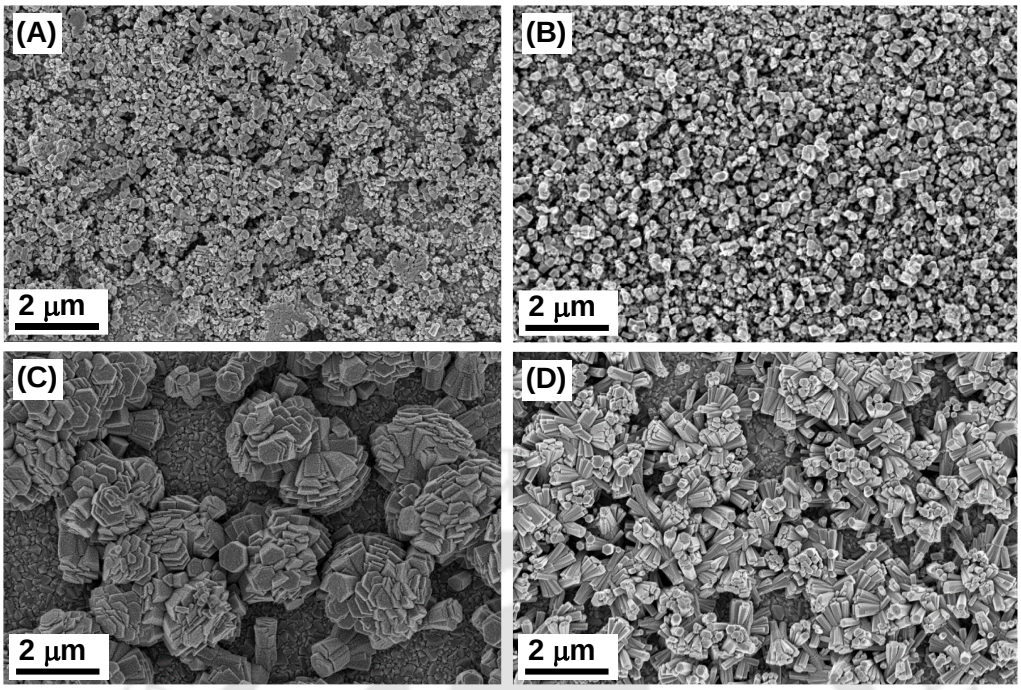

Figure 5.3.5 FESEM images of hierarchical ZnO superstructures synthesized at different Hexamethylenetetramine concentrations (A) 0.10 M, (B) 0.20 M, (C) 0.25 M, and (D) 0.35 M, at fixed temperature 140˚C for 4 hr

Figure 5.3.6 (A-D) represented the FESEM images of as-synthesized hierarchical ZnO superstructures synthesized at different time intervals i.e. 2 hr, 3 hr, 4 hr, and 6 hr at a fixed temperature of 140˚C and fixed concentration of Hexamethylenetetramine 0.25 M respectively. From the figure, it is clear that when the reaction time was 2 hr and other parameters were fixed such as Hexamethylenetetramine concentration (0.25 M) and temperature (140˚C), hierarchical ZnO superstructures were formed by connecting nanocones, but they were not uniformly distributed over the entire surface. As we increased the time up to 4 hr, these superstructures were uniformly distributed throughout the surface, which helped in faster electron transfer and reduced the electron-hole recombination. In case of 6 hr, although ZnO structures were distributed uniformly but these structures were ruptured.

Part of this chapter has been published in **Sol. Energy, 2020, 199, 39-46**

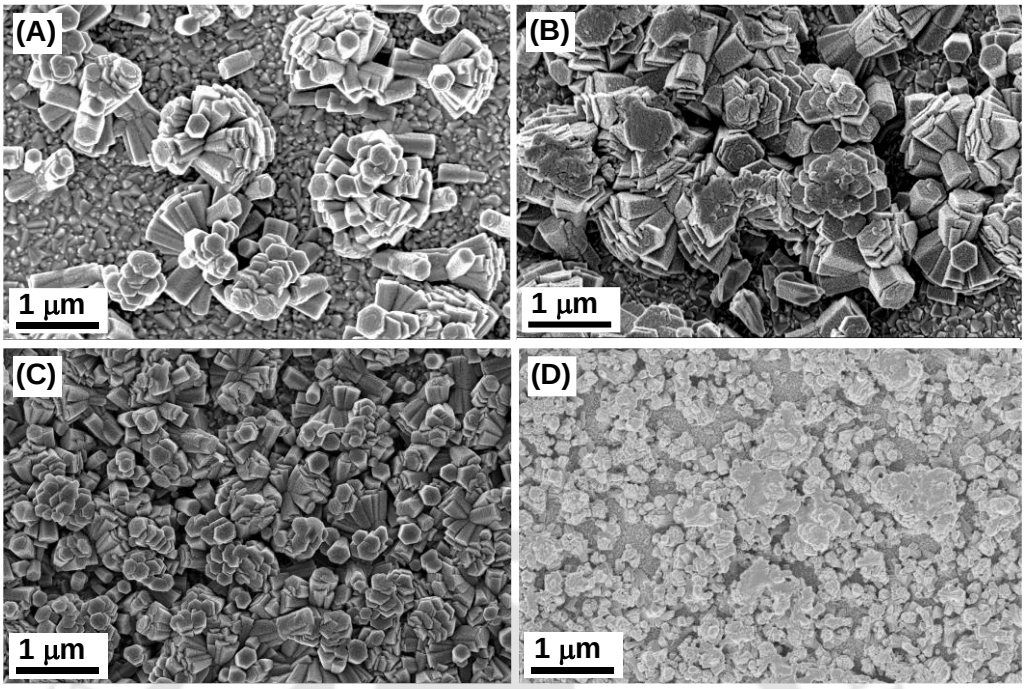

Figure 5.3.6 FESEM images of hierarchical ZnO superstructures synthesized at different time intervals of (A) 2 hr, (B) 3 hr (C) 4 hr, and (D) 6 hr, at fixed temperature 140˚C and fixed concentration of Hexamethylenetetramine 0.25 M

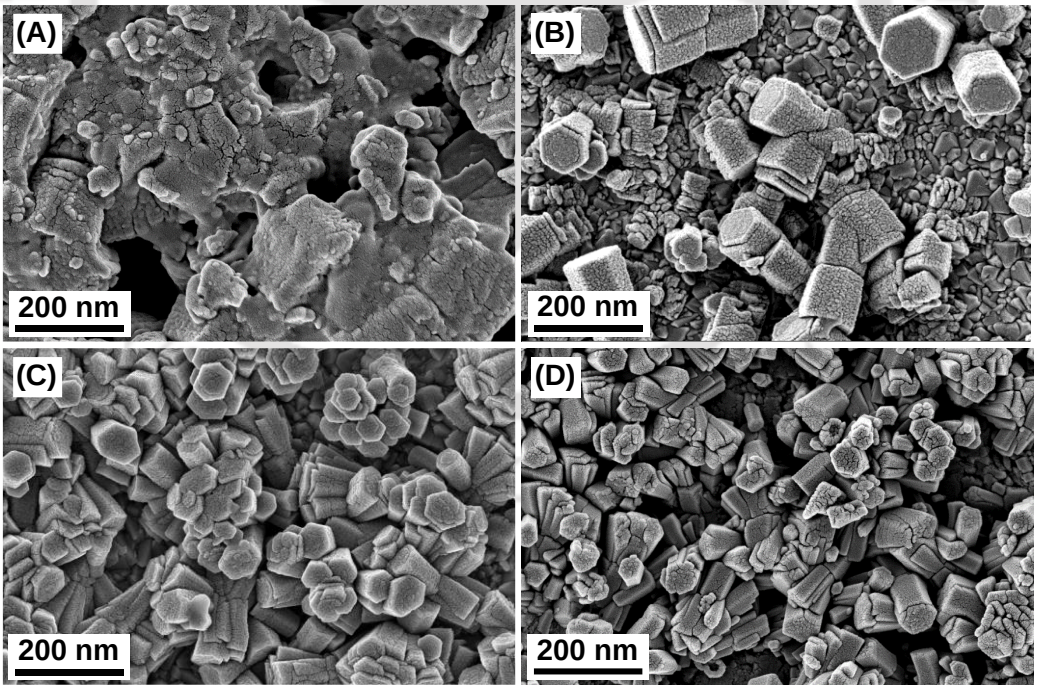

Figure 5.3.7 FESEM images of hierarchical ZnO superstructures synthesized at different temperatures (A) 100˚C, (B) 120˚C (C) 140˚C, and (D) 160˚C, at a fixed concentration of Hexamethylenetetramine 0.25 M and fixed time for 4 hr

Part of this chapter has been published in **Sol. Energy, 2020, 199, 39-46**

Figure 5.3.7 (A-D) represented the FESEM images of ZnO structures synthesized at different temperatures such as 100˚C, 120˚C, 140˚C, and 160˚C respectively while keeping other parameters constant such as (0.25 M Hexamethylenetetramine and time 4 hr). When the temperature was set to 100˚C, ruptured flake-type structures were observed. When we increased the temperature to 120˚C, ZnO nanocones started growing over the surface. As we further increase the temperature to 140˚C, these nanocones were connected to form hierarchical ZnO superstructures. When the temperature was set to 160˚C, these hierarchical ZnO superstructures break into nanocones again.

To further corroborate the structural features of as-synthesized hierarchical ZnO superstructures and modified with GQDs, transmission electron microscopy analysis was carried out, as depicted in **Figure 5.3.8**. Figure 5.3.8 (A&D) represented the TEM and HRTEM images of hierarchical ZnO superstructures. From the TEM image, it is evident that these hierarchical ZnO superstructures were constructed by joining a number of small nanocones, which is in agreement with FESEM analysis. HRTEM image showed the lattice fringes with an interplanar distance of 0.27 nm correspond to (002) crystal plane of ZnO. Figure 5.3.8 (B&E) represented the TEM and HRTEM images of as-synthesized GQDs. The average diameter of these quantum dots was found to be 4-8 nm with an inter-planar distance of 0.21 nm correspond to the (110) plane of graphite[31]. Figure 5.3.8 (C&F) represented the TEM and HRTEM images of ZnO coated with GQDs. From the figure, it is clear that the quantum dots were affixed over the ZnO surface. From HRTEM image the interplanar distance of 0.21 nm for GQDs corresponds to the (110) crystal plane while an interplanar distance of 0.27 nm for ZnO corresponds to the (002) crystal plane.

Part of this chapter has been published in **Sol. Energy, 2020, 199, 39-46**

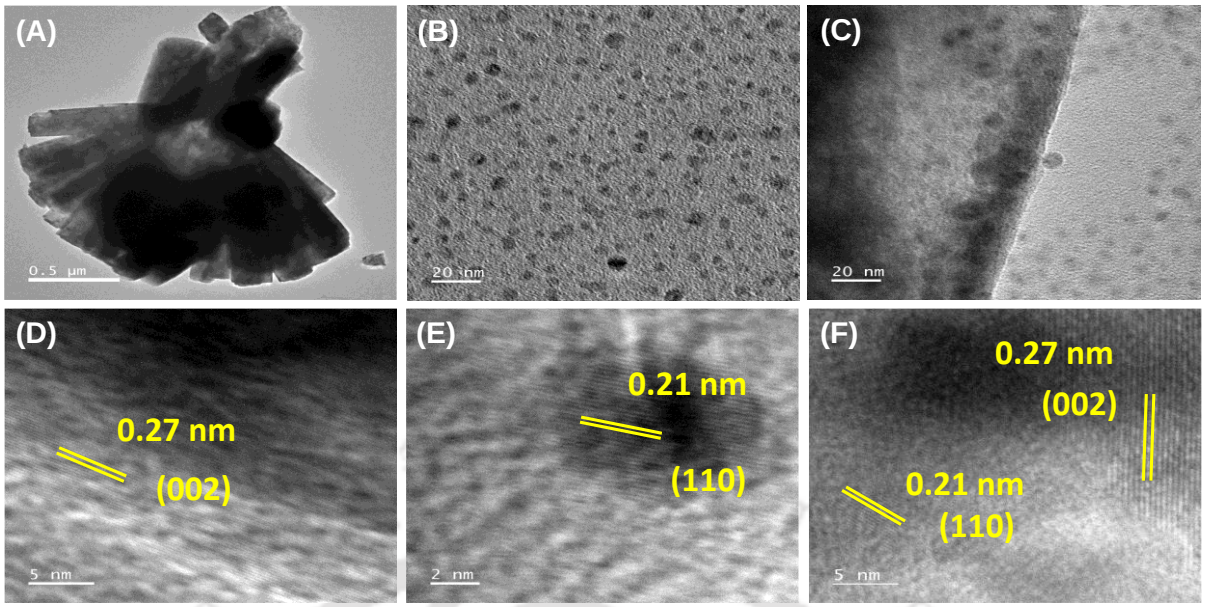

Figure 5.3.8 (A-C) TEM images of hierarchical ZnO superstructures, GQDs, and ZnO coated with GQDs respectively, and (D-F) corresponding HRTEM images

To confirm the presence of all constituent elements, TEM elemental mapping of GQDs modified hierarchical ZnO superstructures was performed, and **Figure 5.3.9** represented the same. As obtained from the figure all the elements i.e. Zn, O, C and N were uniformly distributed in the scan area.

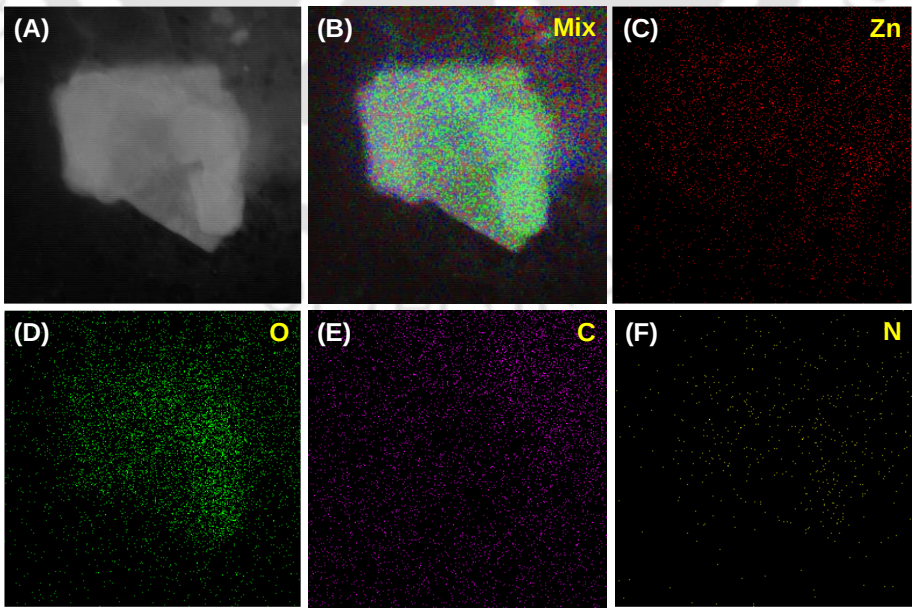

Figure 5.3.9 Elemental mapping of ZnO/GQDs photoanode showing the uniform distribution of all present elements i.e. Zn, O, C and N

Part of this chapter has been published in **Sol. Energy, 2020, 199, 39-46**

5.3.5 Growth Mechanism of Hierarchical ZnO Superstructures

On the basis of the above discussion and as per the morphological analysis, the plausible growth mechanism for the synthesis of hierarchical ZnO superstructures under controlled reaction conditions is illustrated in **Scheme 5.3.1**. In this synthetic procedure, we have used a soft bio-template "Polygalacturonic acid" as an assembling agent of basic building blocks to fabricate hierarchical ZnO superstructures. Polygalacturonic acid is a naturally occurring anionic polysaccharide, extracted from plant cell walls and the chemical structure of this homo-polymer comprises a backbone chain of 1,4-linked D-galacturonic acid units. Hierarchical ZnO superstructures were synthesized via the integration of ZnO nanocrystals by considering the assembling function of the polysaccharide. Traditionally, the growth process of the hierarchical ZnO superstructures can be controlled by two steps viz. nucleation and the crystal growth at the assembling stage. The growth mechanism for assembling small nanocones into microstructures can be described based on crystal aggregation[32]. Here Polygalacturonic acid was first dissolved in the aqueous medium and generated negatively charged ions in the solution due to the presence of hydroxyls and carboxylate groups. Therefore, there is an electrostatic interaction between the negatively charged bio-template and the inorganic ions (positively charged Zn^{2+}) to form adduct (Zn^{2+}–Polygalacturonic acid) in the reaction mixture[26]. The addition of hexamine was responsible to maintain the pH of the reaction mixture and instantaneously generated a light yellow color, probably related to $Zn(OH)_2$. $Zn(OH)_4^{2-}$ and $Zn(NH_3)_4^{2+}$ ions acted as the crystal growth seed units for the formation of ZnO building blocks[33]. Under the hydrothermal reaction, as obtained growth units were transformed into ZnO nuclei, considered as the growth units. Generally, the crystal growth units of ZnO have the tendency to grow along the c-axis by minimizing the surface energy. It is established that ZnO crystal possesses the {+0001} positive crystal surface and {−0001} negative crystal surface, attributed to the Zn^{2+} populated and O^{2-} populated high energy polar facets respectively. So,

Part of this chapter has been published in **Sol. Energy, 2020, 199, 39-46**

the crystal growth units i.e., zincate ions ($Zn(OH)_4^{2-}$) were favorably attached to the {+0001} positive surface of ZnO crystal, which encouraged the formation of ZnO nanocones along the c-axis[34]. Therefore, the growth rate of ZnO crystal is considered to be faster in {+0001} positive crystal surface as compared to {–0001} negative crystal surface, indicative of $Zn(OH)_4^{2-}$ ions are responsible major growth units for the ZnO crystal[35].

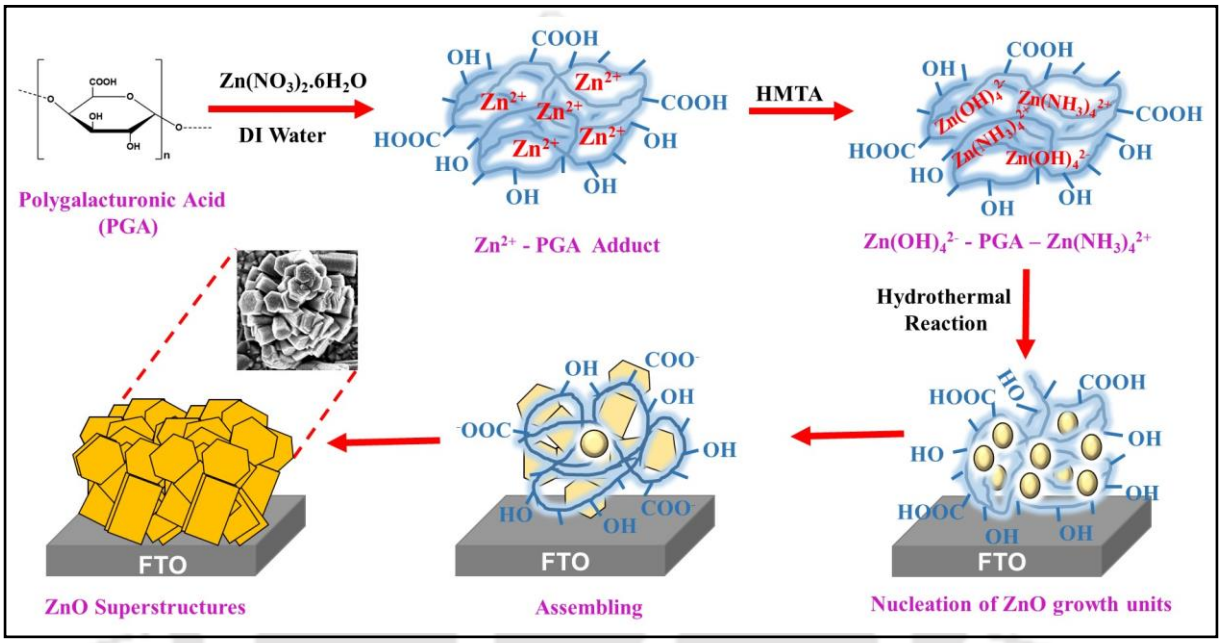

Scheme 5.3.1 Step-by-step possible growth mechanism for bio-template assisted synthesis of hierarchical ZnO superstructures

In this growth mechanism, negatively charged bio-template i.e., Polygalacturonic acid was accountable for the suppressed growth of ZnO nanocones along the c-axis, resulted in the formation of non-uniform dimensions of nanocrystals. During the synthetic procedure, Polygalacturonic acid not only acted as a soft template for the formation of ZnO nanocones but also assisted as an assembling agent to fabricate hierarchical ZnO superstructures. In the absence of a soft template, only nanocones were formed, depicted as the FESEM image in figure 5.3.4 (C). After the complete nucleation of crystal from the precursor, the negatively charged bio-template initiates the assembling of building blocks and arranges them in an array to form hierarchical ZnO superstructures. As the reaction proceeds, nanocones and connected

Part of this chapter has been published in **Sol. Energy, 2020, 199, 39-46**

cones like nanostructures were formed and appear to be attached to a single point. We assumed that the highly directional assembling of nanocones was determined by the surface carboxylate and hydroxyl groups of the bio-template. Additionally, the formation of integrated assemblies of ZnO was mainly due to the anisotropic growth behavior of ZnO crystals along {0001} direction and the dipole-dipole induced oriented attachment of building blocks, as discussed in previous literatures[36-37].

5.3.6 BET Surface Area Analysis

A key requirement to assess the PEC water oxidation is to achieve a high surface area. N_2 adsorption and desorption isotherms for as-synthesized hierarchical ZnO superstructures and coated with GQDs are represented in **Figure 5.3.10**. As obtained surface area for ZnO superstructures was ~32.0 m^2/g, while for GQDs coated ZnO its value was ~45 m^2/g.

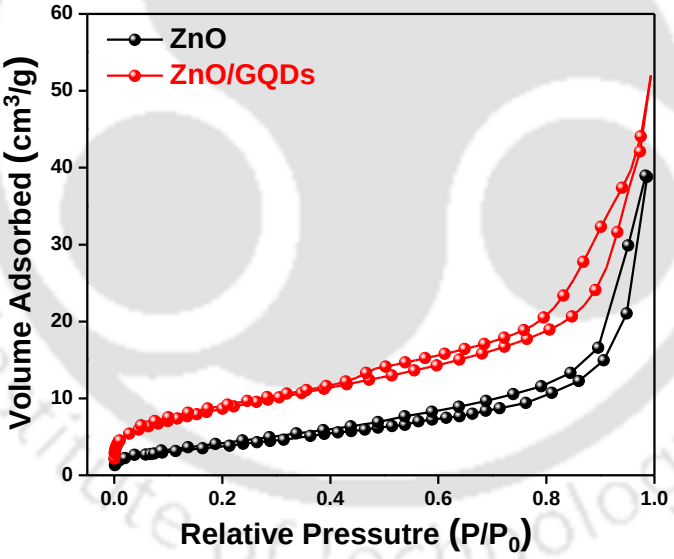

Figure 5.3.10 Nitrogen Adsorption-Desorption isotherm for as-synthesized Hierarchical ZnO superstructures as well as GQDs coated ZnO

5.3.7 Photoelectrochemical Measurements

One of the manifestations of such hierarchical superstructures having better Ohmic response and surface area is the usability for its photoelectrochemical water splitting properties. The photoelectrochemical activity of as-synthesized pristine hierarchical ZnO superstructures

Part of this chapter has been published in **Sol. Energy, 2020, 199, 39-46**

and GQDs modified photoanodes were characterized using a three-electrode system with Ag/AgCl and Pt as a reference and counter electrodes respectively, in 1 M NaOH electrolyte solution by sweeping the potential between -0.8 V to 0.6 V vs Ag/AgCl. PEC performance of ZnO/GQDs superstructures with different reaction times and different concentrations of GQDs were systematically explored to decide the optimal condition in preparing ZnO/GQDs photoanodes, as represented in **Figure 5.3.11 (A) and (B)** respectively.

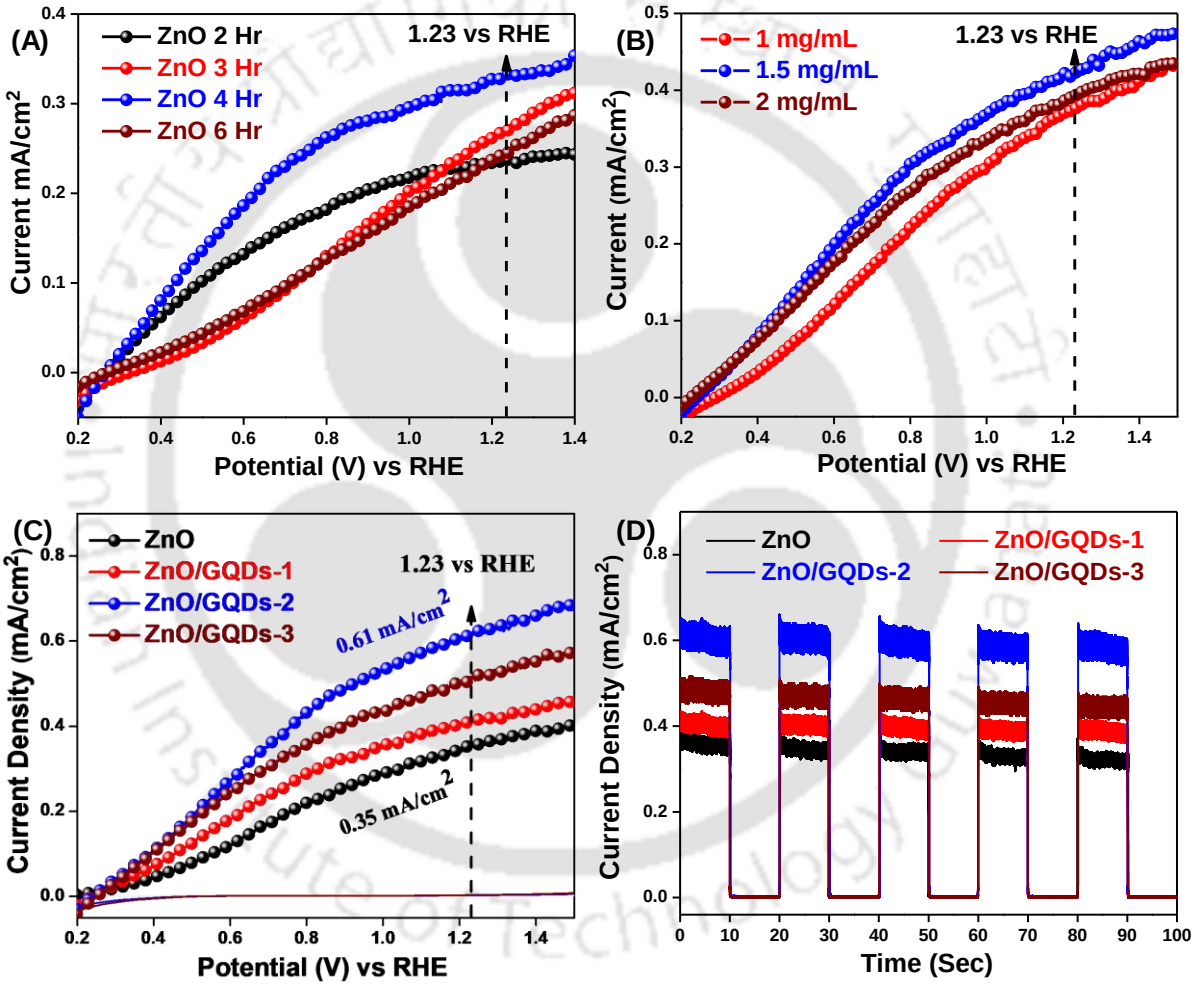

Figure 5.3.11 LSV curves for (A) ZnO superstructures synthesized at a different time i.e. 2 hr, 3 hr, 4 hr, and 6 hr, (B) Different concentrations of GQDs coated over hierarchical ZnO superstructures synthesized, (C) LSV curves at optimized conditions and (D) Corresponding Chronoamperometry curves for both

Figure 5.3.11 (C) represented the linear sweep voltammetry curves of optimized photoanodes as a function of applied bias voltage. As applied potential increases, the

Part of this chapter has been published in **Sol. Energy, 2020, 199, 39-46**

photocurrent density of all photoanodes increases, an indication of a typical n-type semiconductor behavior. Based on the result, it is clear that there was a gradual increase in the photocurrent density and a maximum of 0.61 mA/cm^2 was found in case of ZnO/GQDs-2. The photocurrent density for bare ZnO superstructures was found to be 0.35 mA/cm^2. Photoanodes fabricated with ZnO/GQDs showed higher photocurrent density as compared to pristine ZnO. After the modification with GQDs, the device showed an overall improvement of ~77 % in photocurrent density. This increase in the current density was mainly due to the reduced recombination of the photogenerated excitons, faster electron transport kinetics, and better charge extraction efficiency. The higher surface area provided by the modified ZnO structures ensured exposure to abundant sites and efficient charge transfer. In addition to the surface area, this increase in the photocurrent density was due to the remarkable hole extraction ability of GQDs attributed to the presence of negatively charged oxygen functional groups (Carboxyl and Hydroxyl groups). In case of ZnO/GQDs-3, photocurrent density decreased and was found to be 0.51 mA/cm^2. This decrease in current density can be attributed to the fact that when the ZnO surface is covered with excess quantum dots, chances of electron-hole recombination increases because of the decrease in the effective surface area participating in the oxidation process which in turn in lower photocurrent value. **Figure 5.3.11 (D)** exhibited the transient current responses of all the photoanodes under chopped light illumination in a regular interval as a function of time with a biased potential equivalent to 1.23 V vs RHE. In high accordance with LSV curves, ZnO/GQDs-2 showed the highest photocurrent density without attenuation, followed by ZnO/GQDs-3, ZnO/GQDs-1, and ZnO. In addition, under irradiation cycles, prompt and reproducible current responses were obtained for all photoanodes.

To estimate the efficacy of pristine and GQDs modified ZnO photoanode, applied bias photon-to-current efficiency (ABPE), were determined, as shown in **Figure 5.3.12 (A)**. The curves were plotted based on the current-voltage plots and obtained ABPE values of 0.09 %,

Part of this chapter has been published in **Sol. Energy, 2020, 199, 39-46**

0.13 %, 0.19 % and 0.16 % belongs to ZnO, ZnO/GQDs-1, ZnO/GQDs-2 and ZnO/GQDs-3 respectively. Photocurrent improvement was further confirmed by IPCE measurements. To evaluate the External Quantum Efficiency (EQE), which is a measure of how efficiently the device converts incident light into electrical energy at a given wavelength, IPCE spectra were recorded for devices with the wavelength ranges from 330 nm to 600 nm, displayed in **Figure 5.3.12 (B)**. In general, the EQE of a solar device is indicative of its light-harvesting efficiency, photo-excited electrons injection efficiency, and charge collection efficiency. In figure 5.3.12 (B), ZnO/GQDs-2 exhibited a higher EQE value viz. ~ 14 % as compared to pristine ZnO-based photoanode i.e., ~ 8 %. Observed large EQE value of best-performed photoanode validated the higher J_{sc} value obtained from the linear sweep voltammetry curve. Improvement in photon-to-electron conversion is mainly related to better electron injection, reduced recombination of the photo-generated excitons.

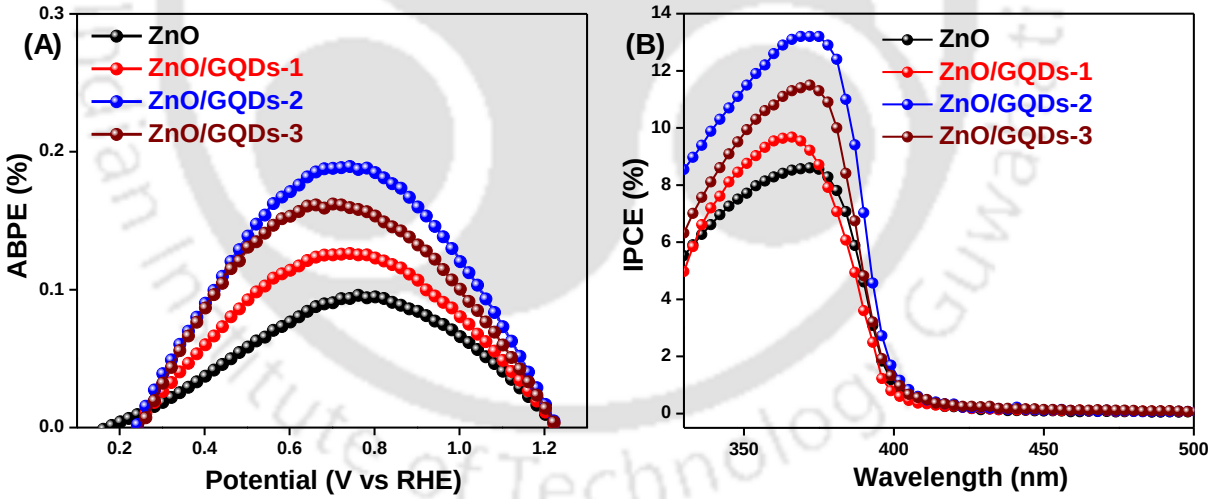

Figure 5.3.12 (A) Applied bias photon-to-current efficiency (ABPE) curves for pristine hierarchical ZnO superstructures and coated with GQDs, and (B) Displays corresponding incident photon to current conversion (IPCE) curves for the same

5.3.8 Electrochemical Impedance Spectroscopy (EIS) Analysis

Electron transport and recombination kinetics occurred at the various interfaces of as-fabricated photoelectrochemical photoanodes were analyzed using electrochemical impedance

Part of this chapter has been published in **Sol. Energy, 2020, 199, 39-46**

spectroscopy (EIS) under light irradiation in the frequency ranges of 0.1 Hz to 100000 Hz. **Figure 5.3.13 (A)** represented the Nyquist plot for the fabricated photoanodes plotted between the imaginary part versus the real part of the complex impedance. The figure comprised the semicircle for all the photoanodes at mid-frequency regions, due to charge transfer resistance (R_{CT}) at the photoanode/electrolyte interface, crucial in revealing the interfacial properties. The equivalent circuit shown in the inset of figure 5.3.13 (A) was used to fit all the impedance parameters. As obtained fitted parameters such as R_S, R_{CT}, were summarized in **Table 5.3.1**. R_S represented the Ohmic resistance between the transparent conductive oxide (TCO) and photoanode, whereas, charge transport resistance R_{CT} specified the charge transport processes across the photoanode/electrolyte interface. The device with pristine ZnO showed the highest charge transfer resistance of 31.26 KΩ, which indicated the poor charge transport properties reflected in low photocurrent value (LSV curve). The value of charge transfer resistance is found to be decreased significantly with GQDs modification. In case of ZnO/GQDs-2, the charge transfer resistance was lowest having the value of 15.55 KΩ, suggesting a better interfacial charge transport with low contact resistance. Therefore, GQDs modification can effectively enhance the charge transport from photoanode to the electrolyte by reducing the electron transfer resistance. Consequently, the recombination rate was reduced, making the PEC water oxidation more efficient.

Further verification for improved charge transfer kinetics after GQDS modification was confirmed by Mott-Schottky analysis. **Figure 5.3.13 (B)** represented the Mott-Schottky plots for pristine and GQDs modified ZnO under dark conditions in 1 M NaOH with an applied frequency of 1 kHz. The positive slope for all the photoanodes confirmed n-type behavior. Charge carrier density (N_D) and flat band potential for as-fabricated photoanodes were calculated using the following equation.

$$\frac{1}{C^2} = \frac{1}{A^2 N_D e \varepsilon \varepsilon_0} \left[E - E_{FB} - \frac{kT}{e} \right] \quad (5.2)$$

Part of this chapter has been published in **Sol. Energy, 2020, 199, 39-46**

Where C represents semiconductor capacitance, A is the surface area of photoanode, N_D denotes charge carrier density of photoanode, e is the electron charge, ε_0 represents vacuum permittivity, ε denotes dielectric constant of semiconductor, E is applied bias, E_{FB} is flat band potential, K represents Boltzmann constant, and T is the temperature. Charge carrier density values calculated from the slope of Mott-Schottky plots for ZnO, ZnO/GQDs-1, ZnO/GQDs-2 and ZnO/GQDs-3 were found to be 1.83 $\times 10^{20}$ cm^{-3}, 2.65 $\times$ 10^{20} cm^{-3}, 3.19 $\times$ 10^{20} cm^{-3} and 3.13 $\times$ 10^{20} cm^{-3} respectively. From the observations, it is clear that there was a significant improvement in the charge carrier density of GQDs modified ZnO, which is in close agreement with the photocurrent values shown in LSV curves. This increase in the carrier density was mainly attributed to the fact that with GQDs modification, the surface trap sites were decreased.

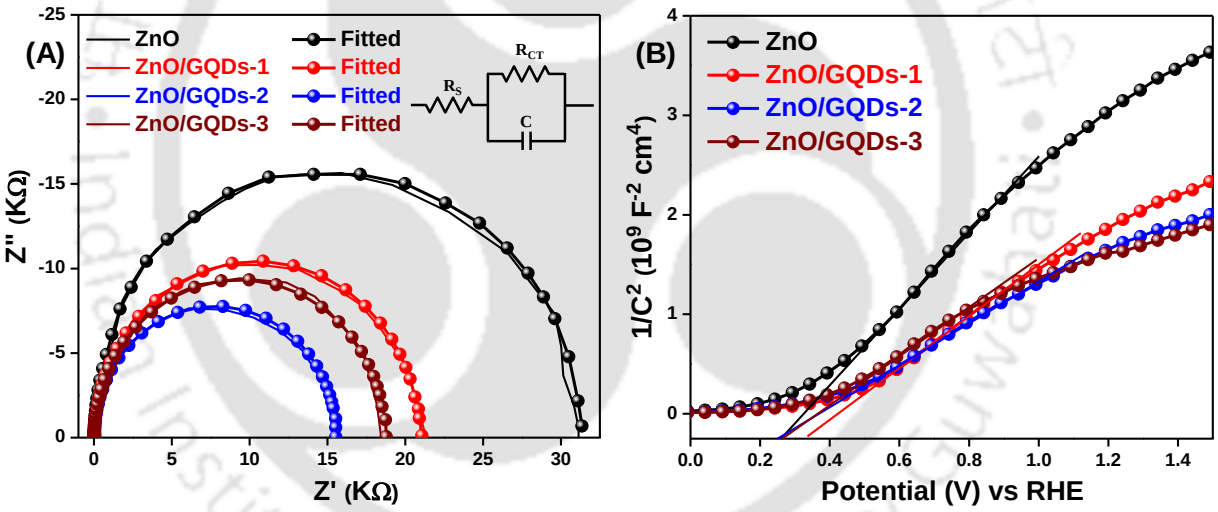

Figure 5.3.13 (A) Represents Nyquist plots of as-synthesized pristine hierarchical ZnO superstructures and modified with GQDs, under light illumination at 1.23 V vs RHE and (B) Mott-Schottky plots for bare and GQDs modified hierarchical ZnO superstructures under dark conditions

Table 5.3.1 Fitted results of Nyquist plot from the equivalent circuit

Part of this chapter has been published in **Sol. Energy, 2020, 199, 39-46**

Photoanode	Series Resistance R_S (Ω)	Charge Transfer Resistance R_{CT} (KΩ)	Carrier Density N_D (cm^{-3})
ZnO	36.43	31.26	1.83×10^{20}
ZnO/GQDs-1	17.97	20.87	2.65×10^{20}
ZnO/GQDs-2	**14.79**	**15.55**	**3.19×10^{20}**
ZnO/GQDs-3	18.06	18.69	3.13×10^{20}

5.3.9 Charge Injection Efficiency (Hole Scavenger Test)

To confirm the reduced recombination of photogenerated excitons, we have carried out the hole scavenger test in the presence of 0.20 M H_2O_2. As an efficient hole scavenger, H_2O_2 can be oxidized on photoanode with favorable kinetics, and thus, the interfacial hole-transfer kinetics on photoanode is normally negligible. **Figure 5.3.14 (A)** represented the current-voltage curves for bare and GQDs modified hierarchical ZnO superstructures with and without H_2O_2, whereas **Figure 5.3.14 (B)** represented the charge injection efficiency. From the figure, it is clear that hierarchical ZnO superstructures give lower current value in the absence of H_2O_2, mainly due to the recombination of photogenerated excitons. On the other hand, in the presence of H_2O_2, the current obtained was comparable to that of current obtained in GQDs modified hierarchical ZnO superstructures. Because of the faster kinetics of H_2O_2 oxidation reaction, reducing H_2O_2 is a more favorable process than the injection of photogenerated electrons to the conduction band of ZnO. This oxidation of H_2O_2 is responsible for the suppressed recombination of excitons and improved photocurrent value throughout the sweeping voltage to get higher PEC activity[38-39]. From figure 5.3.14 (B), charge injection efficiency for GQDs modified hierarchical ZnO superstructures was found to be ~84 %, which is higher than that of bare hierarchical ZnO superstructures (~ 60 %). This analysis further proved that GQDs are superior hole extractors that can extract a greater number of holes from the ZnO surface as compared to the hole scavenging action of H_2O_2.

Part of this chapter has been published in **Sol. Energy, 2020, 199, 39-46**

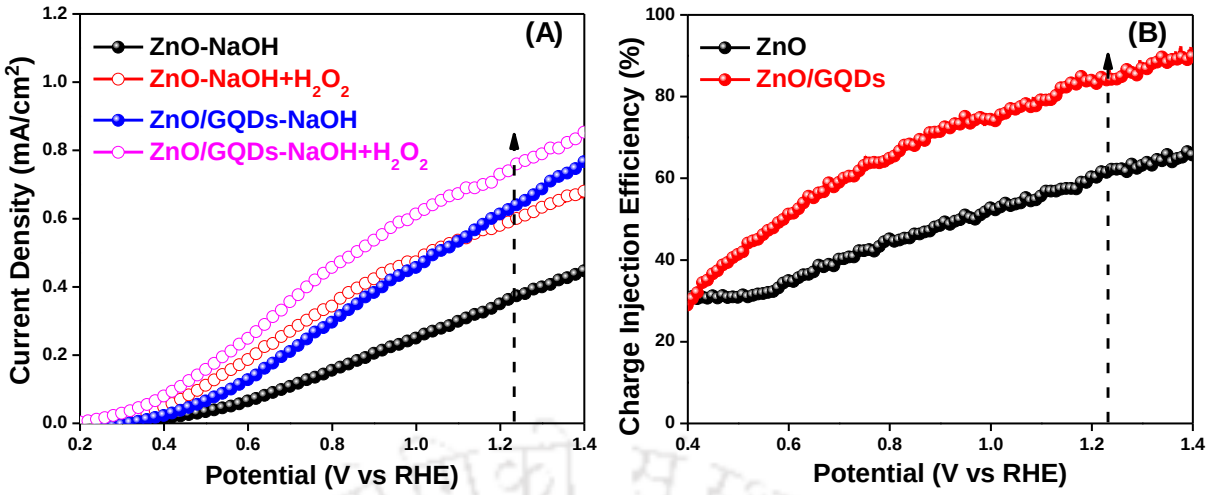

Figure 5.3.14 (A) Photocurrent density vs potential curves for bare and GQDs modified hierarchical ZnO superstructures, with and without H_2O_2 hole scavenger, (B) Represents Charge injection efficiencies for pristine ZnO and GQDs modified ZnO respectively, calculated from current density-voltage curves with and without H_2O_2 as hole scavenger

5.3.10 Faradaic Yield and Stability Measurements

The amount of oxygen evolved was measured to calculate the Faradaic yield of the photoanode, which was the confirmation that the generated photocurrent is only because of the water oxidation, illustrated in **Figure 5.3.15 (A)**. Faradaic yield measurements were carried out using online GC at a fixed potential of 1.23 V vs RHE under 1 Sun illumination in 1 M NaOH electrolyte solution for 60 min. Faradaic yield is the ratio of experimental oxygen production rate to that of the theoretically calculated oxygen production. Experimental amount of oxygen evolved and theoretical evolved oxygen were comparable and an impressive average Faradaic yield of ~83 % was found after 1 hr, indicative that the photocurrent is only because of water oxidation. In addition we have carried out the operational stability test at a fixed potential of 1.23 V vs RHE, depicted in **Figure 5.3.15 (B)**. From the figure, it is clear that after continuous illumination for 1 hr, there was a negligible chage in the current value. Therefore, from this stability test, we can say that both the photoanodes i.e. pristine ZnO and graphene quantum dots modified hierarchical ZnO superstructures were quite stable.

Part of this chapter has been published in **Sol. Energy, 2020, 199, 39-46**

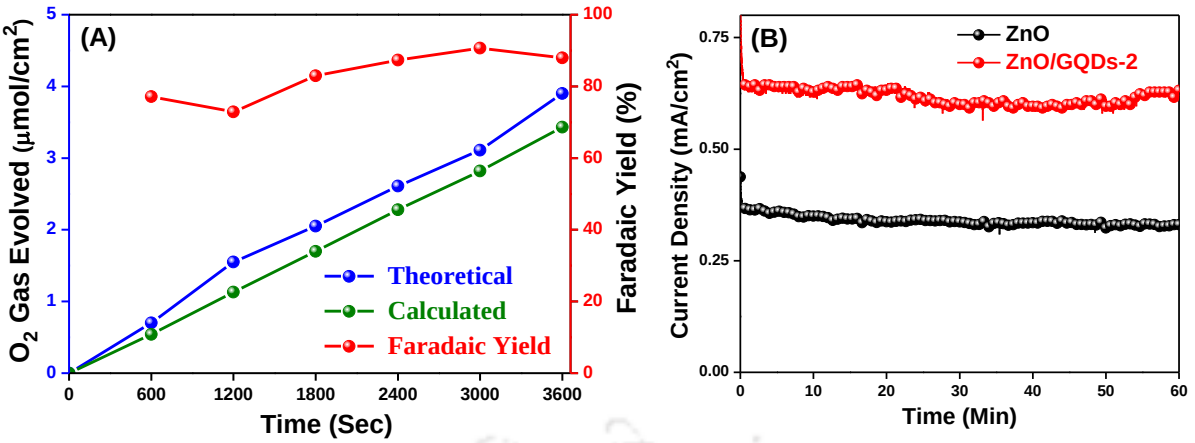

Figure 5.3.15 (A) Represents the Faradaic yield of ZnO/GQDs, the theoretical value of O_2 evolved (blue line) in μmol/cm^2, the calculated value of O_2 (Olive line) in μmol/cm^{2,} and (B) Demonstrate photoelectrochemical operational stability of ZnO and ZnO/GQDs, recorded at 1.23 V vs RHE in NaOH electrolyte under continuous illumination

5.4 Conclusions

In this work, *In-situ* growth of hierarchical ZnO superstructures directly over FTO was carried out under controlled hydrothermal conditions using a naturally abundant bio-template. We also studied the growth mechanism in detail by varying the reaction conditions such as varying the reaction temperature, time, and Hexamethylenetetramine concentration. Further modification of these hierarchical ZnO superstructures was done by coating Graphene Quantum Dots, which acts as a hole extracting agent. It was revealed that well-defined hierarchical ZnO superstructures coated with GQDs showed significant enhancement in PEC water splitting performance. After modification, there is a ~77 % increment in photocurrent response, which was due to the efficient charge separation as well as reduced electron-hole recombination. The presented approach can be extrapolated as a model system in the development of novel photoanodes for the efficient extraction of holes. This work will also be useful to design and development of different morphological structures of metal oxides directly over a conductive glass substrate by using biomass-derived templating agents.

Part of this chapter has been published in **Sol. Energy, 2020, 199, 39-46**

5.5 References

(1) H. Ma, W. Ma, J.-F. Chen, X.-Y. Liu, Y.-Y. Peng, Z.-Y. Yang, H. Tian, and Y.-T. Long, *J. Am. Chem. Soc.*, 2018, **140**, 5272.

(2) Y. Li, L. Zhang, A. Torres-Pardo, J. M. Gonzalez-Calbet, Y. Ma, P. Oleynikov, O. Terasaki, S. Asahina, M. Shima, D. Cha, L. Zhao, K. Takanabe, J. Kubota and K. Domen, *Nat. Commun.*, 2013, **4**, 2566.

(3) X. Zhang, Y. Liu, S.-T. Lee, S. Yang and Z. Kang, *Energy Environ. Sci.*, 2014, **7**, 1409.

(4) H. Zhang, W. Tian, Y. Li, H. Sun, M. O. Tade and S. Wang, *J. Mater. Chem. A*, 2018, **6**, 24149.

(5) S. S. Tang, M. Courte, J. J. Peng and D. Fichou, *Chem. Commun.*, 2019, **55**, 7958.

(6) M. Marelli, A. Naldoni, A. Minguzzi, M. Allieta, T. Virgili, G. Scavia, S. Recchia, R. Psaro and V. Dal Santo, *ACS Appl. Mater. Interfaces*, 2014, **6**, 11997.

(7) F. S. Hegner, I. Herraiz-Cardona, D. Cardenas-Morcoso, N. Lopez, J. R. Galan-Mascaros and S. Gimenez, *ACS Appl. Mater. Interfaces*, 2017, **9**, 37671.

(8) F. Zhan, Y. Yang, W. Liu, K. Wang, W. Li and J. Li, *ACS Sustainable Chem. Eng.*, 2018, **6**, 7789.

(9) H. N. Chen, Z. H. Wei, K. Y. Yan, Y. Bai, Z. L. Zhu, T. Zhang and S. H. Yang, *Small*, 2014, **10**, 4760.

(10) Z. Dong, X. Lai, J. E. Halpert, N. Yang, L. Yi, J. Zhai, D. Wang, Z. Tang and L. Jiang, *Adv. Mater.*, 2012, **24**, 1046.

(11) W. Shi, S. Song and H. Zhang, *Chem. Soc. Rev.*, 2013, **42**, 5714.

(12) Y.-G. Guo, J.-S. Hu and L.-J. Wan, *Adv. Mater.*, 2008, **20**, 2878.

(13) A. Kargar, K. Sun, Y. Jing, C. Choi, H. Jeong, G. Y. Jung, S. Jin and D. Wang, *ACS Nano*, 2013, **7**, 9407.

(14) A. R. Marlinda, N. Yusoff, A. Pandikumar, N. M. Huang, O, Akbarzadeh, S. Sagadevan, Y. A. Wahab, and M. R. Johan, *Int. J. Hydrogen Energy*, 2019, **44**, 17535.

(15) X. Ren, A. Sangle, S. Zhang, S. Yuan, Y. Zhao, L. Shi, R. L. Z. Hoye, S. Cho, D. Li and J. L. MacManus-Driscoll, *J. Mater. Chem. A*, 2016, **4**, 10203.

(16) M. Li, K. Chang, T. Wang, L. Q. Liu, H. B. Zhang, P. Li and J. H. Ye, *J. Mater. Chem. A*, 2015, **3**, 13731.

(17) M. Wang, F. Ren, J. Zhou, G. Cai, L. Cai, Y. Hu, D. Wang, Y. Liu, L. Guo and S. Shen, *Sci Rep*, 2015, **5**, 12925.

Part of this chapter has been published in **Sol. Energy, 2020, 199, 39-46**

(18) E. Emil, G. Alkan, S. Gurmen, R. Rudolf, D. Jenko and B. Friedrich, *Metals*, 2018, **8** 569.

(19) N. Memarian, I. Concina, A. Braga, S. M. Rozati, A. Vomiero and G. Sberveglieri, *Angew. Chem., Int. Ed.*, 2011, **50**, 12321.

(20) Z. Li, S. Feng, S. Liu, X. Li, L. Wang and W. Lu, *Nanoscale*, 2015, **7**, 19178.

(21) S. Xu, Y. Ding, Y. Wei, H. Fang, Y. Shen, A. Sood, D. Polla and Z. Wang, *J. Am. Chem. Soc.*, 2009, **131**, 6670.

(22) T. R. Chetia, M. S. Ansari and M. Qureshi, *ACS Appl. Mater. Interfaces*, 2015, **7**, 13266.

(23) L. Sun, Y. Wang, F. Raziq, Y. Qu, L. Bai and L. Jing, *Sci Rep*, 2017, **7**, 1303.

(24) J. Xie, J. Chen and C. M. Li, *Int. J. Hydrogen Energy*, 2017, **42**, 7158.

(25) D. Ghosh, S. Kapri and S. Bhattacharyya, *ACS Appl. Mater. Interfaces*, 2016, **8**, 35496.

(26) X. Sun, J. Liu and Y. Li, *Chem. Eur. J.*, 2006, **12**, 2039.

(27) M. Huang, Y. Yan, W. Feng, S. Weng, Z. Zheng, X. Fu and P. Liu, *Cryst. Growth Des.*, 2014, **14**, 2179.

(28) H. B. Yang, Y. Q. Dong, X. Wang, S. Y. Khoo and B. Liu, *ACS Appl. Mater. Interfaces*, 2014, **6**, 1092.

(29) T. Gokus, R. R. Nair, A. Bonetti, M. Bohmler, A. Lombardo, K. S. Novoselov, A. K. Geim, A. C. Ferrar and A. Hartschuh, *ACS Nano*, 2009, **3**, 3963.

(30) S. Ahirwar, S. Mallick and D. Bahadur, *ACS Omega*, 2017, **2**, 8343.

(31) M. M. Fan, C. L. Zhu, J. Z. Yang and D. P. Sun, *Electrochim. Acta*, 2016, **216**, 102.

(32) M. Mo, J. C. Yu, L. Zhang and S.-K. A. Li, *Adv. Mater.*, 2005, **17**, 756.

(33) Z. Wang, X. Qian, J. Yin and Z. Zhu, *J. Solid State Chem.*, 2004, **177**, 2144.

(34) X. M. Sun, X. Chen, Z. X. Deng and Y. D. Li, *Mater. Chem. Phys.*, 2003, **78**, 99.

(35) K. Govender, D. S. Boyle, P. B. Kenway and P. O'Brien, *J. Mater. Chem.*, 2004, **14**, 2575.

(36) K. Barick, M. Aslam, V. P. Dravid and D. Bahadur, *J. Phys. Chem. C*, 2008, **112**, 15163.

(37) A. Gasparotto, D. Barreca, Ch. Maccato and E. Tondello, *Nanoscale*, 2012, **4**, 2813.

(38) H. Zhu, S. C. Yan, Z. S. Li and Z. G. Zou, *ACS Appl. Mater. Interfaces*, 2017, **9**, 33887.

(39) A. Sreedhar, I. N. Reddy, Q. T. H. Ta, E. Cho and J.-S. Noh, *Sol. Energy*, 2019, **191**, 151.

CHAPTER 6

Ultrasensitive NO_X detection in simulated exhaled air: Sensing via alumina modification of *in-situ* grown WO_3 nanoblocks

This chapter elucidates the hydrothermal synthesis of WO_3 nanoblocks directly over conductive substrates for selective detection of NO_X. These structures exhibited robust adhesion and good Ohmic contact with conductive substrate owing to their vertical alignment to the surface. Without disturbing the morphology of WO_3 nanostructures, a porous layer of alumina was deposited by anodization, to further facilitate electron transfer by minimizing the surface defect states. Sensing properties were evaluated by fabricating a two-terminal Chemiresistor device based on bare and alumina modified WO_3. Both devices show selectivity towards NO_X.

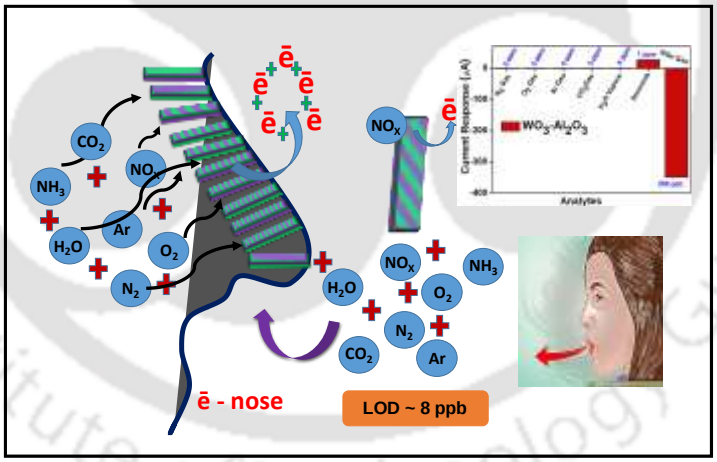

S. Alam *et al.*, **Chem. Asian J.** 2019, 14, 4673–4680

6.1 Introduction

Designing a non-invasive diagnostic tool for the analysis of exhaled breath represents an opportunity for a faster, economical, and simple substitute to tedious pathological screens[1]. Exhaled breath consists of, carbon dioxide, oxygen, nitrogen, nitric oxide, and ammonia along with a number of volatile organic compounds (VOCs). Notably, endogenous molecules that are formed as part of metabolic processes inside the living organisms have clinical significance for the identification of anomalous biochemical processes. Notably, precise detection of VOCs or certain gases in exhaled breath can be correlated to specific disease states[2-7]. For example, abnormal concentrations of hydrogen sulfide, ammonia, acetone, nitric oxide, and toluene are associated with halitosis[8], renal failure[9], diabetes[10], asthma[11,] and lung cancer[12] respectively. Asthma, which is related to the respiratory inflammation of the airways, is a common ailment, where enhanced nitric oxide concentration is observed in exhaled breath. It is primarily produced through enzymatic oxidation of L-arginine to L-citrulline, by constitutively expressed nitric oxide synthases. Out of the three isoforms of this protein, only inducible NO synthase concentration increases to higher levels in asthmatic patients due to induction by IL-13 cytokine in the airways[13-14]. The exhaled NO level in healthy humans is around 20 ppb in children and up to 25 ppb in adults, while its concentration is more than 35 ppb in children and 50 ppb for adults suffering from asthma[15-16]. Despite the knowledge that higher levels of exhaled NO suggest airway inflammation and asthmatic conditions, precise detection of NO is marred due to the presence of other VOCs and interfering gases, thereby complicating breath analysis in asthmatic patients. Thus, there is an impetus to invent newer non-invasive strategies for selective and sensitive NO detection. Numerous techniques are reported to analyze exhaled breath such as mass chromatography, selected ion flow tube mass spectrometry, gas chromatography, and ion mobility spectrometry[17]. However, incorporation of these techniques in a real-time gas sensor is difficult because of the large size of the equipment, operational

Part of this Chapter has been published in **Chem. Asian J., 2019, 14, 4673-4680**

issues, complex and invasive sample collection procedures, and high cost. Therefore, semiconductor metal oxide-based Chemiresistor sensors have been developed for biomedical applications[18-21]. In such devices, gas-solid interactions on the surface of the active sensing area cause a measurable change in resistivity, which gets recorded. However, many semiconductor metal-oxide-based sensors work at elevated temperatures (>400˚C)[22], therefore selective detection of target gases in Chemiresistor devices is a challenging proposition requiring further experimental breakthrough and development. Needless to mention, a metal oxide-based sensor, operating at ambient temperature, with excellent response and recovery properties, is highly desirable. Response of a semiconductor-based sensor is controlled by grain size, changing the surface morphology, or generating mesoporosity, or by the deliberate addition of dopants or impurities[23]. Tungsten Oxide (WO_3), with a bandgap ~2.7 eV, is a multifunctional oxide widely used in gas sensing because of its chemical stability and reasonable electrical conductivity. Subsequent to the exposure of oxidizing gases on WO_3 nanostructures, electrons are extracted from the WO_3 surface resulting in a change of resistivity due to the charge transfer from WO_3 to the gaseous analyte[24]. Such systems are proposed for the detection of gases, using morphologies such as nanoplates, nanowire, and nanorods, for improved gas sensing behavior[25-32]. For example, Kim et al. analyzed acetone concentration using catalyst-loaded WO_3 nanofibers[33], while Koo et al. used Pt/Pd decorated hollow WO_3 nanotubes, on Poly(methyl methacrylate), nanofiber templates for detection of gases[34]. Herein, we describe the *in-situ* growth of monoclinic nanoblocks of WO_3, directly deposited over fluorine-doped tin oxide (FTO) layer for enhancing total surface area suitable for analyte interaction and charge collection by minimizing Ohmic resistance at the interface (**Scheme 6.2.1**). WO_3 nanostructures were further modified by Al_2O_3 deposition, via an anodization process, to minimize surface defects and to provide higher surface area and porosity for gas molecules to adsorb onto the WO_3 surface.

Part of this Chapter has been published in **Chem. Asian J., 2019, 14, 4673-4680**

6.2 Experimental Section

6.2.1 *In-situ* Growth of WO_3 Structures onto Transparent Conducting Oxide

Transparent conductive oxide substrates were first etched with conc. HCl and zinc dust to make active sensing area, which later acts as the active materials for sensing experiments. After etching, these transparent conductive oxide substrates were thoroughly washed with detergent, distilled water, acetone, and isopropanol to confirm that there is no impurity available on substrates. Therefore, the corrosion-causing HCl was completely removed from the system. *In situ* growth of WO_3 structures over the FTO was carried out by the hydrothermal method. First, a calculated amount of Ammonium Metatungstate Hydrate (3.56 mM) was dissolved in 100 mL of deionized water under vigorous stirring until the solution became transparent. After this 3 mL (0.35 M) concentrate HCl (wt. 36 %) was added dropwise into the above solution and allow to stir for 15 min. After this 2 mL of H_2O_2 was added into this solution and leave the solution under stirring for 1 hr. This transparent solution was then transferred into the autoclave and precleaned ozonized FTO were put into the autoclave and heat it at 160˚C for 4 hr. The autoclave was allowed to cool down at room temperature and the substrates were washed with distilled water to remove the residuals and heat at 100˚C for 1 hr. These substrates were then annealed at 500˚C for 2 hr in the furnace with a heating rate of 10˚C/min.

6.2.2 Electrochemical Deposition of Porous γ-Al_2O_3 onto the WO_3 Photoanode by Anodization

In order to deposit the Al_2O_3 layer over hydrothermally grown WO_3 structures, these substrates were moved into the thermal evaporator and a 40 nm of Al layer was deposited under the vacuum (5 x 10^{-6} mbar). After the deposition of Al these films were electrochemically oxidized into Al_2O_3 by applying a constant current of 30 μA and a voltage of 25 V. In this process, 0.3 M Oxalic acid was used as the electrolyte solution, and Pt mesh was used as the

Part of this Chapter has been published in **Chem. Asian J., 2019, 14, 4673-4680**

counter electrode. These films were then rinsed with hot water and dried at 100˚C on a hot plate for 15 min.

6.2.3 Fabrication of Chemiresistive Device

For the fabrication of a two-terminal Chemiresistor device, first, the Fluorine doped tin oxide substrates were etched with the help of HCl (Conc.) and Zn dust in order to make the active area for the sensing device. **Scheme 6.2.1** represents the schematic of the step-by-step fabrication of the device. After the patterning of the FTO, the *in-situ* growth of the WO_3 structure was grown by hydrothermal method followed by the anodization process as discussed above. After the hydrothermal reaction and anodization process, the device is ready for characterization.

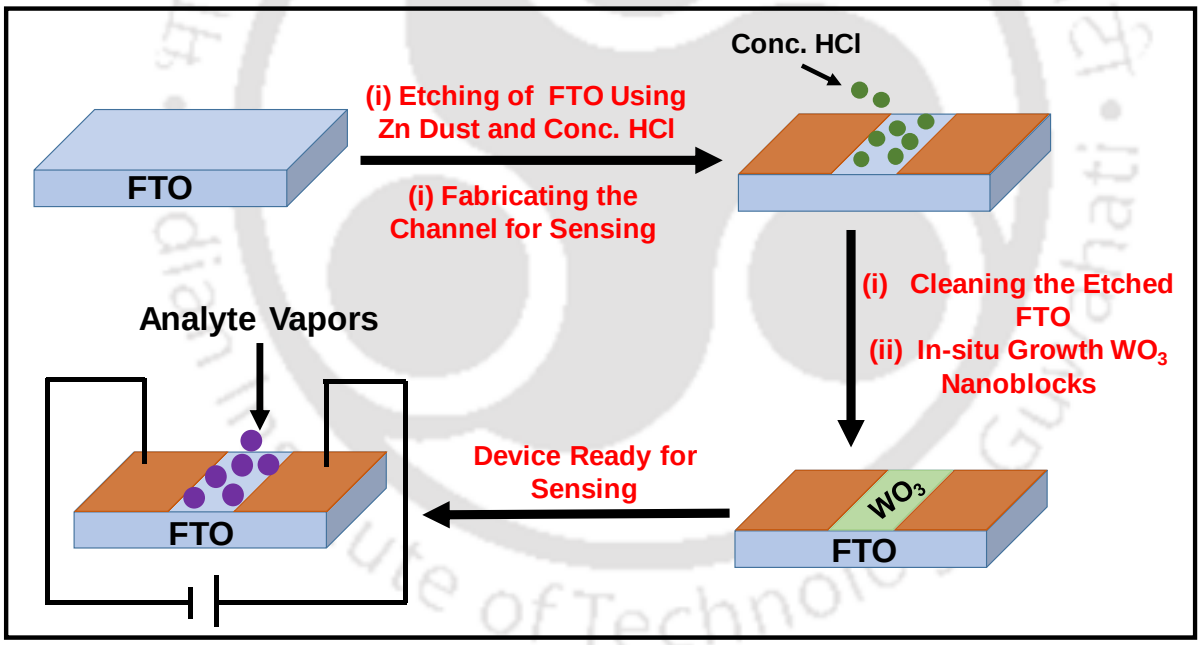

Scheme 6.2.1 Step-by-step fabrication process of a two-terminal Chemiresistor device for gas sensing

6.3 Results and Discussions

6.3.1 X-ray Diffraction Analysis

Formation and the crystal phase purity of as-synthesized WO_3 and Al_2O_3 modified WO_3 devices were characterized by X-ray diffraction analysis and **Figure 6.3.1** shows the diffraction

Part of this Chapter has been published in **Chem. Asian J., 2019, 14, 4673-4680**

pattern of the same. The sharp and intensive peaks indicate a highly crystalline nanostructure with crystal planes (002), (020), (200), (120), (112), (020), (202), (122), (222), (320), (123), (004), (232), (114), (411), (025) and (420) are perfectly indexed to the monoclinic phase of WO_3 (JCPDS no. 43-1035). From the figure, it is clear that there is no peak related to any type of impurity, which indicates that the as-synthesized WO_3 is pure. It can be seen from trace B that coating of alumina overlayer has resulted in a decreased peak intensity of WO_3 device, which is due to the masking of Al_2O_3. From figure 6.3.1 trace B, we can see some signature peaks for porous γ–Al_2O_3 (JCPDS no. 10-0425) at $2\theta \sim 37.6$ and 39. Other peaks remained silent, which is maybe due to the lower X-ray scattering by thin alumina over-layer.

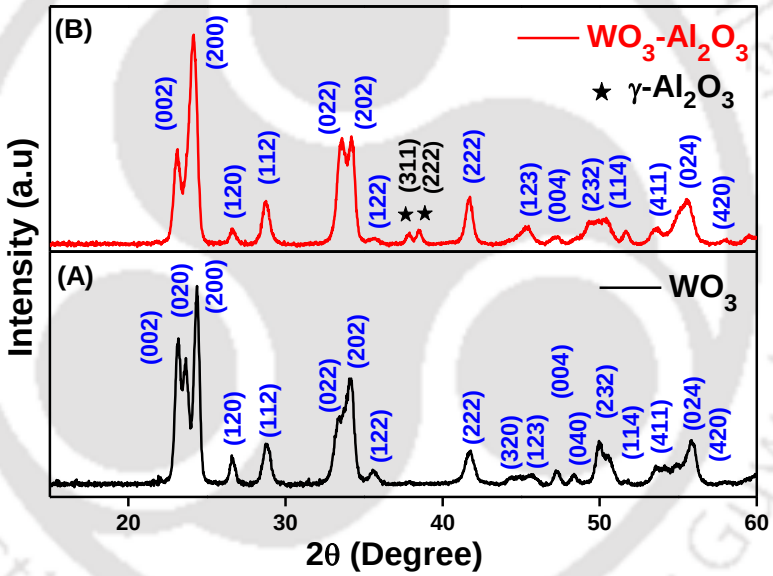

Figure 6.3.1 X-ray diffraction patterns of as-synthesized (A) Bare WO_3 nanostructures and (B) WO_3 modified with Al_2O_3 respectively

6.3.2 Morphological and Structural Analysis

Morphological features of bare WO_3 nanostructures and those having an *in-situ* deposited Al_2O_3 layer were characterized by field emission scanning electron microscopy (FESEM) **(Figure 6.3.2)**, which confirm that WO_3 structures are uniformly grown over FTO substrate. Notably, these structures are grown directly over FTO substrates, without a seed layer, in contrast to earlier reports that allude to an uneven growth over FTO[35]. These structures

Part of this Chapter has been published in **Chem. Asian J., 2019, 14, 4673-4680**

exhibit robust adhesion and good Ohmic contact with FTO owing to vertical alignment to the surface. Without disturbing the morphology of WO_3 nanostructures, a porous layer of alumina is deposited by anodization, to further facilitate electron transfer by minimizing the surface defect states.

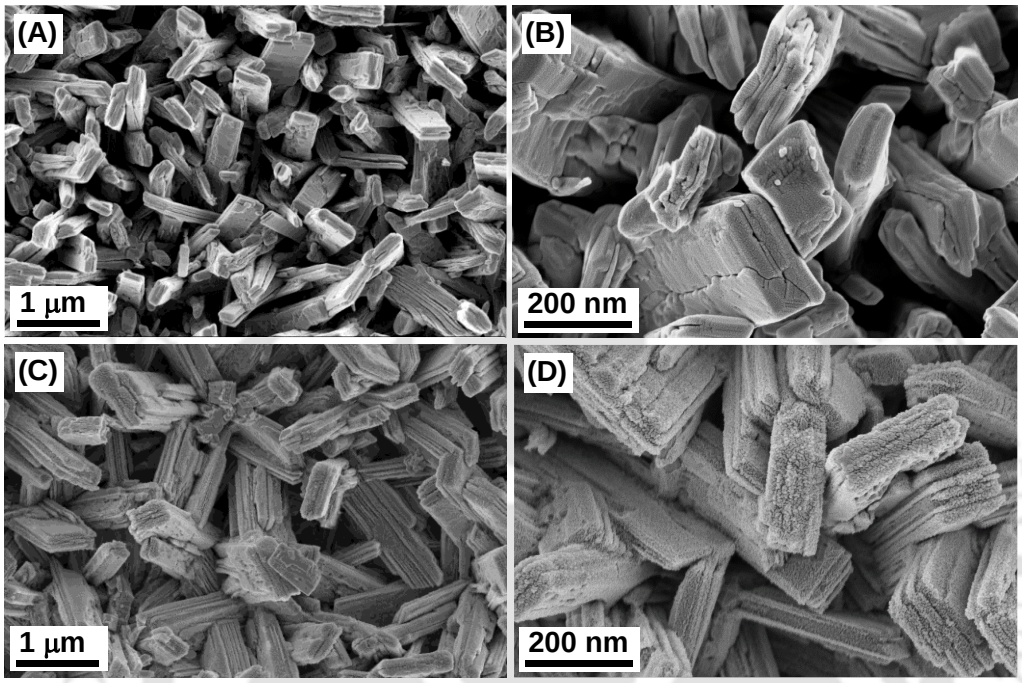

Figure 6.3.2 FESEM images of (A-B) Bare and (C-D) Al_2O_3 modified WO_3 nanostructures at different magnifications

Structural features of *in-situ* grown WO_3 nanostructures were further ascertained by transmission electron microscopy (TEM) represented by **Figure 6.3.3**. Figure 6.3.3 (A-B) represents the TEM and HRTEM images of bare WO_3 respectively. From the HRTEM image, the lattice fringes with an interplanar distance of 0.365 nm correspond to the (200) crystal plane of WO_3. Figure 6.3.3 (C) and (D) represent the TEM and HRTEM images of Al_2O_3 modified WO_3 respectively. A porous thin layer of γ-Al_2O_3 can be seen over WO_3 structures from the TEM micrograph (C). HRTEM micrographs of modified WO_3 shown in trace D show an inter-planar distance of 0.308 and 0.241 nm, which corresponds to (112) and (311) plane of bare WO_3 and WO_3-Al_2O_3, respectively.

Part of this Chapter has been published in **Chem. Asian J., 2019, 14, 4673-4680**

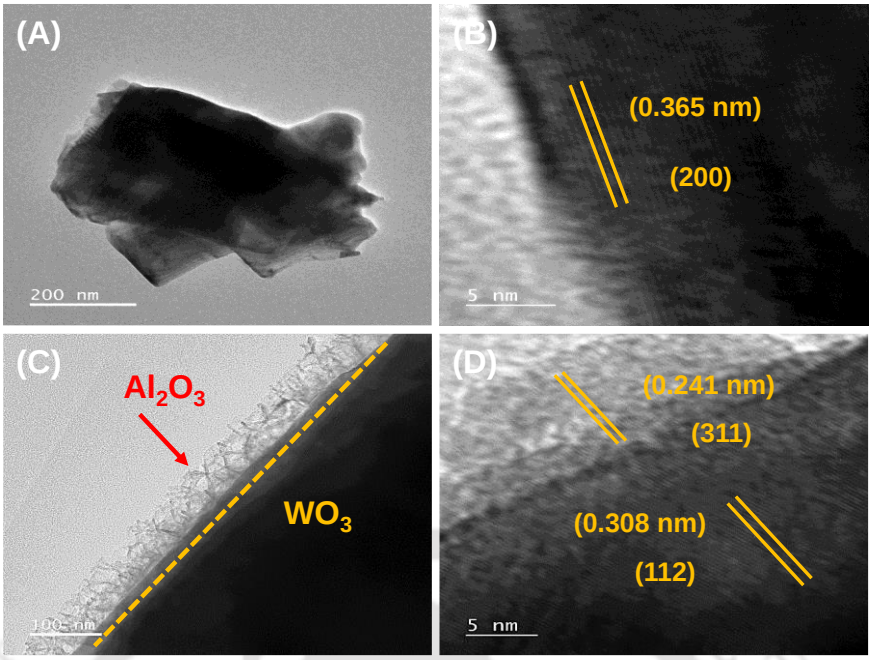

Figure 6.3.3 (A-B) TEM and HRTEM images of bare WO_3, and (C-D) TEM and HRTEM images of Al_2O_3 modified WO_3, respectively

STEM elemental analysis has been used to know the elemental composition and their distribution in Al_2O_3 modified WO_3 based device and **Figure 6.3.4** represents the same. From the figure, it is observed that all the elements i.e. Al, W, and O are homogeneously distributed throughout the materials in the scan area.

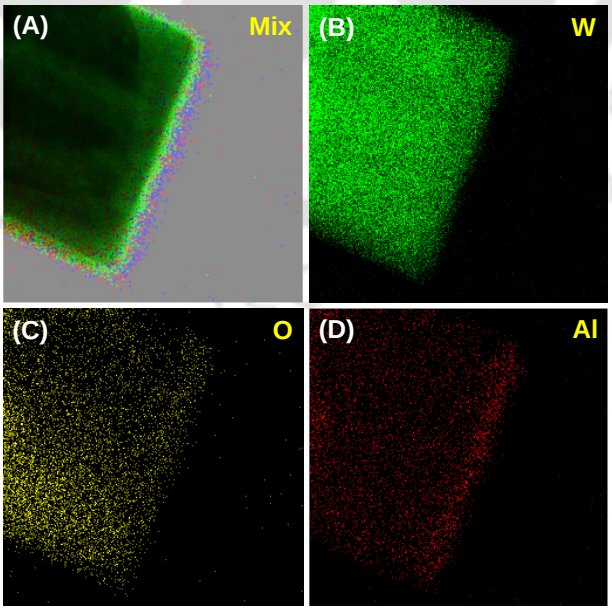

Figure 6.3.4 Elemental mapping of WO_3-Al_2O_3 photoanode showing the uniform distribution of all present elements i.e. W, O, and Al

Part of this Chapter has been published in **Chem. Asian J., 2019, 14, 4673-4680**

6.3.3 BET Surface Area analysis

Surface area and pore size are considered important features to assess the sensing performance of metal oxide-based Chemiresistor devices. From the Barrett-Joyner-Halenda (BJH) pore size distribution plots (**Figure 6.3.5**), the surface area for bare and modified structures is found to be 15.3 and 28.3 m^2/g, respectively. Interestingly, the pore size distribution for modified WO_3 structures suggests the presence of two types of pores, which are contributed from deposited alumina and WO_3 in the device: one in the range of 15-20 nm, while another in the range of 20-25 nm. On the other hand, the pore size distribution for bare WO_3 is in the range of 15-20 nm. The higher surface area and porosity obtained by the modified WO_3 device with Al_2O_3 provides more active sites for the gas molecules to adsorb and diffuse through the pores.

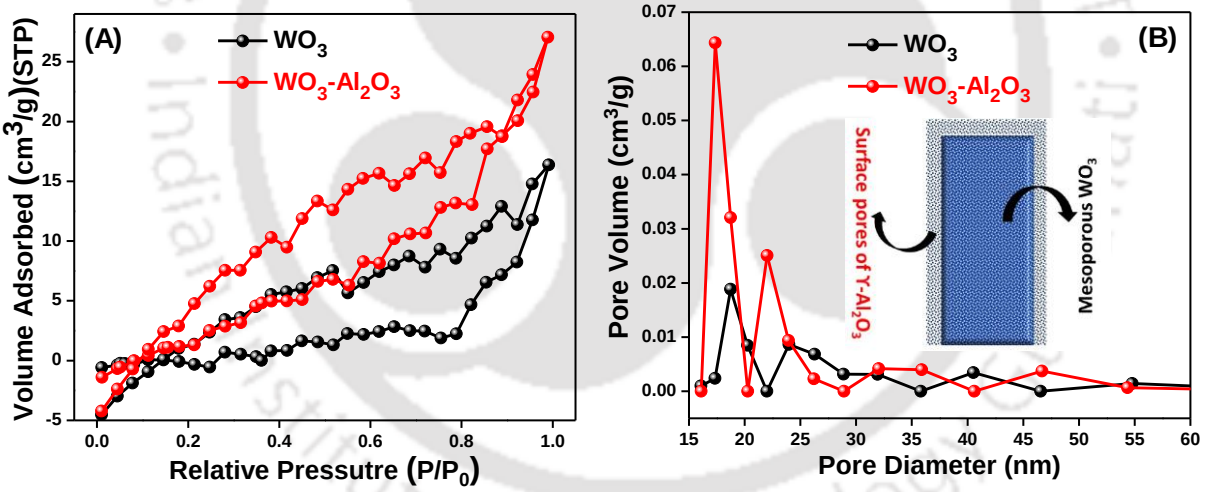

Figure 6.3.5 Barrett-Joyner-Halenda (BJH) (A) Surface area analysis curves and (B) Pore size distribution plots for as-synthesized bare and modified WO_3 respectively. Schematic showing the nature of pores in both WO_3 and its counterpart

6.3.4 X-ray Photoelectron Spectroscopy Analysis

To examine the effect of Alumina overlayer on surface defects of WO_3 surface and chemical information, X-ray photoelectron spectroscopic (XPS) analysis was performed for bare WO_3 and Al_2O_3 modified WO_3. **Figure 6.3.6 (A)** shows the XPS survey spectra of both

Part of this Chapter has been published in **Chem. Asian J., 2019, 14, 4673-4680**

as-synthesized WO_3 and WO_3-Al_2O_3. Here it is worth mentioning that the coverage of Al_2O_3 over the film is not 100 %, therefore characteristics of WO_3 along with Al_2O_3 can be seen in survey spectra complimenting the elemental mapping using STEM (Figure 6.3.4).

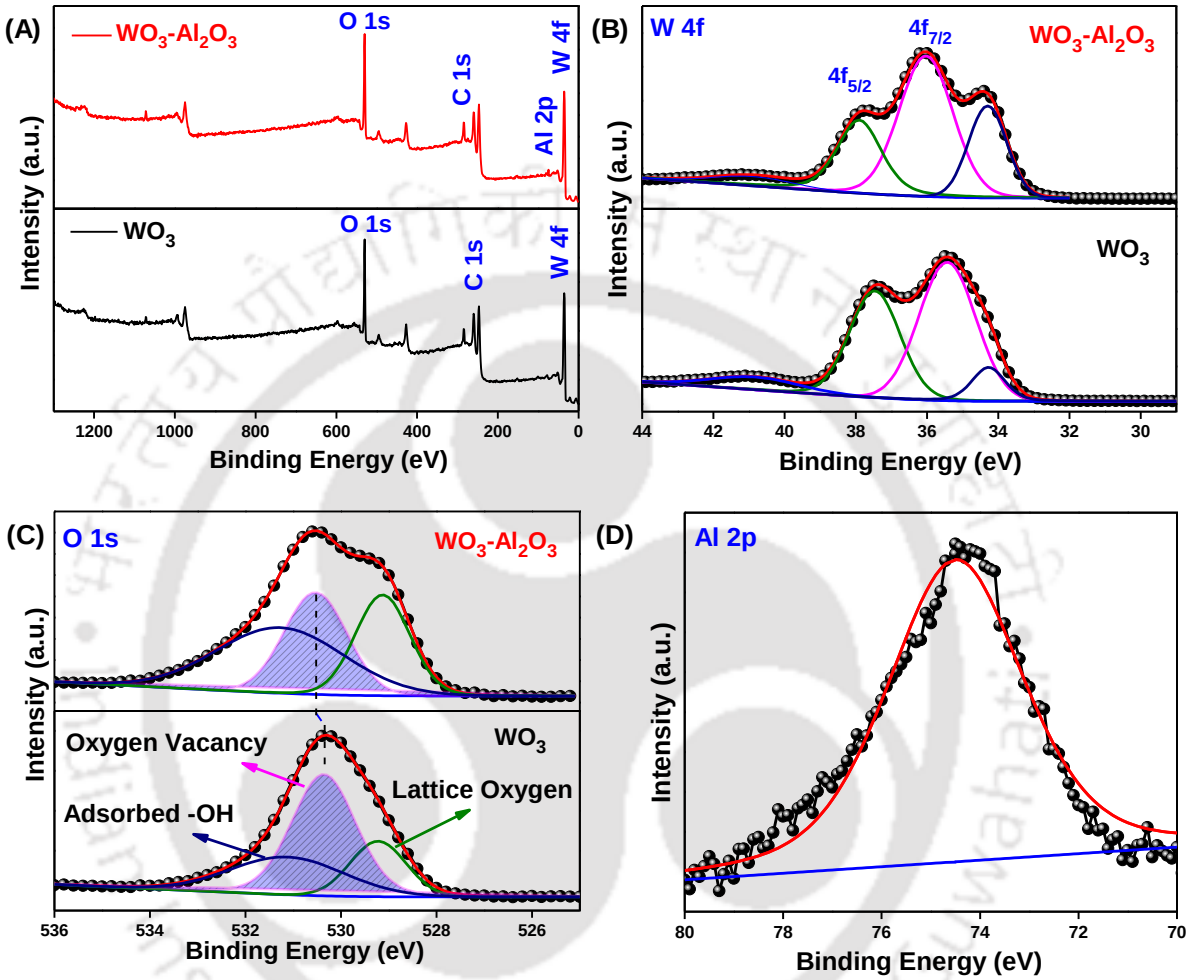

Figure 6.3.6 (A) XPS survey spectra of bare and Al_2O_3 modified WO_3; XPS spectra of (B) W 4f, (C) O 1s core-level XPS spectra of both bare and Al_2O_3 modified WO_3 and the shaded part correspond to the integrated area, and (D) core level spectra of Al 2p

From **Figure 6.3.6 (A)**, we can ascertain the presence of constituent elements, viz., W, and O in WO_3 and W, O, and Al in the composite. **Figure 6.3.6 (B)** depicts the W 4f core-level spectra of as-synthesized WO_3 and modified WO_3. In WO_3, two peaks appeared at binding energy (B. E.) of 35.43 eV and 37.43 eV correspond to W $4f_{7/2}$ and W $4f_{5/2}$, respectively. Similarly, in modified WO_3 two peaks appeared at the B. E. of 36.03 eV and 37.90 eV

Part of this Chapter has been published in **Chem. Asian J., 2019, 14, 4673-4680**

correspond to W $4f_{7/2}$ and W $4f_{5/2}$ respectively. The peak separation energy (Δ B. E.) of 2.04 eV signifying the presence of W (VI). **Figure 6.3.6 (C)** represents the O 1s core-level spectra of as-synthesized WO_3 and alumina modified WO_3. The asymmetric O 1s spectra of WO_3 and WO_3-Al_2O_3 upon deconvolution give three peaks at a binding energy of 529.22 eV, 530.36 eV, 531.13 and 529.13 eV, 530.53, 531.27 eV, respectively. The peak at lower B. E. can be assigned to lattice oxygen (O^{2-}) ($O_{latt.}$), peak at the middle region is due to oxygen vacancies and peak at higher B. E. related to the surface hydroxyl groups ($O_{ads.}$) in both the compounds[36]. A drastic decrease in the integrated area (shown as shaded part) corresponding to oxygen vacancies confirms the reduction in surface trap states with the alumina overlayer. In addition, the binding energy shift in this peak after the modification with alumina confirms the presence of Al – O[37]. **Figure 6.3.6 (D)** depicts the Al 2p core-level spectra of Al_2O_3 modified WO_3. The peak at 74.4 is attributed to the presence of Al^{2+}. This reduction in surface defects is responsible for the higher sensitivity of NO_X for Al_2O_3 modified WO_3 based Chemiresistor devices.

6.3.5 Sensing Studies of Chemiresistor Devices

Gas sensing properties of fabricated Chemiresistor devices were characterized by measuring current responses for selective and sensitive detection of NO_X gas in simulated exhaled breath. The current response is measured by fabricating a two-terminal Chemiresistor device. Different concentrations of gas are exposed onto the sensing surface and change in the current response is measured. It is worth mentioning that NO gas is highly reactive at ambient conditions and traditionally evaluated in the form of NO_X due to its mixed composition with different oxides of nitrogen, such as NO, NO_2, etc[38]. Please note that the initial gas injected onto the sensor is pure NO as generated, however, due to the extreme reactivity of NO gas, when it comes in contact with the atmosphere, some portion of the gas is known to get converted into NO_2, designated as NO_X[38]. The response of as-synthesized devices is ascertained

Part of this Chapter has been published in **Chem. Asian J., 2019, 14, 4673-4680**

via current-voltage (I-V) measurements by sweeping the voltage from -5 to +5 V, as shown in **Figure 6.3.7**.

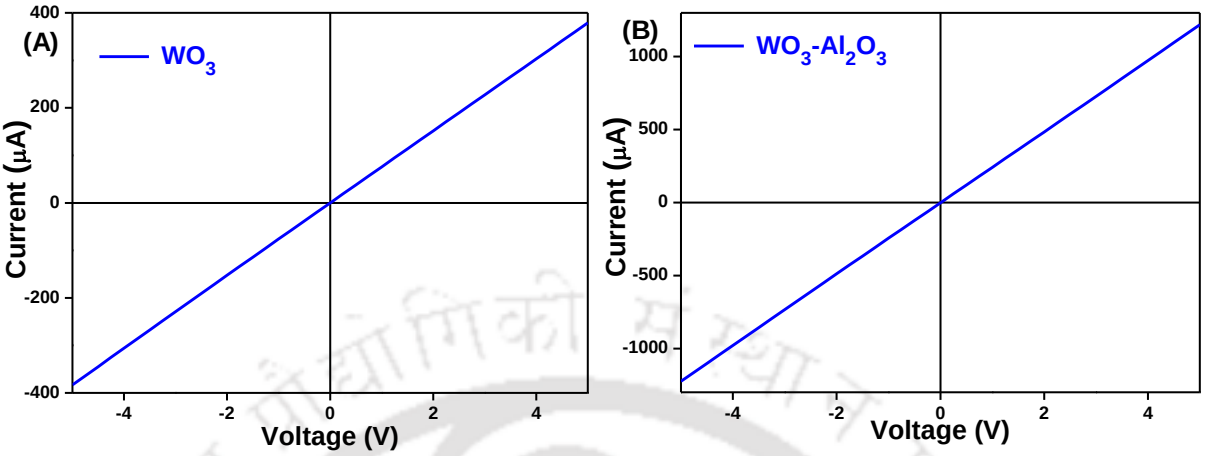

Figure 6.3.7 (A-B) Current-Voltage curves for as-fabricated sensing devices based on bare and modified WO_3 respectively

Calibration of the gas sensor was achieved by determining the change in current response as a function of time, without any analyte gas to minimize the contribution of factors neighboring to the sensor device as presented in **Figure 6.3.8**. These calibration curves are measured at a fixed bias voltage of + 3 V and the obtained current values at this bias for both bare and alumina modified WO_3 sensors are found to be comparable to that of current-voltage (I-V) values obtained in Figure 6.3.7[39].

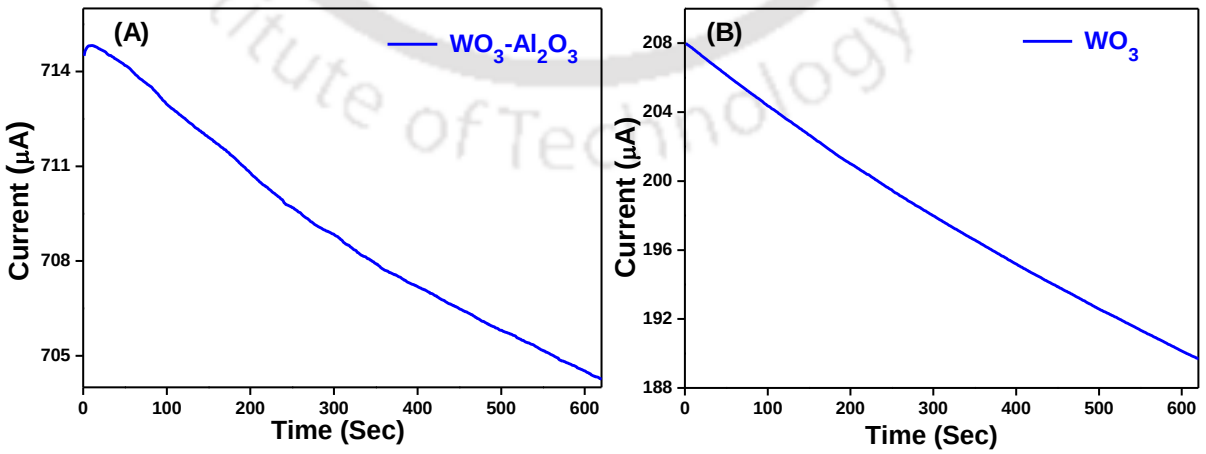

Figure 6.3.8 (A-B) Calibration curves for as-fabricated sensing devices based on bare and modified WO_3 respectively

Part of this Chapter has been published in **Chem. Asian J., 2019, 14, 4673-4680**

Selectivity of Chemiresistor devices is determined by injecting pre-mixed analyte gases, such as nitrogen, oxygen, carbon dioxide, argon along with water vapors (5 ppm), onto the Sensor device. **Figure 6.3.9 (A, B)** shows the current response bar diagram for selectivity plots for bare and modified WO_3 based devices, respectively. In addition, NH_3 vapors (1 ppm) mixed with a very low concentration of NO_X gas (200 ppb), are exposed to the sensing device. Negligible change in current response is observed in devices exposed to nitrogen, oxygen, carbon dioxide, argon, and water vapors. However, both devices exhibit significantly low sensing response for NH_3 vapors, when compared to a large change in the current response values for ultra-low concentrations of NO_X gas.

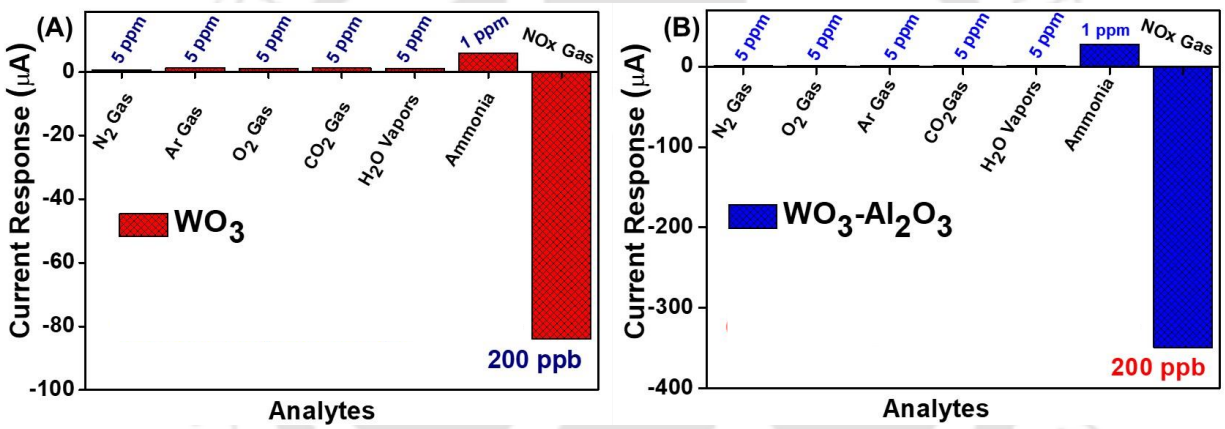

Figure 6.3.9 (A) and (B) Bar Diagram for selectivity plots of the components present in simulated exhaled air over devices based on bare and modified WO_3 respectively

Assessment of device response at saturated concentrations of NO_X gas is critical to assess the limitation of this sensor for practical applications. NO_X concentrations of 40-240 ppb are exposed under ambient conditions and responses are shown in **Figure 6.3.10**. With an increase in the concentrations of NO_X gas, there is a gradual decrease in the current response in both devices, which is in close agreement with literature reports. This response of the sensor is critical in understanding the sensing mechanism of NO_X. The gradual decrease in current response could be ascribed to the exposure of NO_X gas, as it extracts electrons from the WO_3 surface resulting in increased resistance (reduced carriers), which in-turn affords lower current

Part of this Chapter has been published in **Chem. Asian J., 2019, 14, 4673-4680**

values as represented in **Figure 6.3.10 (A)**[40]. Semiconducting metal oxides (SMOs)-based gas sensors are inherently hampered by the requirement of high recovery times, particularly at room temperature to the extent of hours. Gas sensing in SMOs strongly depends on the charge transfer interactions between sensing layers and chemisorbed species, which results in the variation of baseline resistance (thereby current) of the sensing layer. At room temperature, recovery of MO-based sensors or the stability of baseline is very difficult, as most of the reported MOS-based sensors operate at higher temperatures. It is clear from the above observations that both devices show good sensitivity for NO_X gas even at ultra-concentrations, critical for the detection of NO_X levels present in exhaled breath. WO_3-modified with Al_2O_3 was superior in comparison to the device based on bare WO_3. The role of alumina in enhancing the sensing performance of the device is solely based on two factors: (i) providing the surface coverage to minimize the surface defects and offers chemical stability and (ii) additional pore volume and surface area for the analytes to adsorb.

The limit of detection (LOD) of a sensor reflects its sensitivity where lower LOD values are indicative of a better sensitivity. In order to calculate LOD for our devices, different concentrations of NO_X gas are exposed to the sensing platform to obtain the current response pattern. For the determination of LOD, the calibration curve for both the devices are taken at 90 % change of the current response vs. different concentrations of NO_X gas. This calibration curve is represented by **Figure 6.3.10 (C) and (D)** for bare and modified WO_3 respectively. Further, these calibration curves are fitted linearly to get the slope and correlation coefficient (R^2) for both devices.

Part of this Chapter has been published in **Chem. Asian J., 2019, 14, 4673-4680**

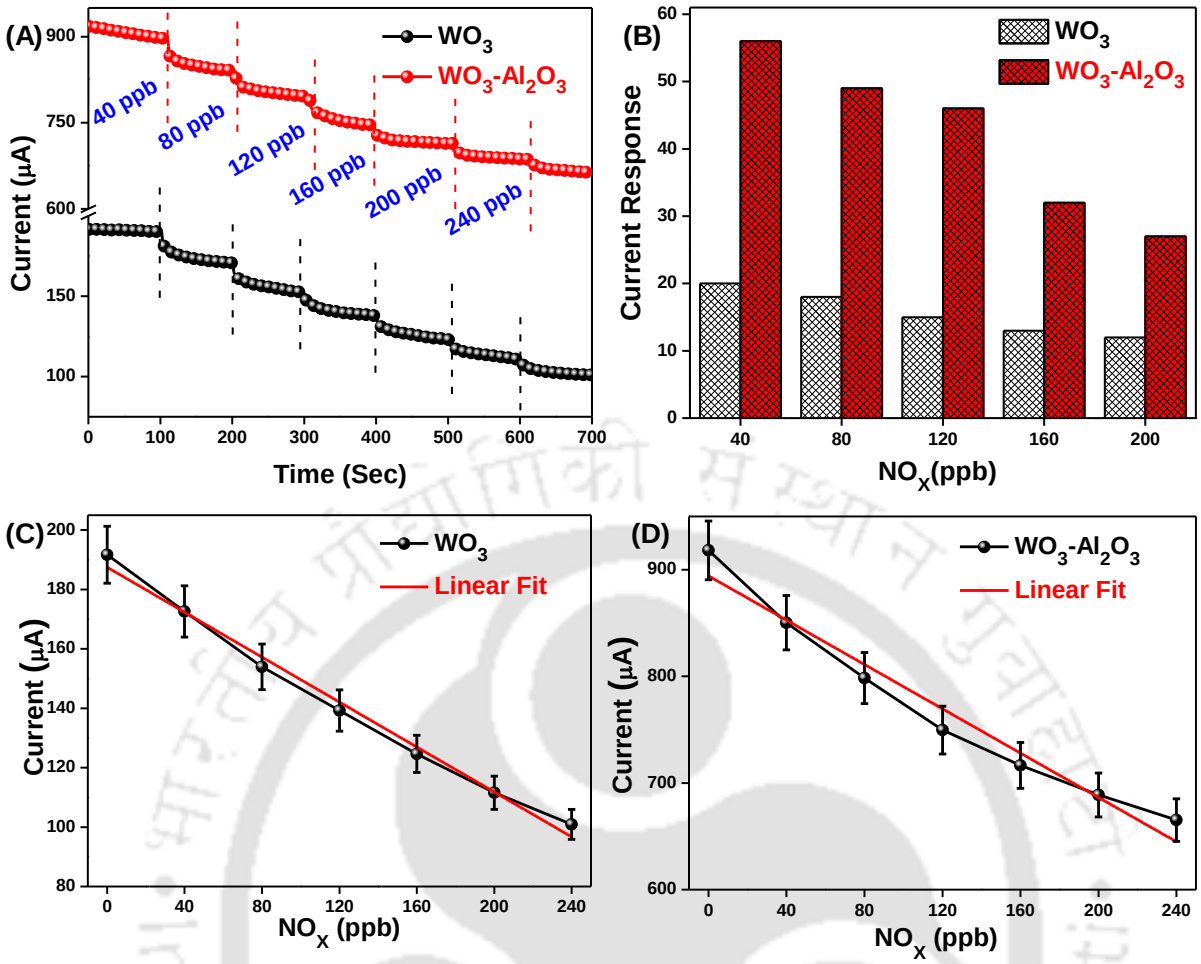

Figure 6.3.10 (A) and (B) Current response of bare and modified WO_3 respectively at different NO_X concentrations, and their corresponding bar diagram, Figure (C) and (D) are the calibration curves of sensing devices with error bars (±5%) based on bare and modified WO_3 for the calculation of LOD, respectively

The LOD for the sensor devices was calculated using the mathematical formula LOD = 3σ/S, where "σ" represents the relative standard deviation in the current responses without the exposure of NO_X gas and 'S' is the slope of the linearly fitted calibration curve. The LOD values obtained for devices based on bare and modified WO_3 are 19 (±5%) ppb and 8 (±5%) ppb respectively. On the basis of these LOD values, we propose that these newly constructed devices are highly sensitive with respect to the concentrations of NO (25 ppb) in healthy people. Introduction of Al_2O_3 in WO_3 based sensor device shows lower LOD value. This is mainly due to the reducing surface defects, higher surface area, and porosity provided by the modified WO_3 nanostructures. It is known that the higher the surface area, more are the active sites for

Part of this Chapter has been published in **Chem. Asian J., 2019, 14, 4673-4680**

binding gas molecules. The larger the pores, the higher is the diffusion of the gas molecules, resulting in higher sensitivity. These observations in the LOD values for higher sensitivities are also supported by BET and XPS analysis.

6.4 Conclusions

In summary, a controlled hydrothermal synthetic route has been described for *in-situ* seedless growth of WO_3 nanoblocks directly over FTO. Surface modification of these nanostructures is done via deposition of porous γ-Al_2O_3 by anodization. These devices are used to selectively detect NO_X gas from simulated human breath for the identification of asthma disease. WO_3-γ-Al_2O_3 based devices show high sensitivity/selectivity with a LOD value of 8 (±5%) ppb for NO_X gas as compared to the device based on bare WO_3, with a LOD value of 19 (±5%) ppb. We propose further development of this strategy and its integration in a hand-held platform for biomedical diagnostics.

6.5 References

(1) J. Shin, S.-J. Choi, I. Lee, D.-Y. Youn, C. O. Park, J.-H. Lee, H. L. Tuller and I.-D. Kim, *Adv. Funct. Mater.*, 2013, **23**, 2357.

(2) Z. Zhu, L. Zheng, S. Zheng, J. Chen, M. Liang, Y. Tian and D. Yang, *J. Mater. Chem. A*, 2018, **6**, 21419.

(3) M. Righettoni, A. Tricoli and S. E. Pratsinis, *Anal. Chem.*, 2010, **82**, 3581.

(4) T. Saidi, D. Palmowski, S. Babicz-Kiewlicz, T. G. Welearegay, N. El Bari, R. Ionescu, J. Smulko and B. Bouchikhi, *Sens. Actuators, B*, 2018, **273**, 1719.

(5) H. G. Moon, Y. Jung, S. D. Han, Y.-S. Shim, W.-S. Jung, T. Lee, S. Lee, J. H. Park, S.-H. Baek, J.-S. Kim, H.-H. Park, C. Kim and C.-Y. Kang, *Sens. Actuators, B*, 2018, **257**, 295.

(6) M. Righettoni, A. Amann and S. E. Pratsinis, *Mater. Today*, 2015, **18**, 163.

(7) H. G. Moon, Y. R. Choi, Y.-S. Shim, K.-I. Choi, J.-H. Lee, J.-S. Kim, S.-J. Yoon, H.-H. Park, C.-Y. Kang and H. W. Jang, *ACS Appl. Mater. Interfaces*, 2013, **5**, 10591.

Part of this Chapter has been published in **Chem. Asian J., 2019, 14, 4673-4680**

(8) S. Awano, T. Ansai, Y. Takata, I. Soh, A. Yoshida, T. Hamasaki, S. Kagiyama, I. Nakamichi, K. Sonoki and T. Takehara, *J. Breath Res.*, 2008, **2**, 017012.

(9) L. R. Narasimhan, W. Goodman, and C. Kumar N. Patel, *Proc Natl Acad Sci U S A.*, 2001, **98**, 4617.

(10) J. Shin, S.-J. Choi, D.-Y. Youn and I.-D. Kim, *J. Electroceram*, 2012, **29**, 106.

(11) P. I. Goumaa and K. Kalyanasundaram, *Appl. Phys. Lett.*, 2008, **93**, 244102.

(12) G. Peng, U. Tisch, O. Adams, M. Hakim, N. Shehada, Y. Y. Broza, S. Billan, R. Abdah-Bortnyak, A. Kuten and H. Haick, *Nature Nanotech*, 2009, **4**, 669.

(13) G. T. De Sanctis, J. A. MacLean, K. Hamada, S. Mehta, J. A. Scott, A. Jiao, C. N. Yandava, L. Kobzik, W. W. Wolyniec, A. J. Fabian, C. S. Venugopal, H. Grasemann, P. L. Huang, and J. M. Drazen, *J. Exp Med.*, 1999, **189**, 1621.

(14) M. Maniscalco, C. Vitale, A. Vatrella, A. Molino, A. Bianco, and G. Mazzarella, *Med Devices (Auckl).*, 2016, **9**, 151.

(15) H. K. Gatty, S. Leijonmarck, M. Anteliusa, G. Stemme and N. Roxheda, *Sens. Actuators, B*, 2015, **209**, 639.

(16) R. A. Dweik, P. B. Boggs, S. C. Erzurum, C. G. Irvin, M. W. Leigh, J. O. Lundberg, A.-C. Olin, A. L. Plummer and D. R. Taylor, *Am J Respir Crit Care Med.*, 2011, **184**, 602.

(17) W. Cao and Y. Duan, *Crit Rev Anal Chem.*, 2007, **37**, 3.

(18) A. Staerz, U. Weimar, and N. Barsan, *Sensors*, 2016, **16**, 1815.

(19) V. Saasa, T. Malwela, M. Beukes, M. Mokgotho, C.-P. Liu and B. Mwakikunga, *Diagnostics*, 2018, **8**, 12.

(20) C. Sun, G. Maduraiveeran and P. Dutta, *Sens. Actuators, B*, 2013, **186**, 117.

(21) E. Wu, Y. Xie, B. Yuan, H. Zhang, X. Hu, J. Liu and D. Zhang, *ACS Sens.*, 2018, **3**, 1719.

(22) A. Dey, *Mater. Sci. Eng., B*, 2018, **229**, 206.

(23) S. J. Kim, S. J. Choi, J. S. Jang, N. H. Kim, M. Hakim, H. L. Tuller and I. D. Kim, *ACS Nano*, 2016, **10**, 5891.

(24) D. Chen, L. Yin, L. Ge, B. Fan, R. Zhang, J. Sun and G. Shao, *Sens. Actuators, B*, 2013, **185**, 445.

(25) M. Drobek, J. H. Kim, M. Bechelany, C. Vallicari, A. Julbe and S. S. Kim, *ACS Appl. Mater. Interfaces*, 2016, **8**, 8323.

(26) L. L. Deng, C. X. Zhao, Y. Ma, S. S. Chen and G. Xu, *Anal. Methods*, 2013, **5**, 3709.

(27) J. Hu, J. Yang, W. D. Wang, Y. Xue, Y. J. Sun, P. W. Li, K. Lian, W. D. Zhang, L. Chen, J. Shi and Y. Chen, *Mater. Res. Bull.*, 2018, **102**, 294.

(28) P. Gouma, K. Kalyanasundaram, X. Yun, M. Stanacevic, and L. Wang, *IEEE Sensors Journal*, 2010, **10**, 49.

(29) S. Chakraborty, D. Banerjee, I. Ray and A. Sen, *Current Science*, 2008, **94**, 237.

(30) Y. Liu, S. Yao, Q. Yang, P. Sun, Y. Gao, X. Liang, F. Liu and G. Lu, *RSC Adv.*, 2015, **5**, 52252.

(31) L. Chen, L. Huang, Y. Lin, L. Sai, Q. Chang, W. Shi and Q. Chen, *Sens. Actuators, B*, 2018, **255**, 1482.

(32) J. Y. Shen, M. Di Wang, Y. F. Wang, J. Y. Hu, Y. Zhu, Y. X. Zhang, Z. J. Li and H. C. Yao, *Sens. Actuators, B*, 2018, **256**, 27.

(33) D.-H. Kim, J.-S. Jang, W.-T. Koo, S.-J. Choi, S.-J. Kim and I.-D. Kim, *Sens. Actuators, B*, 2018, **259**, 616.

(34) W.-T. Koo, S.-J. Choi, N.-H. Kim, J.-S. Jang and I.-D. Kim, *Sens. Actuators, B*, 2016, **223**, 301.

(35) J. Su, L. Guo, N. Bao and C. A. Grimes, *Nano Lett.*, 2011, **11**, 1928.

(36) A. Mozalev, M. Bendova, F. Gispert-Guirado, Z. Pytlicek and E. Llobet, *J. Mater. Chem. A*, 2016, **4**, 8219.

(37) Z. Fan, Z. Xu, S. Yan and Z. Zou, *J. Mater. Chem. A*, 2017, **5**, 8402.

(38) R. Pohle, E. Magori, A. Tawil, P. Davydovskaya, and M. Fleischer, *Proceedings*, 2017, **1**, 490.

(39) M. S. Ansari, A. Banik, A. Kalita, P. K. Iyer and M. Qureshi, *J. Mater. Chem. A*, 2018, **6**, 15868.

(40) D.-H. Kim, J.-W. Jung, S.-J. Choi, J.-S. Jang, W.-T. Koo, and I.-D. Kim, *Sens. Actuators, B*, 2018, **273**, 1269.

Part of this Chapter has been published in **Chem. Asian J., 2019, 14, 4673-4680**

THESIS SUMMARY

AND

FUTURE PERSPECTIVE

Thesis Summary:

This thesis outlined several aspects in design and development of metal oxide-based photoanodic architecture to improve photoelectrochemical water splitting performance. ZnO and $BiVO_4$ have been used as model systems to fabricate photoanodes for photoelectrochemical water oxidation. Several efforts such as different morphology, heterojunction formation, and surface modifications with co-catalysts have been made to enhance the photoelectrochemical activity. This thesis follows the order: firstly, an overview of global energy consumption and future requirement, need for a sustainable energy source to produce zero-emission H_2, is given in **Chapter 1.** Also**,** a brief literature survey on current scenario as well as challenges associated with the fabrication of photoanode is discussed. In the later section, a short introduction to metal oxide-based Chemiresistor sensor devices and performance parameters is also included. At last, this chapter is concluded with the objectives of the present thesis. **Chapter 2** comprises a short discussion on different techniques used for the characterization of as-synthesized materials and fabricated photoanodes. This chapter is concluded with the working principle and performance parameters of Chemiresistor sensor device. The summary and conclusions for each chapter i.e. **chapter 3** to **chapter 6** provide some valuable outcomes which are obtained from the work done during my Ph.D. tenure and summarized as follows:

- In **chapter 3**, we have demonstrated the idea of ternary photoanode which comprises a p-n heterojunction for efficient separation of photogenerated charge carriers. In the process of forming p-n heterojunction, first n-type $BiVO_4$ was electrodeposited over FTO and then p-type CoSn-LDH mixed metal hydroxide was deposited over $BiVO_4$ surface via facile one-step low-temperature hydrothermal method. This p-n heterojunction was then linked with a conductive linker GQDs for efficient extraction and injection of photogenerated charge carriers from $BiVO_4$ surface to CoSn-LDH

active sites, respectively. GQDs provide an extra driving force to extract holes from the $BiVO_4$ surface due to the presence of negatively charged species and further transfer to CoSn-LDH, which accelerates the transportation of holes to the electrolyte for the enhanced water oxidation reaction. A maximum current density of 4.15 mA/cm^2 for $BiVO_4$/GQDs/CoSn-LDH photoanode was obtained, which is 3 more than times higher than pristine $BiVO_4$ (1.33 mA/cm^2). Apart from the enhanced photocurrent density, a cathodic shift of 250 mV in onset potential was also observed, indicates that the lower overpotential is required for water oxidation. Operational stability of $BiVO_4$/GQDs/CoSn-LDH photoanode improved as it preserved ~90 % of the initial value after 4 hr of continuous illumination.

- In **chapter 4,** we have demonstrated the beneficial role of 1-D Co(OH)F nanorods, a noble metal-free redox mediator in enhancing the photoelectrochemical performance. Here, we have used $BiVO_4$ as a model system and modified it with Co(OH)F as co-catalysts to improve the surface kinetics. Presence of F in cobalt-based hydroxides not only improves the conductivity but also helps in increasing the charge mobility. A maximum current density of 3.4 mA/cm^2 was obtained for $BiVO_4$/Co(OH)F photoanode, which is 2.4 times higher than pristine $BiVO_4$ (1.45 mA/cm^2). This significant enhancement in photocurrent density for $BiVO_4$/Co(OH)F photoanode is primarily due to the reduced recombination of photogenerated charge carriers by virtue of redox ability of Co(OH)F as it extracts holes from $BiVO_4$ surface. Mechanistically, Co^{2+} ions are known to act as active sites to receive holes from semiconductors and oxidized to Co^{3+} or/and Co^{4+}. Subsequently these active species, Co^{3+} or/and Co^{4+} release the positive charge to produce O_2 and recover to the initial state. We have also compared the activity of as-synthesized Co(OH)F with benchmark catalysts of cobalt such as Co_3O_4 and $Co(OH)_X$, and result shows the better performance of Co(OH)F.

- In **Chapter 5,** we have synthesized hierarchical ZnO superstructures using biomass-derived templating agent "Polygalacturonic Acid" directly over FTO. Here used Polygalacturonic acid acts as an assembling agent to construct hierarchical structures in a particular direction. We have studied the plausible growth mechanism of ZnO nanocrystals to form superstructures by changing the reaction conditions. Low ohmic resistance offered by *In-situ* grown hierarchical ZnO superstructures, resulting in enhanced transportation and collection of photogenerated charge carriers. Further, these structures were modified with graphene quantum dots as an efficient hole extractor to enhance the photoelectrochemical performance. A maximum photocurrent of 0.61 mA/cm^2 was observed for GQDs modified hierarchical ZnO superstructures, as compared to 0.35 mA/cm^2 for pristine ZnO-based photoanode. Higher surface area of GQDs modified ZnO photoanode provides more active sites for water oxidation as well as the presence of negative charge species on GQDs surface extracts holes from ZnO, resulting in reduced recombination of photogenerated charge carriers.
- In **chapter 6,** we have reported one-step hydrothermal synthesized WO_3 Nanoblocks directly over FTO, followed by the deposition of porous γ-Al_2O_3 for selective and ultrasensitive detection of NO_X in exhaled breath. The importance of these structures is that they are grown directly over FTO without using any seed layer to minimize the Ohmic resistance, beneficial for smooth transfer of charge carriers, thereby enhancing the sensitivity of the device. Gas sensing properties were evaluated by fabricating a two-terminal Chemiresistor device. Selectivity towards NO_X for both the devices was confirmed by exposing different interfering gases as well as volatile organic compounds. Alumina modified WO_3 device shows better sensitivity for NO_X with a LOD value of 8 ppb as compared to 19 ppb for bare WO_3 based device. The better sensitivity of alumina modified device is mainly due to the reduced surface defects

resulting in the smoother transport of electrons to the collection electrode. Also, the higher surface area and porosity of alumina-modified WO_3 based devices provide more active sites for gas molecules to adsorb onto the surface and diffuse through the pores.

Future Perspective

Research work carried out in the presented thesis outlined several aspects and new findings in design and development of metal oxide-based photoelectrochemical/Chemiresistor devices. Extensive study on metal oxide-based photoanodes was carried out to resolve several issues related to charge carrier transportation, surface recombination, and interfacial contacts. Presented approaches have made significant advancements in the field of PEC water splitting, still several challenges remain to further improve the efficiency, stability and to scale up the fabrication.

- ✓ Sensitization of metal oxide-based photoanodes with Pb free stable inorganic perovskites to improve the PEC performance
- ✓ Synthesizing metal oxides with a particular exposed facet and depositing co-catalysts over that facet helps in improving the photoelectrochemical performance
- ✓ Hybridization of semiconductor metal oxide with materials having high specific surface area is a feasible approach to enhance the surface-active sites for photoelectrochemical water oxidation
- ✓ Synthesizing hierarchical morphologies using easily removable soft templates, helps in charge transportation results in improved photoelectrochemical performance
- ✓ Metal oxide surface complexation with organic/inorganic moieties for selective and sensitive detection of volatile organic compounds/toxic gases

LIST OF PUBLICATIONS AND CONFERENCES/WORKSHOPS ATTENDED

Journal Articles:

Included in Thesis:

1. ***Suhaib Alam***, Mohammad Qureshi, Interfacial Bridging Strategy for Charge Extraction/Injection in $BiVO_4$/CoSn-LDH p-n Heterojunction using GQDs for Enhanced Water Oxidation Kinetics. ***J. Phys. Chem. Lett.***, 2021, **12**, 8955-8957.
2. ***Suhaib Alam***, Tushar Kanta Sahu, Mohammad Qureshi, One-Dimensional Co(OH)F as a Noble Metal-Free Redox Mediator and Hole Extractor for Boosted Photoelectrochemical Water Oxidation in Worm-like Bismuth Vanadate. ***ACS Sustainable Chem. Eng.***, 2021, **9**, 5155-5165.
3. ***Suhaib Alam***, Tushar Kanta Sahu, Devipriya Gogoi, Nageswara Rao Peela, Mohammad Qureshi, Bio-template Assisted Hierarchical ZnO Superstructures Coupled with Graphene Quantum Dots for Enhanced Water Oxidation Kinetics. ***Sol. Energy***, 2020, **199**, 39-46.
4. ***Suhaib Alam***, Mohamad Shaad Ansari, Avishek Banik, Rafat Ali, Sandeep Verma, Mohammad Qureshi, Ultrasensitive NO_X Detection in Simulated Exhaled Air: Enhanced Sensing via Alumina Modification of *In-Situ* Grown WO_3 Nanoblocks. ***Chem. – Asian J.***, 2019, **14**, 4673-4680.

Work Contributed Off the Thesis:

1. Tushar Kanta Sahu, ***Suhaib Alam***, Sourav Bhowmick, Manoj Kumar Mohanta, Mohammad Qureshi, Phosphorus Nitride Nano-dots as a Versatile and Metal-free Support for Efficient Photoelectrochemical Water Oxidation. ***Chem. Commun.***, 2021, **57**, 6157-6160.
2. Sourav Bhowmick, ***Suhaib Alam***, Adit Kumar Shah, Mohammad Qureshi, Bimetallic Cyclic Redox Couple in Di-manganese Copper Oxide Supported by Nickel Borate for Boosted Alkaline Electrocatalytic Oxygen Evolution Reaction. ***Sustain. Energy Fuels***, 2021, **5**, 2517-2527.
3. Tushar Kanta Sahu, ***Suhaib Alam***, Devipriya Gogoi, Nageswara Rao Peela, Mohammad Qureshi, Effect of Catalytically Silent Cerium Hydroxide in Cobalt–Cerium Mixed Double Hydroxide for Enhanced Water Oxidation Kinetics in a $BiVO_4$ Photoanode. ***ACS Appl. Energy Mater.***, 2020, **3**, 6, 5610-5619.

4. Manoj Kumar Mohanta, Tushar Kanta Sahu, ***Suhaib Alam***, Mohammad Qureshi, Tuning the Electronic Structure of Monoclinic Tungsten Oxide Nanoblocks by Indium Doping for Boosted Photoelectrochemical Performance. ***Chem. – Asian J.***, 2020, **15**, 3886-3896.
5. Mohammad Shaad Ansari, Avishek Banik, ***Suhaib Alam***, Mohammad Qureshi, Combined Effect of *in-situ* Grown p-type $CuSbS_2$/n-type CdS Coupled with Hierarchical ZnO Nano- disks for Improved Photovoltaic Light Harvesting Efficiency. ***J. Power Sources***, 2019, **425**, 204-216.
6. Avishek Banik, Mohammad Shaad Ansari, ***Suhaib Alam***, Mohammad Qureshi, Thermodynamic Barrier and Light Scattering Effects of Nano-cube Assembled $SrTiO_3$ in Enhancing the Photovoltaic Properties of Zinc Oxide Based Dye-Sensitized Solar Cells. ***J. Phys. Chem. C***, 2018, **122**, 29, 16550-16560.

Conferences/Workshops:

1. International Conference on Recent Advances and Innovations in Solar Energy (**RAiSE-2021**) 2-4 December, 2021, Indian Institute of Technology Madras, Chennai, India (Oral Presentation)
2. International Conference on Light Matter Interaction (**ICLMIN-2021**), 19-21 May, 2021, Indira Gandhi Centre for Atomic Research (IGCAR), Kalpakkam, India (Attended)
3. 5th International Conference on Advanced Nanomaterials and Nanotechnology (**ICANN-2017**), 18-21 December, 2017, Indian Institute of Technology Guwahati, Guwahati, India (Poster Presented)
4. Research Conclave'17, 16-19 March, 2017, Indian Institute of Technology Guwahati, Guwahati, India (Poster Presented)
5. 3rd National Workshop on MEMS/NEMS and Theranostic Devices, 21-23 March, 2017, Indian Institute of Technology Guwahati, Guwahati, India (Attended)
6. One Day Workshop on "Biomedical Device Technology" 18th December, 2017, Indian Institute of Technology Guwahati, Guwahati, India (Attended)
7. International Conference on Frontiers in Chemical Sciences (**FICS-2018**), 6-8 December, 2018, Indian Institute of Technology Guwahati, Guwahati, India (Poster Presented)
8. Research Conclave'18, 08-11 March, 2018, Indian Institute of Technology Guwahati, Guwahati, India (Poster Presented)
9. 6th International Conference on Advanced Nanomaterials and Nanotechnology (**ICANN-2019**), 18-21 December, 2019, Indian Institute of Technology Guwahati, Guwahati, India (Poster Presented)
10. Indo-US Webinar and Lecture Series, 1-9 June, 2021, Jamia Millia Islamia, New Delhi, India (Attended)